UNIVERSITI TEKNOLOGI MARA

OPTIMIZATION AND STEPWISE CHEMICAL MODIFICATIONS OF SUNFLOWER OIL UNSATURATED FATTY ACIDS FOR THE PRODUCTION OF BIOLUBRICANT BASE STOCK

MUHAMMAD MUIZZUDDIN BIN KHAIRUDDIN

PhD

August 2026

UNIVERSITI TEKNOLOGI MARA

OPTIMIZATION AND STEPWISE CHEMICAL MODIFICATIONS OF SUNFLOWER OIL UNSATURATED FATTY ACIDS FOR THE PRODUCTION OF BIOLUBRICANT BASE STOCK

MUHAMMAD MUIZZUDDIN BIN KHAIRUDDIN

Thesis submitted in fulfilment
of the requirements for the degree of
Doctor of Philosophy
(Science)

Faculty of Applied Sciences

August 2026

CONFIRMATION BY PANEL OF EXAMINERS

I certify that a Panel of Examiners has met on 14 July 2026 to conduct the final examination of Muhammad Muizzuddin Bin Khairuddin on his Doctors of Philosophy thesis entitled "Optimization and Stepwise Chemical Modifications of Sunflower Oil Unsaturated Fatty Acids for the Production of Biolubricant Base Stock" in accordance with Universiti Teknologi MARA Act 1976 (Akta 173). The Panel of Examiner recommends that the student be awarded the relevant degree. The Panel of Examiners was as follows:

Raja Razuan Raja Deris, PhD
Associate Professor
Faculty of Applied Sciences
Universiti Teknologi MARA
(Chairman)

Noraini Hamzah, PhD
Associate Professor
Faculty of Applied Sciences
Universiti Teknologi MARA
(Internal Examiner)

Muhammad Rahimi Yusof, PhD
Professor
Faculty of Science and Technology
Universiti Kebangsaan Malaysia
(External Examiner)

PROF DR HJH ZURAEDA IBRAHIM
Dean
Institute of Postgraduates Studies
Universiti Teknologi MARA

Date: 14 August 2026

AUTHOR'S DECLARATION

I declare that the work in this thesis was carried out in accordance with the regulations of Universiti Teknologi MARA. It is original and is the results of my own work, unless otherwise indicated or acknowledged as referenced work. This thesis has not been submitted to any other academic institution or non-academic institution for any degree or qualification.

I, hereby, acknowledge that I have been supplied with the Academic Rules and Regulations for Post Graduate, Universiti Teknologi MARA, regulating the conduct of my study and research.

Name of Student	:	Muhammad Muizzuddin Bin Khairuddin
Student ID. No.	:	2022804196
Programme	:	Doctor of Philosophy (Science) – AS950
Faculty	:	Applied Sciences
Thesis Title	:	Optimization and Stepwise Chemical Modifications of Sunflower Oil Unsaturated Fatty Acids for the Production of Biolubricant Base Stock
Signature of Student	:	
Date	:	August 2026

ABSTRACT

This study focuses on the production of renewable biolubricant base stocks derived from sunflower oil (SFO) as sustainable alternatives to conventional mineral oil–based lubricants. Plant oils offer significant advantages, including renewability, high biodegradability and reduced environmental impact. However, their direct application as lubricant base oils is limited by the low oxidative stability caused by the presence of β-hydrogen on the glycerol backbone and carbon–carbon double bonds (C=C) in the fatty acid chains. To overcome these limitations, stepwise chemical modifications involving esterification, epoxidation and ring-opening reactions were employed to enhance oxidative stability and low-temperature properties. SFO was first hydrolyzed using 2.4 M ethanolic KOH at 51 °C for 1.4 hours to produce sunflower oil fatty acids (SFOFA). The fatty acids were then separated into unsaturated (SFOUFA) and saturated (SFOSFA) fractions using methanol crystallization at a 1:15 oil-to-methanol ratio, −15 °C and 24 hours. The SFOUFA fraction was then esterified with different polyhydric alcohol (neopentyl glycol (NPG), trimethylolpropane (TMP) and pentaerythritol (PE)) under optimized conditions to produce several polyol esters: SFOUFANPGE (molar ratio 3.2:1, 1.37% H_2SO_4, 149 °C, 4 hours), SFOUFATMPE (molar ratio 4:1, 1.13% H_2SO_4, 154 °C, 6 hours) and SFOUFAPEE (molar ratio 5:1, 1.08% H_2SO_4, 177 °C, 6.9 hours). Among these polyol esters, SFOUFATMPE exhibited the highest oxidative stability and was selected for further modification. Epoxidation of SFOUFATMPE was carried out using formic acid and hydrogen peroxide (7:2 molar ratio), with 1.2% H_2SO_4 at 41 °C for 3.5 hours to reduce the C=C and further improve oxidative stability, producing ESFOUFATMPE. Subsequently, ring-opening of the epoxidized product with oleic acid (4.6 mol, 1.09% H_2SO_4, 130 °C, 4.9 hours) was performed to introduce molecular branching and enhance low-temperature performance, yielding DOSFOUFATMPE. All reactions were optimized using response surface methodology (RSM) based on a D-optimal experimental design. The final ring-opened biolubricant (DOSFOUFATMPE) exhibited a pour point of −24 °C, flash point of 310 °C, kinematic viscosities of 60.02 cSt at 40 °C and 12.03 cSt at 100 °C, a viscosity index of 150, oxidative stability of 33 minutes and Newtonian rheological behaviour. The stepwise modification successfully overcame the main limitations of plant oils by removing the β-hydrogen through polyol ester formation and reducing the reactivity of C=C through the epoxidation resulting in the improvement of oxidative stability. Overall, this study demonstrates that stepwise chemical modification combined with RSM optimization is an effective strategy for producing a sunflower oil–based biolubricant base stocks with strong potential to replace mineral oil lubricants. The findings also support the development of sustainable and renewable materials in line with the Sustainable Development Goals (SDG), particularly responsible consumption and production (SDG 12) and climate action (SDG 13).

ACKNOWLEDGEMENT

With profound gratitude and a sense of deep appreciation, I offer my heartfelt thanks to the Almighty for His blessings and guidance. It is through His benevolence and permission that I have completed this PhD thesis. This achievement marks the successful completion of years of dedication, perseverance, and learning, and it would not have been possible without the unwavering support, encouragement, and assistance of many individuals, to whom I am sincerely and profoundly grateful.

I extend my sincerest thanks to Dr. Nurazira Mohd Nor, my main supervisor, whose wisdom and guidance have been invaluable throughout this research journey. Dr. Nurazira provided not only academic counsel but also unwavering encouragement, inspiring me to persevere even when faced with challenges. Despite my occasional lapses in heeding her advice, she remained dedicated to offering her insights and support. I would also like to express my heartfelt appreciation to my co-supervisor, Ts. Dr. Asiah Abdullah, who generously shared her expertise, guidance and unflagging support without reservation.

In addition to my esteemed mentors, I am deeply grateful to my beloved family members: my father, Khairuddin Mustapha, my mother, my brother, Muhammad Hafizzuddin Khairuddin and my younger siblings, Nur Humaira and Muhammad Faizzuddin Khairuddin. Their unwavering encouragement and boundless enthusiasm have been a constant source of motivation for me throughout this research journey.

I would also like to express my sincere appreciation to my friends, Farez Ammar, Nurnabila, Khairi Hamdan, Hafizol, Zulfadzly, Aiman Aidi and Anis Farhana, as well as all my friends from Kawan Sampai Syurga who have always been by my side. Their friendship, encouragement and continuous support throughout this journey have been a great source of motivation and strength.

In addition, my heartfelt thanks are extended to my laboratory mates, Azhan Arif, Aisyah Zamzuri, Jannah and Najiha, including the Hikers group, for their cooperation, assistance and positive environment in the laboratory. Their support and companionship made the research process more enjoyable and meaningful.

Lastly, I extend my sincere and profound appreciation to the staff of the chemistry laboratory and the lecturers at PPKAS. Their direct and indirect assistance, technical guidance, provision of materials and access to laboratory facilities were instrumental in the successful completion of my research.

TABLE OF CONTENTS

		Page
CONFIRMATION BY PANEL OF EXAMINERS		**ii**
AUTHOR'S DECLARATION		**iii**
ABSTRACT		**iv**
ACKNOWLEDGEMENT		**v**
TABLE OF CONTENTS		**vi**
LIST OF TABLES		**xiii**
LIST OF FIGURES		**xxii**
LIST OF SYMBOLS		**xxix**
LIST OF ABBREVIATIONS		**xxx**
CHAPTER 1 INTRODUCTION		**1**
1.1	Research Background	1
1.2	Problem Statement	3
1.3	Scope and Limitation of Study	4
1.4	Significance of Study	6
1.5	Objectives of Study	7
CHAPTER 2 LITERATURE REVIEW		**9**
2.1	Lubricant	9
2.2	Biolubricant from Plant Oil	13
2.3	Sunflower oil	18
2.4	Hydrolysis of Plant Oil	21
2.5	Separation of Fatty Acids	23
2.6	Esterification Reaction	25
2.7	Polyol Ester	27
2.8	Epoxidation Reaction	30
2.9	Ring Opening Reaction	32
2.10	Response Surface Methodology	34
2.11	Physicochemical Properties of Oil	36

2.11.1 Iodine Value 36
2.11.2 Acid Value and Free Fatty Acids 37
2.11.3 Saponification Value 38
2.11.4 Pour Point 39
2.11.5 Flash Point 40
2.11.6 Viscosity and Viscosity Index 40
2.11.7 Oxidative stability 41
2.12 Previous Studies Related to Biolubricant 41

CHAPTER 3 RESEARCH METHODOLOGY 43
3.1 Material 43
3.1.1 Raw Material 43
3.1.2 Chemicals 43
3.1.3 Apparatus 43
3.2 Determination of Physicochemical properties and Characterization of Sunflower Oil 44
3.2.1 Physicochemical Properties of SFO 44
3.2.1.1 Iodine Value 44
3.2.1.2 Acid Value 45
3.2.1.3 Free Fatty Acids Value 45
3.2.1.4 Moisture Content 46
3.2.1.5 Saponification Value 46
3.2.1.6 Pour Point 47
3.2.1.7 Flash Point 47
3.2.1.8 Viscosity and Viscosity Index 47
3.2.1.9 Oxidative Stability 48
3.2.1.10 Rheology 48
3.2.2 Characterization of SFO 49
3.2.2.1 Gas Chromatography Mass Spectroscopy 49
3.2.2.2 Fourier Transform Infrared Spectroscopy 49
3.2.2.3 Nuclear Magnetic Resonance 50
3.3 Hydrolysis of Sunflower Oil 50
3.3.1 Screening Factors of Hydrolysis Process 50
3.3.2 Optimization of Hydrolysis Process 51

3.3.3 Characterization of SFOFA 51
3.4 Separation of SFOFA via Low Temperature Methanol Crystallization 52
3.4.1 Characterization and Analysis Test of SFOUFA and SFOSFA 52
3.4.2 Analysis Test for SFOUFA and SFOSFA 53
3.5 Esterification of Sunflower Oil Unsaturated Fatty Acids with Polyhydric Alcohol 53
3.5.1 Screening Factors of Esterification Reaction with Polyhydric Alcohol 53
3.5.2 Optimization of Esterification Reaction with Polyhydric Alcohol 55
3.5.3 Characterization of SFOUFANPGE, SFOUFATMPE and SFOUFAPEE 55
3.5.4 Evaluation of Physicochemical Properties of SFOUFANPGE, SFOUFATMPE and SFOUFAPEE 56
3.6 Epoxidation of Sunflower Oil Unsaturated Fatty Acids Trimethylolpropane Ester 56
3.6.1 Screening Factor of Epoxidation Reaction 57
3.6.2 Optimization of Epoxidation Reaction 58
3.6.3 Analysis Test for ESFOUFATMPE 58
3.6.4 Characterization of ESFOUFATMPE 59
3.6.5 Evaluation of Physicochemical Properties of ESFOUFATMPE 59
3.7 Ring Opening of Epoxidized Sunflower Oil Unsaturated Fatty Acids Trimethylolpropane Ester 60
3.7.1 Screening Factor of Ring Opening Reaction 60
3.7.2 Optimization of Ring Opening Reaction 61
3.7.3 Analysis Test for DOSFOUFATMPE 61
3.7.4 Characterization of DOSFOUFATMPE 62
3.7.5 Evaluation of Physicochemical Properties of DOSFOUFATMPE 62
3.8 Flowchart of Research 63

CHAPTER 4 RESULTS AND DISCUSSION 64
4.1 Sunflower Oil 64
4.1.1 Physicochemical Properties of SFO 64
4.1.2 Characterization of SFO 67
4.1.2.1 Gas Chromatography Mass Spectrometer 67

4.1.2.2 Fourier Transform Infrared Spectroscopy 69
4.1.2.3 Nuclear Magnetic Resonance 70
4.2 Hydrolysis of Sunflower Oil 73
4.2.1 Factor Screening Process 73
4.2.2 Optimization of Hydrolysis of SFO 76
4.2.2.1 Determination of Selected Model 77
4.2.2.2 Identification of Model Accuracy 79
4.2.2.3 Analysis of Variance 83
4.2.2.4 Interaction of Factors for Optimum Responses 85
4.2.2.5 Verification Model 87
4.2.2.6 Optimum Condition of Hydrolysis Process 89
4.2.3 Characterization of Sunflower Oil Fatty Acids 90
4.2.3.1 Gas Chromatography 90
4.2.3.2 Fourier Transform Infrared Spectroscopy 91
4.2.3.3 Nuclear Magnetic Resonance 92
4.3 Separation of Sunflower Oil Fatty Acids via Low Temperature Methanol Crystallization 95
4.3.1 Methanol Crystallization Method 95
4.3.2 Characterization of SFOUFA and SFOSFA 96
4.3.2.1 Gas Chromatography 96
4.3.2.2 Fourier Transform Infrared Spectroscopy 98
4.3.2.3 Nuclear Magnetic Resonance 100
4.3.2.4 Iodine Value 103
4.4 Synthesis of Sunflower Oil Unsaturated Fatty Acids Neopentyl Glycol Ester 104
4.4.1 Esterification of SFOUFA with NPG 104
4.4.2 Factor Screening Process 105
4.4.3 Optimization of Esterification of SFOUFA with NPG 106
4.4.3.1 Determination of Selected Model 108
4.4.3.2 Identification of Model Accuracy 109
4.4.3.3 Analysis of Variance 112
4.4.3.4 Interaction Between Variables 114
4.4.3.5 Verification Model 117
4.4.3.6 Optimum Condition of Esterification Reaction 118

4.4.4 Characterization of SFOUFANPGE 119
4.4.4.1 Gas Chromatography 119
4.4.4.2 Fourier Transform Infrared Spectroscopy 120
4.4.4.3 Nuclear Magnetic Resonance 121
4.4.5 Physicochemical Properties of SFOUFANPGE 124
4.5 Synthesis of Sunflower Oil Unsaturated Fatty Acids Trimethylolpropane Ester 125
4.5.1 Esterification of SFOUFA with TMP 125
4.5.2 Factor Screening Process 126
4.5.3 Optimization of Esterification of SFOUFA with TMP 128
4.5.3.1 Determination of Selected Model 129
4.5.3.2 Identification of Model Accuracy 130
4.5.3.3 Analysis of Variance 133
4.5.3.4 Interaction Between Variables 134
4.5.3.5 Model Verification 137
4.5.3.6 Optimum Condition of Esterification Reaction 138
4.5.4 Characterization of SFOUFATMPE 139
4.5.4.1 Gas Chromatography 139
4.5.4.2 Fourier Transform Infrared Spectroscopy 140
4.5.4.3 Nuclear Magnetic Resonance 141
4.5.5 Physicochemical Properties of SFOUFATMPE 144
4.6 Synthesis of Sunflower Oil Unsaturated Fatty Acids Pentaerythritol Ester 145
4.6.1 Esterification of SFOUFA with PE 145
4.6.2 Screening Factor Process 146
4.6.3 Optimization of Esterification of SFOUFA with PE 148
4.6.3.1 Determination of Selected Model 149
4.6.3.2 Identification of Model Accuracy 150
4.6.3.3 Analysis of Variance 154
4.6.3.4 Interaction Between Variables 155
4.6.3.5 Verification Model 158
4.6.3.6 Optimum Condition of Esterification Reaction 160
4.6.4 Characterization of SFOUFAPEE 160
4.6.4.1 Gas Chromatography 160
4.6.4.2 Fourier Transform Infrared Spectroscopy 161

4.6.4.3 Nuclear Magnetic Resonance 163
4.6.5 Physicochemical Properties of SFOUFAPEE 165
4.7 Comparison of Esterification Yield and Physicochemical properties of SFOUFANPGE, SFOUFATMPE and SFOUFAPEE 167
4.7.1 Esterification Yield 168
4.7.2 Pour Point 168
4.7.3 Flash Point 169
4.7.4 Kinematic Viscosity and Viscosity Index 170
4.7.5 Oxidative Stability 171
4.7.6 Rheology 172
4.7.7 Determination of Polyol Ester for Further Reaction 174
4.8 Synthesis of Epoxidized Sunflower Oil Unsaturated Fatty Acids Trimethylolpropane Ester 175
4.8.1 Epoxidation of SFOUFATMPE 175
4.8.2 Factor Screening Process 176
4.8.3 Optimization of Epoxidation of SFOUFATMPE 178
4.8.3.1 Determination of Selected Model 182
4.8.3.2 Identification of Model Accuracy 185
4.8.3.3 Analysis of Variance 191
4.8.3.4 Interaction Between Variables 195
4.8.3.5 Verification Model 207
4.8.3.6 Optimum Condition of Epoxidation Reaction 209
4.8.4 Characterization of ESFOUFATMPE 211
4.8.4.1 Fourier Transform Infrared Spectroscopy 211
4.8.4.2 Nuclear Magnetic Resonance 212
4.8.5 Physicochemical Properties of ESFOUFATMPE 214
4.9 Synthesis of Dioleate Sunflower Oil Unsaturated Fatty Acids Trimethylolpropane Ester 217
4.9.1 Ring Opening Reaction of ESFOUFATMPE with Oleic Acid 217
4.9.2 Factor Screening Process 219
4.9.3 Optimization of Ring Opening Reaction of ESFOUFATMPE 220
4.9.3.1 Determination of Selected Model 224
4.9.3.2 Identification of Model Accuracy 229
4.9.3.3 Analysis of Variance 235

4.9.3.4 Interaction Between Variables 239
4.9.3.5 Verification Model 247
4.9.3.6 Optimum Condition of Ring Opening Reaction 250
4.9.4 Characterization of DOSFOUFATMPE 251
4.9.4.1 Fourier Transform Infrared Spectroscopy 251
4.9.4.2 Nuclear Magnetic Resonance 252
4.9.5 Physicochemical Properties of DOSFOUFATMPE 254
4.10 Comparison on Physicochemical Properties of Synthesized Polyol Ester as Biolubricant Base Stock 257

CHAPTER 5 CONCLUSION AND RECOMMENDATION 261
5.1 Conclusion 261
5.2 Recommendation 262

REFERENCES 265

APPENDICES 278

AUTHOR'S PROFILE 305

LIST OF TABLES

Tables	Title	Page
Table 2.1	Lubrication Properties of Mineral Oil	13
Table 2.2	Benefits of Using Biolubricant	16
Table 2.3	Taxonomy of *Helianthus annuus*	20
Table 2.4	Composition of Triacylglycerol in Sunflower Oil	20
Table 2.5	Fatty Acids Composition in Sunflower Oil	21
Table 2.6	Physicochemical Properties of Sunflower Oil	21
Table 2.7	Solubility of Fatty Acids in Plant Oil at Different Temperature in Methanol	25
Table 2.8	Comparison of the Molecular Structures of NPG, TMP and PE and the Physicochemical Properties of the Corresponding Polyol Esters	30
Table 2.9	Summary of Previous Studies on Polyol Ester Biolubricants from Plant Oils	42
Table 3.1	Range of Parameter Used for Screening of Hydrolysis of SFO	51
Table 3.2	Range of Parameter Used for Screening of Esterification of SFOUFA with NPG	54
Table 3.3	Range of Parameter Used for Screening of Esterification of SFOUFA with TMP	54
Table 3.4	Range of Parameter Used for Screening of Esterification of SFOUFA with PE	55
Table 3.5	Range of Parameter Used for Screening of Epoxidation of SFOUFATMPE	57
Table 3.6	Range of Parameter Used for Screening of Ring Opening of ESFOUFATMPE	61
Table 4.1	Physicochemical Properties of SFO	64
Table 4.2	Percentage Fatty Acids Composition in SFO	69
Table 4.3	Summary of Functional Groups and Wavenumber of SFO	70
Table 4.4	Type of Proton and Chemical Shift of SFO	72

Table 4.5	Type of Carbon and Chemical Shift of SFO	73
Table 4.6	Parameter and Level for D-Optimal Design of Hydrolysis of SFO	75
Table 4.7	Experimental Run, Factors and Response for Percentage Yield of SFOFA from D-Optimal Design	76
Table 4.8	Sequential Model Sum of Square of Percentage Yield of SFOFA	77
Table 4.9	Lack of Fits Test for Percentage Yield of SFOFA	78
Table 4.10	Model Summary Statistic for Percentage Yield of SFOFA	78
Table 4.11	Summary of ANOVA Analysis for Percentage Yield of SFOFA	83
Table 4.12	ANOVA Analysis Factors for Percentage Yield of SFOFA	85
Table 4.13	Restraints for Optimization of Hydrolysis of SFO Parameter and Responses for D-Optimal Design	87
Table 4.14	Actual and Predicted Data for Verification Model for Percentage Yield of SFOFA	89
Table 4.15	Actual and Predicted Data for Optimum Condition for Percentage Yield of SFOFA	89
Table 4.16	Fatty Acids Composition in SFOFA	91
Table 4.17	Functional Group and Wavenumber for FTIR Spectra SFO and SFOFA	92
Table 4.18	Type of Proton and Chemical Shift of SFO and SFOFA	93
Table 4.19	Type of Carbon and Chemical Shift of SFO and SFOFA	94
Table 4.20	Melting Point of Fatty Acids	96
Table 4.21	Fatty Acids Composition in SFOUFA and SFOSFA After Separation	98
Table 4.22	Functional Group and Wavenumber for FTIR of SFOFA, SFOUFA and SFOSFA	100
Table 4.23	Type of Proton and Chemical Shift of SFOSFA and SFOUFA	101
Table 4.24	Type of Carbon and Chemical Shift of SFOSFA and SFOUFA	103
Table 4.25	Parameter and Level for D-Optimal Design of Esterification of SFOUFA with NPG	106
Table 4.26	Experimental Run, Factors and Response for Percentage Yield of SFOUFANPGE from D-Optimal Design	107

Table 4.27	Sequential Model Sum of Squares of Percentage Yield of SFOUFANPGE	108
Table 4.28	Lack of Fit Test for Percentage Yield of SFOUFANPGE	109
Table 4.29	Summary Statistic for Percentage Yield of SFOUFANPGE	109
Table 4.30	Summary of ANOVA Analysis for Percentage Yield of SFOUFANPGE	113
Table 4.31	ANOVA Analysis Factors for Percentage Yield of SFOUFANPGE	114
Table 4.32	Restraints for Optimization of Esterification of SFOUFA with NPG Parameter and Response for D-Optimal Design	117
Table 4.33	Actual and Predicted Data for Verification Model for Percentage Yield of SFOUFANPGE	118
Table 4.34	Actual and Predicted Data for Optimum Condition for Percentage Yield of SFOUFANPGE	119
Table 4.35	Functional Group and Wavenumber for FTIR Spectra of SFOUFA and SFOUFANPGE	121
Table 4.36	Type of Proton and Chemical Shift of SFOUFA and SFOUFANPGE	122
Table 4.37	Type of Carbon and Chemical Shift for SFOUFA and SFOUFANPGE	123
Table 4.38	Physicochemical Properties of SFOUFANPGE and Others NPGE	124
Table 4.39	Parameter and Level for D-Optimal Design of Esterification of SFOUFA with TMP	127
Table 4.40	Experimental Runs, Factors and Response for Percentage Yield of SFOUFATMPE from D-Optimal Design	128
Table 4.41	Sequential Model Sum of Square of Percentage Yield of SFOUFATMPE	129
Table 4.42	Lack of Fit Test for Percentage Yield of SFOUFATMPE	129
Table 4.43	Model Summary Statistic for Percentage Yield of SFOUFATMPE	130

Table 4.44	Summary of ANOVA Analysis for Percentage Yield of SFOUFATMPE	133
Table 4.45	ANOVA Analysis Factors for Percentage Yield of SFOUFATMPE	134
Table 4.46	Restraints for Optimization of Esterification of SFOUFA with TMP Parameter and Response for D-Optimal Design	137
Table 4.47	Actual and Predicted Data for Verification Model for Percentage Yield of SFOUFATMPE	138
Table 4.48	Actual and Predicted Data for Optimum Condition for Percentage Yield of SFOUFATMPE	139
Table 4.49	Functional Group and Wavenumber for FTIR Spectra of SFOUFA and SFOUFATMPE	141
Table 4.50	Type of Proton and Chemical Shift for SFOUFA and SFOUFATMPE	142
Table 4.51	Type of Carbon and Chemical Shift for SFOUFA and SFOUFATMPE	143
Table 4.52	Physicochemical Properties of SFOUFATMPE and Others TMPE	144
Table 4.53	Parameter and Level for D-Optimal Design of Esterification of SFOUFA with PE	147
Table 4.54	Experimental Run, Factors and Response for Percentage Yield of SFOUFAPEE from D-Optimal Design	148
Table 4.55	Sequential Model Sum of Squares of Percentage Yield of SFOUFAPEE	149
Table 4.56	Lack of Fit Test of Percentage Yield of SFOUFAPEE	150
Table 4.57	Model Summary Statistic for Percentage Yield of SFOUFAPEE	150
Table 4.58	Summary of ANOVA Analysis for Percentage Yield of SFOUFAPEE	154
Table 4.59	ANOVA Analysis Factors for Percentage Yield of SFOUFAPEE	155
Table 4.60	Restraints for Optimization of Esterification of SFOUFA with PE Parameter and Response for D-Optimal Design.	158

Table 4.61	Actual and Predicted Data for Verification Model for Percentage Yield of SFOUFAPEE	159
Table 4.62	Actual and Predicted Data for Optimum Condition for Percentage Yield of SFOUFAPEE	160
Table 4.63	Functional Group and Wavenumber of SFOUFA and SFOUFAPEE	162
Table 4.64	Type of Proton and Chemical Shift for SFOUFA and SFOUFAPEE	164
Table 4.65	Type of Carbon and Chemical Shift for SFOUFA and SFOUFAPEE	165
Table 4.66	Physicochemical Properties of SFOUFAPEE and Others PEE	165
Table 4.67	Percentage Yield and Physicochemical Properties of SFOUFANPGE, SFOUFATMPE and SFOUFAPEE	167
Table 4.68	Parameter and Level for D-Optimal Design of Epoxidation Reaction of SFOUFATMPE	178
Table 4.69	Experimental Run, Factors and Response for Percentage Yield of ESFOUFATMPE	179
Table 4.70	Experimental Run, Factors and Response for Percentage of OOC of ESFOUFATMPE	180
Table 4.71	Experimental Run, Factors and Response for Iodine Value of ESFOUFATMPE	181
Table 4.72	Sequential Model Sum of Squares of Percentage Yield of ESFOUFATMPE	182
Table 4.73	Sequential Model Sum of Squares of Percentage OOC of ESFOUFATMPE	182
Table 4.74	Sequential Model Sum of Squares of Iodine Value of ESFOUFATMPE	183
Table 4.75	Lack of Fit Test for Percentage Yield of ESFOUFATMPE	183
Table 4.76	Lack of Fit Test for Percentage OOC of ESFOUFATMPE	183
Table 4.77	Lack of fit test for Iodine value of ESFOUFATMPE	184
Table 4.78	Model Summary Statistic for Percentage Yield of ESFOUFATMPE	184
Table 4.79	Model Summary Statistic for Percentage OOC of ESFOUFATMPE	185

Table 4.80	Model Summary Statistic for Iodine Value of ESFOUFATMPE	185
Table 4.81	Summary of ANOVA Analysis for Percentage Yield, Percentage OOC and Iodine Value of ESFOUFATMPE	192
Table 4.82	ANOVA Analysis Factors for Percentage Yield of ESFOUFATMPE	193
Table 4.83	ANOVA Analysis Factors for Percentage OOC of ESFOUFATMPE	194
Table 4.84	ANOVA Analysis Factors for Iodine Value of ESFOUFATMPE	195
Table 4.85	Restraints for Optimization of Epoxidation of SFOUFATMPE Parameter and Response for D-Optimal Design	207
Table 4.86	Actual and Predicted Data for Verification Model for Percentage Yield of ESFOUFATMPE	209
Table 4.87	Actual and Predicted Data for Verification Model for Percentage OOC of ESFOUFATMPE	209
Table 4.88	Actual and Predicted Data for Verification Model for Iodine Value of ESFOUFATMPE	209
Table 4.89	Actual and Predicted Data for Optimum Condition for Percentage Yield of ESFOUFATMPE	210
Table 4.90	Actual and Predicted Data for Optimum Condition for Percentage OOC of ESFOUFATMPE	210
Table 4.91	Actual and Predicted Data for Optimum Condition for Iodine Value of ESFOUFATMPE	210
Table 4.92	Functional Group and Wavenumber for FTIR Spectra of SFOUFATMPE and ESFOUFATMPE	212
Table 4.93	Type of Proton and Chemical Shift for SFOUFATMPE and ESFOUFATMPE	213
Table 4.94	Type of Carbon and Chemical Shift for SFOUFATMPE and ESFOUFATMPE	214
Table 4.95	Physicochemical Properties of ESFOUFATMPE and Others ETMPE	214
Table 4.96	Parameter and Level for D-Optimal Design of Ring Opening Reaction	220

Table 4.97	Experimental Run, Factors and Response for Percentage Yield of DOSFOUFATMPE	221
Table 4.98	Experimental Run, Factors and Response for Percentage OOC of DOSFOUFATMPE	222
Table 4.99	Experimental Run, Factors and Response for Iodine Value of DOSFOUFATMPE	223
Table 4.100	Experimental Run, Factors and Response for Hydroxyl Value of DOSFOUFATMPE	224
Table 4.101	Sequential Model Sum of Squares of Percentage Yield of DOSFOUFATMPE	225
Table 4.102	Sequential Model Sum of Squares of Percentage OOC of DOSFOUFATMPE	225
Table 4.103	Sequential Model Sum of Squares of Iodine Value of DOSFOUFATMPE	226
Table 4.104	Sequential Model Sum of Squares of Hydroxyl Value of DOSFOUFATMPE	226
Table 4.105	Lack of Fit Test for Percentage Yield of DOSFOUFATMPE	227
Table 4.106	Lack of Fit Test for Percentage OOC of DOSFOUFATMPE	227
Table 4.107	Lack of Fit Test for Iodine Value of DOSFOUFATMPE	227
Table 4.108	Lack of Fit Test for Hydroxyl Value of DOSFOUFATMPE	227
Table 4.109	Model Summary Statistic for Percentage Yield of DOSFOUFATMPE	228
Table 4.110	Model Summary Statistic for Percentage OOC of DOSFOUFATMPE	228
Table 4.111	Model Summary Statistic for Iodine Value of DOSFOUFATMPE	229
Table 4.112	Model Summary Statistic for Hydroxyl Value of DOSFOUFATMPE	229
Table 4.113	Summary of ANOVA Analysis for Percentage Yield, Percentage OOC Iodine Value and Hydroxyl Value of DOSFOUFATMPE	236
Table 4.114	ANOVA Analysis Factors for Percentage Yield of DOSFOUFATMPE	237

Table 4.115 ANOVA Analysis Factors for Percentage OOC of DOSFOUFATMPE 238
Table 4.116 ANOVA Analysis Factors for Iodine Value of DOSFOUFATMPE 238
Table 4.117 ANOVA Analysis Factors for Hydroxyl Value of DOSFOUFATMPE 239
Table 4.118 Restraints for Optimization of Ring Opening of ESFOUFATMPE Parameter and Response for D-Optimal Design 248
Table 4.119 Actual and Predicted Data for Verification Model for Percentage Yield of DOSFOUFATMPE 249
Table 4.120 Actual and Predicted Data for Verification Model for Percentage OOC of DOSFOUFATMPE 249
Table 4.121 Actual and Predicted Data for Verification Model for Iodine Value of DOSFOUFATMPE 249
Table 4.122 Actual and Predicted Data for Verification Model for Hydroxyl Value of DOSFOUFATMPE 249
Table 4.123 Actual and Predicted Data for Optimum Condition for Percentage Yield of DOSFOUFATMPE 250
Table 4.124 Actual and Predicted Data for Optimum Condition for Percentage OOC of DOSFOUFATMPE 250
Table 4.125 Actual and Predicted Data for Optimum Condition for Iodine Value of DOSFOUFATMPE 250
Table 4.126 Actual and Predicted Data for Optimum Condition for Hydroxyl Value of DOSFOUFATMPE 251
Table 4.127 Functional Group and Wavenumber for FTIR Spectra of ESFOUFATMPE and DOSFOUFATMPE 252
Table 4.128 Type of Proton and Chemical Shift for ESFOUFATMPE and DOSFOUFATMPE 253
Table 4.129 Type of Carbon and Chemical Shift for ESFOUFATMPE and DOSFOUFATMPE 254
Table 4.130 Physicochemical Properties of DOSFOUFATMPE and Others DOPE 255

Table 4.131 The Physicochemical Properties of SFO, SFOUFANPGE, SFOUFATMPE, SFOUFAPEE, ESFOUFATMPE and DOSFOUFATMPE. 257

LIST OF FIGURES

Figures	Title	Page
Figure 1.1	Development of Global Lubricants Demand Over the Years	1
Figure 1.2	Beta Elimination Reaction of Triacylglycerol for β-hydrogen	3
Figure 1.3	Hydroperoxide Formation in Linoleic Acid	4
Figure 2.1	General Classification of Lubricant	10
Figure 2.2	Shear Rate versus Shear Stress of Newtonian and Non-Newtonian Fluid	12
Figure 2.3	General Structure of Triacylglycerol in Plant Oil	14
Figure 2.4	Life Cycle of Biolubricant	15
Figure 2.5	Critical Point for β-CH and Carbon Double Bond in Triacylglycerol	16
Figure 2.6	Oxidation Mechanism of Plant Oil	17
Figure 2.7	*Helianthus annuus* and the Seeds	19
Figure 2.8	General Chemical Equation for Hydrolysis Process	22
Figure 2.9	General Mechanism for Hydrolysis Process	23
Figure 2.10	General Chemical Equation for Esterification	26
Figure 2.11	General Mechanism for Esterification for Acid Catalyst	26
Figure 2.12	Structure of Polyhydric Alcohol	27
Figure 2.13	General Structure of Polyol Ester Produced from NPG	28
Figure 2.14	General Structure of Polyol Ester Produced from TMP	28
Figure 2.15	General Structure of Polyol Ester Produced from PE	29
Figure 2.16	Formation of Peracid	32
Figure 2.17	General Mechanism of Epoxidation Reaction	32
Figure 2.18	General Chemical Equation for Ring Opening Reaction	33
Figure 2.19	Structure of Oleic Acid	34
Figure 2.20	Chemical Reaction Involve in IV through Wijs Method	37
Figure 2.21	Chemical Reaction Between Fatty Acids and NaOH an Acid-Base Titration	38
Figure 4.1	Shear Stress versus Shear Rate of SFO	67
Figure 4.2	Viscosity versus Shear Rate of SFO	67

Figure 4.3	GC-MS Chromatogram of Fatty Acids Composition in SFO	68
Figure 4.4	FTIR Spectrum of SFO	70
Figure 4.5	^{1}H NMR Spectrum of SFO	71
Figure 4.6	^{13}C NMR Spectrum of SFO	73
Figure 4.7	The Effect of Factors for Hydrolysis on the Percentage Yield of SFOFA	75
Figure 4.8	Normal Plot of Residuals for Percentage Yield of SFOFA	79
Figure 4.9	Residuals versus Predicted Plot for Percentage Yield of SFOFA	80
Figure 4.10	Predicted versus Actual Plot for Percentage Yield of SFOFA	80
Figure 4.11	Residual versus Run Number for Percentage Yield of SFOFA	81
Figure 4.12	Cook's Distance Plot for Percentage Yield of SFOFA	82
Figure 4.13	Box-Cox Plot for Percentage Yield of SFOFA	82
Figure 4.14	3D Surface Plot for a) AB, b) AC and c) BC for Percentage Yield of SFOFA	86
Figure 4.15	D-Optimal Predicted Model at Optimum Condition for Hydrolysis of SFO	88
Figure 4.16	Sunflower Oil Fatty Acids (SFOFA)	89
Figure 4.17	GC-MS Chromatogram of Fatty Acids Composition in SFOFA	90
Figure 4.18	FTIR Spectra of SFO and SFOFA	92
Figure 4.19	^{1}H NMR Spectrum for SFOFA	93
Figure 4.20	^{13}C NMR Spectrum of SFOFA	94
Figure 4.21	(a) Sunflower Oil Saturated Fatty Acids and (b) Sunflower Oil Unsaturated Fatty Acids	96
Figure 4.22	GC-MS Chromatogram of Fatty Acids Composition in SFOUFA	97
Figure 4.23	GC-MS Chromatogram of Fatty Acids Composition in SFOSFA	98
Figure 4.24	FTIR Spectra of SFOFA, SFOUFA and SFOSFA	99
Figure 4.25	^{1}H NMR Spectra of SFOSFA and SFOUFA	101
Figure 4.26	^{13}C NMR Spectra of SFOSFA and SFOUFA	102
Figure 4.27	Iodine Value Before and After Separation via Methanol Crystallization Method	104

Figure 4.28	Esterification Reaction Scheme of SFOUFA with NPG	104
Figure 4.29	Reaction Mechanism Esterification of SFOUFA and NPG for Monoester	105
Figure 4.30	The Effect of Factors for Esterification on the Percentage Yield of SFOUFANPGE	106
Figure 4.31	Normal Plot of Residual for Percentage Yield of SFOUFANPGE	110
Figure 4.32	Residual versus Predicted Plot for Percentage Yield of SFOUFANPGE	110
Figure 4.33	Actual versus Predicted for Percentage Yield of SFOUFANPGE	111
Figure 4.34	Residual versus Run Number for Percentage Yield of SFOUFANPGE	111
Figure 4.35	Cook's Distance Plot for Percentage Yield of SFOUFANPGE	112
Figure 4.36	Box-Cox Plot for Percentage Yield of SFOUFANPGE	112
Figure 4.37	3D Surface Plot for a) AB, b) AC, c) AD, d) BC, e) BD and f) CD for Percentage Yield of SFOUFANPGE	115
Figure 4.38	D-Optimal Predicted Model at Optimum Condition for Esterification of SFOUFA with NPG	118
Figure 4.39	Sunflower Oil Unsaturated Fatty Acids Neopentyl Glycol Ester (SFOUFANPGE)	119
Figure 4.40	GC-FID Chromatogram of Ester Composition in SFOUFANPGE	120
Figure 4.41	FTIR Spectra of SFOUFA and SFOUFANPGE	121
Figure 4.42	^{1}H NMR Spectrum for SFOUFANPGE	122
Figure 4.43	^{13}C NMR Spectrum for SFOUFANPGE	123
Figure 4.44	Esterification Reaction Scheme of SFOUFA and TMP	125
Figure 4.45	Reaction Mechanism Esterification of SFOUFA and TMP for Monoester	126
Figure 4.46	The Effect of Factors for Esterification on the Percentage Yield of SFOUFATMPE	127
Figure 4.47	Normal Plot of Residual for Percentage Yield of SFOUFATMPE	130

Figure 4.48	Residual versus Predicted Plot for Percentage Yield of SFOUFATMPE	131
Figure 4.49	Actual versus Predicted for Percentage Yield of SFOUFATMPE	131
Figure 4.50	Residual versus Run Number for Percentage Yield of SFOUFATMPE	132
Figure 4.51	Cook's Distance Plot for Percentage Yield of SFOUFATMPE	132
Figure 4.52	Box-Cox Plot for Percentage Yield of SFOUFATMPE	133
Figure 4.53	3D Surface Plot for a) AB, b) AC, c) AD, d) BC, e) BD and f) CD for Percentage Yield of SFOUFATMPE	135
Figure 4.54	D-Optimal Predicted Model at Optimum Condition for Esterification of SFOUFA with TMP	138
Figure 4.55	Sunflower Oil Unsaturated Fatty Acids Trimethylolpropane Ester (SFOUFATMPE)	139
Figure 4.56	GC-FID Chromatogram of Ester Composition in SFOUFATMPE	140
Figure 4.57	FTIR Spectra of SFOUFA and SFOUFATMPE	141
Figure 4.58	^{1}H NMR Spectrum for SFOUFATMPE	142
Figure 4.59	^{13}C NMR spectrum for SFOUFATMPE	143
Figure 4.60	Esterification Reaction Scheme of SFOUFA with PE	145
Figure 4.61	Reaction Mechanism Esterification of SFOUFA with PE for Monoester	146
Figure 4.62	The Effect of Factor for Esterification on the Percentage Yield of SFOUFAPEE	147
Figure 4.63	Normal Plot of Residual for Percentage Yield of SFOUFAPEE	151
Figure 4.64	Residual versus Predicted Plot for Percentage Yield of SFOUFAPEE	152
Figure 4.65	Actual versus Predicted for Percentage Yield of SFOUFAPEE	152
Figure 4.66	Residual versus Run Number for Percentage Yield of SFOUFAPEE	153
Figure 4.67	Cook's Distance Plot for Percentage Yield of SFOUFAPEE	153
Figure 4.68	Box-Cox Plot for Percentage Yield of SFOUFAPEE	154
Figure 4.69	3D Surface Plot for a) AB, b) AC, c) AD, d) BC, e) BC and f) CD for Percentage Yield of SFOUFAPEE	156

Figure 4.70	D-Optimal Predicted Model at Optimum Condition for Esterification of SFOUFA	159
Figure 4.71	Sunflower Oil Unsaturated Fatty Acids Pentaerythritol Ester (SFOUFAPEE)	160
Figure 4.72	GC-FID Chromatogram of Ester Composition in SFOUFAPEE	161
Figure 4.73	FTIR Spectra of SFOUFA and SFOUFAPEE	162
Figure 4.74	^{1}H NMR Spectrum for SFOUFAPEE	163
Figure 4.75	^{13}C NMR Spectrum for SFOUFAPEE	165
Figure 4.76	Rheological Properties Shear Stress versus Shear Rate of (a) SFOUFANPGE, (b) SFOUFATMPE and (c) SFOUFAPEE	173
Figure 4.77	Rheological Properties Viscosity versus Shear Rate of (a) SFOUFANPGE, (b) SFOUFATMPE and (c) SFOUFAPEE	174
Figure 4.78	Formation of Perfomic Acid	175
Figure 4.79	Mechanism of Epoxidation Reaction	175
Figure 4.80	Epoxidation of SFOUFATMPE	176
Figure 4.81	The Effect of Factor for Epoxidation Reaction on the Percentage Yield of ESFOUFATMPE	177
Figure 4.82	Normal Plot of Residual for (a) Percentage Yield, (b) Percentage OOC and (c) Iodine Value of ESFOUFATMPE	186
Figure 4.83	Residual versus Predicted Plot for (a) Percentage Yield, (b) Percentage OOC and (c) Iodine Value of ESFOUFATMPE	187
Figure 4.84	Actual versus Predicted for (a) Percentage Yield, (b) Percentage OOC and (c) Iodine Value of ESFOUFATMPE	188
Figure 4.85	Residual versus Run Number for (a) Percentage Yield, (b) Percentage OOC and (c) Iodine Value of ESFOUFATMPE	189
Figure 4.86	Cook's Distance Plot for (a) Percentage Yield, (b) Percentage OOC and (c) Iodine Value of ESFOUFATMPE	190
Figure 4.87	Box-Cox Plot for (a) Percentage Yield, (b) Percentage OOC and (c) Iodine Value of ESFOUFATMPE	191
Figure 4.88	3D Surface Plot for a) AB, b) AC, c) AD, d) AE e) BC and f) BD for Percentage Yield of ESFOUFATMPE	196
Figure 4.89	3D Surface Plot for g) BE, h) CD, i) CE and j) DE for Percentage Yield of ESFOUFATMPE	197

Figure 4.90	3D Surface Plot for a) AB, b) AC, c) AD, d) AE e) BC and f) BD for Percentage OOC of ESFOUFATMPE	200
Figure 4.91	3D Surface Plot for g) BE, h) CD, i) CE and j) DE for Percentage OOC of ESFOUFATMPE	201
Figure 4.92	3D Surface Plot for a) AB, b) AC, c) AD, d) AE e) BC and f) BD for Iodine Value of ESFOUFATMPE	204
Figure 4.93	3D Surface Plot for g) BE, h) CD, i) CE and j) DE for Iodine Value of ESFOUFATMPE	205
Figure 4.94	D-Optimal Predicted Model at Optimum Condition for Epoxidation of SFOUFATMPE	208
Figure 4.95	Epoxidized Sunflower Oil Unsaturated Fatty Acids Trimethylolpropane Ester (ESFOUFATMPE)	210
Figure 4.96	FTIR Spectra of SFOUFATMPE and ESFOUFATMPE	211
Figure 4.97	^{1}H NMR Spectrum for ESFOUFATMPE	212
Figure 4.98	^{13}C NMR Spectrum for ESFOUFATMPE	213
Figure 4.99	Shear Stress vesus Shear Rate of ESFOUFATMPE	216
Figure 4.100	Viscosity versus Shear Rate of ESFOUFATMPE	216
Figure 4.101	Ring Opening Reaction of ESFOUFATMPE	217
Figure 4.102	Reaction Mechanism of Ring Opening Reaction	218
Figure 4.103	The Effect of Factor for Ring Opening Reaction on the Percentge yield of DOSFOUFATMPE	219
Figure 4.104	Normal Plot of Residual for (a) Percentage Yield, (b) Percentage OOC, (c) Iodine Value and (d) Hydroxyl Value of DOSFOUFATMPE	230
Figure 4.105	Residual versus Predicted Plot for (a) Percentage Yield, (b) Percentage OOC, (c) Iodine Value and (d) Hydroxyl Value of DOSFOUFATMPE	231
Figure 4.106	Predicted versus Actual for (a) Percentage Yield, (b) Percentage OOC, (c) Iodine Value and (d) Hydroxyl Value of DOSFOUFATMPE	232
Figure 4.107	Residual versus Run Number for (a) Percentage Yield, (b) Percentage OOC, (c) Iodine Value and (d) Hydroxyl Value of DOSFOUFATMPE	233

Figure 4.108	Cook's Distance for (a) Percentage Yield, (b) Percentage OOC, (c) Iodine Value and (d) Hydroxyl Value of DOSFOUFATMPE	234
Figure 4.109	Box-Cox Plot for (a) Percentage Yield, (b) Percentage OOC, (c) Iodine Value and (d) Hydroxyl Value of DOSFOUFATMPE	235
Figure 4.110	3D Surface Plot for a) AB, b) AC, c) AD, d) BC, e) BD and f) CD for Percentage Yield of DOSFOUFATMPE	240
Figure 4.111	3D Surface Plot for a) AB, b) AC, c) AD, d) BC, e) BD and f) CD for Percentage OOC of DOSFOUFATMPE	242
Figure 4.112	3D Surface Plot for a) AB, b) AC, c) AD, d) BC, e) BD and f) CD for Iodine Value of DOSFOUFATMPE	244
Figure 4.113	3D Surface Plot for a) AB, b) AC, c) AD, d) BC, e) BD and f) CD for Hydroxyl Value of DOSFOUFATMPE	246
Figure 4.114	D-Optimal Predicted Model at Optimum Condition for Ring Opening of ESFOUFATMPE	248
Figure 4.115	Dioleate Sunflower Oil Unsaturated Fatty Acids Trimethylolpropane Ester (DOSFOUFATMPE)	251
Figure 4.116	FTIR Spectra of ESFOUFATMPE and DOSFOUFATMPE	252
Figure 4.117	^{1}H NMR Spectrum for DOSFOUFATMPE	253
Figure 4.118	^{13}C NMR Spectrum for DOSFOUFATMPE	254
Figure 4.119	Shear Stress versus Shear Rate of DOSFOUFATMPE	256
Figure 4.120	Viscosity versus Shear Rate of DOSFOUFATMPE	256

LIST OF SYMBOLS

Symbols

β	Beta
°C	Degree Celsius
cSt	Centistoke
g	Gram
h	Hour
M	Molarity
mg	Milligram
mL	Millilitre
N	Normality
Psi	Pound per square inch
s^{-1}	Shear rate
τ	Shear stress
μ	Coefficient of friction
μN/σ	Dimensionless parameter

LIST OF ABBREVIATIONS

Abbreviations

β-CH	Beta hydrogen
CO_2	Carbon dioxide
C=O	Carbonyl group
CCD	Central composite design
CPO	Crude palm oil
CPOFAs-NPG	Crude palm oil fatty acids neopentyl glycol
DiPE	Di-pentaerythritol
DPE	Di-oleate polyol ester
DiTMP	Di-trimethylolpropane
DOSFOUFATMPE	Dioleate sunflower oil unsaturated fatty acids trimethylolpropane ester
H^+	Electrophilic hydrogen
EPE	Epoxidized polyol ester
ESFOUFATMPE	Epoxidized sunflower oil unsaturated fatty acids trimethylolpropane ester
FAME	Fatty acid methyl ester
$COO^- K^+$	Fatty acid potassium
FP	Flash point
HCOOH	Formic acid
HOFA	High oleic fatty acid

HCl	Hydrochloric acid
HV	Hydroxyl value
OH	Hydroxyl group
H_2O_2	Hydrogen peroxide
IUPAC	International Union of Pure and Applied Chemistry
ISO	Internation Standard Organization
IV	Iodine value
NPG	Neopentyl glycol
NPGE	Neopentyl glycol ester
OOC	Oxirane oxygen content
POFAs	Palm oil fatty acid
PE	Pentaerythritol
PEE	Pentaerythritol ester
HCOOOH	Performic acid
PP	Pour point
PTSA	p-toluenesulphonic acid
RSM	Response Surface Methodology
RPVOT	Rotating pressure vessel oxidation test
SFA	Saturated fatty acid
NaOH	Sodium hydroxide
H_2SO_4	Sulfuric acid
SFO	Sunflower oil

SFOFA	Sunflower oil fatty acids
SFOSFA	Sunflower oil saturated fatty acids
SFOUSFA	Sunflower oil unsaturated fatty acids
SFOUFANPGE	Sunflower oil unsaturated fatty acids neopentyl glycol ester
SFOUFAPEE	Sunflower oil unsaturated fatty acids pentaerythritol ester
SFOUFATMPE	Sunflower oil unsaturated fatty acids trimethylolpropane ester
TAG	Triacylglycerol
TMP	Trimethylolpropane
TMPE	Trimethylolpropane ester
USFAs	Unsaturated fatty acid
VI	Viscosity index

CHAPTER 1
INTRODUCTION

1.1 Research Background

Mineral oil has been widely used as lubricants throughout the world for the past ten years. This mineral oil comes from petroleum that has been refined through the distillation process (Jain and Suhane, 2012). As shown in Figure 1.1, the global demand for lubricants has remained consistently high, ranging from approximately 32 to 38 million metric tonnes between 2000 and 2022, indicating the continued dependence on mineral oil-based lubricants. Although a temporary decline was observed in 2009 due to the global economic recession and in 2022, the overall demand has remained substantial (Sazzad et al., 2024). Since mineral oil accounts for the majority of commercial lubricants, its extensive use inevitably increases the generation of waste lubricants through leakage, spills, and improper disposal (Nor et al., 2018a). Consequently, either intentionally or unintentionally, mineral oil is released into the environment, causing serious environmental and health concerns. Furthermore, mineral oil is non-biodegradable and originates from non-renewable petroleum resources, making it environmentally unsustainable (Nor et al., 2018). These problems have raised awareness among the community about the harmful of mineral oil to the environment.

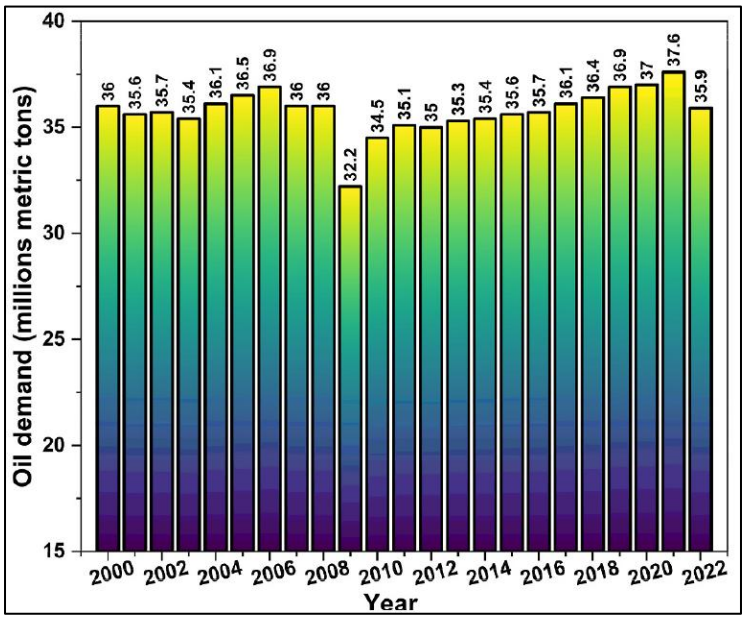


Figure 1.1 Development of Global Lubricants Demand Over the Years

Many researchers are currently looking for alternate substitute sources to replace the use of mineral oil. Due to the quicker pace of depletion and non-renewability of conventional energy sources, it is crucial to replace them (Borugadda and Goud, 2015). This raises public awareness of the benefits of the product made using plant oils. Because plant-based goods are environmentally beneficial and do not harm the environment, their use does not raise any concerns (Srivastava and Sahai, 2013). Since it is crucial to attain sustainability in the energy sector, developed and industrialised nations must significantly boost their usage of renewable energy (Oyedepo, 2012).

Plant oil is the best alternative source to replace mineral oil in the production of lubricants due to its renewable, biodegradable and non-toxic properties. Plant oil-based lubricants also have good lubricating properties by exhibiting a high viscosity index. Lubricants produced from plant oils are known as biolubricants (Owuna et al., 2020).

Like a coin with two sides, plant oils have drawbacks of their own. Although they have excellent physical properties that make them suitable for use as lubricants, they have low oxidative stability that prevent them from being directly used as raw materials (Panchal et al., 2017; Owuna et al., 2020). Plant oils can be chemically modified to solve this issue, by modifying the molecular structure of the plant oil through the esterification, epoxidation and ring opening processes.

Sunflower oil (SFO) is one of the plant oils that can be used to replace the use of mineral oil in the production of lubricant base stock. SFO was selected as the feedstock due to its high content of unsaturated fatty acids, making it a suitable candidate for this study, which focuses on the chemical modification of unsaturated fatty acids. In this study, SFO was hydrolyzed to produce sunflower oil fatty acids (SFOFA) then separated into sunflower oil saturated fatty acids (SFOSFA) and unsaturated fatty acids (SFOUFA). SFOUFA was used as a starting material in the esterification process where it reacted with neopentyl glycol (NPG), trimethylolpropane (TMP) pentaerythritol (PE) in the presence of sulfuric acid (H_2SO_4) as a catalyst for the synthesis of polyol ester. The product that being produce were sunflower oil unsaturated fatty acids neopentyl glycol ester (SFOUFANPGE), sunflower oil unsaturated fatty acids trimethylolpropane ester (SFOUFATMPE), sunflower oil unsaturated fatty acids pentaerythritol ester (SFOUFAPEE). The synthesized sunflower oil unsaturated fatty acids trimethylolpropane ester (SFOUFATMPE) was then subjected to an epoxidation process to produce epoxidized sunflower oil unsaturated fatty acids trimethylolpropane ester (ESFOUFATMPE). The resulting epoxidized intermediate was then further the

reaction through a ring-opening reaction to obtain dioleate sunflower oil unsaturated fatty acids trimethylolpropane ester (DOSFOUFATMPE).

1.2 Problem Statement

The production of biolubricants from plant oils has received widespread attention. Plant oils are composed of triacylglycerols in which glycerol molecules are bound to three long-chain fatty acids through ester bonds. Fatty acids that have long carbon chains provide characteristics as film filters that interact strongly with the iron surface (Adhvaryu et al., 2005). The resulting film is able to reduce the inherent friction. However, plant oils have several disadvantages that can cause instability and limit their direct application in the lubricant industry. This include low oxidative stability (Nor et al., 2019).

The low oxidative stability of plant oil will cause plant oil to undergo oxidation easily. The oxidation of plant oil will form a precipitate that will increase the viscosity of the oil. High oil viscosity will interfere with the function of the lubricant to reduce friction, further disrupting the operation of the engine (Owuna 2020). Low oxidative stability is attributed to the presence of beta- hydrogen (β-CH), which act as an active oxidation site within the glycerol backbone of plant oil, as well the presence of double bonds in the fatty acids chain that highly susceptible to oxidative degradation (Nor et al., 2018, Nor et al., 2019; Jamaluddin et al., 2024).

The presence of β-CH on the glycerol backbone in triacylglycerol makes plant oil easily damaged and unstable at high temperatures. Formation of olefins (unsaturated compound) and acid occurs when β-CH is removed and the unsaturated compound will polymerize which causes the viscosity of plant oil increases due to the formation of precipitation (Fox and Stachowiak, 2007). This problem can be overcome by chemical modification of plant oil via esterification. Figure 1.2 shows the beta elimination reaction in triacylglycerol for beta hydrogen.

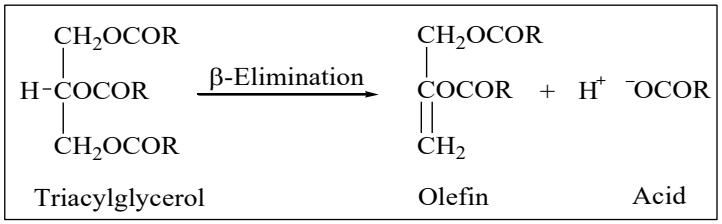


Figure 1.2 Beta Elimination Reaction of Triacylglycerol for β-hydrogen

The second factor contributing to reduced oxidative stability is the existence of bis allylic protons on the double bond. The removal of these bis allylic protons from the double bond generates free radicals (Nor et al., 2018b). Subsequently, these free radicals interact with oxygen to form peroxy radicals, which then attack other fat molecules by displacing their hydrogen atoms. This process results in the formation of hydroperoxides and additional free radicals, effectively accelerating the oxidation process (Choe and Min, 2006). These bis allylic protons are mainly present in linoleic and linolenic acid which are highly susceptible to oxidation This will lead to the increasing in the viscosity of oil. Figure 1.3 illustrates the formation of hydroperoxides in linoleic acid as it is the major fatty acids present in SFO.

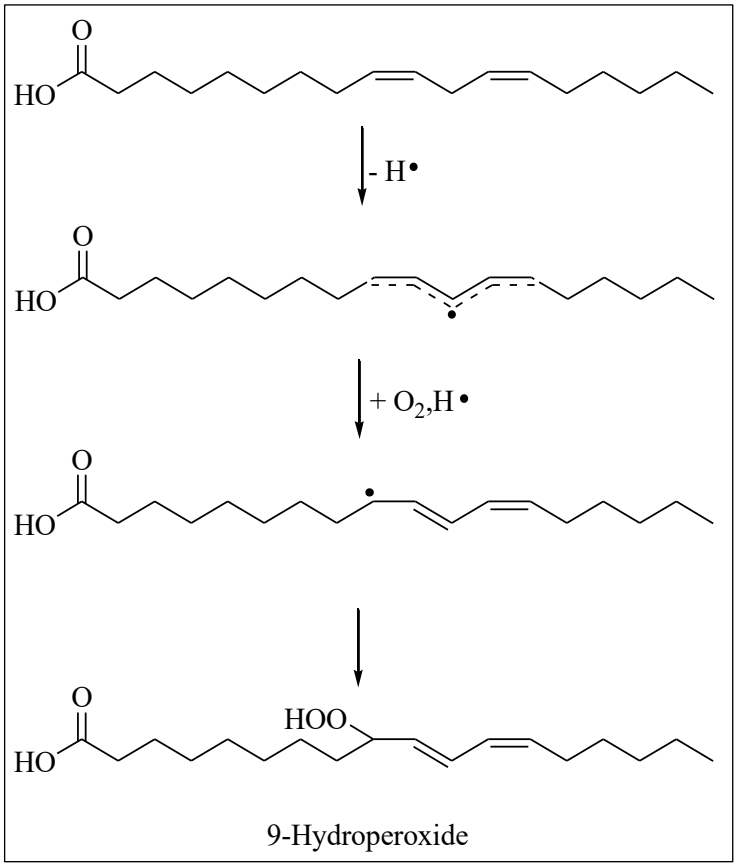


Figure 1.3 Hydroperoxide Formation in Linoleic Acid

1.3 Scope and Limitation of Study

This study focuses on the development of biolubricant base stock, derived from sunflower oil unsaturated fatty acids. SFO was selected as the feedstock due to its high unsaturated fatty acids (more than 80%), which make it easier for chemical modification

and suitable for further structural improvement. Since this study specifically emphasizes the modification of unsaturated fatty acids to enhance the biolubricant performance, SFO was a good candidate as a raw material. This study involves the separation of unsaturated fatty acids from sunflower oil using a methanol crystallization method to obtain unsaturated fraction that suitable as starting material for biolubricant synthesis. Unlike the previous studies that only utilized mixture of fatty acids without the separation process in the production of biolubricant base stock. Following the separation, SFOUFA were esterified with polyhydric alcohol (NPG, TMP and PE) to produce SFOUFANPGE, SFOUFATMPE and SFOUFAPEE as polyol ester for biolubricant base stock. This study aims to address the weakness of plant oil, due to the presence of beta hydrogen that led to low oxidative stability. Further structural modification was carried out through epoxidation (ESFOUFATMPE) to address the bis allylic proton located in the double bond to improve the oxidative stability followed by ring opening reaction (DOSFOUFATMPE) that help the low temperature properties and overall performance of the biolubricant. The synthesized products were characterized using analytical and physicochemical test including gas chromatography equipped with flame ionization detector (GC-FID), Fourier transform infrared (FTIR), nuclear magnetic resonance (NMR), pour point, flash point, kinematic viscosity, viscosity index and oxidative stability and rheological analysis. This study addresses the limited availability of reported data on sunflower oil derived polyol ester by presenting the synthesis selected polyol ester along with their structural characterization and physicochemical properties, thereby supporting the production of renewable biolubricant base stock.

This study was strictly limited to the utilization of commercial-grade SFO as the renewable feedstock for biolubricant base stock production. Accordingly, the findings were specific to SFO and may not be directly applicable to other plant oils with different fatty acid compositions. The chemical modification was confined to a three-step pathway, comprising hydrolysis and crystallization for the separation of SFOUFA, polyol esterification using three polyhydric alcohols, followed by epoxidation and ring-opening reactions. The synthesized products were evaluated solely through physicochemical, structural, thermal, oxidative stability and rheological characterizations to determine their suitability as biolubricant base stocks in accordance with relevant ASTM and ISO standard methods. Furthermore, all experiments were conducted under controlled laboratory-scale conditions. Therefore, the findings do not

represent pilot-scale or industrial-scale production. Tribological performance evaluation, biodegradability assessment, and the formulation and performance evaluation of finished biolubricants containing performance additives were beyond the scope of this study.

1.4 Significance of Study

Since the demand for mineral oil in the industrial sector continues to increase, it is crucial to develop suitable alternatives to replace its use. Replacing mineral oil with plant-based oils offers significant advantages, particularly in terms of environmental sustainability. The primary objective of this study is to produce a biolubricant base stock from renewable, biodegradable and non-toxic sources, specifically plant oil, by modifying its molecular structure through chemical processes. Sunflower oil was selected as the feedstock and chemical modifications were employed to overcome the inherent limitations of plant oils, particularly their low oxidative stability. By replacing mineral oil with plant oil–based lubricants, the negative environmental impact associated with petroleum-derived lubricants can be significantly reduced.

Sunflower oil (SFO) was chosen as the alternative to mineral oil due to its renewability and availability. As a renewable resource, SFO can be produced within a relatively short cultivation cycle, making large-scale utilization feasible. Sunflowers are cultivated worldwide, ensuring a stable and accessible supply of SFO. According to global market data, sunflower is the third most widely cultivated oilseed crop, with approximately 45 million tons of sunflower oil produced annually between 2014 and 2018, accounting for about 9% of global oilseed production (Pilorgé, 2020). In addition, sunflower oil is biodegradable and non-toxic, which contributes to reducing environmental pollution and ecological risks associated with lubricant leakage and disposal.

However, the direct use of plant oils as lubricants is limited due to their poor oxidative stability, which is mainly attributed to the presence of β-hydrogen (β-CH) atoms in the triacylglycerol structure. These β-CH groups are highly susceptible to oxidation, leading to rapid degradation during high-temperature or long-term applications. To address this limitation, esterification is carried out to replace the glycerol backbone containing β-CH with polyhydric alcohols. Polyhydric alcohols contain multiple hydroxyl groups and do not possess β-CH in their molecular structure,

thereby significantly improving the oxidative stability of the resulting polyol esters. The esterification reaction produces polyol esters that are suitable for use as biolubricant base stocks.

Furthermore, additional chemical modifications such as epoxidation and subsequent ring-opening reactions are employed to further enhance the performance of the biolubricant. Epoxidation converts carbon–carbon double bonds into epoxide groups, which reduces unsaturation and improves oxidative stability. However, epoxidized oils may exhibit poor low-temperature properties. This limitation can be overcome through ring-opening reactions, which introduce bulky ester side chains and hydroxyl functionalities into the molecular structure. The ring-opening modification disrupts molecular packing, improves low-temperature flow behavior and enhances overall lubricant performance.

Although many plant oils have been investigated as potential biolubricant base stocks, studies focusing on sunflower oil remain limited compared to widely studied oils such as palm oil and soybean oil. Moreover, existing studies often utilize fatty acids obtained directly from hydrolysis, which contain a mixture of saturated and unsaturated fatty acids. Research focusing specifically on esterification using separated unsaturated fatty acids from sunflower oil, followed by epoxidation and ring-opening modifications, is still scarce. Therefore, this study contributes new knowledge by exploring a systematic chemical modification approach to produce a biolubricant base stock derived from sunflower oil.

1.5 Objectives of Study

This study aimed to develop a biolubricant base stock through the stepwise chemical modification and RSM optimization of unsaturated fatty acids derived from sunflower oil. The specific objectives were:

a) To determine the physicochemical properties of sunflower oil.
b) To optimize the reaction parameters of hydrolysis, esterification, epoxidation and ring opening via response surface methodology.
c) To characterize the fatty acid composition of SFO, SFOFA, SFOSFA and SFOUFA using GC-MS, the ester composition of SFOUFANPGE, SFOUFATMPE and SFOUFAPEE using GC-FID and the chemical structures

of SFO, SFOFA, SFOSFA, SFOUFA, SFOUFANPGE, SFOUFATMPE, SFOUFAPEE, ESFOUFATMPE and DOSFOUFATMPE using FTIR and NMR.

d) To evaluate the physicochemical properties of SFOUFANPGE, SFOUFATMPE, SFOUFAPEE, ESFOUFATMPE and DOSFOUFATMPE.

CHAPTER 2
LITERATURE REVIEW

2.1 Lubricant

Lubricant is one of the antifriction agents used between two moving surfaces to reduce friction, increase efficiency and reduce wear on the surfaces of moving part (Owuna et al., 2020; Almasi et al., 2021; Prathiba et al., 2022). They are also used to transfer heat from equipment during operation and prevent corrosion. Lubricants come in various forms such as solid, semi-solid, liquid and gas (Singh et al., 2017). These lubricants play an important role in the manufacturing, transportation and domestic life sectors. Lubricants are very important because they can protect the surface from corrosion caused due to contact with other surfaces, can prevent heat loss from the surface contact, reduce the risk of mechanical failures and act as an insulator (Prathiba et al., 2022).

Normally, lubricants consist of two important components which are base oil and additives (Prathiba et al., 2022). Usually, base oil contains around 80% to 90% in the lubricant. Base oil can be divided into three categories, which are mineral oil, synthetic oil and plant oil (Owuna et al., 2020; Pawar et al., 2022). For mineral oil, it is derived from crude petroleum oil through the fractional distillation process. This oil can be classified into three types according to its chemical form which are paraffinic (straight hydrocarbon chain), naphthenic (cyclic carbon atoms in structure with no carbon double bond) and aromatic (carbon atoms including benzene like compound).

For synthetic oil, it is produced from chemical modification of petroleum products and artificially made that contains uniform hydrocarbon molecules in their chemical structure. This oil is made to overcome the limitation of mineral oil. There are three types of synthetic oil which are silicon oil, synthetic hydrocarbon and organohalogens (Pawar et al., 2022).

Nowadays, mineral and synthetic oils are universal lubrication oils in the production of lubricants for industrial and commercial use (Pawar et al., 2022). Figure 2.1 shows the general classification of lubricant as mention by Srivyas and Charoo, (2018) and Pawar et al., (2022).

For additives, it contains around 10% to 20% in lubricant and it depends on the specific characteristics of the lubricant. Additives that are often used such as antioxidants, rust inhibitors, wear reducers and viscosity modifiers (Salimon et al., 2010). The use of additives in the lubricant affects the lubrication properties and the final performance of the produced lubricating oil.

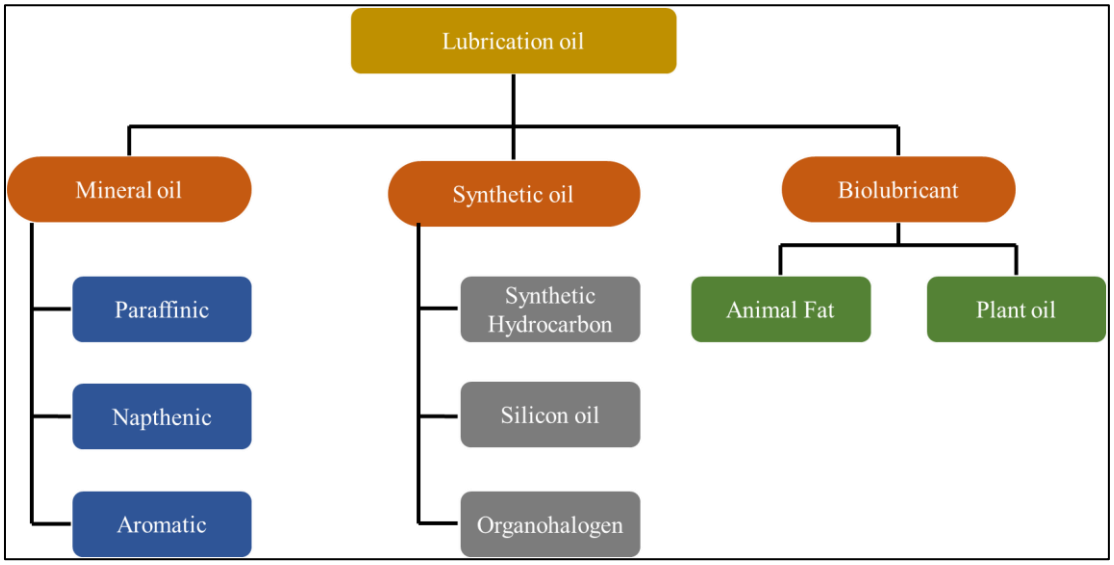


Figure 2.1 General Classification of Lubricant

There are several parameters used to determine the quality of a lubricant. The parameters are oxidative stability, viscosity, viscosity index, flash point and pour point. Oxidative stability is a parameter in determining the performance and lifespan of a lubricant when used in higher temperature conditions and other extreme applications (Owuna et al., 2020). Stachowiak and Batchelor (2014) stated that a lubricant that can withstand at high temperatures without breaking down or make a rearranging molecules is a lubricant that has high oxidative stability and this statement also supported by Ohifuemen et al. (2020). When the lubricant is exposed to air, especially at high temperatures, oxidation process is occurred that will lower the quality of the lubricant. The oxidation process will increase the corrosion, acidity, viscosity and volatility of the lubricating oil (Owuna et al., 2020).

The second parameter is viscosity index (VI). VI of a lubricant is a measurement of how viscosity changes as the temperature changes. A machine that operates across a wide temperature range will need a lubricant with a higher VI since the viscosity of a lubricant is inversely related to its temperature (Dabai et al., 2018; Owuna et al., 2020).

The ideal lubricant is lubricant that can maintain a constant viscosity during temperature changes (from low temperature to high temperature). The importance of this VI can be seen in automotive lubricants, where lubricants with a high VI will prevent excessive thickening when the engine is cold, prevent excessive thinning when the engine is hot, provide full lubrication and avoid excessive oil consumption (Salimon et al., 2012). Lubricant's viscosity will affect the effectiveness of a lubricant in reducing friction between two surfaces. A lubricant that has a moderate viscosity is a good lubricant because if the viscosity is too high it will increase the amount of energy required to move the object (Owuna et al., 2020). Meanwhile, when the viscosity is too low it will cause the surface to rub easily and increase friction due to the contact between the two surfaces of the object. Salimon et al. (2011) state that an increase in temperature will cause the viscosity of the lubricant to decrease.

The third parameter is pour point (PP) where PP is the lowest temperature that the lubricant can flow with only gravity. The PP is very important for equipment used at low temperatures because at low temperatures the viscosity of the lubricant will increase due to the formation of wax that may prevent the lubricant from flowing. The lower the PP, the better the performance of the lubricant at low temperatures (Salimon et al., 2014; Ohifuemen et al., 2020; Owuna et al., 2020).

The fourth parameter is the flash point (FP). Flash point is the lowest temperature at which the lubricant begins to vaporize and can be ignited by an external fire source (Owuna et al., 2020). FP is important to determine how to safely transport and store lubricants. The FP of lubricating oils determines their flammability hazard for safe handling. A good lubricant has a high FP (Salimon et al., 2014; Owuna et al., 2020).

In addition, rheological studies are also important to evaluate the quality and performance of lubricant. Rheological studies are carried out to see the change in shape and flow of a fluid. Rheological properties are very important to control oil film stability and anti-wear effectiveness during use (Widyatmoko, 2016). The rheological condition is evaluated by referring to the curve of shear rate against shear stress (Derawi and Salimon, 2013). Figure 2.2 shows the shear rate versus shear stress plots of Newtonian and non-Newtonian fluid. Newtonian fluids and non-Newtonian fluids are the state in rheological studies. A Newtonian fluid is a fluid that viscosity of lubricant is unaffected by the shear rate (Palagi et al., 2017). From Figure 2.2, it shows that for Newtonian fluid, the shear stress is directly proportional to the shear rate. Non-Newtonian fluid is a fluid viscosity of lubricant is affected by the shear rate (Palagi et al., 2017). Based on

Figure 2.2 it shows that non-Newtonian fluids can be divided into two types, which are dilatant fluids which is shear thickening and pseudoplastic fluids which is shear thinning. Dilatant fluids show an increase in viscosity as shear stress increases, while pseudoplastic fluids show a decrease in viscosity as shear stress increases. Bingham plastic fluids require minimal shear stress to flow (Nor, 2019).

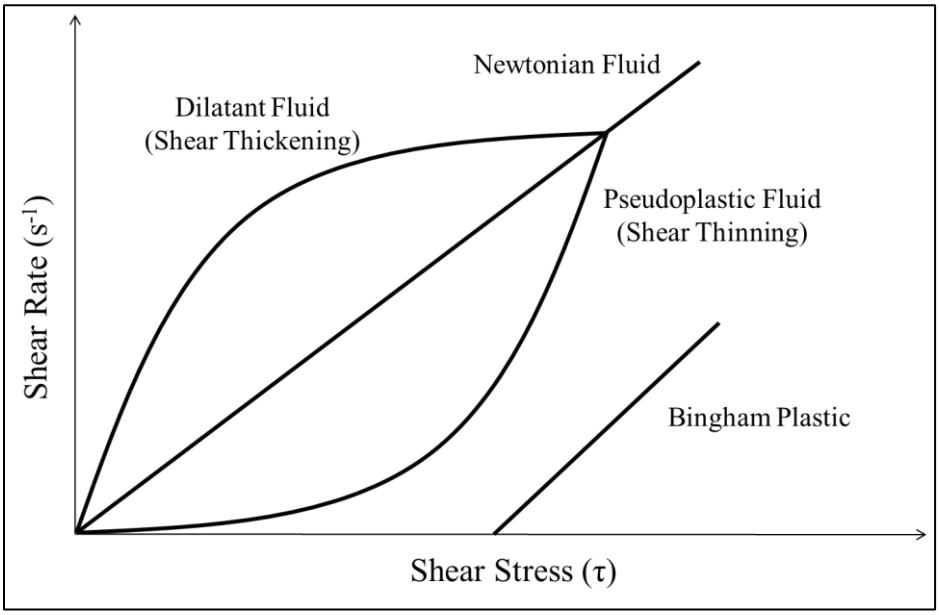


Figure 2.2 Shear Rate versus Shear Stress of Newtonian and Non-Newtonian Fluid

Among the three types of base oils used in the production of lubricants (mineral oil, synthetic oil and plant), mineral oil is the oil that is often used. Therefore, mineral oils are known as universal lubrication oils. Mineral oil is used because it has good physicochemical properties and is cheaper than other oils, but due to its non-biodegradable properties make it necessary to change its use to plant oil. Table 2.1 shows the lubrication properties of mineral oil. High viscosity index, high flash point, thermal stability, high oxidative stability (resistance to oxidation), low pour point and ability to prevent corrosion are all qualities that a lubricant should possess to produce a good and high quality of lubricant (Ohifuemen et al., 2020).

Table 2.1
Lubrication Properties of Mineral Oil

Properties	Mineral Oil
Density	0.85
Viscosity index	128
Kinematic viscosity at 40 °C	112 mm2/s
Kinematic viscosity at 100 °C	13 mm^2/s
Flash point	234 °C
Pour point	-29 °C
Oxidative stability	Good
Shear stability	Good

Source: Charoo and Wani (2016); Trzepieciński (2020)

2.2 Biolubricant from Plant Oil

Due to the accessibility, affordability and compatibility with engineering materials, mineral oil is now regarded as the most widely used commercial lubricating oil (Zainal et al., 2018). However, the continuous use of mineral oil-based lubricants has led to the reduction of petroleum oil resources and the problem of petroleum price instability. This is because petroleum resources are non-renewable and require a long period of time to be produced at the bottom of the earth. Due to the increasing demand on the dwindling raw material resources, the price of petroleum is becoming higher and more unstable. Indirectly, it will cause an increase in the production cost of mineral oil-based lubricants (Zahid et al., 2018; Pawar et al., 2022).

Petroleum-based lubricants have a low biodegradability rate which is 10 to 30%, it has polluted the groundwater for up to 100 years, stunt tree development and shorten the life span of aquatic life. Up to one million litres of water could be contaminated by only one litre of mineral oil (Hamdan et al., 2018; Bellini et al., 2021). According to the research, between 2010 to 2015, 33,000 tonnes of oil were lost to the environment, with 700 tonnes of oil spills being documented in 11 incidents. Human, animal and plant life are all seriously harmed by an oil spill. It will be exceedingly difficult for sea life and plants to thrive if there is an oil spill since it will float on top of the ocean and block sunlight from penetrating the water. These concerns have led to the search for renewable

environmentally friendly alternative sources to replace mineral oil. One of the potential alternative sources for mineral oil replacement is plant oil.

Naturally, plant oils contain almost 95 to 98% of triacylglycerol (TAG) and the structure is made up of one molecule of glycerol (organic alcohol) chemically bonded to three fatty acids (organic acid) (Yara-Varón et al., 2017). Figure 2.3 shows the general structure of triacylglycerol. Saturated and unsaturated fatty acids are divided based on how many double bonds that contain in the carbon chain (Ruggieroa et al., 2017). The carbon chain of saturated fatty acid does not have any double bonds such as stearic and palmitic acid. The carbon chain of unsaturated fatty acids has double bonds. Unsaturated fatty acid can be divided into two which are monounsaturated and polyunsaturated. Monounsaturated fatty acid is fatty acid that contain only one carbon double bond such as oleic acid. Polyunsaturated fatty acids, on the other hand, are those that have two or more double bonds such as linoleic (two double bond) and linolenic acid (three double bond) (Salih and Salimon, 2021) .The long fatty acid chains and the presence of polar groups in the structure of plant oils make them amphiphilic in nature and cause them to be used as hydrodynamic and boundary lubricants. Polar ester groups are able to attach to metal surfaces and produce good boundary lubrication (Quinchia et al., 2014).

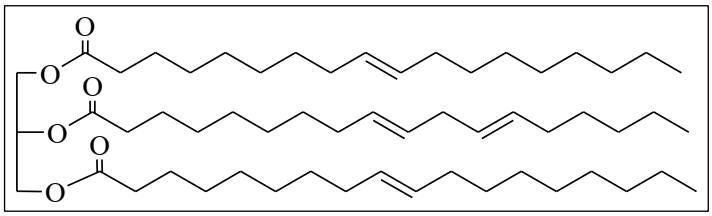


Figure 2.3 General Structure of Triacylglycerol in Plant Oil

Lubricants produced from natural sources such as plant oils are known as biolubricants. Plant oil-based biolubricants are not only favored because they are a renewable raw material, but they are also biodegradable and low toxicity and does not cause harm to the environment. Biodegradable rate for plant oil-based biolubricant is higher compared to other based oil which is 95 to 98% (Ohifuemen et al., 2020). Biodegradation is a process where materials organic compounds are broken down by enzymes produced by living organism (Singh and Chhibber, 2013). Biodegradation is the chemical change of materials through organisms or enzymes (Salimon et al., 2010). Organic matter that can be decomposed via aerobically which is with oxygen or

anaerobically which is without oxygen is considered a biodegradable material (Sarma and Vinu, 2022). Figure 2.4 shows the life cylce of biolubricant. Cycle of biolubricant is from Sarma and Vinu (2022) has been re-illustrated and slightly modified.

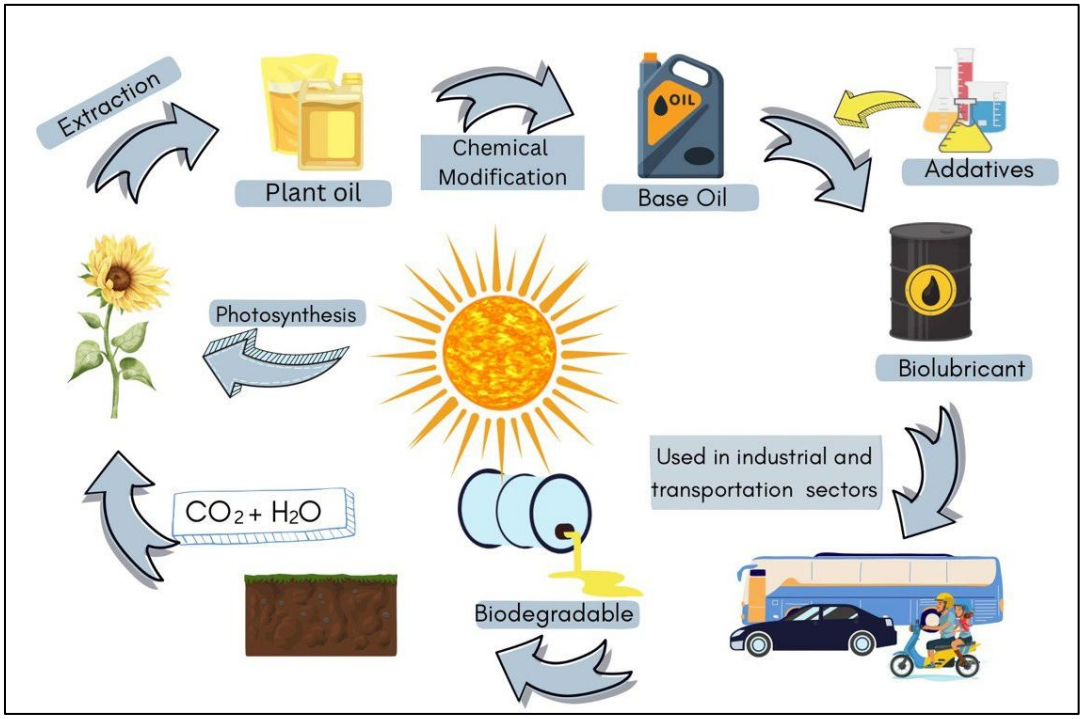


Figure 2.4 Life Cycle of Biolubricant

Based on Figure 2.4, the cycle for biolubricants begins with plant oil being extracted and undergoes chemical modification to improve the physicochemical properties of the plant oil as a biolubricant base oil. Next, the additive is introduced to the base oil enhancing the performance of the biolubricant. Biolubricants are often used in the industrial and transportation sectors. Biolubricants that have reached their usage limit will decompose and produce carbon dioxide (CO_2). CO_2 that being produce will be used by other plants to produce the next plant oil. This cycle will always continue because plant oil is derived from renewable sources.

Besides that, plant oil exhibits the necessary properties of good lubricant such as high viscosity index, low volatility, good lubrication and high biodegradability (Cecilia et al., 2020). Furthermore, plant oil has a high dissolving power for molecules of polar pollutants and additives. Plant oils also have anti-corrosion properties due to the high affinity to the metal surface. Plant oil with high flash point value of more than 300 °C are classifies as a non-flammable liquid (Salimon et al., 2010). Table 2.2 shows the benefits of using biolubricant from plant-based.

Table 2.2
Benefits of Using Biolubricant

Benefits of biolubricant
Higher boiling point (less emissions)
Higher biodegradability (free of aromatics)
Higher lubricity
Lower volatility
Better skin compatibility
Higher shear stability
Higher tool life
Higher viscosity index
Higher safety on shop floor

Source: Cecilia et al. (2020)

Although plant oil has many advantages, it also has some disadvantages that limit its direct use as a biolubricant. Among them are low oxidative stability properties and poor low temperature properties (Nor et al., 2021a). The low oxidative stability in plant oil is due to the presence of the oxidation active site, which is beta hydrogen (β-CH) in the triacylglycerol structure and the double bond in the unsaturated fatty acids of plant oils. Figure 2.5 shows the critical point in triacylglycerol.

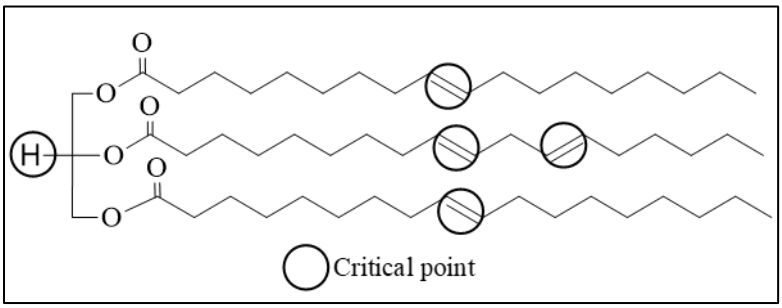


Figure 2.5 Critical Point for β-CH and Carbon Double Bond in Triacylglycerol

The presence of β-CH causes the triacylglycerols of the oil to be unstable at high temperatures (Nor et al., 2022). This is because the β-CH is easily removed from the triacylglycerol molecule and forms acids and olefins (unsaturated compounds). The resulting unsaturated compounds will undergo polymerization and will cause the formation of a precipitate that will increase the viscosity of the plant oil (Erhan et al., 2006; Nor et al., 2018a).

The low oxidative stability that come from carbon double bond was shown in Figure 2.6. The mechanism of oxidation of lipid or also known as oxidation of

hydrocarbon have three stages which are initiation, propagation and termination stage (Owuna, 2020). At the first stage, the removal of a hydrogen atom from the methyl group adjacent to the double bond will form a free radical. Free radicals will easily react with oxygen to form peroxy radicals. Peroxy radicals will attack other fat molecules to remove one hydrogen atom and form hydroperoxides and other free radicals. This situation will double the oxidation process (Fox and Stachowiak, 2007; Cecilia et al., 2020; Owuna, 2020). This oxidation also produces insoluble precipitates and will increase the acidity and viscosity of the oil (Salimon et al., 2010). High oil viscosity will interfere with the function of the lubricant to reduce friction, further disrupting the operation of the engine. Figure 2.6 shows the oxidation mechanism of plant oil (Owuna, 2020).

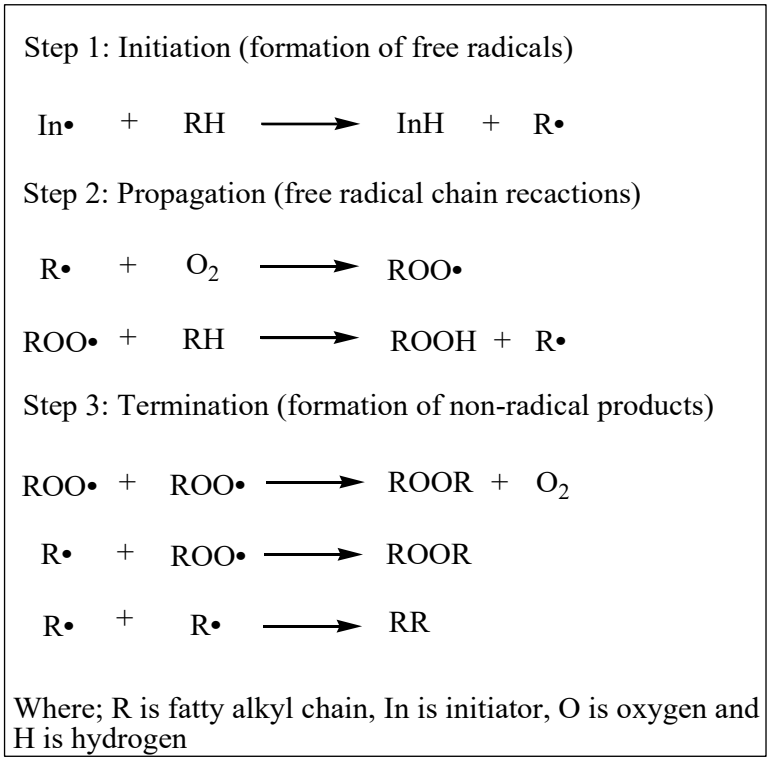


Figure 2.6 Oxidation Mechanism of Plant Oil

According to previous studies, when exposed to low temperatures for an extended period of time, most plant oils experience cloudiness, precipitation, poor flow and solidification at -10 °C (Erhan et al., 2006; Salimon et al., 2012). Poor low temperature properties of plant oil was determine based on the pour point value. Plant oils have a high pour point value due to the tendency to form macrocrystalline structures at low temperatures through the uniform arrangement of linear triacylglycerol

molecules. These microcrystals hinder the flow of the system due to the loss of kinetic energy of individual molecules during self-arrangement.

Chemical modification can be used to address the issue of low oxidative stability and poor low temperature properties. Plant oil's molecular structure will be altered chemically, which will increase their oxidative stability (Moser and Erhan, 2007). Chemical modifications that can be done to plant oil are esterification reaction (to solve the problem of the presence of beta hydrogen) and epoxidation reaction (to solve the problem of the presence of double bonds). This study focusing on chemical modification through the esterification, epoxidation reaction to solve the oxidative stability and ring opening reaction to solve the low temperature properties.

2.3 Sunflower oil

Sunflower oil (SFO) is one of the plant oils that can be used in the production of biolubricants. SFO can be obtained from seed of sunflower plant and the scientific name is *Helianthus annuus* L. SFO can be obtained using different types of extraction methods such as by pressing, cold pressing method and extraction with chemicals by using a suitable solvent such as hexane (Arianto and Cindy, 2019). Sunflower seeds are plants that originate from North America. It was first brought to Europe by Spanish travellers in the sixteenth century from native temperate climes (temperatures between 20 and 25 °C) of North America (Vilvert et al., 2018). Figure 2.7 shows *Helianthus annuus* plant.

The Greek name *Helianthus*, which is derived from the words *helios* (the sun) and *anthos* (a flower), means "sunflower" in English (Fernández-Luqueño et al., 2014). The word "sunflower" comes from the plant's size and appearance, which is similar to the sun. The name is also derived from the revolving around the sun. The big, spherical, yellow inflorescence flower head of the sunflower, which bears achenes that eventually mature into seeds and faces the sun directly, as well as its long taproot, hairy stems and its rough, broad, coarsely serrated leaves, are its distinguishing features. Different cultivars of sunflowers range in size and colour from cream to yellow, revealing their aesthetic and ornamental benefits (Adeleke and Babalola, 2020). Figure 2.7 shows the *Helianthus annuus* and Table 2.3 shows taxonomy of *Helianthus annuus*.



Figure 2.7 *Helianthus annuus* and the Seeds (Dwivedi and Sharma, 2014)

Nowadays, sunflower seed is grown all over the world. The production of sunflowers as an oilseed plant around the world has improved due to their ability to adapt to various climatic and soil conditions (Adeleke and Babalola, 2020). Sunflower oil is one of the top three oilseed crops after soybeans and rapeseed. SFO has also been recognized as the main source of high-quality cooking oil that is important for culinary purposes.

About 16 million tonnes of SFO were produced worldwide in 2017, with Ukraine and Russia producing the most. Accordingly, it was stated in 2014, the global output of SFO reached 15.8 million tonnes, with the production rate per nation being as follows: Ukraine is generating 4.4 million tonnes, followed by Russia with 4.1 million tonnes, Argentina with 0.9 million tonnes, Bulgaria with 0.8 million tonnes and Turkey with at least 0.7 million tonnes (Lai et al., 2017).

The main component in SFO is triacylglycerol (TAG) and the rest are diacylglycerol and monoacylglycerol. 1-oleoyl-2,3-dilinoleoyl-glycerol (OLL) is the highest percentage TAG that contain in SFO which is 29.8%, followed by 1,2,3-trilinoleoyl-glycerol (LLL) at 28.2% and then the other TAGs are stated in the Table 2.4 shows the composition of triacylglycerol in SFO.

In addition, SFO also contains various types of fatty acids consisting of 15% of saturated fatty acid (SFA) and 85% of unsaturated fatty acid (USFA) (Akkaya, 2018). In SFO, SFA that are commonly found are palmitic and stearic acid while for USFA are oleic, linoleic and linolenic acid. Table 2.5 shows fatty acids composition in SFO and Table 2.6 shows the physicochemical properties of SFO.

Table 2.3
Taxonomy of *Helianthus annuus*

Taxonomy of H. annuus L.	
Kingdom	Plantae
Subkingdom	Viridaeplantae
Infrakingdom	Streptophyta
Division	Tracheophyta
Subdivision	Spermatophytina
Infradivision	Angiospermae
Class	Magnoliopsida
Superorder	Asteranae
Order	Asterales
Family	Asteraceae
Subfamily	Helianthoideae
Tribe	Heliantheae
Genus	Helianthus
Species	*annuus*

Source: Fernández-Luqueño et al. (2014)

Table 2.4
Composition of Triacylglycerol in Sunflower Oil

TAG	Chemical Name	ECN	Percentages
LLL	1,2,3-trilinoleoyl-glycerol	39.9	28.2
OLL	1-oleoyl-2,3-dilinoleoyl-glycerol	42.0	29.8
PLL	1-palmitoyl-2,3-dilinoleoyl-glycerol	42.6	9.6
OLO	1,3-dioleoyl-2-linoleoyl-glycerol	44.1	11.0
PLO	1-palmitoyl-2-linoleoyl-3-oleoyl-glycerol	44.7	10.0
PLP	1,3-dipalmitoyl-2-linoleoyl-glycerol	45.3	0.6
OOO	1,2,3-oleoyl-glycerol	46.2	3.0
POO	1-palmitol-2,3-dioleoyl-glycerol	46.8	3.5
POP	1,3-dipalmitoyl-2-oleoyl-glycerol	47.4	0.5
PPP	1,2,3-tripalmitoyl-glycerol	48.0	0.8
SOO	1-stearoyl-2,3-oleoyl-glycerol	48.8	1.1
POS	1-palmitoyl-2-oleoyl-3-stearoyl-glycerol	49.4	0.4
PPS	1,2-dipamitoyl-3-stearoyl-glycerol	50.0	0.4

Note: TAG = triacylglycerol; ECN = equivalent carbon number; L = linoleic acid; O = oleic acid; P = palmitic acid; S = stearic acid

Source: Dian et al. (2018)

Table 2.5
Fatty Acids Composition in Sunflower Oil

Fatty Acid	Systematic Name	Structure	Formula	Percentage (%)
Palmitic	Hexadecenoic	C 16:0	$C_{16}H_{32}O_2$	5.2
Stearic	Octadecanoic	C 18:0	$C_{18}H_{36}O_2$	2.7
Oleic	*cis*-9-octadecanoic	C 18:1	$C_{18}H_{34}O_2$	37.2
Linoleic	*cis*-9, *cis*-12-octadecadienoic	C 18:2	$C_{18}H_{32}O_2$	53.8
Linolenic	*cis*-9, *cis*-12, *cis*-15-octadecatrienoic	C 18:3	$C_{18}H_{30}O_2$	1.0

Source: Saurabh et al. (2011); Wai and Jiang (2019)

Table 2.6
Physicochemical Properties of Sunflower Oil

Parameter	Value
Free Fatty Acid (FFA, %)	0.042
Acid Value (mgKOH/g)	0.953
Saponification Value (mgKOH/g)	182.233
Iodine Value (mgI_2/100g)	119.921
Peroxide Value (mgO_2/kg)	6.322

Source: Aboki et al. (2012)

2.4 Hydrolysis of Plant Oil

Hydrolysis is a process where fat or oil is broken down to separate fatty acid from glycerol by breaking the ester bond that forms the triacylglycerol (TAG). This process happens in stages where TAG was be converted into diacylglyceride, monoacylglyceride and then into fatty acids and glycerol. There are several catalysts that can be used for hydrolysis to separate fatty acids from glycerol. Hydrolysis can be catalyzed by using acid, base, enzymes and subcritical water (Salimon et al., 2011; Bahadi et al., 2020). Among those catalysts, the base catalyst or also known as saponification has become a choice for researchers nowadays because this reaction is one way and does not reverse. It also makes the product (fatty acid) easier to separate (Salimon et al., 2011).

There are two stages in the hydrolysis process, namely saponification process and acidification process. The hydrolysis process begins with a saponification process where a mixture of oil and alkaline alcohol is heated under a reflux condenser. Usually,

the alkaline alcohol used is sodium hydroxide (NaOH) or potassium hydroxide (KOH). This saponification process produces fatty acids potassium and glycerol. The acidification process is carried out by using mineral acids such as hydrochloric acid to neutralize the mixture and then glycerol can be separated from fatty acids (Nor, 2019). Figure 2.8 shows the general chemical equation for the hydrolysis process.

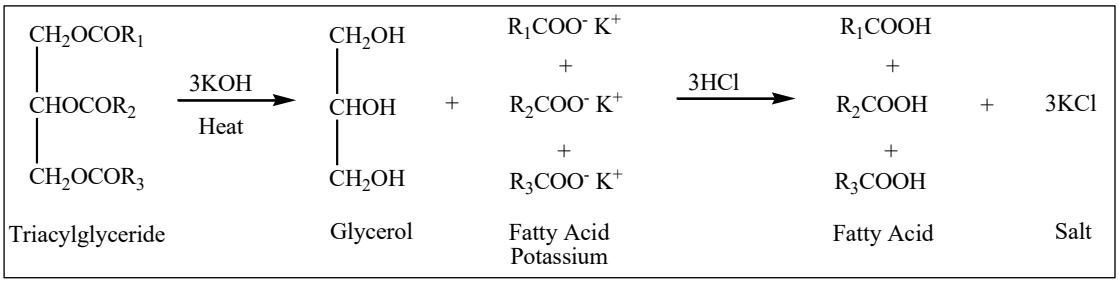


Figure 2.8 General Chemical Equation for Hydrolysis Process

For the mechanism in the hydrolysis process, during the saponification process, the addition of nucleophilic from alkaline alcohol which is hydroxide ion (OH^-) occurs on carbonyl ester oil (C=O) which is electrophilic and forms an intermediate tetrahedral structure. Next, there is a rearrangement of the intermediate tetrahedral structure through electron transfer, followed by the breaking of the ester bond that binds the fatty acid to glycerol. The breaking of the ester bond causes the separation of fatty acids from glycerol. The negatively charged glycerol acts as a base and attacks the acidic proton on the fatty acid and produces fatty acid potassium ($ROO^- K^+$) (Klein, 2021).

In the acidification process, fatty acid potassium ($RCOO^-K^+$) that is formed is acidified using hydrochloric acid (HCl), further forming fatty acids. Through the addition of hydrochloric acid (HCl), the oxygen on the fatty acid potassium, which is nucleophilic, attacks the electrophilic hydrogen (H^+) on the hydrochloric acid and forms a hydroxyl group. The formation of the hydroxyl group (OH) converts fatty acid potassium ($RCOO^-K^+$) to fatty acid (RCOOH) (Nor, 2019). Figure 2.9 shows the general mechanism of hydrolysis process.

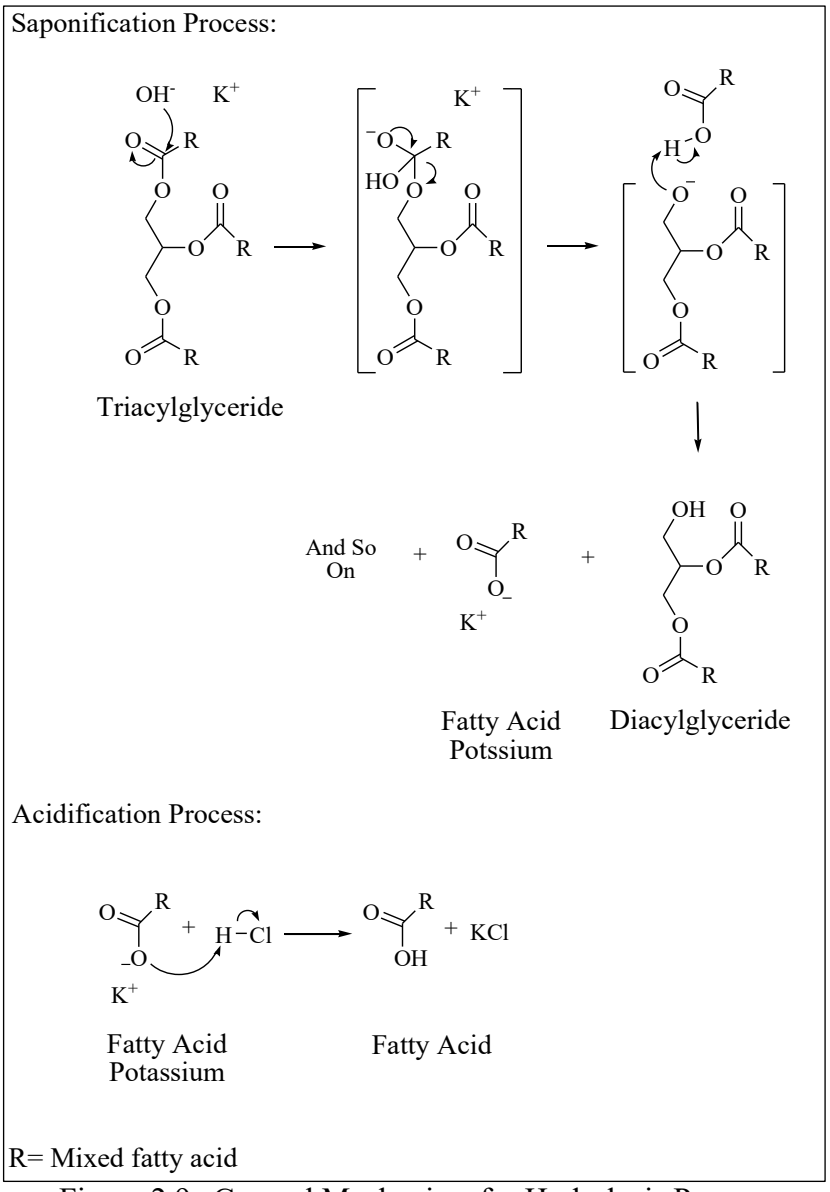


Figure 2.9 General Mechanism for Hydrolysis Process

2.5 Separation of Fatty Acids

The separation of fatty acids from plant oils is a critical step in producing a biolubricant base stock, as plant oils consist of mixed saturated and unsaturated fatty acids that exhibit different reactivities and physicochemical properties. Studies have reported several separation techniques, including urea complexation (Salimon et al., 2012), molecular distillation (Cermaks et al., 2012) and solvent crystallization (Jumaah et al., 2019; Fadzel et al., 2021). Although urea complexation is effective for separating saturated fatty acids through urea inclusion complexes, it involves multiple chemicals, additional purification steps and potential environmental concerns due to urea residue

and solvent recovery requirements. These limitations have motivated the search for simpler and more environmentally friendly separation approaches.

In the separation of fatty acids into saturated fatty acids and unsaturated fatty acids using the low-temperature solvent crystallization (LTSC) method, methanol was employed as the solvent due to its capacity for crystallizing fatty acids. The solubility of fatty acids plays a crucial role in this methanol crystallization process. Specifically, saturated fatty acids exhibit lower solubility compared to unsaturated fatty acids (Japir et al., 2018). Fatty acids in SFO consist of both saturated and unsaturated types. The composition includes approximately 20% SFOSFA and 80% SFOUFA. Among the saturated fatty acids, those with longer carbon chains, such as palmitic and stearic acids (C16 and above), were considered non-polar compounds. On the other hand, shorter-chain saturated fatty acids like myristic and lauric acids (C14 and below) were marginally more polar than their longer-chain counterparts. The polarity of saturated fatty acids decreases with the number of carbon atoms, leading to greater non-polarity as the carbon chain lengthens. In contrast, unsaturated fatty acids, encompassing both monounsaturated and polyunsaturated varieties, possess higher polarity compared to saturated fatty acids (Jumaah et al., 2019). These unsaturated fatty acids demonstrate greater solubility in methanol during the low-temperature crystallization process.

The selection of methanol as the solvent for LTSC was based on its preferential dissolution of unsaturated fatty acids (SFOUFA) over saturated fatty acids (SFOSFA) due to its polar nature. As the temperature decreases during the crystallization process, the solubility of less polar saturated fatty acids diminishes, leading to their precipitation as crystals. Conversely, more polar unsaturated fatty acids remain in solution due to their higher solubility at lower temperatures (Jumaah et al., 2019; Fadzel et al., 2021). According to the "like dissolve like" principle, polar solvents favor the dissolution of polar compounds, while non-polar solvents favor non-polar compounds (Japir et al., 2018). Given that methanol was a polar solvent, unsaturated fatty acids, which possess greater polarity, exhibit enhanced solubility compared to saturated fatty acids, which were less polar. The solubility of the SFOFA mixture in methanol follows the order from most to least polar as linolenic acid, linoleic acid, oleic acid, paullinic acid, palmitic acid, stearic acid, arachidic acid, behenic acid, tricosanoic acid and lignoceric acid. The solubility of fatty acids in methanol was determined by the polarity and hydrogen bonding properties of the compounds present in the mixture. Table 2.7 from Foreman and Brown (1944) shows the solubility of each fatty acids in methanol.

Table 2.7
Solubility of Fatty Acids in Plant Oil at Different Temperature in Methanol

Temperature (°C)	Solubility						
	C16:0	C18:0	C18:1	C18:2	C18:3	C20:0	C22:0
10	1.310	0.259	-	-	-	0.096	0.042
0	0.396	0.092	-	-	-	0.065	0.010
-10	0.146	0.032	-	-	-	-	-
-20	0.063	0.010	4.020	-	-	-	-
-30	0.020	-	0.708	-	-	-	-
-40	-	-	0.329	-	-	-	-
-50	-	-	0.089	2.520	-	-	-
-60	-	-	0.052	0.925	-	-	-
-62	-	-	-	-	1.76	-	-
-70	-	-	0.032	0.394	-	-	-

Source: Foreman and Brown (1944)

However, most reported studies focus on general fatty acid mixtures or biodiesel feedstocks, with limited attention given to the selective separation of sunflower oil unsaturated fatty acids for biolubricant applications. Furthermore, many biolubricant studies utilize fatty acids obtained directly from hydrolysis without prior separation, resulting in mixed fatty acid feedstocks that limit control over subsequent esterification, epoxidation and ring-opening reactions. Therefore, the application of methanol crystallization to selectively isolate unsaturated fatty acids from sunflower oil represents a research gap and its integration into biolubricant synthesis offers a novel approach to improving molecular control and final lubricant performance.

2.6 Esterification Reaction

Esterification reaction is a reaction where carboxylic acid and alcohol are reacted in the presence of heat and catalyst. It is also known as the condensation process between carboxylic acid and alcohol. Esterification reaction is one of the important reactions in biolubricant production. The result of esterification gives ester as the final product and water as a side product. The removal of water during esterification is very important to avoid the reverse reaction that will cause the resulting ester to be hydrolyzed.

This esterification reaction can be catalyzed using chemical catalysts. For chemical catalyst, the acid catalyst that is often used is strong mineral acid such as

hydrochloric acid (HCl) and sulfuric acid (H_2SO_4) (Annisa and Widayat, 2018). Figure 2.10 shows the general chemical equation for esterification using acid catalyst.

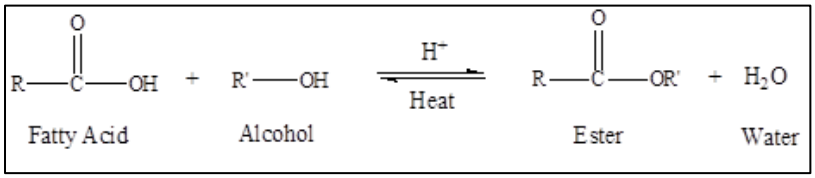


Figure 2.10 General Chemical Equation for Esterification

For the acid catalyst mechanism, protonation of the carbonyl oxygen occurs and activates the carboxylic acid. Nucleophilic attack by alcohols produces a tetrahedral intermediate. A proton is transferred from one oxygen atom to another producing a second tetrahedral intermediate and converts the OH group to a good leaving group. Finally, loss of protons and production of water regenerates the acid catalyst and produces the ester product (Klein, 2021). Figure 2.11 shows the general mechanism of esterification for acid catalyst.

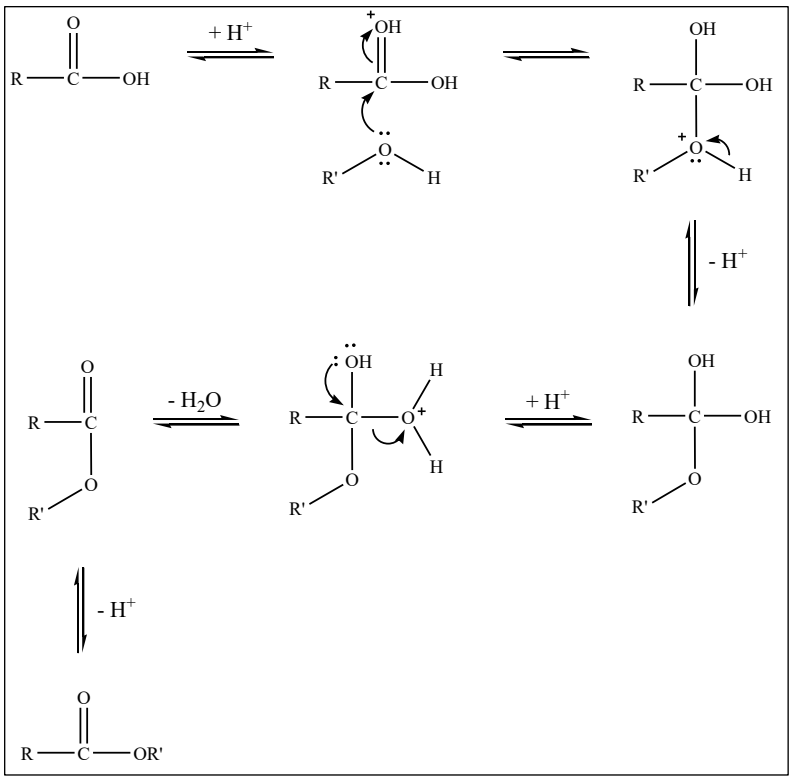


Figure 2.11 General Mechanism for Esterification for Acid Catalyst

2.7 Polyol Ester

Biolubricants are usually come from the reaction of plant oil or fatty acid with polyhydric alcohol where it produces polyol ester. Esterification (fatty acid react with polyhydric alcohol) and transesterification (fatty acid methyl ester (FAME) react with polyhydric alcohol) are reactions that are often used for the production of polyol ester (Annisa and Widayat, 2018; Bahadi et al., 2022). Previous studies have shown that lubricants from polyol ester provide better lubrication than mineral oil (Ohifuemen et al., 2020). Polyhydric alcohol is a compound that has more than one hydroxyl (OH) group in its chemical structure. Polyhydric alcohol is the best substance to replace glycerol because it does not have beta hydrogen. The polyhydric alcohols that are often used in the production of polyol esters are neopentyl glycol (NPG), trimethylolpropane (TMP), pentaerythritol (PE), di-trimethylolpropane (Di-TMP) and di-pentaerythritol (Di-PE) (Bahadi et al., 2022). NPG has two hydroxyl (OH) groups, TMP has three OH groups, PE and DiTMP have four OH groups and DiPE has six OH groups. Figure 2.12 shows the molecular structure of polyhydric alcohol. This study was focusing on the use of NPG, TMP and PE as polyhydric alcohols to produce polyol esters.

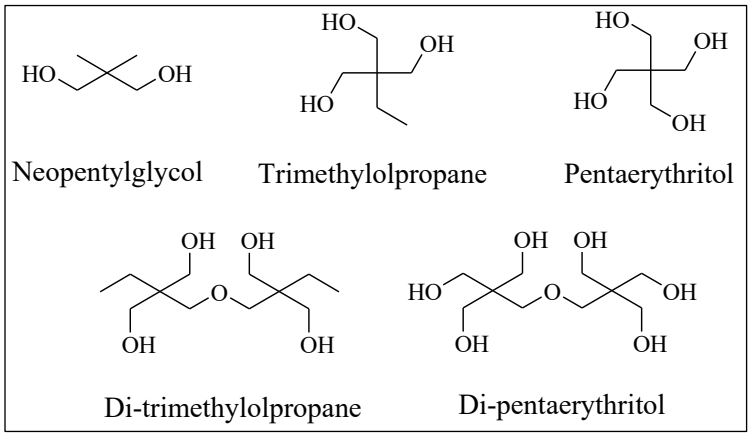


Figure 2.12 Structure of Polyhydric Alcohol

Neopentyl glycol or also known as NPG contains two hydroxyl (OH) groups in its molecular structure and its molecular formula is $C_5H_{12}O_2$ with molecular weight 104.148 g/mol. The name of NPG based on International Union of Pure and Applied Chemistry (IUPAC) is 2,2-dimethylpropane-1,3-diol. The melting point of NPG is 129 °C and its boiling point is 208 °C. At room temperature, NPG exists as a white solid.

The reaction of NPG with fatty acid produce diester as a major product in NPG-based biolubricant. Figure 2.13 shows the general structure of NPG polyol ester.

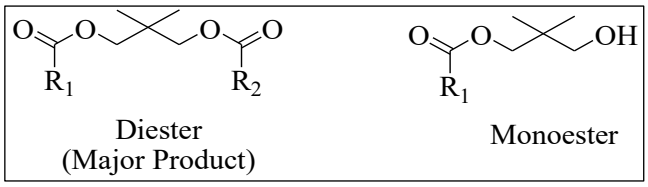


Figure 2.13 General Structure of Polyol Ester Produced from NPG

Trimethylolpropane with IUPAC name 2-ethyl-2(hydroxymethyl)-1,3-propanediol is a polyhydric alcohol that has three groups of hydroxyl (OH). The molecular weight of TMP is 134.17 g/mol with the molecular formula $C_6H_{14}O_3$. The melting point of TMP is at 58 °C and the boiling point is at 295 °C. At room temperature, TMP exists as a white solid. The reaction of TMP with fatty acid produce triester as a major product in TMP-based biolubricant. Figure 2.14 shows the general structure of TMP polyol ester.

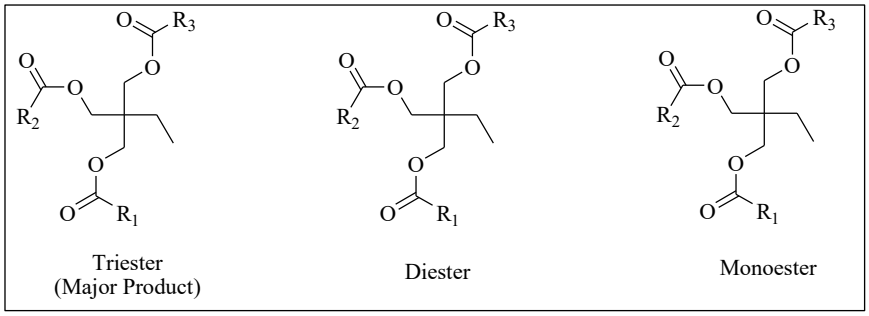


Figure 2.14 General Structure of Polyol Ester Produced from TMP

Pentaerythritol or also known as PE contains four OH groups in its molecular structure and its molecular formula is $C_5H_{12}O_4$ with molecular weight 136.15 g/mol. The name of PE based on International Union of Pure and Applied Chemistry (IUPAC) is 2,2-Bis(hydroxymethyl)propane-1,3-diol. The melting point of PE is 260 °C and its boiling point is 276 °C. At room temperature, PE exists as a white solid. The reaction of PE with fatty acid produce tetraester as a major product in PE-based biolubricant. Figure 2.15 shows general structure of ester in polyol ester from PE-based.

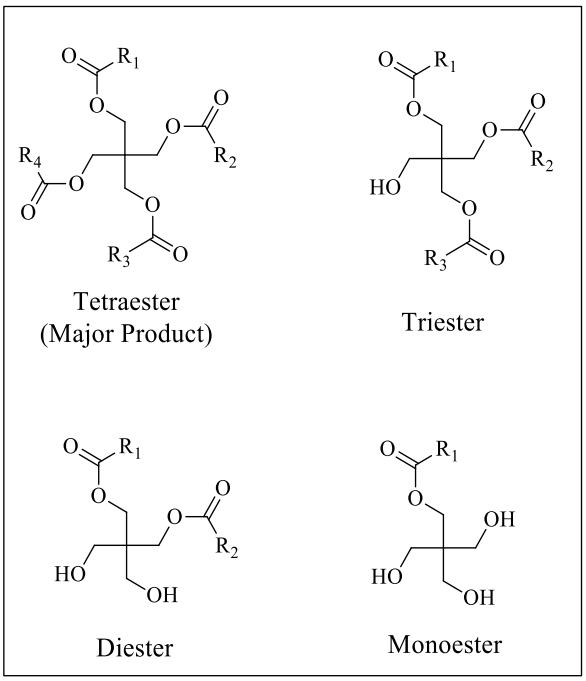


Figure 2.15 General Structure of Polyol Ester Produced from PE

NPG, TMP and PE contain two, three and four OH groups, respectively, enabling the formation of diesters, triesters and tetraesters through esterification. The increase in the number of hydroxyl groups provides more reactive sites for ester bond formation, resulting in a higher degree of esterification and a more highly branched molecular structure. Unlike plant oils, which possess a triacylglycerol backbone containing β-hydrogen (β-CH) atoms, polyhydric alcohols do not contain β-hydrogen atoms. The absence of β-hydrogen suppresses thermal degradation through β-hydrogen elimination and reduces the susceptibility of the ester molecules to thermal decomposition, thereby enhancing the thermal and oxidative stability of the resulting polyol esters (Kania et al., 2015; Nor et al., 2022a). Consequently, polyol esters generally exhibit greater thermal stability and longer service life than unmodified plant oils, making them more suitable for high-temperature lubrication applications.

In addition to improving thermal and oxidative stability, the molecular structure of polyhydric alcohols also significantly influences the physicochemical properties of the resulting polyol esters. Table shows the comparison of the molecular structures of NPG, TMP and PE and the physicochemical properties of the corresponding polyol esters. As the number of hydroxyl groups increases from NPG to TMP and PE, the number of ester linkages and the molecular size of the esters also increase, leading to stronger intermolecular interactions and a more compact branched molecular structure (Zhang et al., 2023). These structural characteristics generally contribute to higher

viscosity, improved viscosity index and higher flash points because larger and more branched molecules require greater energy to evaporate and maintain a stable lubricating film under elevated temperatures (Padmaja et al., 2012). Furthermore, the branched molecular structure disrupts the regular packing of molecules and reduces crystallization at low temperatures, thereby improving low-temperature fluidity and lowering the pour point compared with straight-chain esters (Kania et al., 2015). Therefore, increasing the number of hydroxyl groups from NPG to TMP and PE generally enhances the high-temperature performance and overall physicochemical characteristics of polyol esters, making these polyhydric alcohols attractive building blocks for the production of high-performance biolubricant base stocks.

Table 2.8
Comparison of the Molecular Structures of NPG, TMP and PE and the Physicochemical Properties of the Corresponding Polyol Esters

Polyhydric alcohol	Neopentyl glycol	Trimethylolpropane	Pentaerythritol
Number of hydroxyl groups	2	3	4
Type of ester formed	Diester	Triester	Tetraester
β-Hydrogen	Absent	Absent	Absent
Esterification capability	Forms two ester linkages	Forms three ester linkages	Forms four ester linkages
Branching / molecular compactness	Lowest	Moderate	Highest
Intermolecular interactions	Lowest	Moderate	Highest
Thermal stability	High	Higher	Highest
Viscosity	Lowest	Moderate	Highest

2.8 Epoxidation Reaction

Epoxidation represents a chemical modification technique employed to enhance the oxidative stability of plant oils, with this reaction primarily occurring at double bonds in the structure of oil (Lee et al., 2008). The process of epoxidation entails the utilization of double bonds in conjunction with peracids (Abdullah and Salimon, 2010). Epoxidation holds significance as one of the oxidation products utilized as a medium in the synthesis of fine chemicals, as elucidated by Hincapie et al. (2018). Moreover, it plays a crucial role in alkene addition reactions, as highlighted by Lee et al. (2008).

During the epoxidation process, oxygen atoms are introduced into double bonds (C=C), thereby transforming the double bond into an epoxy group (C-O-C), commonly

referred to as an epoxide ring (Bach et al., 1997). Various methods are employed to generate epoxide rings, including epoxidation with in-situ carboxylic acid (Goud et al., 2006), epoxidation utilizing both organic and inorganic peroxides (Aerts and Jacobs, 2004), epoxidation with halohydrins involving hypohalous acid and their salts and epoxidation using oxygen molecules (Goud et al., 2006).

In the context of plant oil epoxidation, achieving a pristine and high-quality epoxidized plant oil is typically accomplished through the utilization of percarboxylic acid, commonly referred to as peracid (Goud et al., 2006). Peracids are renowned for their effectiveness as oxidizing agents (Hong et al., 2015). The epoxidation procedure involving peracid is conducted in an in-situ manner, wherein the reaction occurs immediately upon mixing. This in-situ approach is preferred due to the inherent risk associated with the production of peracid, which can be prone to explosion (Nor et al., 2019b). Employing the in-situ method ensures safety during the execution of the epoxidation process.

Commonly, epoxidizing agents employed for the generation of peracids include formic acid and acetic acid. The initial utilization of formic acid for epoxidation dates back to 1945, attributed to Findley, while epoxidation using acetic acid was pioneered in 1955 by Gall and Greenspan, as documented by Findley et al. (1945), Greenspan and Gall (1956) and Latourette et al. (1960). The method employing formic acid to generate peracids is favored for its simplicity, as the separation of formic acid from the reaction product is straightforward due to differences in solubility between epoxidized oil and water. Furthermore, the use of formic acid obviates the necessity for employing a catalyst in the reaction process (Derawi and Salimon, 2010). Conversely, acetic acid is less commonly utilized due to its demand for higher concentrations and the requirement for a catalyst to ensure the completeness of the epoxidation process. In terms of reactivity, formic acid surpasses acetic acid, forming more reactive peracids (Abdullah and Salimon, 2010). It's worth noting that while formic acid offers superior performance, its production cost exceeds that of acetic acid (Derawi and Salimon, 2010).

To generate peracids, formic acid undergoes an in-situ reaction with hydrogen peroxide (H_2O_2). In this process, H_2O_2 serves as an oxygen donor, while formic acid functions as an oxygen carrier. This method, known as formic acid auto-catalyst preparation, derives its name from the relatively rapid reaction kinetics, which do not necessitate the presence of a catalyst (Sun et al., 2011). During this reaction, oxygen

atoms from hydrogen peroxide are transferred to formic acid, resulting in the formation of peracid. Figure 2.16 illustrates the general reaction involved in peracid formation.

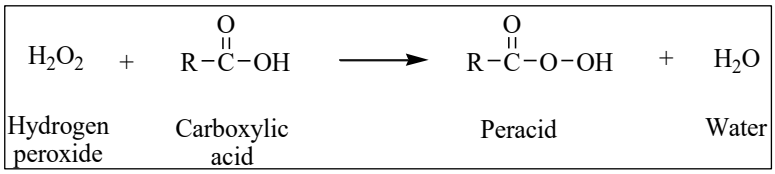


Figure 2.16 Formation of Peracid

In the epoxidation mechanism, a series of changes occur within a single step. The double bond (C=C) present in plant oil functions as the nucleophile, while the oxygen atoms within the peracids act as electrophiles. The double bonds selectively attack the more positively charged oxygen atoms, leading to the subsequent cleavage of the relatively weak oxygen-oxygen bonds. This cleavage results in the formation of new carbonyl groups. During this carbonyl formation, a rearrangement process occurs, leading to the release of electrophilic oxygen and the consequent formation of the epoxide ring. The mechanism of epoxidation was shown in Figure 2.17.

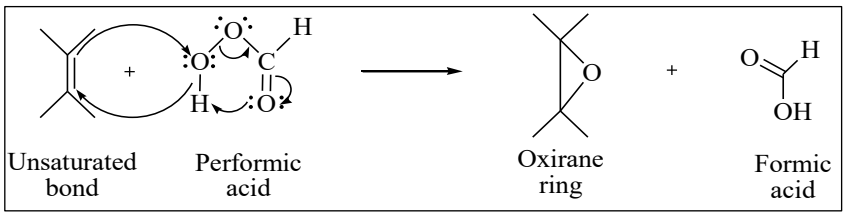


Figure 2.17 General Mechanism of Epoxidation Reaction

2.9 Ring Opening Reaction

The epoxidation reaction which was conducted has removed the unsaturated site on the polyol ester structure which provides better oxidative stability. However, it will produce a high pour point due to the absence of double bonds in the polyol ester chemical structure. Therefore, further modification should be carried out on the epoxidized polyol ester and one of the ways that is often used is through the epoxide ring opening reaction. This reaction was intended to increase molecular branching within the structure, thereby disrupting regular molecular packing and effectively reducing the pour point value.

Usually, alcohol and carboxylic acid that act as nucleophilic agents are used in the opening of the epoxide ring. Epoxide ring opening occurs through the cleavage of one of the carbon oxygen carbons (C-O-C) bonds. Alcohol and carboxylic acid will produce different products where if epoxide ring opening uses alcohol, it will produce ether group (ROR) and hydroxyl group (OH). Whereas if epoxide ring opening is done using carboxylic acid, the result is an ester group (RCOOR) and a hydroxyl group (OH) which is called a hydroxyl ester (Nor, 2019). Figure 2.18 shows the general chemical equation for ring opening reaction.

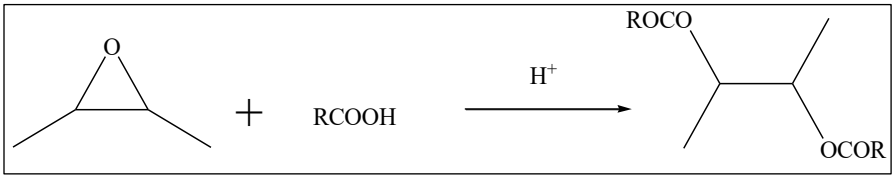


Figure 2.18 General Chemical Equation for Ring Opening Reaction

The presence of a catalyst in the epoxide ring opening reaction is a good step. Usually, p-toluenesulfonic acid (PTSA) and sulfuric acid (H_2SO_4) was used as a catalyst for this epoxide ring opening reaction because it leads to the maximum opening of epoxide rings and causes no side reaction (Nor et al., 2021b). In epoxide ring opening, the epoxide ring reacts with an acid causing protonation of the oxygen atom to form a protonated epoxide intermediate. Then the nucleophilic will attack the epoxide ring that is cut from the side opposite to the epoxide group. This is because the oxygen atom prevents the attack from the front side. Attacked carbon experiences an inversion of configuration. The C-O bond formed is opposite to the original epoxide ring. The acid catalyst provides a good leaving group (OH) on the carbon attacked by the nucleophilic agent.

Oleic acid, also known as 9-octadecanoic acid according to IUPAC nomenclature, belongs to the family of unsaturated fats. It occurs naturally in various plant oils, with olive oil being a particularly rich source. Figure 2.19 shows the structure of oleic acid. This fatty acid consists of 18 carbon atoms in its long-chain structure and features a single double bond positioned between the ninth and tenth carbon atoms, denoted as C18:1. Its chemical formula is $C_{18}H_{34}O_2$. Oleic acid is typically in a liquid state at room temperature, appearing as a light yellow-colored, odorless substance. It is

noteworthy that oleic acid can be found in several food sources, including olive oil, canola oil, sunflower oil and safflower oil.

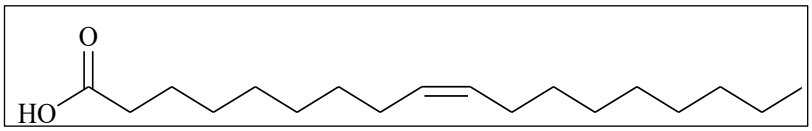


Figure 2.19 Structure of Oleic Acid

In the context of biolubricant, the presence of oleic acid in the chemical structure of polyol ester provides good lubricating properties, which are oxidative stability and better flow properties at low temperatures. Oleic acid is the best fatty acid compared to other fatty acids due to the presence of mono unsaturated fatty acids. The oleic acid structure that has a monounsaturated provides better oxidative stability compared to polyunsaturated fatty acids (linoleic and linolenic acid). It also provides better low temperature flow than saturated fatty acids.

2.10 Response Surface Methodology

Reaction optimization has traditionally been performed using the one-factor-at-a-time (OFAT) approach, in which a single process variable is varied while all other variables are kept constant. Although simple to implement, this approach is inefficient for multistep organic synthesis because it does not evaluate the interaction between process variables and often requires a large number of experimental runs (Baş and Boyacı, 2007). Consequently, OFAT increases reagent consumption, experimental cost, and optimization time while limiting the ability to identify the true optimum operating conditions (Almeida et al., 2008). Furthermore, it cannot adequately describe nonlinear or quadratic relationships among variables, making it unsuitable for complex chemical reactions where several factors, such as reactant molar ratio, catalyst loading, reaction temperature and reaction time, simultaneously influence multiple response variables (Baş and Boyacı, 2007; Almeida et al., 2008).

To overcome these limitations, Response Surface Methodology (RSM) has become one of the most widely used statistical tools for process modelling and optimization. First introduced by Box and Wilson in 1951 (Mäkelä, 2018; Senaras, 2019), RSM combines mathematical and statistical techniques to evaluate the effects of several independent variables on one or more responses while minimizing the number

of experimental trials (Madadi et al., 2020). Unlike OFAT, RSM simultaneously investigates the individual, interaction and quadratic effects of process variables and develops empirical polynomial models capable of predicting optimum operating conditions within the selected experimental region (Madadi et al., 2020). The adequacy and predictive capability of the developed models are commonly evaluated using analysis of variance (ANOVA), regression coefficients, coefficient of determination (R^2), adjusted R^2, predicted R^2, lack-of-fit tests and residual analyses (Geiger, 2014).

In RSM, the optimization process generally involves selecting the process variables and their experimental ranges, constructing an appropriate experimental design, developing and validating the regression model and analysing the response surface and contour plots to determine the optimum operating conditions (Wanasundara et al., 1999; Geiger, 2014). Several experimental designs are available within the RSM framework, including Central Composite Design (CCD), Box–Behnken Design (BBD) and D-optimal Design. CCD is widely employed for fitting quadratic models but generally requires a relatively large number of experimental runs, whereas BBD is more economical because it uses fewer experiments and avoids extreme operating conditions. However, BBD is less suitable when the experimental region is irregular or constrained (Pattanaik and Rayasam, 2018; Zahmatkesh et al., 2022). In contrast, D-optimal Design is a computer-generated design that selects experimental runs by maximizing the determinant of the information matrix ($|X'X|$), thereby maximizing the precision of parameter estimation (Pattanaik and Rayasam, 2018). Unlike CCD and BBD, D-optimal Design does not require a fixed geometric arrangement of experimental points and can accommodate constrained factor ranges, irregular experimental regions, categorical variables and prohibited combinations of operating conditions (Zahmatkesh et al., 2022; Rahman et al., 2022).

RSM has been extensively applied in chemical engineering, biotechnology, food processing, pharmaceutical formulation and plant oil-based biolubricant production because many chemical processes are governed by several operating variables and multiple interrelated responses (Madadi et al., 2020). In biolubricant synthesis, RSM has been successfully used to optimize epoxidation, oxirane ring-opening, esterification, transesterification and polyol ester synthesis by investigating variables such as reactant molar ratio, catalyst concentration, reaction temperature and reaction time (Madadi et al., 2020). The corresponding responses commonly include oxirane oxygen content, conversion yield, iodine value, acid value, hydroxyl value, kinematic

viscosity, viscosity index and pour point. By simultaneously modelling these responses, RSM enables the identification of optimum reaction conditions while reducing experimental effort, material consumption and overall research cost (Wanasundara et al., 1999; Geiger, 2014). Therefore, D-optimal Design was selected in the present study because it provides greater flexibility for constrained experimental regions while maintaining model accuracy with fewer experimental runs than conventional RSM designs (Pattanaik and Rayasam, 2018; Zahmatkesh et al., 2022; Rahman et al., 2022).

2.11 Physicochemical Properties of Oil

2.11.1 Iodine Value

Iodine value (IV) test is used to measure the degree of unsaturation of fatty acids (C=C) contained in the oil sample. Specifically, IV can be defined as the number of grams of iodine that can be absorbed by 100 grams of the oil with unit I_2/100 g (Salimon et al., 2006). The IV of oils is indicative of their degree of unsaturation, with higher values corresponding to a greater number of double bonds. Oils with higher IVs tend to have lower melting points and remains in liquid form at room temperature due to the presence of more unsaturated fatty acids while oils with lower IVs have fewer double bonds and tend to have higher melting points and becomes a solid form at room temperature. The IV is a useful parameter for predicting the physical properties of oils based on their degree of unsaturation.

In IV test, the double bond in unsaturated fatty acids reacts with iodine and this reaction is known as halogenation of double bond. Where the double bond in the oil sample is open and iodine is added that leads to the formation of carbon-iodine (C-Cl). The formation of iodine-adduct compounds is a characteristic reaction of unsaturated compounds, where iodine molecules add across the carbon-carbon double bonds. Common examples of iodine-adduct compounds that can be formed during the iodine value test which is iodine monochloride (ICl) (Salimon et al., 2006; He and Liu, 2019). These compounds are typically brown or dark-colored. Reaction equation in iodine value is shown in Figure 2.20 (Pulassery et al., 2022). The excess iodine that does not react will be reduced with titrate by sodium thiosulphate.

Sodium thiosulphate solution ($Na_2S_2O_3$) is used as a standard solution in the IV test. The $Na_2S_2O_3$ solution used is the primary standard that acts as a reducing agent. It

undergoes a redox reaction with the excess iodine. When $Na_2S_2O_3$ reacts with iodine, $Na_2S_2O_3$ reduces the iodine from I_2 to iodide ion (I^-) and $Na_2S_2O_3$ being oxidized to sodium tetrathionate ($Na_2S_4O_6$). In its reaction with iodine, each thiosulphate ion will lose one electron. Starch solution is used as an indicator in the IV test.

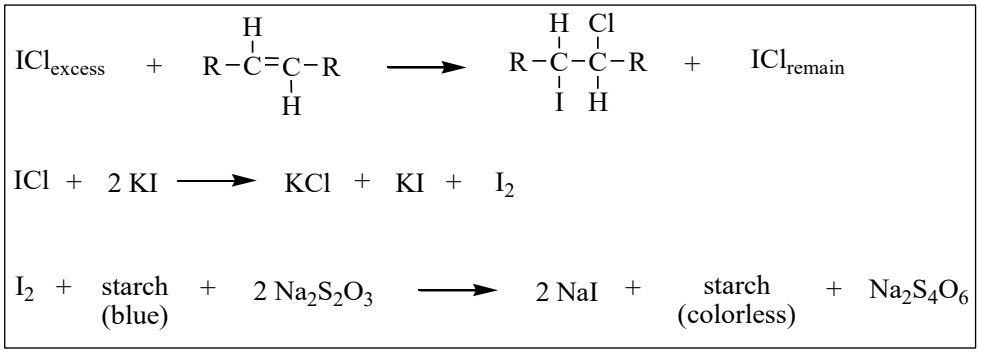


Figure 2.20 Chemical Reaction Involve in IV through Wijs Method

Starch solution is used as an indicator where it changes the color of the solution from colorless to dark blue. It is the result of iodine absorption into the B-amylose chain (macromolecule component in starch). The action of active bacteria in the starch solution makes the solution easily degrade in just a few days. The starch solution that has been degraded will give an effect the IV analysis where it may be oxidized by iodine. Therefore, a starch solution is prepared by mixing starch powder with boiling water to slow down the activity of bacteria on the solution.

2.11.2 Acid Value and Free Fatty Acids

Acid value can be defined as the number of milligrams of potassium hydroxide required to neutralize free fatty acids in one gram of oil (Salimon et al., 2006). The acid value test is conducted in order to provide an overview of the presence of fatty acids that are not bound to the triacylglycerol group. These fatty acids are released from the triacylglycerol chain due to the hydrolysis reaction. This hydrolysis reaction occurs because of the presence of water (moisture) which promotes the hydrolysis process and further makes the acid value high (Jurid et al., 2020). Moisture test and acid value test are complementary to each other.

A high acid value indicates that the free fatty acid from the triacylglycerol chain is high. AV also gives an idea of the quality of the oil whether the oil is in good condition

or not. A high AV value indicates that the oil is of poor quality, it has already degraded reducing its shelf life. Free fatty acid (FFA) is a fatty acid that is not bound to the glycerol molecule in the oil. The value of acidity and free fatty acid is generally a measurement that shows the level of lipid hydrolysis by the enzymatic action of lipase.

This acid value and FFA value uses the concept of neutralization where fatty acids are neutralized by an alkaline solution through the titration method. Sodium hydroxide (NaOH) is a standard solution that is often used in the neutralization process because it is a strong alkali. The use of strong alkali (NaOH) in this test is because it can promote a complete reaction and subsequently can provide accurate and clear final value results. Figure 2.21 shows the reaction between fatty acids and NaOH in acid-base titration. Potassium hydrogen phthalate ($KHC_8H_4O_4$) also known as KHP is the most common chemical used to standardize NaOH solutions (Salimon et al., 2006).

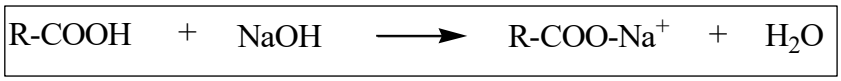


Figure 2.21 Chemical Reaction Between Fatty Acids and NaOH an Acid-Base Titration

Phenolphthalein is an indicator that is often used because it has a specific pH range and is very suitable for acid-base titration. Indicators are used to determine the endpoint of titration. Phenolphthalein is very sensitive to pH changes where the solution will change from colorless to pink when the pH increases from acidic to slightly alkaline. At the endpoint, all the free fatty acids in the sample have been neutralized by the titration solution.

2.11.3 Saponification Value

The saponification value, also known as the saponification number, is a parameter used to measure the average molecular weight of fatty acids or ester linkage in the sample of fat or oil. SV can be defined as the amount of alkali, typically expressed in milligrams, required to completely saponify a specific quantity of fat or oil. It represents the weight of potassium hydroxide (KOH) or sodium hydroxide (NaOH) required to neutralize the fatty acids present in one gram of fat (Salimon et al., 2006). Saponification is the hydrolysis reaction of fats and oils in the presence of an alkali. During this process, the ester bonds of the triacylglycerols in the fat or oil are cleaved

by the alkali, resulting in the formation of glycerol and fatty acid salts (soaps). This reaction is the basis for soap-making and is also used to determine the saponification value. The saponification value is determined through a titration method. A known quantity of the fat or oil sample is dissolved in a suitable solvent and an excess amount of alkali (KOH or NaOH) is added. The remaining excess alkali is then back-titrated with an acid, such as hydrochloric acid (HCl), using 1% phenolphthalein as indicator. The saponification value (SV) of a sample was determined by the length of the fatty acids chains present in the triacylglycerols. A low SV indicates the presence of long chain fatty acids (e.g., C18 and C16) in the glycerol backbone, whereas a high SV suggests the predominance of triacylglycerols with shorter fatty acyl chains (Odoom and Edusei, 2015; Ivanova et al., 2022).

2.11.4 Pour Point

The pour point is the temperature at which an oil undergoes a transition from a free-flowing liquid to a semi-solid state, limiting its ability to pour easily. It is a crucial parameter for oils used in cold climates or low-temperature conditions. When the temperature drops below the pour point, the oil can solidify or form waxy deposits, impeding its flow characteristics and making handling more challenging (Ohifuemen et al., 2020).

The pour point is determined by the composition and molecular structure of the oil. Oils with a higher content of unsaturated fatty acids tend to exhibit lower pour points compared to oils primarily composed of saturated fatty acids. The presence of double bonds in the fatty acid chains introduces molecular kinks or bends, which disrupt the close packing of oil molecules. This disruption impedes the oil's solidification or wax formation at lower temperatures, resulting in improved flow properties and lower pour points for oils rich in unsaturated fatty acids (Salih et al., 2013).

It is important to note that the pour point is influenced by factors other than the presence of unsaturated fatty acids, such as the overall oil composition and the presence of other components, including waxes. However, the inclusion of unsaturated fatty acids in the oil composition contributes to its lower pour point.

2.11.5 Flash Point

The flash point is the temperature at which the vapor of a substance can be ignited by an external ignition source (Owuna et al., 2020). It serves as an indicator of the temperature at which a liquid can produce flammable vapor and undergo combustion. Typically, plant oils exhibit high flash points, ranging from 250 to 300 °C. Oils with flash points exceeding 300 °C are categorized as non-flammable liquids. The flash point of an oil is influenced by the number of carbon atoms present in its triacylglycerol molecules. Liquids with flash points below 38 °C generally require special precautions during handling due to their higher flammability (Salimon et al., 2014; Owuna et al., 2020). Therefore, the flash point value plays a crucial role in assessing the flammability hazard associated with oils.

2.11.6 Viscosity and Viscosity Index

Viscosity is a fundamental property that characterizes the resistance of a fluid to flow. In the context of plant oils, viscosity plays a crucial role in determining their performance and behavior across different applications. The viscosity of plant oils is mainly influenced by temperature (Igwe, 2004).

Compared to other oil types, plant oils generally exhibit higher viscosities due to their unique molecular structures. These oils consist of long-chain fatty acids, which contribute to their elevated viscosity levels. The size and shape of the fatty acid molecules have a significant impact on the intermolecular interactions and the overall flow behavior of the oil. Generally, plant oils with longer fatty acid chains tend to have higher viscosities (Wahyudi et al., 2018).

The viscosity index (VI) serves as a measure of how the viscosity of an oil changes with variations in temperature (Dabai et al., 2018; Owuna et al., 2020). This index is an important parameter that indicates the oil's resistance to viscosity alterations in response to temperature fluctuations. Oils with higher viscosity indices tend to demonstrate less viscosity variation as temperatures change, thereby offering greater stability and suitability across a wider range of operating temperatures.

2.11.7 Oxidative stability

Thermal stability refers to the capacity of a plant oil to resist or retard the process of oxidation at high temperature, which can result in the deterioration and spoilage of the oil (Owuna et al., 2020). Plant oils are comprised of unsaturated fatty acids that are susceptible to oxidation when exposed to oxygen, heat and light. The oxidative stability of plant oil is influenced by a range of factors, including the composition of fatty acids, the presence of antioxidants, processing techniques, storage conditions and environmental parameters. Unsaturated fatty acids, particularly polyunsaturated fatty acids (PUFA), render plant oils more prone to oxidation. PUFA possess multiple double bonds within their molecular structure, providing reactive sites for oxidative attack by oxygen species, consequently initiating oxidation reactions. Oils containing higher proportions of PUFA, such as linoleic acid and linolenic acid, generally exhibit greater susceptibility to oxidation when compared to oils with higher levels of saturated or monounsaturated fatty acids (Syed, 2016).

2.12 Previous Studies Related to Biolubricant

Nowadays, many studies have been conducted on plant oils in the production of biolubricants through chemical modification. Previous studies had reported the production of biolubricant base stocks from various plant oils using polyhydric alcohols such as NPG, TMP and PE. Plant oils including palm oil, soybean oil, sunflower oil, corn oil, palm kernel oil and canola oil have been widely used as feedstocks for polyol ester synthesis via esterification or transesterification reactions as shown in Table 2.9. The synthesized polyol esters generally demonstrated improved physicochemical properties compared to the original oils, such as higher flash points, better viscosity index and improved low-temperature performance. Some studies reported further modification through epoxidation to enhance the stability and viscosity behaviour of the esters. These findings indicate that plant-oil-based polyol esters possess significant potential as renewable and environmentally friendly biolubricant base stocks for various industrial lubrication applications.

Table 2.9
Summary of Previous Studies on Polyol Ester Biolubricants from Plant Oils

Source	Reaction	Kinematic viscosity		Pour point (ºC)	Flash point (ºC)	Viscosity index	Yield (%)	Reference
		40 ºC	100 ºC					
Palm oil	Transesterification with NPG	7.4	2.5	10	174.2	183.3	35-40	Hambali and Raof (2026)
Soybean oil	Transesterification with NPG	10.5	3.2	-3	N/A	198	>95	Aguieiras et al. (2020)
Palm oil	Esterification with NPG	50.1	15.5	7	245	190	87.6	Nor et al. (2022b)
Sunflower oil	Transesterification with TMP	39.52	8.83	-37	>330	213	87.7	Esipovich et al. (2025)
Corn oil	Esterification with TMP	48.92	9.60	-20	300	N/A	97.93	Jamaluddin et al. (2024)
Palm kernel oil	Esterification with TMP	41.76	8.73	-10	320	154.8	86.13	Bahadi et al. (2022)
Palm oil	Esterification with TMP	61.79	14.0	8	290	158	92.0	Nor et al., (2019a)
Palm kernel oil	Esterification with PE	87.6	14.55	-8	320	140.86	80.85	Bahadi et al. (2022)
Palm oil	Transesterification with PE	68.4	12.7	-20	302	N/A	40.13	Aziz et al. (2014)
Palm oil	Esterification with PE	57.47	10.87	17	300	147	85.0	Nor and Salimon (2023)
Palm kernel TMP ester	Epoxidation	45.69	10.54	-19	335	187	92.5	Salimon and Salih (2023)
Canola oil TMP ester	Epoxidation	236.17	27.02	-3	298	157	95.2	Kamyab et al. (2024)

CHAPTER 3
RESEARCH METHODOLOGY

3.1 Material

3.1.1 Raw Material

Sunflower oil (SFO) was purchased from Melbelle Natural company, Selangor, Malaysia.

3.1.2 Chemicals

The chemicals used in this study included 95% ethanol (CH_3CH_2OH), potassium hydroxide (KOH), potassium iodide (KI), sodium hydrogen carbonate ($NaHCO_3$), sodium chloride (NaCl), ethyl acetate, hydrogen peroxide (H_2O_2), formic acid (HCOOH), isopropyl alcohol (IPA), sodium hydroxide (NaOH), glacial acetic acid (CH_3COOH), acetic anhydride, butanol, sodium thiosulphate ($Na_2S_2O_3$), crystal violet, starch, cyclohexane and phenolphthalein from SYSTERM. Hydrochloric acid (37% HCl), sulfuric acid (H_2SO_4) and hydrogen bromide (HBr) were obtained from Fisher Scientific. N-hexane, anhydrous sodium sulphate (Na_2SO_4) and methanol (CH_3OH) were supplied by R&M Chemicals. Neopentyl glycol (NPG), trimethylolpropane (TMP), pentaerythritol (PE) and oleic acid were purchased from Sigma-Aldrich. Wijs solution was obtained from Merck. All chemicals used were of analytical grade and used without further purification.

3.1.3 Apparatus

The apparatus used were three-neck round bottom flask, round bottom flask (RBF), beaker, Dean-Stark, reflux condenser, thermometer (100 °C, 250 °C and 360 °C), hotplate, magnetic stirrer, Whatmann No. 1 filter paper, filter funnel, Erlenmeyer vacuum flask, conical flask, Erlenmeyer flask, crucible, borosilicate glass filter funnel, separatory funnel, Scott bottle, glass rod, measuring cylinder, U tube, volumetric flask, burette and pipette.

3.2 Determination of Physicochemical properties and Characterization of Sunflower Oil

3.2.1 Physicochemical Properties of SFO

The physicochemical properties of SFO were evaluated based on iodine value (IV), acid value (AV), free fatty acids (FFA) value, moisture content, saponification value, flash point, pour point, oxidative stability, kinematic viscosity, viscosity index and rheology.

3.2.1.1 Iodine Value

Based on method used by Japir et al. (2018) for the IV test, 0.5 g of oil sample was weighed and placed in a conical flask. 25 mL of Wijs solution and 20 mL of solution mixture (1:1 ratio of cyclohexane and acetic acid) was added to the conical flask. The conical flask was shaken and stored in a dark place for 1 hour. After 1 hour, 20 mL of potassium iodide solution and 150 mL of distilled water was added to the conical flask. The conical flask was swirled and titrated with sodium thiosulfate ($N_2S_2O_3$) solution until the yellow colour disappears. 1 mL of starch solution was added to the solution and used as an indicator. The titration process continue until the blue colour disappears and turn to white solution. The same condition was also be used to conduct blank test. IV can be calculated using Equation 3.1.

$$IV = \frac{N \times 12.69 \times (V_2 - V_1)}{W} \quad (3.1)$$

Where,

V_2 = volume (mL) of $Na_2S_2O_3$ solution used for the blank test

V_1 = volume (mL) of $Na_2S_2O_3$ solution used for the sample test

N = normality of $Na_2S_2O_3$ solution

W = weight (g) of the sample

3.2.1.2 Acid Value

5 grams of oil sample was weighted into an Erlenmeyer flask. 50 mL isopropyl alcohol that has been neutralized was put into a flask and heated at a temperature of 40 °C to dissolve the oil and IPA. The mixture is titrated with sodium hydroxide (NaOH) solution until a pink color appears and remains for at least 30 seconds (Salimon et al., 2006). Acid value is determined using Equation 3.2.

$$\mathrm{AV} = \frac{28.2 \times N \times V \times 1.99}{W} \tag{3.2}$$

Where,

N = normality of NaOH solution

V = volume (mL) of NaOH solution

W = weight (g) of the sample

3.2.1.3 Free Fatty Acids Value

Method for FFA value was referring to Bahadi et al. (2020) with slight modification. 5 g of oil sample was weighted and 50 mL of neutralized isopropyl alcohol was added into the conical flask. The mixture was heated up to 40 °C until the oil was fully dissolved. Then, 1 mL of indicator (phenolphthalein) was added to the mixture. Next, the mixture was titrated with 0.1N sodium hydroxide (NaOH) until light pink colour appeared. The percentage FFAs as oleic acid was calculated using Equation 3.3.

$$\%\ FFA\ as\ Oleic\ acid = \frac{28.2 \times N \times V}{W} \tag{3.3}$$

Where,

N = normality of NaOH solution

V = volume (mL) of NaOH solution

W = weight (g) of the sample

3.2.1.4 Moisture Content

Method for moisture content using oven and Karl Fischer method was referring to Salimon et al. (2006). For the moisture content test using the oven method, the empty beaker was first weighed and then 5 grams of the oil sample was placed into the beaker. The beaker was put in the oven at a temperature of 100 °C and left overnight. Afterward, the oil sample was cooled in a desiccator and the beaker was reweighed. The moisture content was calculated using Equation 3.4.

$$\% \text{ Moisture content} = \frac{(W_0 - W_1)}{W_0} x\ 100 \quad (3.4)$$

Where,

W_0 = weight sample before drying

W_1 = weight sample after drying

For the moisture content test using the Karl Fischer method, an oil sample of approximately 0.5 mL was drawn using a 1 mL syringe and weighed. The weighed sample was then injected into the reaction vessel through the sample port and the syringe's weight was recorded again. The weight of the sample was key in to the instrument and the start button was pressed to initiate the titration process. The moisture content in the oil was displayed on the Karl Fischer instrument's screen.

3.2.1.5 Saponification Value

2 g of the oil sample was placed in a 100 mL round bottom flask. Afterward, 25 mL of 0.5 N ethanolic potassium hydroxide was added to the sample. The mixture was refluxed, boiled uniformly and stir constantly for 1 hour. After 1 hour, the mixture was titrated with 0.5 N hydrochloric acid (HCl) and 1 ml of phenolphthalein (1%) was used as indicator (Japir et al., 2017). Saponification value was calculated using Equation 3.5.

$$SV = \frac{N \times 56.1 \times (V_2 - V_1)}{W} \quad (3.5)$$

Where,

V_2 = volume (mL) of HCl solution used for the blank test

V_1 = volume (mL) of HCl solution used for the sample test

N = normality of HCl solution

W = weight (g) of the sample

3.2.1.6 Pour Point

According from ASTM D97, the sample was poured into a U-shaped glass tube for the pour point test until it reaches a height of 4 cm. The U-tube had the thermometer attached to one end and parafilm was used to seal both ends of the tube. To ensure that the sample freezes completely, the U tube containing the oil was kept in the refrigerator for 24 hours at a low temperature which is -30 °C. The U tube was taken out and turned upside down the next day after being left overnight. When the sample starts to flow from the higher level to the lower level, the temperature was measured (Nor, 2019).

3.2.1.7 Flash Point

2 mL of the sample was put in a crucible and heated on a heating plate for the flash point testing according to ASTM D93 The sample temperature was determined using a thermometer with a maximum reading temperature of 360 °C. When the temperature reaches 100 °C, flash point readings started to be evaluated by aiming the fire toward the crucible. Up until a flame is formed, this procedure was repeated with a 4 °C temperature rise and the result of flash point temperature was recorded (Nor, 2019).

3.2.1.8 Viscosity and Viscosity Index

The viscosity and viscosity index of the oil sample was measured using the Rheometer Anton Paar (Physica MCR 301 model) according to ASTM D445. The rotor spindle used was a type of cone CP 25-2 with diameter 0.051 mm. The sample was tested at two different temperature which were 40 °C and 100 °C (Derawi and Salimon, 2013). The viscosity index of sample was calculated using Equation 3.6.

$$Viscosity\ Index\ = \frac{(L-U)}{(L-H)} \times 100 \quad (3.6)$$

Where,

U = oil's kinematic viscocity at 40 °C

L and H = value based on the viscosity index table

3.2.1.9 Oxidative Stability

The oxidative stability of the SFO was evaluated using the Rotating Pressure Vessel Oxidation Test (RPVOT) following the procedure outlined in ASTM D2272. This technique was employed to assess the resistance of the ester to oxidation under accelerated conditions. In this test, the ester sample was introduced into a sealed stainless-steel pressure vessel together with a copper catalyst and subsequently charged with high-purity oxygen to an initial pressure of 90 psi. The vessel was heated and maintained at a constant temperature of 150 °C while rotating continuously. Oxidative stability was determined by monitoring the pressure decrease caused by oxygen consumption during oxidation and the induction time was defined as the duration required for a 25 psi pressure drop. The recorded induction time was used as an indicator of the oxidative stability of the ester.

3.2.1.10 Rheology

The Anton Paar Rheometer (Physica MCR 301) with cone and plate geometry was used to investigate the rheological properties of the SFO according to ASTM D5279. The rotor spindle used is a type of cone CP 25-2 and has a diameter of 0.051 mm. Shear rate parameters was manipulated between 0 to 100 s^{-1} with a temperature of 25 °C. The effect of shear rate on shear stress was studied and the type of fluid was determined based on the resulting shear stress trend. The fluid was determined to be either Newtonian or non-Newtonian fluid (Derawi and Salimon, 2013).

3.2.2 Characterization of SFO

Gas chromatography mass spectroscopy (GC-MS) was used to determine the fatty acids composition in oil while Fourier Transform Infrared Spectroscopy (FTIR) and Nuclear Magnetic Resonance (NMR) were used for the characterization of SFO.

3.2.2.1 Gas Chromatography Mass Spectroscopy

The composition of fatty acid in SFO was determined by Agilent Technologies 7890A gas chromatograph coupled with an Agilent Technologies 5975 mass spectrometer and equipped with an HP-88 fused silica capillary column (100 m x 250 µm x 0.25 µm i.d., film thickness 0.25 µm; Agilent, USA). For preparation of determination of fatty acids composition using GC analysis, 0.1 mL of SFO sample and 1 mL of hexane was mixed in a sealed container. 1 mL of sodium methoxide solution (1.15 g of sodium hydroxide in 50 mL methanol) was added and mixed with a vortex stirrer for five minutes at a speed of 1000 rpm. It takes the mixture 15 minutes to separate into two layers. The top layer that contained fatty acids methyl ester (FAME) was taken and up to 1 µL was injected into the injector hole. The sample was evaporated as a result of the injector being placed at a temperature above the FAME sample's boiling point (>200 °C) (Nor et al., 2018a).

The GC-MS operating conditions were adapted from Abdullah et al. (2019) with minor modifications. A sample injection volume of 1 µL was used with a split ratio of 90:1 and helium served as the carrier gas at a flow rate of 25 mL/min. The oven temperature was initially held at 150 °C for 5 min, then increased to 240 °C at a heating rate of 4 °C/min and maintained for 20 min. The injector and detector temperatures were set at 250 °C and 260 °C, respectively.

3.2.2.2 Fourier Transform Infrared Spectroscopy

The sample of SFO was analyzed using Attenuated Total Reflectance Fourier Transform Infrared Spectroscopy (ATR-FTIR). A small amount of each sample was placed directly onto the crystal surface of the ATR accessory for analysis. The ATR-FTIR spectra were recorded in the range of 4000 to 650 cm^{-1} using a PerkinElmer Infrared Model GX spectrometer with 32 scans.

3.2.2.3 Nuclear Magnetic Resonance

The sample of SFO was analyzed using proton (^{1}H) and carbon (^{13}C) nuclear magnetic resonance (NMR) spectroscopy. The NMR spectra were recorded on a JEOL ECP-400 spectrometer operating at 400 MHz for ^{1}H-NMR and 100.61 MHz for ^{13}C-NMR, using deuterated chloroform ($CDCl_3$) as the solvent. For sample preparation, a small amount of each sample was dissolved in $CDCl_3$ and transferred into an NMR tube prior to analysis. The acquired NMR data were processed and analyzed using TopSpin software version 4.4.1.

3.3 Hydrolysis of Sunflower Oil

Hydrolysis process was carried out to separate the fatty acids sunflower oil (SFO) from the glycerol backbone to obtain sunflower oil fatty acids (SFOFA). The hydrolysis method is according to Nor et al. (2019). There were two stages of the hydrolysis process which saponification and acidification. In saponification process, 50 g of SFO was mixed with 300 mL ethanolic potassium hydroxide (KOH) in 500 mL three-neck round bottom flask connected to reflux condenser, the mixture was heated. and stirred continuously. In order to neutralize the alkaline solution, the mixture undergo an acidification process where 100 mL of 6N hydrochloric acid (HCl) was then added. The washing proceed with 200 mL of distilled water and 100 mL of hexane was used as the solvent. Anhydrous sodium sulphate was added to the product which sunflower oil fatty acids (SFOFA), to absorb any leftover water. The product was filtered by Whatman No 1 filter paper and the solvent used was removed by a rotary evaporator at 70 °C. The hydrolysis conditions were optimized using RSM, where the parameters studied were the molarity of ethanolic KOH, reaction temperature and reaction time, following a preliminary screening process.

3.3.1 Screening Factors of Hydrolysis Process

A preliminary screening study was conducted to determine the significant reaction for parameter influencing the hydrolysis of SFO for the production of SFOFA. The hydrolysis was carried out using ethanolic KOH as alkaline medium. Three independent variables that investigated were molarity of ethanolic KOH (0.5 to 2.5 M),

reaction temperature (40 to 80 °C) and reaction time (0.5 to 2.5 hours). The screening process was conducted to select the significant parameters based on their effect on the percentage yield of SFOFA. Table 3.1 shows the range of the parameter for screening factor for hydrolysis of SFO.

Table 3.1
Range of Parameter Used for Screening of Hydrolysis of SFO

Parameter	Unit	Range	
		Minimum	maximum
Molarity of ethanolic KOH	M	0.5	2.5
Temperature	°C	40	80
Time	h	0.5	2.5

3.3.2 Optimization of Hydrolysis Process

Following the screening study, the hydrolysis of SFO was further optimized using RSM via D-optimal design. Prior to the optimization, the screening process was conducted to evaluate three variables which were molarity of alkaline ethanol (M), reaction temperature (°C) and reaction time (h). The result obtained from screening study were used to identified the significant parameter and determine the appropriate range of condition for the optimization process. In the RSM analysis, the response was percentage yield of SFOFA. Based on the three selected parameters, a total 20 experimental runs were generated from the D-optimal design (refer Appendix 11).

3.3.3 Characterization of SFOFA

The fatty acids composition of SFOFA was determine using GC-MS. The FAME preparation method for SFOFA samples was different from SFO samples. In the preparation of FAME from fatty acids, 1 gram of fatty acids sample was weighed into a 100 mL 2 neck round flask. 12.5 mL of a solution of hydrochloric acid in methanol (1 N) was added to the round bottom flask. The round flask was connected to a condenser and heated at a temperature of 65 °C for 1.5 hours. After the heating stopped, the neutralization process was carried out using 7.5 mL of hexane and 5 mL of distilled water. A total of 0.1 mL of FAME obtained was mixed with 1 mL of hexane into a sealed vial. The mixture was centrifuged using a vortex stirrer and the resulting FAME

was analyzed using GC-MS (Nor et al., 2018a). The GC-MS operation conditions was as described in Section 3.2.2.1. The structural characterization of SFOFA were carried out using FTIR and NMR following the procedure outlined in Section 3.2.2.2 and 3.2.2.3, respectively.

3.4 Separation of SFOFA via Low Temperature Methanol Crystallization

The separation process of sunflower oil unsaturated fatty acids (SFOUFA) and saturated fatty acids (SFOSFA) in sunflower oil fatty acids (SFOFA) was carried out using the low temperature methanol crystallization method, according to Japir et al. (2018). The fatty acid mixture was crystallized using fatty acid to methanol ratio of 1:15 (w/v), the temperature at -15 °C and the crystallization time of 24 hours. After 24 hours, two layers of fatty acids was formed. The top layer was supposed to be the extracted SFOUFA with methanol while the bottom layer was supposed to be the SFOSFA. The solidified mixture was filtered with a borosilicate glass filter funnel connected to a vacuum pump to speed up the filtration uniformly. The solid SFOSFA was rinsed using cold methanol to dissolve the remaining SFOUFA. The process was repeated three times by dissolving the SFOSFA and SFOUFA in methanol until the separation result has been completely ensured. The methanol was recovered from the SFOUFA using a rotary evaporator. SFOSFA was dried in desiccator for 24 hours to give final products. The end product was called as sunflower oil unsaturated (SFOUFA) and saturated fatty acids (SFOSFA).

3.4.1 Characterization and Analysis Test of SFOUFA and SFOSFA

The characterization of separated SFOUFA and SFOFA were carried out using several analytical techniques. The fatty acids composition of SFOUFA and SFOFA were determined using GC-MS as described in Section 3.3.3. Functional group analysis was performed using FTIR (Section 3.2.2.2) while structural characterization was conducted using NMR (Section 3.2.2.3).

3.4.2 Analysis Test for SFOUFA and SFOSFA

The degree of unsaturation of SFOUFA and SFOUFA were determined through iodine value as described in Section 3.2.1.1.

3.5 Esterification of Sunflower Oil Unsaturated Fatty Acids with Polyhydric Alcohol

For esterification using sulfuric acid as catalyst, method from Nor et al. (2019a) was used with some modification. The esterification process was carried out using sunflower oil unsaturated fatty acid (SFOUFA), polyhydric alcohol (PA) and sulfuric acid as catalysts. SFOUFA, PA (NPG, TMP and PE) and sulfuric acid was weighed and put into a 500 mL three-neck round bottom flask. 100 mL of toluene was added to the mixture and the round bottom flask was connected to Dean-Stark and condenser. The mixture was heated and stirred continuously. After the esterification, the neutralization process was carried out by putting the product into the separatory funnel. The product was washed using 5% sodium hydrogen carbonate solution ($NaHCO_3$), 5% sodium chloride solution (NaCl) and ethyl acetate. The product of this esterification known as polyol ester. Anhydrous sodium sulphate was added to the product to absorb the remaining water and filtered using Whatman no1. After filtering, the solvent was removed using a rotary evaporator at a temperature of 70 °C. The esterification reaction conditions were optimized using RSM, where the parameters studied were the molar ratio of SFOUFA, percentage catalyst, reaction temperature and reaction time, following a preliminary screening process.

3.5.1 Screening Factors of Esterification Reaction with Polyhydric Alcohol

A preliminary screening study was carried out to determine the significant reaction parameters that influence the esterification of SFOUFA with NPG. Four independent variables were investigated which were molar ratio of SFOUFA to NPG (2 to 4 mole), percentage catalyst (0.5 to 3.5 w/w %), reaction temperature (130 to 160 °C) and reaction time (2 to 8 hours). These parameters were selected to evaluate the effects on the percentage yield of sunflower oil unsaturated fatty acids neopentyl glycol ester (SFOUFANPGE). The screening process was conducted to select the significant

parameters based on their effect on the percentage yield of SFOUFANPGE. Table 3.2 shows the range of parameter used for screening of esterification of SFOUFA with NPG.

Table 3.2
Range of Parameter Used for Screening of Esterification of SFOUFA with NPG

Parameter	Unit	Range	
		Minimum	maximum
Molar ratio SFOUFA:NPG	mole	2	4
Percentage of catalyst	w/w %	0.5	3.5
Temperature	°C	130	160
Time	h	2	8

For the screening of esterification with TMP, four independent variables were investigated which were molar ratio of SFOUFA to TMP (3 to 5 mole), percentage catalyst (0.5 to 3.5 w/w %), reaction temperature (130 to 190 °C) and reaction time (3 to 9 hours). These parameters were selected to evaluate the effects on the percentage yield of sunflower oil unsaturated fatty acids trimethylolpropane ester (SFOUFATMPE). The screening process was conducted to select the significant parameters based on their effect on the percentage yield of SFOUFATMPE. Table 3.3 shows the range of parameter used for screening of esterification of SFOUFA with TMP.

Table 3.3
Range of Parameter Used for Screening of Esterification of SFOUFA with TMP

Parameter	Unit	Range	
		Minimum	maximum
Molar ratio SFOUFA:TMP	mole	3	5
Percentage of catalyst	w/w %	0.5	3.5
Temperature	°C	130	190
Time	h	3	9

For the screening of esterification with PE, four independent variables were investigated which were molar ratio of SFOUFA to PE (4 to 6 mole), percentage catalyst (0.5 to 3.5 w/w %), reaction temperature (140 to 200 °C) and reaction time (4 to 10 hours). These parameters were selected to evaluate the effects on the percentage yield

of sunflower oil unsaturated fatty acids pentaerythritol ester (SFOUFAPEE). The screening process was conducted to select the significant parameters based on their effect on the percentage yield of SFOUFAPEE. Table 3.4 shows the range of parameter used for screening of esterification of SFOUFA with PE.

Table 3.4
Range of Parameter Used for Screening of Esterification of SFOUFA with PE

Parameter	Unit	Range	
		Minimum	maximum
Molar ratio SFOUFA:PE	mole	4	6
Percentage of catalyst	w/w %	0.5	3.5
Temperature	°C	140	200
Time	h	4	10

3.5.2 Optimization of Esterification Reaction with Polyhydric Alcohol

Based on the screening study, the esterification of SFOUFA with polyhydric alcohol (NPG, TMP and PE) were optimized using RSM via D-optimal design. Prior to the optimization, the screening process was conducted to evaluate four variables which were molar ratio SFOUFA:PA (NPG, TMP and PE), percentage catalyst (w/w %), reaction temperature (°C) and reaction time (h). The result obtained from screening study were used to identified the significant parameter and determine the appropriate range of condition for the optimization process. In the RSM analysis, the responses were percentage yield of SFOUFANPGE for NPG, percentage yield of SFOUFATMPE for TMP and percentage yield of SFOUFAPEE for PE. Based on the four selected parameters, a total 25 experimental runs were generated from the D-optimal design for esterification of SFOUFA with NPG, TMP and PE were presented in Appendix 12, Appendix 13 and Appendix 14, respectively.

3.5.3 Characterization of SFOUFANPGE, SFOUFATMPE and SFOUFAPEE

The characterization of SFOUFANPGE, SFOUFATMPE and SFOUFAPEE were carried out using several analytical techniques. The ester composition of SFOUFANPGE, SFOUFATMPE and SFOUFAPEE were determined using GC-FID. The composition of ester in SFOUFANPGE, SFOUFATMPE and SFOUFAPEE was

prepared using method from Aziz et al. (2014). The polyol ester was prepared by diluting the 0.01 g in 1.0 mL ethyl acetate for 1 min using vortex. The mixture was mixed with 0.5 mL N,O-bis (trimethylsilyl)trifluoroacetamide (BSTFA) for derivatization and the mixture was vortex for 1 min. After that, the mixture was heated at 40 °C in water bath for 10 min. The mixture was left to cool at room temperature before injected to the GC-FID.

The analysis was carried out using an Agilent Technologies 7890A gas chromatograph equipped with an DB-5HT column (15 m × 0.10 µm × 0.25 mm i.d.; Agilent, USA). The GC-FID operating conditions were from Bahadi et al. (2021) with small modifications. The volume of injection was 1 µL and hydrogen gas was used as carried gas at flowrate 43 mL/min. The oven temperature was initially held at 100 °C for 1 min, then increased to 380 °C at a heating rate of 5 °C/min and maintained for 10 min and it was kept constant for 67 min. The injector and detector temperatures were set at 380 °C and 400 °C, respectively.

Functional group analysis of SFOUFANPGE, SFOUFATMPE and SFOUFAPEE were performed using FTIR (Section 3.2.2.2) while structural characterization was conducted using NMR (Section 3.2.2.3).

3.5.4 Evaluation of Physicochemical Properties of SFOUFANPGE, SFOUFATMPE and SFOUFAPEE

The physicochemical properties of SFOUFANPGE, SFOUFATMPE and SFOUFAPEE were evaluated based on pour point (Section 3.2.1.6), flash point (Section 3.2.1.7), viscosity and viscosity index (Section 3.2.1.8), oxidative stability (Section 3.2.1.9) and rheology (Section 3.2.1.10).

3.6 Epoxidation of Sunflower Oil Unsaturated Fatty Acids Trimethylolpropane Ester

The epoxidation process was carried out according to Nor et al. (2018b) with some modification by using SFOUFATMPE and performic acid (HCOOOH) to synthesize epoxidized sunflower oil unsaturated fatty acids trimethylolpropane ester (ESFOUFATMPE). SFOUFATMPE was mixed with formic acid in a 250 mL three-neck RBF equipped with a magnetic stirrer, thermometer and reflux condenser. The

mixture of SFOUFATMPE and formic acid were heated and stirred continuously at a speed of 900 rpm using a magnetic stirrer. Hydrogen peroxide was added slowly drop by drop. At the end of the epoxidation reaction, the heating was discontinued and the product, ESFOUFATMPE, was neutralized with a 5% sodium hydrogen carbonate solution, 5% sodium chloride solution and distilled water. To absorb the remaining water, anhydrous sodium sulphate was added to the product and left overnight. Then, the product was filtered using Whatmann No. 1 filter paper. The solvent was removed using rotary evaporator. The epoxidation reactions were optimized using RSM, where the parameters studied were the molar ratio of HCOOH, molar ratio of H_2O_2, percentage catalyst, reaction temperature and reaction time, following a preliminary screening process.

3.6.1 Screening Factor of Epoxidation Reaction

A preliminary screening study was conducted to determine the significant reaction for parameter influencing the synthesis of ESFOUFATMPE. Five independent variables that investigated were molar ratio of HCOOH:SFOUFATMPE (3 to 9 mole), molar ratio of H_2O_2:SFOUFATMPE (1 to 4 mole), percentage catalyst (1 to 3 w/w %), reaction temperature (30 to 70 °C) and reaction time (1 to 5 h). The screening process was conducted to select the significant parameters based on their effect on the percentage yield of ESFOUFATMPE. Table 3.5 shows the range of the parameter for screening factor for epoxidation of SFOUFATMPE.

Table 3.5
Range of Parameter Used for Screening of Epoxidation of SFOUFATMPE

Parameter	Unit	Range	
		Minimum	maximum
Molar ratio of SFOUFA:PE	mole	3	9
Molar ratio of H_2O_2	mole	1	4
Percentage of catalyst	w/w %	1	3
Temperature	°C	30	70
Time	h	1	5

3.6.2 Optimization of Epoxidation Reaction

Following the screening study, the epoxidation of SFOUFATMPE was further optimized using RSM via D-optimal design. Prior to the optimization, the screening process was conducted to evaluate five variables which were molar ratio of HCOOH:SFOUFATMPE, molar ratio of H_2O_2:SFOUFATMPE, percentage catalyst, reaction temperature and reaction time. The result obtained from screening study were used to identified the significant parameter and determine the appropriate range of condition for the optimization process. In the RSM analysis, the responses were percentage yield of ESFOUFATMPE, percentage oxirane oxygen content (OOC) and iodine value. Based on the five selected parameters, a total 31 experimental runs were generated from the D-optimal design (refer Appendix 15).

3.6.3 Analysis Test for ESFOUFATMPE

The percentage of OOC of ESFOUFATMPE was used determine the epoxide (oxirane) group in epoxidized compound. For the OOC test, 0.3 g of the ESFOUFATMPE sample was weighed and placed in a 50 mL conical flask. Then, 10 mL of glacial acetic acid was added and the flask was shaken gently until all samples dissolve. Afterward, 5 drops of crystal violet indicator was added and the solution will turn dark purple. The mixture was titrated with 0.1 N hydrogen bromide (HBr) solution until the purple color turns greenish blue and remains stable for at least 30 seconds (Nor, 2019). The oxirane oxygen value in the sample was determined using Equation 3.7.

$$\text{OOC Value} = \frac{\text{volume of HBr used (mL) x N x 1.6}}{\text{W}} \tag{3.7}$$

Where,

N = normality of HBr solution

W = weight (g) of the sample

The oxirane oxygen content value obtained next was compared to the oxirane oxygen content theory value where the value of oxirane oxygen content theory (OOC_{theory}) was calculated using Equation 3.8.

$$OOC_{theory} = \left[\frac{\left(\frac{IV_o}{2 \cdot A_i}\right)}{100 + \left(\frac{IV_o}{2 \cdot A_i}\right) \cdot A_o}\right] \times A_o \times 100 \quad (3.8)$$

Where,

A_i = relative molecular mass of iodine (126.9)

A_o = relative molecular mass of oxugen (16.0)

IV_o = initial iodine value

The percentage conversion of the oxirana ring was calculated using Equation 3.9 based on the oxirane oxygen content titrated ($OOC_{titrated)}$ value with the oxirane oxygen content (OOC_{theory}) value:

$$\text{Percentage conversion} = \frac{OOC_{titrated}}{OOC_{theory}} \times 100 \quad (3.9)$$

The degree of unsaturation of ESFOUFATMPE was determined through iodine value as described in Section 3.2.1.1.

3.6.4 Characterization of ESFOUFATMPE

The structural characterization of ESFOUFATMPE was carried out using FTIR and NMR following the procedure outlined in Section 3.2.2.2 and 3.2.2.3, respectively.

3.6.5 Evaluation of Physicochemical Properties of ESFOUFATMPE

The physicochemical properties of ESFOUFATMPE was evaluated based on pour point (Section 3.2.1.6), flash point (Section 3.2.1.7), viscosity and viscosity index (Section 3.2.1.8), oxidative stability (Section 3.2.1.9) and rheology (Section 3.2.1.10).

3.7 Ring Opening of Epoxidized Sunflower Oil Unsaturated Fatty Acids Trimethylolpropane Ester

Epoxide ring opening process was carried out according to Nor et al. (2021b) with some modification by using ESFOUFATMPE and oleic acid with the presence of H_2SO_4 as a catalyst. ESFOUFATMPE and oleic acid was weighed and put into 250 ml three-neck RBF. This mixture was heated and stirred continuously and H_2SO_4 was added drop by drop in the epoxide ring opening process. Toluene was added to the mixture and the round bottom flask was connected to Dean-Stark and condenser. After the reaction process was over, the product was neutralized using 5% sodium hydrogen carbonate solution, 5% sodium chloride solution and ethyl acetate. The product produced was dioleoate sunflower oil unsaturated fatty acids trimethylolpropane ester (DOSFOUFATMPE) was mixed with anhydrous sodium sulphate to absorb the remaining water and filtered using Whatman no1. Ethyl acetate was removed using a rotary evaporator. The ring opening reactions were optimized using RSM, where the parameters studied were the molar ratio of oleic acid, percentage catalyst, reaction temperature and reaction time, following a preliminary screening process.

3.7.1 Screening Factor of Ring Opening Reaction

A preliminary screening study was conducted to determine the significant reaction for parameter influencing the synthesis of DOSFOUFATMPE via ring opening reaction. Four independent variables that investigated were molar ratio of ESFOUFATMPE: oleic acid (2 to 6 mole), percentage catalyst (1 to 3 w/w %), reaction temperature (120 to 150 °C) and reaction time (2 to 6 h). The screening process was conducted to select the significant parameters based on their effect on the percentage yield of DOSFOUFATMPE. Table 3.6 shows the range of the parameter for screening factor for ring opening of ESFOUFATMPE.

Table 3.6
Range of Parameter Used for Screening of Ring Opening of ESFOUFATMPE

Parameter	Unit	Range	
		Minimum	maximum
Molar ratio ESFOUFATMPE:OA	mole	2	6
Percentage of catalyst	w/w %	1	3
Temperature	°C	120	150
Time	h	2	6

3.7.2 Optimization of Ring Opening Reaction

Based on the screening study, the ring opening of ESFOUFATMPE was further optimized using RSM via D-optimal design. Prior to the optimization, the screening process was conducted to evaluate four variables which were molar ratio of ESFOUFATMPE: oleic acid, percentage catalyst, reaction temperature and reaction time. The result obtained from screening study were used to identified the significant parameter and determine the appropriate range of condition for the optimization process. In the RSM analysis, the responses were percentage yield of DOSFOUFATMPE, percentage oxirane oxygen content (OOC), iodine value (IV) and hydroxyl value (HV). Based on the four selected parameters, a total 25 experimental runs were generated from the D-optimal design (refer Appendix 16).

3.7.3 Analysis Test for DOSFOUFATMPE

The HV was used to determine the amount of hydroxyl (OH) group present in the DOSFOUFATMPE according to Nor, 2019. For the hydroxyl value test, 1 gram of oil sample was weighed into a 250 mL conical flask for the acetylation. 5 mL of reagent solution (acetic anhydride in pyridine) was added to the conical flask and mixed by swirling. The conical flask was capped and stored at room temperature for 24 hours. A blank test was done under the same conditions. After 24 hours, 10 mL of distilled water was added to the conical flask. The lid and walls of the conical flask was rinsed with distilled water and pyridine. The conical flask was closed and swirled so that the contents in the conical flask are mixed. The conical flask was left for 30 minutes. Then, the cap and the wall of the conical flask was rinsed with 25 mL of butanol. 1 mL of phenolphthalein indicator solution was added and the mixture titrated with 0.5 N

potassium hydroxide (KOH) solution in ethanol until a pink color is obtained (Nor, 2019).

For the determination of the acidity value, 5 g of the oil sample was weighed in a 250 mL conical flask. 10 mL of pyridine, 10 mL of distilled water and 25 mL of neutralized butanol was added to the conical flask and mixed by swirling. 1 mL of phenolphthalein indicator solution was added and the mixture titrated with 0.5 N potassium hydroxide solution until a pink color is obtained. The hydroxyl value was calculated using Equation 3.10.

$$\text{HV} = \frac{B + \left(\frac{WA}{C}\right) - S\ x\ N\ X\ 56.1}{W} \tag{3.10}$$

Where,

A = volume (mL) of alkaline KOH solution (acidity)

B = volume (mL) of alkaline KOH solution (blank)

C = weight (g) of the sample (acidity)

S = volume (mL) of alkaline KOH solution (acetylation)

W = weight (g) of the sample (acetylation)

The iodine value was measured according to the method described in Section 3.2.1.1, while the oxirane oxygen content was determined following the procedure outlined in Section 3.6.3.

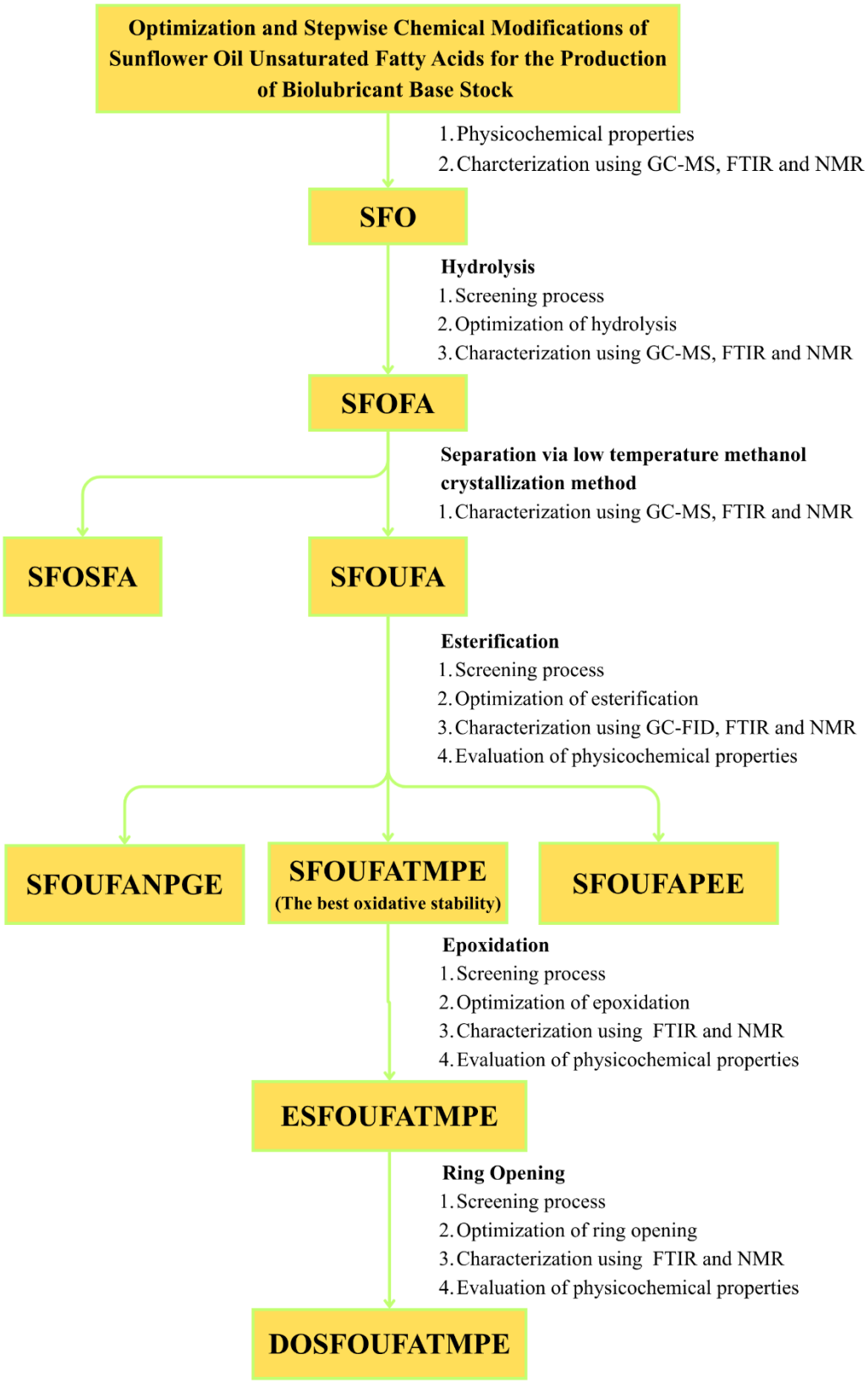
3.7.4 Characterization of DOSFOUFATMPE

Functional group analysis of DOSFOUFATMPE was performed using FTIR (Section 3.2.2.2) while structural characterization was conducted using NMR (Section 3.2.2.3).

3.7.5 Evaluation of Physicochemical Properties of DOSFOUFATMPE

The physicochemical properties of DOSFOUFATMPE was evaluated based on pour point (Section 3.2.1.6), flash point (Section 3.2.1.7), viscosity and viscosity index (Section 3.2.1.8), oxidative stability (Section 3.2.1.9) and rheology (Section 3.2.1.10).

3.8 Flowchart of Research



CHAPTER 4
RESULTS AND DISCUSSION

4.1 Sunflower Oil

4.1.1 Physicochemical Properties of SFO

Analysis of the physicochemical properties of oil is very important to determine the quality of the oil sample as a starting material before the experimental begins. Physicochemical properties that have been done were iodine value, acid value, free fatty acid (FFA), saponification value, moisture content, pour point, flash point, kinematic viscosity, viscosity index, oxidative stability and rheology. Table 4.1 shows the physicochemical properties of SFO.

Table 4.1
Physicochemical Properties of SFO

Physicochemical properties	Result	Previous study*
Iodine value (g I_2/100g)	118.01	119.92[a]
Acid value (mg KOH/g)	0.140	0.953[a]
Free fatty acid value (%)	0.072	0.042[a]
Saponification value	190.37	182.23[a]
Moisture content (%)	0.091	N/A
Pour point (°C)	-13	-15[b]
Flash point (°C)	280	274[b]
Kinematic viscosity at 40 °C (cSt)	30.54	33.20[c]
Kinematic viscosity at 100 °C (cSt)	7.22	7.90[c]
Viscosity index	163	222[c]
Oxidative Stability (min)	22	N/A
Rheology	Newtonian	N/A

Sources: [a]Aboki et al. (2012); [b]Karmakar et al. (2017); [c]Ashrafi et al. (2017)

The iodine value of SFO obtained from this study was 118.01 g I_2/100 g, which falls within the typical range of 110 to 143 g I_2/100 g reported for the SFO as stated by Seneviratne and Jayathilaka (2016). This result also close agreement with the value reported by Aboki et al. (2012) which was 119.92, indicating good consistency with the previous finding. The high iodine value in SFO was mainly attributed to its high content

of unsaturated fatty acids, particularly linoleic (C18:2) and oleic acid (C18:1). These unsaturated fatty acids contain double bond that contribute to a higher degree of unsaturation that led to increase in iodine value.

The acids value (AV) of SFO obtained was 0.14 mg KOH/g which shows slightly lower than the range of 0.2 to 0.5 mg KOH/g reported by Thanh et al. (2012) and it also significantly lower than the value reported by Aboki et al. (2012) which was 0.953 mg KOH/g. This further confirm by determination of free fatty acids value (FFA) of 0.072% in SFO which below the maximum limit of 0.25% that specified by the Bureau of Indian standard (BIS). The low acid value indicated that the SFO used in this study contains low amount of free fatty acids and it in good quality. Oil with high AV and FFA content were generally considered to be poor quality because the indicate hydrolytic degradation of TAG (Di Pietro et al., 2020).

The percentage of moisture content in the SFO sample was 0.08% (oven method) and 0.0913% (Karl Fisher method). According to Asian and Pacific Coconut Community (APCC) the maximum limit of moisture in edible oils should be between 0.1 to 0.5% (Odoom and Edusei, 2015). The SFO sample has a moisture content of less than 0.1%, indicating that the oil is in good condition and can be used as a starting material in this study.

The saponification value (SV) of a sample was determined by the length of the fatty acid's chains present in the triacylglycerols. A low SV indicates the presence of long chain fatty acids (e.g., C18 and C16) in the glycerol backbone, whereas a high SV suggests the predominance of triacylglycerols with shorter fatty acyl chains (Odoom and Edusei, 2015; Ivanova et al., 2022). In the case of SFO, its SV of 190.37 mg KOH/g was attributed to the abundance of long chain fatty acids, including palmitic (C16:0), stearic (C18:0), oleic (C18:1) and linoleic acid (C18:2). Seneviratne and Jayathilaka, (2016) state that the range SV for SFO was 188 to 194 mg KOH/g where it shows the SV value obtained was acceptable because the value was within the specified range.

The pour point of SFO was determine at -13 °C in this study, which slightly higher than value of -15 °C that reported by Karmakar et al. (2017). Plant with a higher content of unsaturated fatty acids tend to exhibit lower pour points compared to oils primarily composed of saturated fatty acids (Salih et al., 2013). This behaviour attributed to the presence of double bond in unsaturated fatty acids that being confirm by high iodine value.

The flash point of SFO obtained in this study was 280 °C which slightly higher than the value reported by Karmakar et al. (2017) at 274 °C. Generally, plant oil has high flash point ranging between 250 to 300 °C due to the presence of long chain fatty acids and their low volatility (Salimon et al., 2014). Therefore, the flash point value plays a crucial role in assessing the flammability hazard associated with oils. This finding indicates that SFO was not a flammable material and can be safely handled.

The kinematic viscosity of SFO obtained in this study was 30.54 cSt at 40 °C and 7.22 cSt at 100 °C, with the viscosity index of 163. This value was slightly lower that previous study report by Ashrafi which recorded the kinematic viscosity of 33.2 cSt at 40 °C and 7.9 cSt at 100 °C with viscosity index of 222. Generally, plant oils with longer fatty acid chains tend to have higher viscosities (Wahyudi et al., 2018). A high viscosity index of SFO indicating its viscosity did not change drastically despite variations in temperature.

The oxidative stability of SFO was recorded at 22 minutes. SFO contains a high proportion of unsaturated fatty acids particularly polyunsaturated fatty acids such as linoleic acids which contributed to the low oxidative stability. Oils that containing higher proportions of polyunsaturated fatty acids, such as linoleic acid and linolenic acid, generally exhibit greater susceptibility to oxidation when compared to oils with higher levels of saturated or monounsaturated fatty acids (Syed, 2016).

The rheological behavior of SFO was evaluated to understand its flow characteristics under varying shear conditions. The results from Figure 4.1 indicate that SFO exhibits Newtonian fluid behavior, which is characterized by a constant viscosity regardless of changes in shear rate (Nakayama, 2018). The linear relationship between shear stress and shear rate observed for SFO confirms its Newtonian nature, where shear stress increases proportionally with increasing shear rate. This linearity demonstrates that the internal molecular structure of SFO does not undergo significant rearrangement when subjected to shear. Furthermore, the viscosity shear rate profile in Figure 4.2 shows that the viscosity of SFO remains nearly constant over the tested shear rate range, indicating the absence of shear-thinning or shear-thickening behavior.

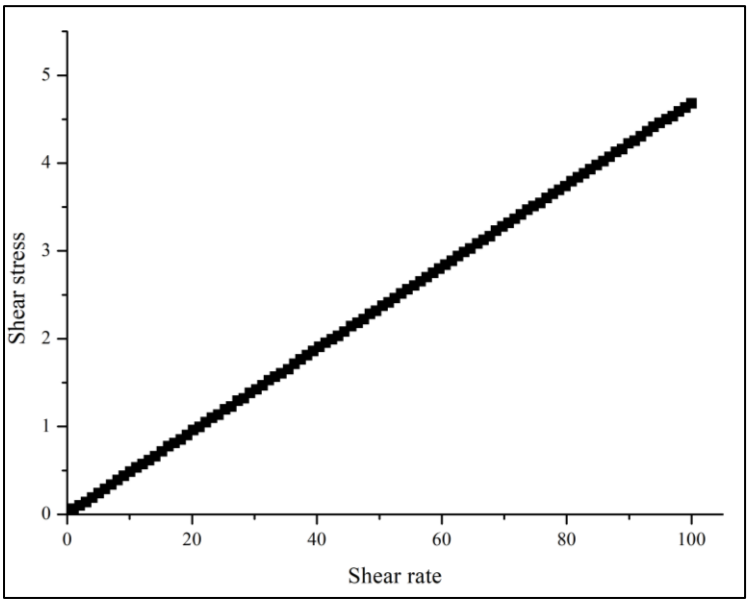


Figure 4.1 Shear Stress versus Shear Rate of SFO

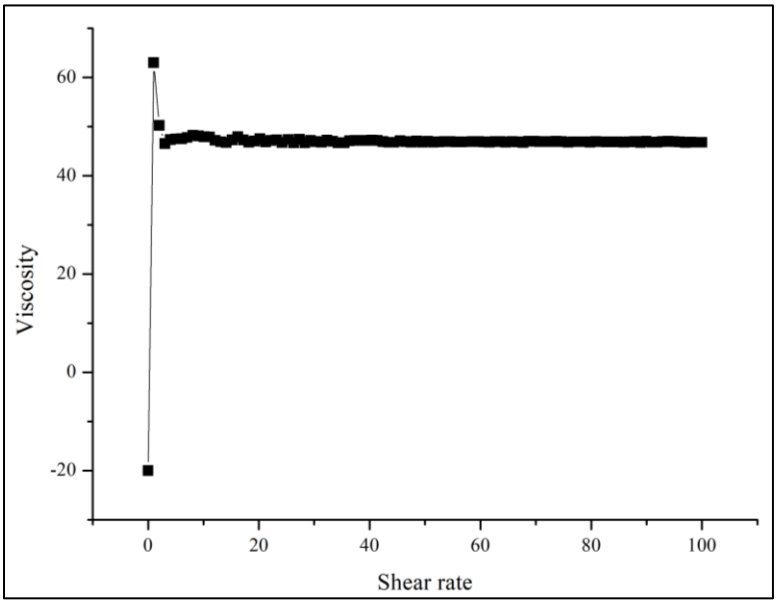


Figure 4.2 Viscosity versus Shear Rate of SFO

4.1.2 Characterization of SFO

4.1.2.1 Gas Chromatography Mass Spectrometer

The fatty acid composition of SFO was determined using gas chromatography mass spectrometry (GC-MS) with a HP-88 column. The results revealed that SFO contains varying proportions of different fatty acids. Among the fatty acids analyzed, linoleic acid exhibited the highest composition, accounting for 51.18% of the total fatty

acids present in SFO. It was followed by oleic acid with a composition of 33.11%, palmitic acid with 8.12%, stearic acid with 5.06%, behenic acid with 1.23%, arachidic acid with 0.40%, lignoceric acid with 0.38%, linolenic acid with 0.25%, paullinic acid with 0.23% and tricosanoic acid with 0.04%. Figure 4.3 shows the chromatogram of fatty acid composition and Table 4.2 shows the percentage fatty acid composition in SFO.

The analysis also indicated that SFO predominantly consists of unsaturated fatty acids, with a composition of 84.77%, whereas saturated fatty acids accounted for 15.23% of the total fatty acids in SFO. This composition aligns with the expected profile of SFO, as it was known to have a higher proportion of unsaturated fatty acids compared to saturated fatty acids as reported by Wai and Jiang (2019).

The use of GC-MS and the HP-88 column allowed for accurate identification and quantification of the fatty acid components in SFO, providing valuable insights into its molecular composition. The results highlight the significant presence of oleic acid and linoleic acid, which are both unsaturated fatty acids and contribute to the overall composition and characteristics of SFO.

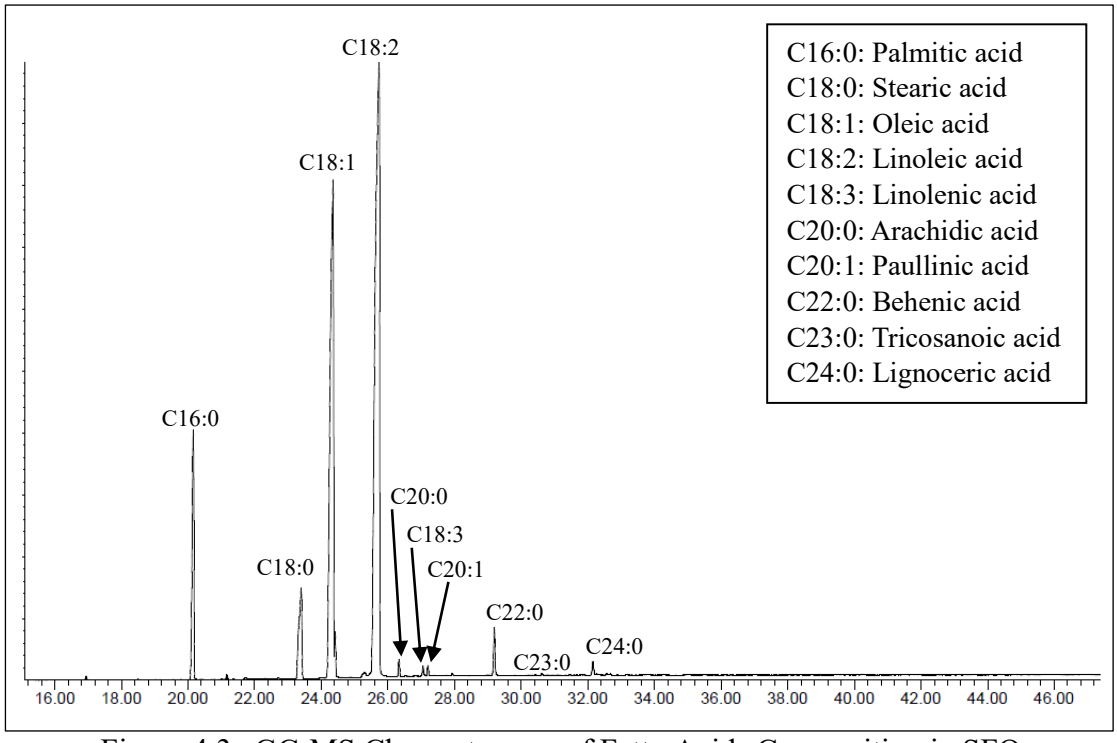


Figure 4.3 GC-MS Chromatogram of Fatty Acids Composition in SFO

Table 4.2
Percentage Fatty Acids Composition in SFO

Fatty acid	Structure	Percentage composition (%)
Palmitic acid	C16:0	8.12
Stearic acid	C18:0	5.06
Oleic acid	C18:1	33.11
Linoleic acid	C18:2	51.18
Linolenic acid	C18:3	0.25
Arachidic acid	C20:0	0.40
Paullinic acid	C20:1	0.23
Behenic acid	C22:0	1.23
Tricosanoic acid	C23:0	0.04
Lignoceric acid	C24:0	0.38
Saturated fatty acid		15.23
Unsaturated fatty acid		84.77

4.1.2.2 Fourier Transform Infrared Spectroscopy

ATR-FTIR of Perkin Elmer model 100 spectrometer was used to identify functional groups in SFO. Figure 4.4 shows the FTIR spectrum of SFO and Table 4.3 shows a summary of the functional group and wavenumber for SFO. According to Pavia et al. (2015), the ester group can be determined based on the presence of two types of peaks that can be seen which are C=O ester at wavenumber 1730 to 1750 cm^{-1} and C-O at wavenumber 1000 to 1300 cm^{-1}. Based on Figure 4.4, it shows a sharp peak at 1746.33 cm^{-1} which indicates C=O stretching vibration for ester and a peak for C-O stretching vibration at 1232.81 and 1163.52 cm^{-1}. Wavenumber at 2926.56 and 2857.78 cm^{-1} shows the peak for C-H stretching vibration for aliphatic (sp^3) and 3007.93 cm^{-1} shows C=C bending vibration for aliphatic (sp^2).

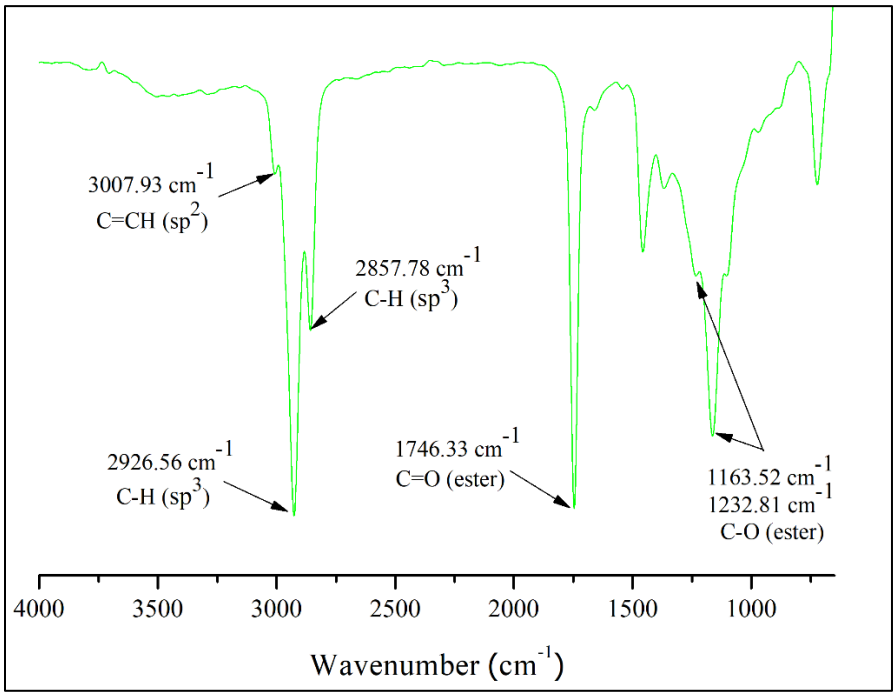


Figure 4.4 FTIR Spectrum of SFO

Table 4.3
Summary of Functional Groups and Wavenumber of SFO

Functional group	Wavenumber (cm^{-1})
C=C bending vibration (aliphatic)	3007.93
C-H stretching vibration (aliphatic)	2926.56 and 2857.78
C=O stretching vibration (ester)	1746.33
-C-O stretching vibration (ester)	1232.81 and 1163.52

4.1.2.3 Nuclear Magnetic Resonance

A JOEL-ECP 400 Spectrometer was used to identify the type of proton (^{1}H-NMR) and type of carbon (^{13}C-NMR) in SFO. Figure 4.5 shows the ^{1}H-NMR spectrum of SFO. Based on Figure 4.5, it shows the proton peak at the chemical shift 0.88 to 0.92 ppm which represents the peak for the methyl group (-C**H**$_3$) and the proton peak at the chemical shift 1.29 to 1.41 ppm represents the peak for the methylene group (-C**H**$_2$-). Based on references from Pavia et al. 2015, the proton peak range for the methyl group (-C**H**$_3$) was at a chemical shift of 0.70 to 1.3 ppm while the proton peak range for the methylene group (-C**H**$_2$-) was at a chemical shift of 1.2 to 1.4 ppm.

The presence of a peak at the chemical shift of 2.00 to 2.09 ppm indicates a proton peak for the group -CH=CH-C**H**$_2$- while a peak at 2.77 to 2.8 ppm indicates a

proton peak for the group =CH-C**H**$_2$-C=. Chemical shift 5.28 to 5.41 ppm represents the group -C**H**=CH-. Chemical shifts of 2.00 to 2.09, 2.77 to 2.8 and 5.28 to 5.41 ppm indicate the presence of double bonds in SFO. According to Pavia the chemical shift for -CH=CH-C**H**$_2$- was in the range of 1.6 to 2.6 ppm while for =CH-C**H**$_2$-C= it was in the range of 2.5 to 3.0 ppm and for -C**H**=CH- it was in the range of 4.5 to 6.5 ppm.

The two proton groups detected on the glycerol backbone are -C**H**$_2$-COOR- and -C**H**-COOR-. The chemical shift of -C**H**$_2$-COOR- was at 4.14 to 4.18 ppm while that of -C**H**-COOR- was at a chemical shift of 4.29 to 4.33 ppm. Chiplunkar and Pratap (2016) stated that the range for -C**H**$_2$-COOR- and -C**H**-COOR- was in the chemical shift range of 4.0 to 4.5 ppm.

In the determination of the ester group, there are two types of protons which are O=C-CH$_2$-C**H**$_2$- and O=C-C**H**$_2$-. The peak for O=C-CH$_2$-C**H**$_2$- was at chemical shift 1.61 to 1.63 ppm while the peak for O=C-C**H**$_2$- was at chemical shift 2.30 to 2.35 ppm. Based on Pavia et al. (2015), the peak for O=C-CH$_2$-C**H**$_2$- was at a chemical shift of 1.5 to 2.0 ppm and the peak for O=C-C**H**$_2$- was at a chemical shift of 2.1 to 2.5 ppm. Table 4.4 shows a summary of the type of proton and chemical shift for SFO.

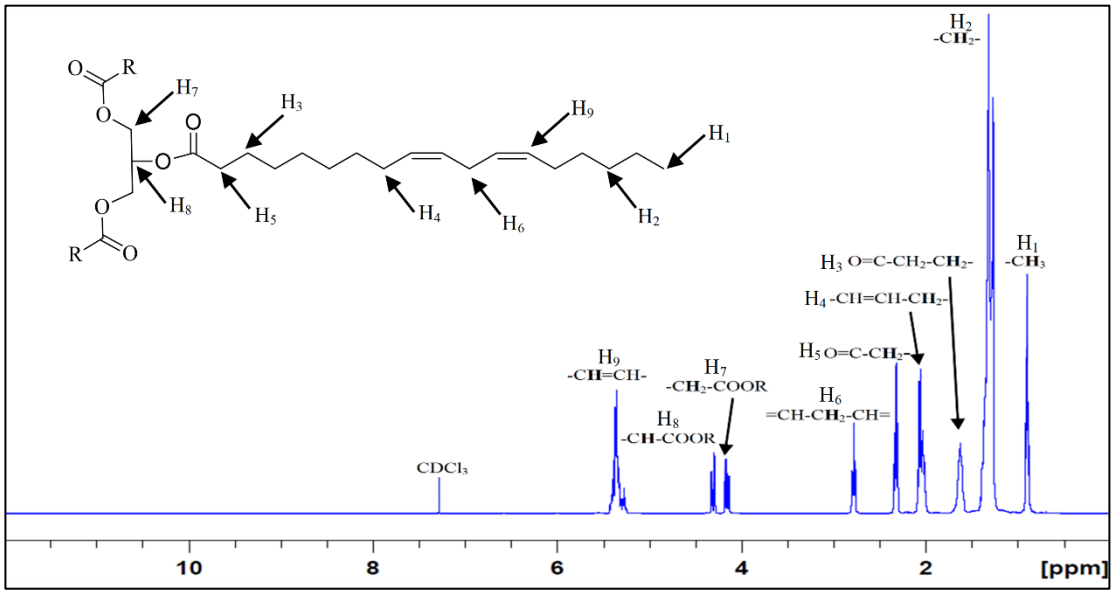


Figure 4.5 ^{1}H NMR Spectrum of SFO

Table 4.4
Type of Proton and Chemical Shift of SFO

	Type of proton	Chemical shift (ppm)	
		SFO	Theoretical*
H_1	-C**H**$_3$	0.88-0.92	0.70-1.3
H_2	-C**H**$_2$-	1.29-1.41	1.2-1.4
H_3	O=C-CH$_2$-C**H**$_2$-	1.61-1.63	1.5-2.0
H_4	-CH=CH-C**H**$_2$-	2.00-2.09	1.6-2.6
H_5	O=C-C**H**$_2$-	2.30-2.35	2.1-2.5
H_6	=CH-C**H**$_2$-CH=	2.77-2.80	2.5-3.0
H_7	-C**H**$_2$-COOR- (glycerol)	4.14-4.18	4.0-4.5
H_8	-C**H**-COOR- (glycerol)	4.29-4.33	4.0-4.5
H_9	-CH=C**H**-	5.28-5.41	4.5-6.5

Source: *Pavia et al. (2015)

The ^{13}C-NMR spectrum (Figure 4.6) shows that there was a peak at the chemical shift of 14.05 to 14.09 ppm which represents the carbon for the methyl group (-**C**H$_3$) and the peak at the chemical shift of 22.56 to 34.18 ppm represents the carbon of the methylene group (-**C**H$_2$-). This value matches the range of values reported by Pavia et al. (2015) which was at a chemical shift of 8 to 30 (-**C**H$_3$) and 15 to 55 ppm (-**C**H$_2$-). The peak at the chemical shift of 127.90 to 130.20 ppm indicates the type and carbon of the alkene (-**C**=**C**-) and the value reported by Pavia was the same which was 100 to 150 ppm.

The carbon of carbonyl ester (**C**=O) was detected at a chemical response of 172.79 to 173.21 ppm and the value was close to the range of Pavia et al. (2015) (155 to 185 ppm). The chemical shift at 62.09 ppm represents -**C**H$_2$-O- while the chemical shift at 68.90 ppm represents -**C**H-O. These two carbons come from the carbon that were found in the glycerol backbone. These two values were according to the values reported by Pavia et al. (2015) which were 40 to 80 ppm. Table 4.5 shows a summary of the type of proton and chemical shift for SFO.

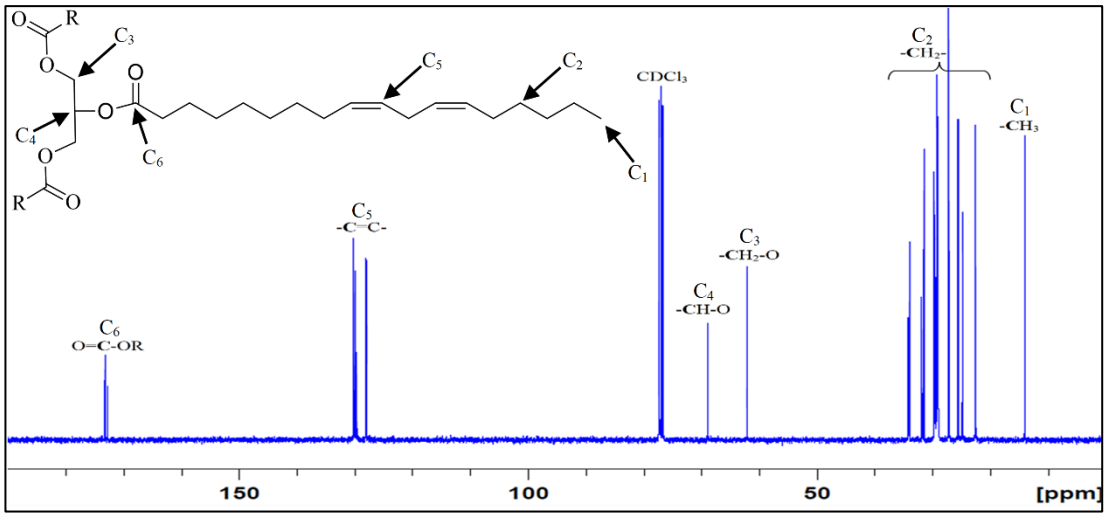


Figure 4.6 ^{13}C NMR Spectrum of SFO

Table 4.5
Type of Carbon and Chemical Shift of SFO

	Type of carbon	Chemical shift (ppm)	
		SFO	Theoretical*
C_1	-**C**H_3	14.05-14.09	8-30
C_2	-**C**H_2-	22.56-34.18	15-55
C_3	-**C**H_2-O (glycerol)	62.09	40-80
C_4	-**C**H-O (glycerol)	68.90	40-80
C_5	-C=**C**-	127.90-130.20	100-150
C_6	O=**C**-OR	172.79-173.21	155-185

Source: *Pavia et al. (2015)

4.2 Hydrolysis of Sunflower Oil

The hydrolysis process was carried out to produce sunflower oil fatty acids (SFOFA) from SFO. Before the optimization of hydrolysis was carried out, the screening process for factors was done taking into account the parameters such as molarity of ethanolic potassium hydroxide (KOH) (M), temperature (°C) and time (h).

4.2.1 Factor Screening Process

The screening process was carried out using the one factor at a time (OFAT) approach to determine the significant parameters affecting the hydrolysis of SFO on the percentage yield of SFOFA. The first factor investigated was the molarity of ethanolic

KOH. As shown in Figure 4.7 (a), the percentage yield of SFOFA slightly increased when the molarity of ethanolic KOH increased from 0.5 M to 1.0 M and reached an optimum at 1.5 M. This increase can be attributed to the higher availability of hydroxide ions (OH^-), which enhance the cleavage of triacylglycerol ester bonds and promote the hydrolysis reaction. However, further increase in molarity from 1.5 M to 2.5 M resulted in a decrease in SFOFA yield. Excess alkaline concentration may promote side reactions such as saponification, leading to soap formation and difficulties in fatty acid recovery during acidification. Similar findings have been reported where excessive alkaline concentration reduced fatty acid yield due to emulsion formation and soap stabilization, which hinder phase separation (Salimon et al., 2011). Therefore, the suitable molarity range was selected between 1.0 M to 2.5 M for further optimization.

The second factor studied was reaction temperature. Figure 4.7 (b) shows that the percentage yield of SFOFA increased gradually as temperature increased from 40 to 60 °C. The increase in temperature enhances molecular collision frequency and reaction kinetics, thereby accelerating triacylglycerol hydrolysis. However, when the temperature increased beyond 60 °C, the percentage yield began to decrease. Excessive temperature may lead to increased saponification and possible thermal degradation of fatty acids, which reduces the effective yield of recoverable fatty acids. In alkaline hydrolysis systems, elevated temperature can also intensify emulsion formation, making separation less efficient (Salimon et al., 2011; Bahadi et al., 2020). Thus, the temperature range of 50 to 70 °C was selected as the appropriate range for optimization.

The final factor evaluated was reaction time. As illustrated in Figure 4.7 (c), the percentage yield of SFOFA increased significantly when the reaction time increased from 0.5 h to 1.5 h, indicating that sufficient time is required for complete hydrolysis of triacylglycerol into fatty acids and glycerol. However, prolonging the reaction time beyond 1.5 h resulted in a decrease in yield. Extended reaction time may lead to secondary reactions such as soap formation and oxidation of fatty acids, which reduce the recoverable fatty acid content. Previous studies have reported that excessive reaction time in alkaline hydrolysis promotes soap formation and decreases fatty acid recovery efficiency (Salimon et al., 2011). Therefore, the reaction time range of 0.5 to 2.5 h was selected for the optimization.

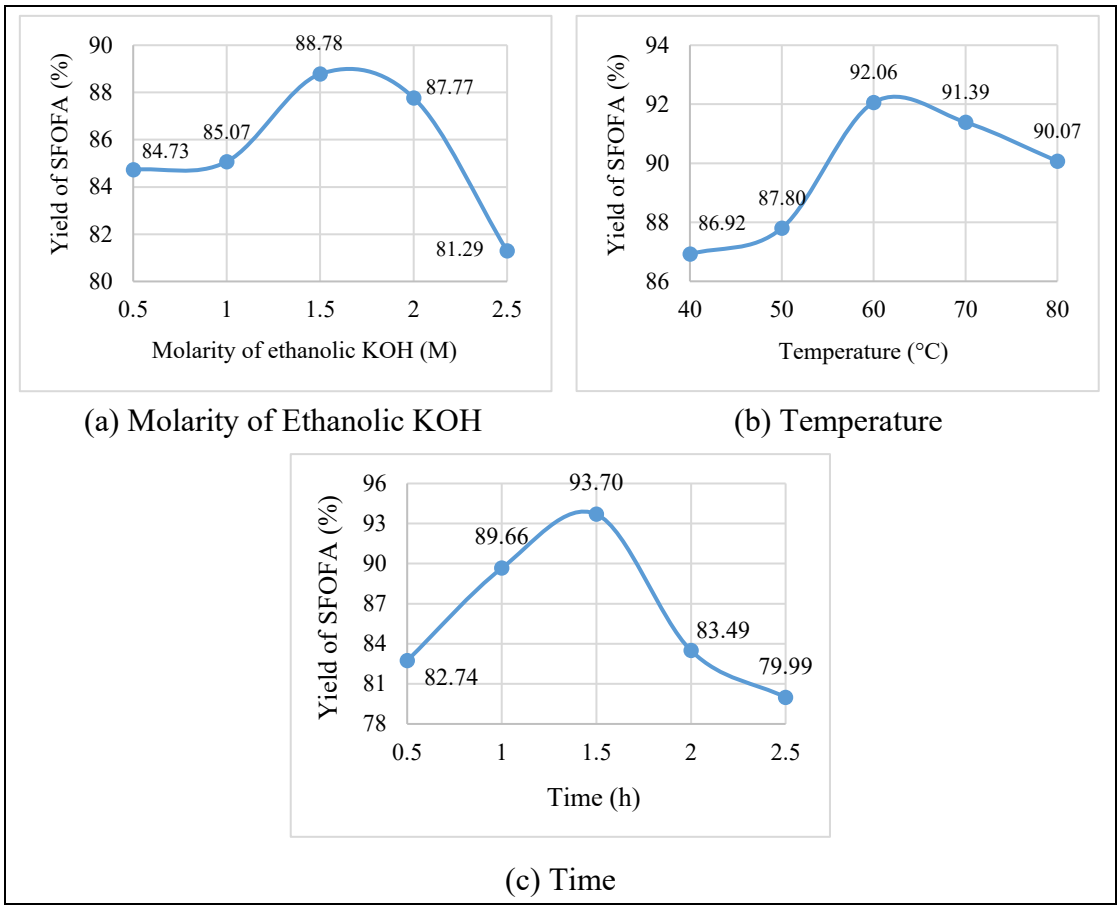


Figure 4.7 The Effect of Factors for Hydrolysis on the Percentage Yield of SFOFA

Based on the change in percentage yield of SFOFA shown in Figure 4.7, it can be concluded that these three factors have an effect on the hydrolysis process of SFO. These three factors were used for optimization process. The range of factors was identified and each factor was recorded at three levels, namely low (-1), middle (0) and high (+1) as shown in Table 4.6.

Table 4.6
Parameter and Level for D-optimal Design of Hydrolysis of SFO

Parameter	Unit	Variable level		
		-1	0	+1
Molarity of ethanolic KOH	M	1.0	1.75	2.5
Temperature	°C	50	60	70
Time	h	0.5	1.5	2.5

4.2.2 Optimization of Hydrolysis of SFO

The hydrolysis optimization using D-optimal design from Design Expert 13.0 involved conducting 20 experiments to examine the impact of factors such as the molarity of ethanolic KOH, temperature and reaction time on the percentage yield of SFOFA. The results of the response, including both the actual values obtained in the experiments and the predicted values for percentage yield of SFOFA, was presented in Table 4.7 where it demonstrates a close similarity between the actual response values and the predicted response values.

Table 4.7
Experimental Run, Factors and Response for Percentage Yield of SFOFA from D-optimal Design

Run	Factors			Response	
	Molarity ethanolic KOH (M)	Reaction temp. (°C)	Reaction time (h)	Yield of SFOFA (%)	
				Actual	Predicted
1	1.7	50	1.60	95.81	95.70
2	1.0	57	2.50	82.70	82.79
3	2.4	60	0.59	89.91	89.90
4	1.7	61	1.91	91.02	90.67
5	1.7	61	0.53	90.53	90.70
6	2.5	70	0.50	85.80	85.75
7	1.0	50	0.50	90.00	90.07
8	1.7	61	0.53	90.97	90.70
9	2.5	50	2.50	94.20	94.21
10	1.7	50	1.60	95.73	95.70
11	1.0	57	1.39	88.31	88.23
12	2.0	70	2.50	88.60	88.29
13	2.5	61	1.60	90.76	90.53
14	1.0	70	2.50	86.19	86.13
15	2.0	70	2.50	88.03	88.29
16	1.0	70	1.25	90.79	90.78
17	2.5	61	1.60	90.32	90.53
18	1.8	70	1.20	91.70	91.89
19	1.7	61	1.91	90.20	90.67
20	2.5	50	0.50	96.37	96.43

4.2.2.1 Determination of Selected Model

The analysis model was executed based on several analyses, including sequential model sum of squares, lack of fit tests, model summary statistics and fit summary. The model selection was based on the highest order polynomial where all additional terms are significant and the model was non-aliased. The analysis of sequential model sum of squares revealed that the suitable model to explain the study's variables for response was the quadratic model, based on the *F*-value and *p*-value. For the percentage yield of SFOFA, the *F*-value was 276.52 and the *p*-value was < 0.0001. Table 4.8 shows the sequential model sum of square for percentage yield of SFOFA. The analysis of sequential model sum of squares for the percentage yield of SFOFA indicated significance in the quadratic model, with the highest *F*-value and the lowest *p*-value, suggesting the suitability of the model.

Table 4.8
Sequential Model Sum of Square of Percentage Yield of SFOFA

Source	Sum of Squares	dF	Mean Square	*F*-value	*p*-value model	
Mean vs Total	1.634E+05	1	1.634E+05			
Linear vs Mean	97.66	3	32.55	4.18	0.0231	
2FI vs Linear	58.69	3	19.56	3.93	0.0356	
Quadratic vs 2FI	65.17	3	21.72	276.52	< 0.0001	Suggested
Cubic vs Quadratic	0.0901	5	0.0180	0.1296	0.9787	Aliased
Residual	0.6954	5	0.1391			
Total	1.637E+05	20	8198.01			

Furthermore, the model selection was also based on models that had a lack of fit that was not significant, where the *p*-value had to exceed 0.05. For the percentage yield of SFOFA, the *F*-value was 0.1296, while the *p*-value was 0.9787. The lack of fit analysis test indicated that the quadratic model was suitable for response based on the non-significant *p*-values of the model. Table 4.9 shows the Lack of Fit Tests for percentage yield of SFOFA.

Table 4.9
Lack of Fits Test for Percentage Yield of SFOFA

Source	Sum of Squares	dF	Mean Square	*F*-value	*p*-value model	
Linear	123.95	11	11.27	81.01	< 0.0001	
2FI	65.26	8	8.16	58.64	0.0002	
Quadratic	0.0901	5	0.0180	0.1296	0.9787	Suggested
Cubic	0.0000	0				Aliased
Pure error	0.6954	5	0.1391			

The analysis of model summary statistics can also be used to determine the suitable model by comparing the R^2 values. The model summary statistics for the percentage yield of SFOFA show satisfactory R^2 values for the quadratic model, as they approach 1. The errors in the model can be determined based on the standard deviation values. A low standard deviation value indicates a good model and this value was related to the R^2 and adjusted R^2 values. A low standard deviation value also indicates the precision of the quadratic model for response, with a standard deviation of 0.2803 for the percentage yield of SFOFA. The R^2 value for the percentage yield of SFOFA was 0.9965 and the adjusted R^2 was 0.9933. A value of 1.0 for R^2 indicates that 100% of the variability in the study can be explained by the selected model. Table 4.10 shows the model summary statistic for percentage yield of SFOFA.

The Predicted Error Sum of Squares (PRESS) predicts the sum of squared errors of R^2, where it lies between the predicted R^2 and adjusted R^2 to indicate the suitability of the model. The model with the smallest PRESS was the preferred model. The analysis of the model summary statistics for both responses shows the smallest values, indicating the selection of the quadratic model. The PRESS for the percentage yield of SFOFA was 2.28.

Table 4.10
Model Summary Statistic for Percentage Yield of SFOFA

Source	Standard Deviation	R^2	Adjusted R^2	Predicted R^2	PRESS	
Linear	2.79	0.4393	0.3342	0.0377	213.92	
2FI	2.25	0.7033	0.5664	-0.1067	246.01	
Quadratic	0.2803	0.9965	0.9933	0.9898	2.28	Suggested
Cubic	0.3729	0.9969	0.9881			Aliased

4.2.2.2 Identification of Model Accuracy

The accuracy of the model can be determined by examining several analysis plots, such as the normal probability plot of residuals (Figure 4.8), residual versus predicted plot (Figure 4.9), actual versus predicted (Figure 4.10), residual versus run number plot (Figure 4.11), Cook's Distance plot (Figure 4.12) and Box-Cox plot (Figure 4.13). The normal probability plot (Figure 4.8) shows that the residuals were scattered randomly along the straight regression line for the percentage yield of SFOFA. This indicates that the residuals follow a normal distribution, supporting the accuracy of the model. The residual versus predicted plot (Figure 4.9) shows scattered points clustered around the zero line. The plot between predicted versus actual also shows all the points were close to the line as shown in Figure 4.10. This indicates that there were no significant abnormalities in the residuals and the model's variability was stable. This further confirms that the proposed model was suitable for the dataset.

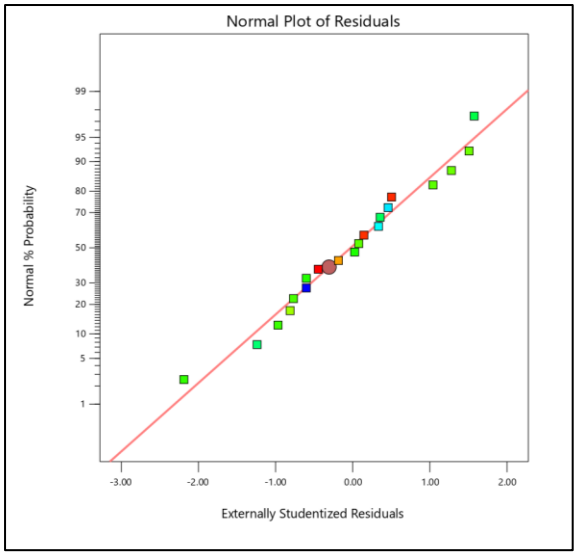


Figure 4.8 Normal Plot of Residuals for Percentage Yield of SFOFA

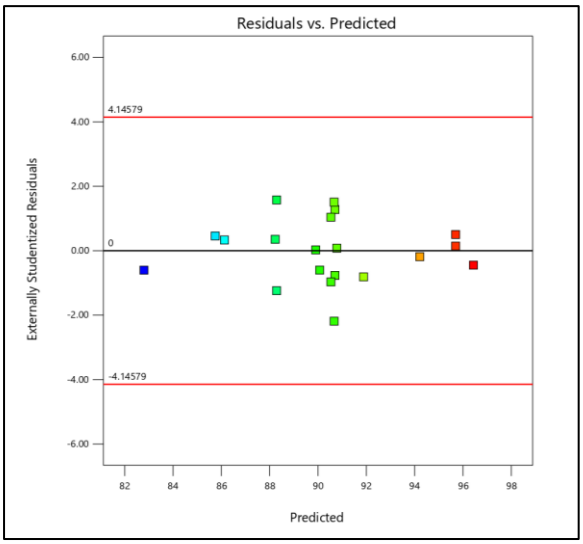


Figure 4.9 Residuals versus Predicted Plot for Percentage Yield of SFOFA

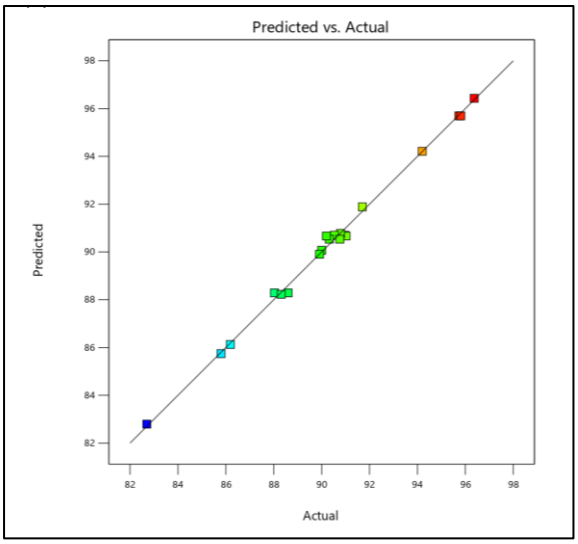


Figure 4.10 Predicted versus Actual Plot for Percentage Yield of SFOFA

An outlier was an observation that deviates significantly from other observations in a dataset. It was a data point that lies far away from the majority of the data points, either in terms of its numerical value or its relationship to other variables. Outliers can have a significant impact on statistical analyses and models because they can skew the results and affect the estimated parameters or relationships. Therefore, it was important to identify and handle outliers appropriately in data analysis. Based on the figures for residual versus run number for the percentage yield of SFOFA (Figure 4.11) all the test points fall within the defined range of 4.14579 to -4.14579. This indicates that the chosen model was appropriate because all the data points were within the specified range.

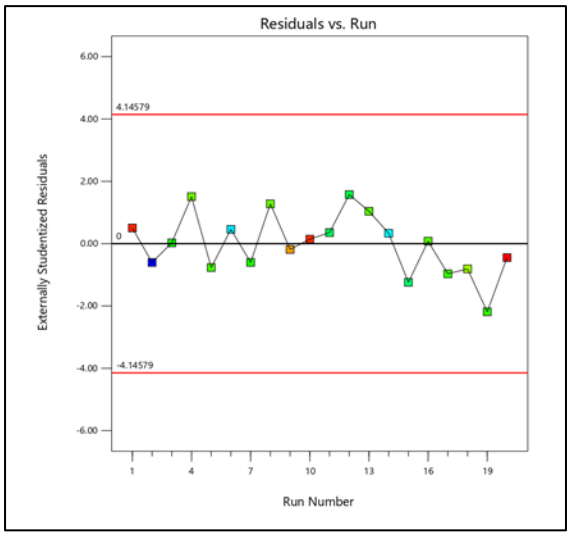


Figure 4.11 Residual versus Run Number for Percentage Yield of SFOFA

Cook's distance was a statistical metric used to evaluate the influence of individual data points on a regression model. It detects influential observations that can significantly affect the model's outcomes. Cook's distance was computed for each data point and quantifies the potential impact on the regression coefficients if that observation were excluded. It considers both the leverage and residual values of each observation to determine its influence on the model. Higher values of Cook's distance indicate greater influence of the corresponding data point on the model's results. Figure 4.12 shows the Cook's Distance for percentage yield of SFOFA. From the Figure 4.12, all points were located below the threshold line of 1 and most points were below 0.2. This indicates that the model was accurate in predicting the response variable. The fact that the points were close to zero suggests that the model's predicted values were in good agreement with the actual observed values. Overall, the plot demonstrates the model's accuracy and its ability to capture the variability in the data.

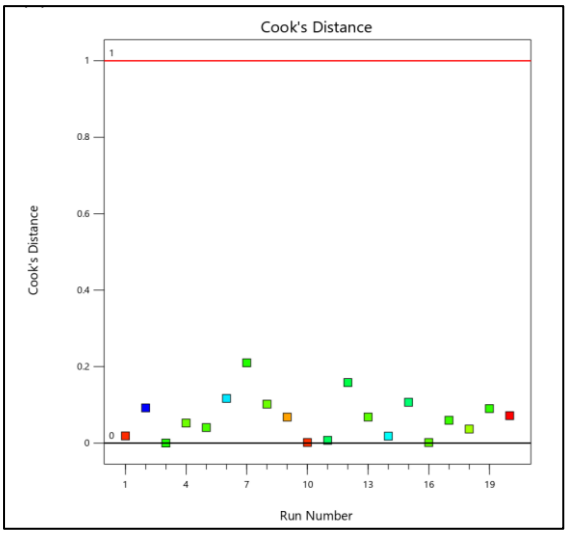


Figure 4.12 Cook's Distance Plot for Percentage Yield of SFOFA

The Box-Cox plot can also be used to evaluate the accuracy of the model. Box-Cox was a method used to transform the response variable in a regression analysis to meet the assumptions of normality, constant variance and linearity. The Box-Cox transformation helps to stabilize the variance and improve the distributional properties of the response variable. The purpose of the Box-Cox transformation was to find the optimal lambda value that maximizes the likelihood of the transformed data being normally distributed. By transforming the response variable, the assumptions of the regression analysis can be met, leading to more reliable and accurate model results. The Box-Cox plot (Figure 4.13) indicates the optimal lambda values of 1.48 for percentage yield of SFOFA. No transformation was recommended for the percentage yield of SFOFA because the lambda value was close to unity and considered the best.

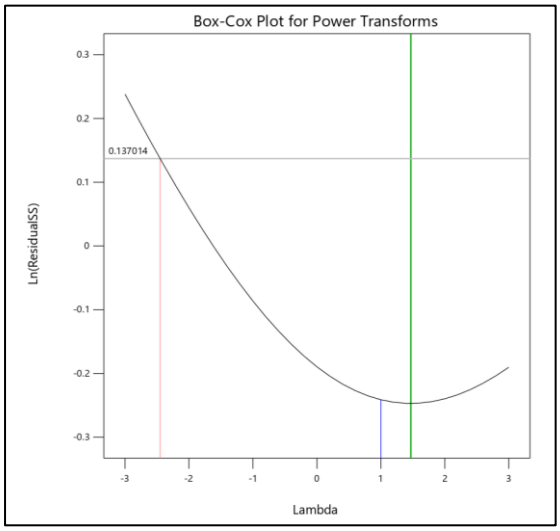


Figure 4.13 Box-Cox Plot for Percentage Yield of SFOFA

4.2.2.3 Analysis of Variance

Analysis of Variance (ANOVA) was a statistical tool used to determine the significance of the linear, quadratic or interaction effects of independent variables on a response. The significance of the variables can be determined based on the *F*-value and *p*-value, where the *p*-value should be less than 0.05 to indicate a significant model, while a *p*-value exceeding 0.05 indicates a non-significant model. A lower *p*-value indicates a higher significance of the variable. The *p*-value was used to assess the importance of each factor. Based on the ANOVA, the models for the percentage yield of SFOFA was highly significant as the *p*-values were less than 0.0001. The *p*-values for lack of fit was 0.9787 for the percentage yield of SFOFA indicating that the lack of fit was not significant in relation to pure error. The *F*-values suggest that there was a 97.87% chance for the lack of fit *F*-value in the percentage yield of SFOFA to occur due to noise. The non-significance of the lack of fit supports the suitability of the selected model for the experimental data. Table 4.11 shows the summary of ANOVA analysis for percentage yield of SFOFA.

Table 4.11
Summary of ANOVA Analysis for Percentage Yield of SFOFA

Source	Yield SFOFA (%)
p-value model	< 0.0001
F-value model	313.32
p-value Lack of Fit	0.9787
F-value Lack of Fit	0.0180
R^2	0.9965
Adjusted R^2	0.9933
Predicted R^2	0.9898
Standard deviation	0.2803
Coefficient of variation (C.V %)	0.3101
Adequate precision	68.8142

The precision of the model was evaluated based on the standard deviation and coefficient of variation (C.V%). The coefficient of variation was a statistical measure that represents the relative variability or dispersion of a dataset. It was calculated by

dividing the standard deviation of the dataset by the mean and then multiplying by 100 to express the result as a percentage. A lower C.V.% indicates higher precision, while a higher C.V.% indicates lower precision of the model. The C.V.% for percentage yield of SFOFA was 0.3101 and the standard deviation was 0.2803 for percentage yield of SFOFA. The low values of standard deviation and C.V.% indicate the precision of the quadratic model for the response.

For model adequacy, it was evaluated through the coefficient of determination (R^2). R^2 was a statistical measure that represents the proportion of the variability in the response variable that can be explained by the model. R^2 ranges from 0 to 1, with 0 indicating that the model does not explain any of the variability in the response variable and 1 indicating that the model explains all of the variability. The R^2 values for percentage yield of SFOFA was 0.9965 and the R^2 values for both quadratic models were satisfactory and close to 1, indicating that approximately 99.65% of the variation in the experimental data was accounted for by the quadratic models for each response. This implies that the quadratic models was suitable for interpreting the optimum conditions, while only 0.35% of the total variation for the response was unexplained by the models.

A high R^2 value (approaching 1) indicates that the selected model was accurate in capturing the variation in the data and it reflects the true relationship between the response and the significant variables. The Adjusted R^2 values for percentage yield of SFOFA support the high R^2 values, as they were also close to 1. On the other hand, the predicted R^2 represents the Predicted Error Sum of Squares (PRESS). For percentage yield of SFOFA, the predicted R^2 was 0.9898 and the adjusted R^2 was 0.9933. The predicted R^2 values for both responses show reasonable agreement with the adjusted R^2, as the difference was less than 0.2. Based on the values of predicted and adjusted R^2, it indicates that the obtained values have good correlation statistics with the predicted data. Therefore, the regression model provides a very good explanation of the relationship between the independent variables and the response variable. Overall, the selected quadratic model can be used for prediction purposes.

Adequacy Precision, also known as Adeq Precision, was a measurement that assesses the signal-to-noise ratio in a statistical model. It was specifically used in RSM to evaluate the reliability of the model's predictions. Adeq Precision was calculated as the ratio of the range or variation of the predicted response values to the average prediction error. It provides an indication of how well the model can predict the

response variable within the experimental region. A high Adeq Precision value, typically above 4, suggests that the model's predictions were reliable and accurate within the experimental data. For the percentage yield of SFOFA, the Adeq Precision was 68.8142. The Adeq Precision values for the response indicate adequate signal-to-noise ratio, as the ratio was greater than 4. This implies that the quadratic model can be used effectively to navigate the design space and make reliable predictions.

Table 4.12 show the ANOVA analysis factors for percentage yield of SFOFA. The response for percentage yield of SFOFA shows that all linear terms A (molarity of ethanolic KOH), B (temperature) and C (time) were highly significant, with *p*-values less than 0.01. For the interaction terms, AB and AC and BC were highly significant ($p < 0.01$). Regarding the quadratic terms, A^2, B^2 and C^2 were all highly significant ($p < 0.01$). The regression equations for percentage yield of SFOFA was shown below:

$$\text{Yield (\%)} = 91.98 + 1.57A - 2.13B - 1.46C - 2.59AB + 0.9725AC + 0.6271BC - 2.50A^2 + 2.11B^2 - 2.56C^2$$

Table 4.12
ANOVA Analysis Factors for Percentage Yield of SFOFA

Source	Sum of Squares	dF	Mean Square	*F*-value	*p*-value model	Significance
A-molarity ethanolic KOH	24.69	1	24.69	314.28	< 0.0001	Significant
B-temperature	44.86	1	44.86	571.13	< 0.0001	Significant
C-time	20.47	1	20.47	260.63	< 0.0001	Significant
AB	37.40	1	37.40	476.09	< 0.0001	Significant
AC	5.33	1	5.33	67.81	< 0.0001	Significant
BC	2.35	1	2.35	29.87	0.0003	Significant
A^2	25.00	1	25.00	318.23	< 0.0001	Significant
B^2	18.19	1	18.19	231.62	< 0.0001	Significant
C^2	22.34	1	22.34	284.34	< 0.0001	Significant

4.2.2.4 Interaction of Factors for Optimum Responses

For the response, all the interaction terms and factors were significant ($p < 0.05$). This further reinforces the screening results, which indicate that all linear terms for both the percentage yield of SFOFA was significant.

The interaction between variables can be illustrated through a 3-dimensional (3D) response surface plot. For the percentage yield of SFOFA, all three interaction terms (AB, AC and BC) were chosen. Figure 4.14 show the 3D response surface for the interaction between variables and response.

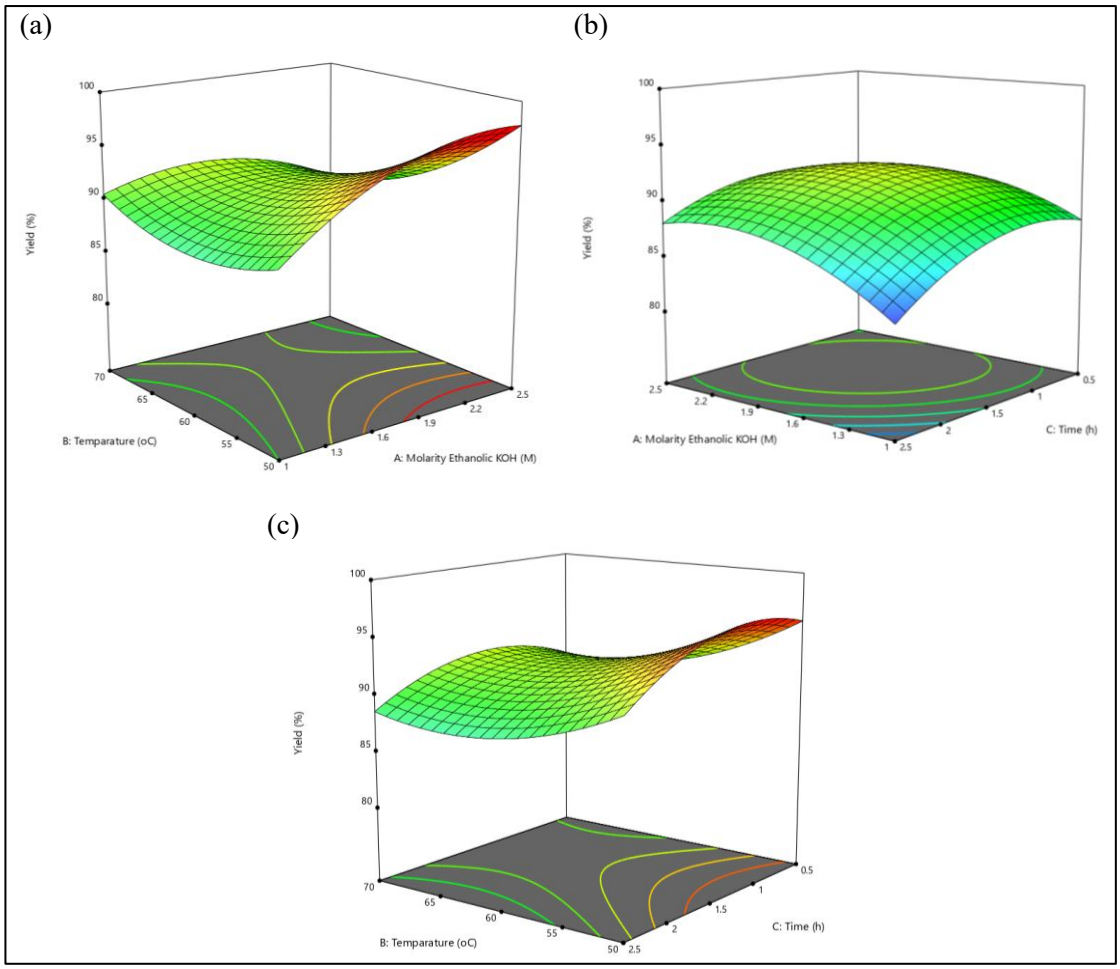


Figure 4.14 3D Surface Plot for a) AB, b) AC and c) BC for Percentage Yield of SFOFA

Based on the Figure 4.14 (a) plot, the 3D surface plot shows that as the molarity of ethanolic KOH increases from 1 M to 2.5 M, the percentage yield of SFOFA also increases. On the other hand, as the temperature increases from 50 to 70 °C, the percentage yield of SFOFA decreases. This indicates that higher molarity of ethanolic KOH and lower temperature result in higher percentage yield of SFOFA. For the Figure 4.14 (b) plot, the 3D surface plot shows that as the molarity of ethanolic KOH increases, the percentage yield of SFOFA also increases. However, as the time increases from 0.5 to 2.5 hours, the percentage yield of SFOFA decreases. This suggests that higher molarity of ethanolic KOH and shorter reaction time lead to higher percentage yield of

SFOFA. For Figure 4.14 (c) the 3D surface plot shows that as the temperature and time decrease, the percentage yield of SFOFA increases.

The increase in the molarity of ethanolic KOH as a catalyst leads to a higher percentage yield of SFOFA. This phenomenon occurs because the catalyst offers an alternative reaction pathway with a lower activation energy, ultimately resulting in increased percentage yield of SFOFA. Furthermore, elevating the temperature results in a general acceleration of the hydrolysis rate due to the greater kinetic energy of molecules. Higher temperatures encourage more vigorous collisions between oil and hydroxide (OH) molecules, promoting the cleavage of ester bonds within the oil. Similarly, extending the reaction time also leads to higher yield in the hydrolysis process. However, it's worth noting that under optimal conditions, using a high molarity of ethanolic KOH may necessitate lower temperatures and shorter reaction times.

4.2.2.5 Verification Model

Numerical optimization was conducted to find the optimal conditions for the hydrolysis of SFO. The parameters A, B and C were adjusted within a specific range to achieve the highest percentage yield of SFOFA. The accuracy of the model increases as the desirability of the functions increases. Table 4.13 provides a summary of the applied constraints to determine the optimum condition, aiming for the higher percentage yield of SFOFA. The parameters A, B and C were varied while the response was set to their maximum values. The desirability of the predicted model was equal to 1.00, indicating that the model provides the ideal value. Figure 4.15 illustrates the predicted outcomes obtained from the numerical optimization model for the hydrolysis of SFO.

Table 4.13
Restraints for Optimization of Hydrolysis of SFO Parameter and Responses for D-optimal Design

Parameter and responses	Goal	Lower limit	Upper limit	Weight	Importance
A: Molarity ethanolic KOH	in range	1.0	2.5	1	3
B: Reaction temperature	in range	50.0	70.0	1	3
C: Reaction time	in range	0.5	2.5	1	3
Yield of SFOFA	maximize	82.70	96.37	1	3

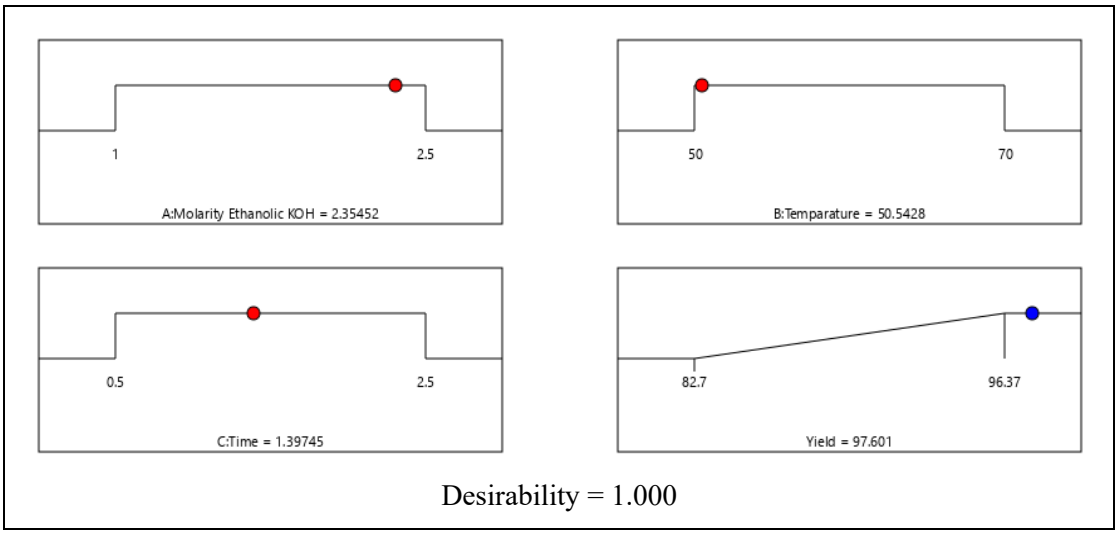


Figure 4.15 D-Optimal Predicted Model at Optimum Condition for Hydrolysis of SFO

The effectiveness of the model generated through D-optimal design was verified by conducting the hydrolysis process using three randomly chosen sets of reaction conditions. To ensure the accuracy of the model, the actual and predicted values were compared by calculating the Residual Standard Error (RSE) for each experiment. The RSE was a statistical metric that measures the average level of variation or discrepancy between the predicted values and the observed values in a regression or prediction model. It was computed as the square root of the mean squared error (MSE) and represents the standard deviation of the residuals. Residuals were the differences between the observed and predicted values for each data point in the model. RSE serves as an indicator of how well the model aligns with the data and accurately predicts the response variable. A lower RSE reflects a better fit and greater accuracy of the model, indicating that the predicted values closely align with the observed values. Conversely, a higher RSE suggests a larger amount of unexplained variation or error in the model. Only those experiments with RSE values below 5% were considered acceptable. The results presented in Table 4.14 demonstrate that all RSE values were less than 5%, indicating the model's suitability.

Table 4.14
Actual and Predicted Data for Verification Model for Percentage Yield of SFOFA

Molarity ethanolic KOH (M)	Reaction temperature (°C)	Reaction time (h)	Yield SFOFA (%)		
			Actual	Predicted	RSE
2.2	55.0	1.5	93.60	94.39	0.84
2.1	65.0	2.0	88.95	90.05	1.22
1.9	69.0	2.1	90.42	90.19	0.26

4.2.2.6 Optimum Condition of Hydrolysis Process

The D-optimal design successfully provided the predicted optimal conditions for the hydrolysis of SFO. The optimal conditions include a molarity of 2.4 M for ethanolic KOH, a reaction temperature of 50.62 °C and a reaction time of 1.37 hours. Using these conditions, percentage yield of SFOFA of 96.41% was obtained. Table 4.15 present the actual and predicted data for the optimum condition. The validation of the optimum condition was performed by calculating the RSE, which confirmed that the values below 5% for percentage yield of SFOFA. Figure 4.16 shows the product of SFOFA.

Table 4.15
Actual and Predicted Data for Optimum Condition for Percentage Yield of SFOFA

Molarity ethanolic KOH (M)	Reaction temperature (°C)	Reaction time (h)	Yield SFOFA (%)		
			Actual	Predicted	RSE
2.4	51	1.4	96.41	97.60	1.22



Figure 4.16 Sunflower Oil Fatty Acids (SFOFA)

4.2.3 Characterization of Sunflower Oil Fatty Acids

4.2.3.1 Gas Chromatography

The fatty acid composition of SFOFA was determined using gas chromatography mass spectrometry (GC-MS) with a HP-88 column. After turning SFO into SFOFA through hydrolysis process, the types of fatty acids in SFOFA were pretty much the same as SFO. The most common fatty acid in both SFO and SFOFA was linoleic acid, which was about 54.01%. Next was oleic acid at about 32.33%, followed by palmitic acid at 7.44%, stearic acid at 4.29%, behenic acid at 0.91%, lignoceric acid at 0.31%, arachidic acid at 0.30%, linolenic acid at 0.21%, paullinic acid at 0.18% and tricosanoic acid at 0.02%. Figure 4.17 shows the GC-MS chromatogram of SFOFA and Table 4.16 shows the fatty acids composition in SFOFA.

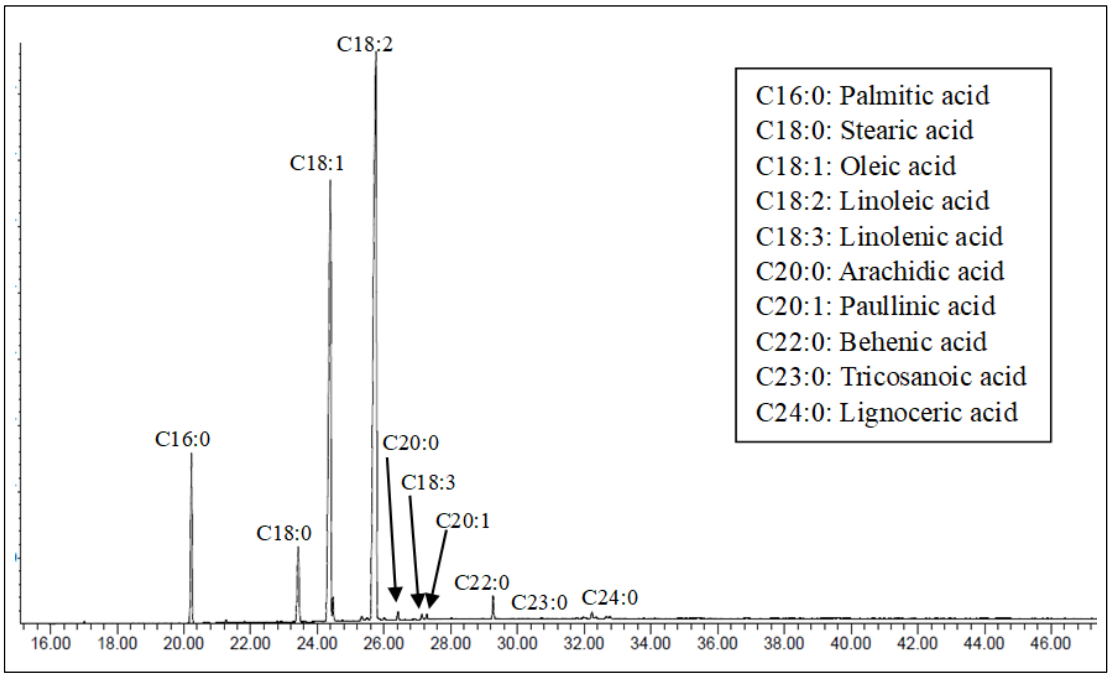


Figure 4.17 GC-MS Chromatogram of Fatty Acids Composition in SFOFA

Table 4.16
Fatty Acids Composition in SFOFA

Fatty acid	Structure	Percentage composition (%)
Palmitic acid	C16:0	7.44
Stearic acid	C18:0	4.29
Oleic acid	C18:1	32.33
Linoleic acid	C18:2	54.01
Linolenic acid	C18:3	0.21
Arachidic acid	C20:0	0.30
Paulinic acid	C20:1	0.18
Behenic acid	C22:0	0.91
Tricosanoic acid	C23:0	0.02
Lignoceric acid	C24:0	0.31
Saturated fatty acid		13.27
Unsaturated fatty acid		86.73

4.2.3.2 Fourier Transform Infrared Spectroscopy

FTIR spectroscopy is used to identify functional groups and the presence of carboxylic acid in SFOFA. Figure 4.18 shows FTIR spectra of SFO and SFOFA. Based on Figure 4.18 there were some differences in the two spectra. Before the hydrolysis (SFO), a sharp peak appeared at 1746.33 cm^{-1} indicating stretching vibration for C=O (ester carbonyl). After hydrolysis (SFOFA), the peak for C=O (ester carbonyl) has disappeared and a new sharp peak appeared at 1710.23 cm^{-1} indicating stretching vibration for C=O (carboxylic acid) and broad OH peak for COOH appeared at range 2400 to 3400 cm^{-1} which shows hydrolysis has successfully converted from ester to carboxylic acid. Table 4.17 shows a summary of the functional group and wavenumber for SFO and SFOFA.

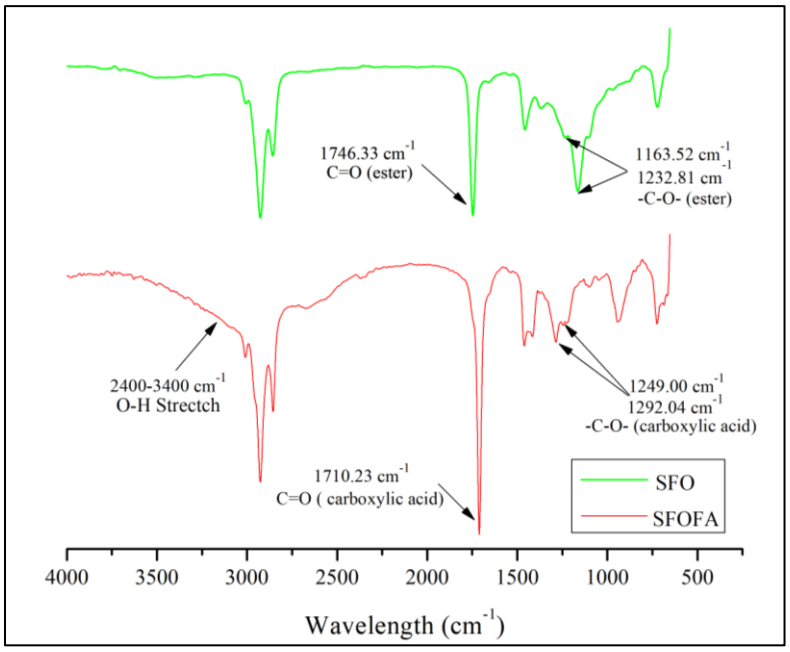


Figure 4.18 FTIR Spectra of SFO and SFOFA

Table 4.17
Functional Group and Wavenumber for FTIR Spectra SFO and SFOFA

Functional group	Wavenumber (cm^{-1})	
	SFO	SFOFA
OH stretching (carboxylic acid)	-	2400-3400
C=C bending vibration (aliphatic)	3007.93	3009.18
C-H stretching vibration (aliphatic)	2926.56 and 2857.78	2926.93 and 2856.16
C=O stretching vibration (ester)	1746.33	-
C=O stretching vibration (carboxylic acid)	-	1710.23
-C-O stretching vibration (ester)	1232.81 and 1163.52	-
-C-O stretching vibration (carboxylic acid)	-	1292.04 and 1249.00

4.2.3.3 Nuclear Magnetic Resonance

The ^{1}H NMR spectra of SFOFA, along with the corresponding chemical shifts, are presented in Figure 4.19 and summarized in Table 4.18. Three specific peaks were analyzed to assess the successful conversion of ester to fatty acid. In the ^{1}H NMR spectrum of SFO, notable peaks were observed within the range of chemical shift 4.14 to 4.18 ppm and 4.29 to 4.33 ppm, representing -C**H**$_2$-COOR- and -C**H**-COOR- respectively. These peaks correspond to protons from the glycerol backbone in SFO and their absence in the ^{1}H NMR spectrum of SFOFA indicates the successful hydrolysis process. Additionally, a new peak emerged in the downfield region at chemical shift

10.61 ppm in the ^{1}H NMR spectrum of SFOFA, confirming the presence OH group in the fatty acid (-COOH) in SFOFA. This signal falls within the characteristic chemical shift range of 10–12 ppm for OH carboxylic acids, as reported by Pavia et al. (2015). As the SFOFA was dissolved in deuterated chloroform ($CDCl_3$), the solvent peak appeared at 7.28 ppm.

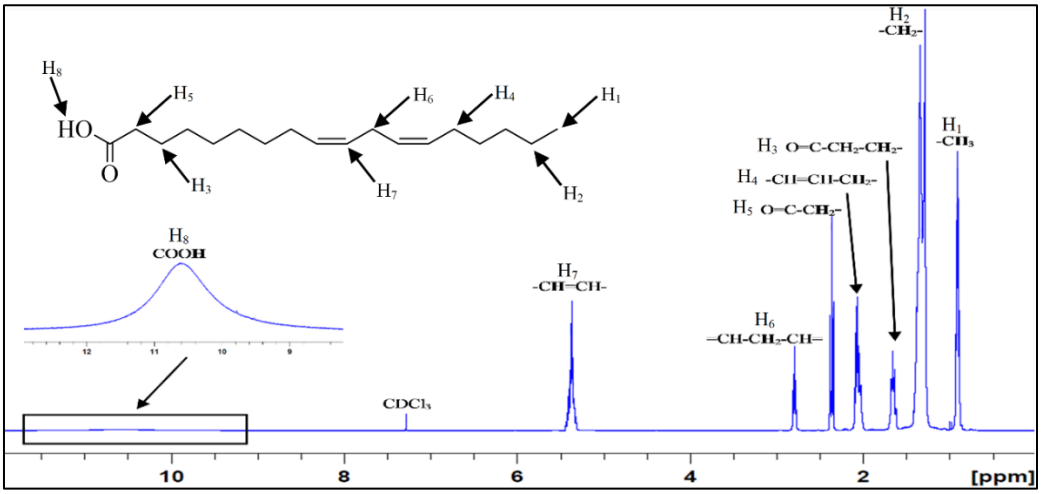


Figure 4.19 ^{1}H NMR Spectrum for SFOFA

Table 4.18
Type of Proton and Chemical Shift of SFO and SFOFA

	Type of proton	Chemical shift (ppm)		
		SFO	SFOFA	Theoretical*
H_1	-C**H**$_3$	0.88-0.92	0.89-0.93	0.70-1.3
H_2	-C**H**$_2$-	1.29-1.41	1.29-1.40	1.2-1.4
H_3	O=C-CH$_2$-C**H**$_2$-	1.61-1.63	1.64-1.68	1.5-2.0
H_4	-CH=CH-C**H**$_2$-	2.00-2.09	2.03-2.10	1.6-2.6
H_5	O=C-C**H**$_2$-	2.30-2.35	2.35-2.38	2.1-2.5
H_6	=CH-C**H**$_2$-CH=	2.77-2.80	2.78-2.81	2.5-3.0
-	-C**H**$_2$-COOR- (glycerol)	4.14-4.18	-	4.0-4.5
-	-C**H**-COOR- (glycerol)	4.29-4.33	-	4.0-4.5
H_7	-CH=C**H**-	5.28-5.41	5.34	4.5-6.5
H_8	COO**H**	-	10.61	10-12

Source: *Pavia et al. (2015)

The ^{13}C-NMR spectrum (Figure 4.20) shows that there was a peak at the chemical shift of 14.02 ppm which represents the carbon for the methyl group (-**C**H$_3$) and the peak at the chemical shift of 22.65 to 34.10 ppm represents the carbon of the

methylene group (-**C**H_2-). This value matches the range of values reported by Pavia et al. (2015) which at a chemical shift of 8 to 30 (-**C**H_3) and 15 to 55 ppm (-**C**H_2-). The peak at the chemical shift of 127.90 to 130.17 ppm indicates the type and carbon of the alkene (-**C**=**C**-) and the value reported by Pavia was the same which at 100 to 150 ppm.

The disappearance of the carbonyl ester (**C**=O) peak in the range of 172.79 to 173.21 ppm, along with the appearance new carbonyl peak corresponding to C=O carboxylic acid confirms the successful hydrolysis of SFO into SFOFA. In addition, the absence peak at 62.09 ppm and 68.90 ppm which correspond to -**C**H_2-O- and -**C**H-O from the glycerol backbone in SFO verified the successful removal of the glycerol moiety and conversion of SFO to SFOFA. Table 4.19 shows a summary of the type of carbon and chemical shift for SFOFA.

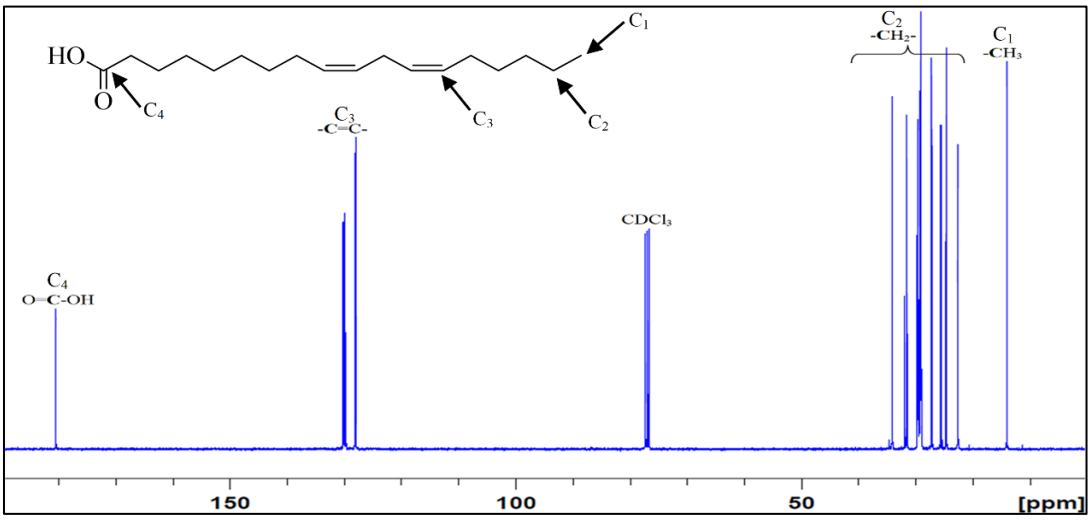


Figure 4.20 ^{13}C NMR Spectrum of SFOFA

Table 4.19
Type of Carbon and Chemical Shift of SFO and SFOFA

	Type of carbon	Chemical shift (ppm)		
		SFO	SFOFA	Theoretical*
C_1	-**C**H_3	14.05-14.09	14.02	8-30
C_2	-**C**H_2-	22.56-34.18	22.65-34.10	15-55
-	-**C**H_2-O (glycerol)	62.09	-	40-80
-	-**C**H-O (glycerol)	68.90	-	40-80
C_3	-**C**=C-	127.90-130.20	127.90-130.17	100-150
-	O=**C**-OR (ester)	172.79-173.21	-	155-185
C_4	O=**C**-OH (carboxylic acid)	-	180.45	155-185

Source: *Pavia et al. (2015)

4.3 Separation of Sunflower Oil Fatty Acids via Low Temperature Methanol Crystallization

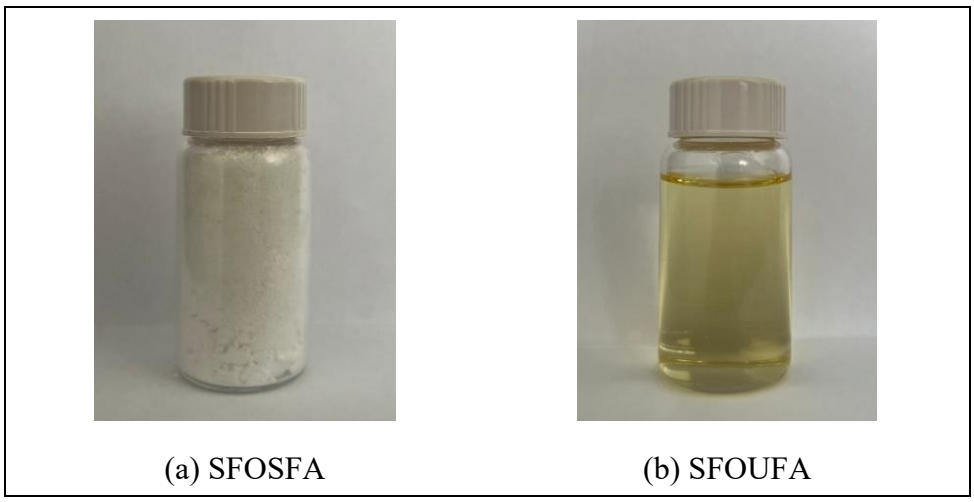
4.3.1 Methanol Crystallization Method

The separation of mixture fatty acids in SFOFA was carried out via low temperature methanol crystallization. The separation of SFOSFA and SFOUFA from the mixture of SFOFA yielded 13.60% for SFOSFA and 86.32% for SFOUFA. This successful separation can be attributed to the differential solubility of individual fatty acids in methanol and the solvent used in the LTSC process. The high solubility of linolenic, linoleic and oleic and paullinic acid in methanol enables them to remain in solution, contributing to the higher yield of SFOUFA. In contrast, the lower solubility of palmitic, stearic, arachidic behenic, tricosanoic and lignoceric acid in methanol causes them to preferentially crystallize out during the LTSC process, leading to the enrichment of SFOSFA. The solubility of fatty acids was closely related to their melting points, which, in turn, were influenced by the number of carbon atoms and the degree of unsaturation in the fatty acid molecules (Jumaah et al., 2019; Japir et al., 2018). These factors make the separation of SFOFA into SFOSFA and SFOUFA feasible. Notably, the solubility of fatty acids increases with rising temperature (Fadzel et al., 2021). This behavior was evident in the LTSC process, where high melting point fatty acids display lower solubility in methanol compared to low melting point fatty acids. Consequently, at lower temperatures during crystallization, the less soluble fatty acids with higher melting points tend to precipitate, allowing the selective separation of SFOSFA from SFOUFA (Fadzel et al., 2021; Jumaah et al., 2019). The melting point for each fatty acid in SFOFA was shown in Table 4.20. Figure 4.21 shows the separation product which were saturated and unsaturated fatty acids.

Table 4.20
Melting Point of Fatty Acids

Fatty Acids	Temperature (°C)
Palmitic acid	62.9
Stearic acid	70.1
Oleic acid	16.3
Linoleic acid	-6.5
Linolenic acid	-5.0
Arachidic acid	76.1
Behenic acid	80.0
Tricosanoic acid	77-79
Lignoceric acid	84.2

Source: Japir et al. (2018)



(a) SFOSFA (b) SFOUFA

Figure 4.21 (a) Sunflower Oil Saturated Fatty Acids and (b) Sunflower Oil Unsaturated Fatty Acids

4.3.2 Characterization of SFOUFA and SFOSFA

4.3.2.1 Gas Chromatography

The chromatograms of SFOUFA and SFOSFA were presented in Figure 4.22 and Figure 4.23, respectively. After the successful separation of SFOFA into SFOUFA and SFOSFA, the chromatogram of SFOUFA demonstrated a remarkably high content of unsaturated fatty acids, nearly 98.89% of the product. This unsaturated fraction was predominantly composed of 59.91% linoleic acid (C18:2), 38.35% oleic acid (C18:1),

0.34% linolenic acid (C18:3) and 0.29% paullinic acid(C20:1). There was only a small amount of palmitic in SFOUFA which was 1.11%.

In contrast, the chromatogram of SFOSFA exclusively exhibited saturated fatty acids, with no detectable presence of unsaturated fatty acids. Specifically, palmitic (C16:0), stearic (C18:0) arachidic (C20:0), behenic (C22:0), tricosanoic (C23:0) and lignoceric acid (C24:0) were identified, constituting 29.28%, 41.24%, 4.55%, 17.48%, 0.72% and 6.73% of the composition, respectively. This successful separation of SFOFA into its unsaturated and saturated fatty acid components demonstrates the effectiveness of the methanol crystallization process. Table 4.21 shows the fatty acids composition in SFOUFA and SFOSFA.

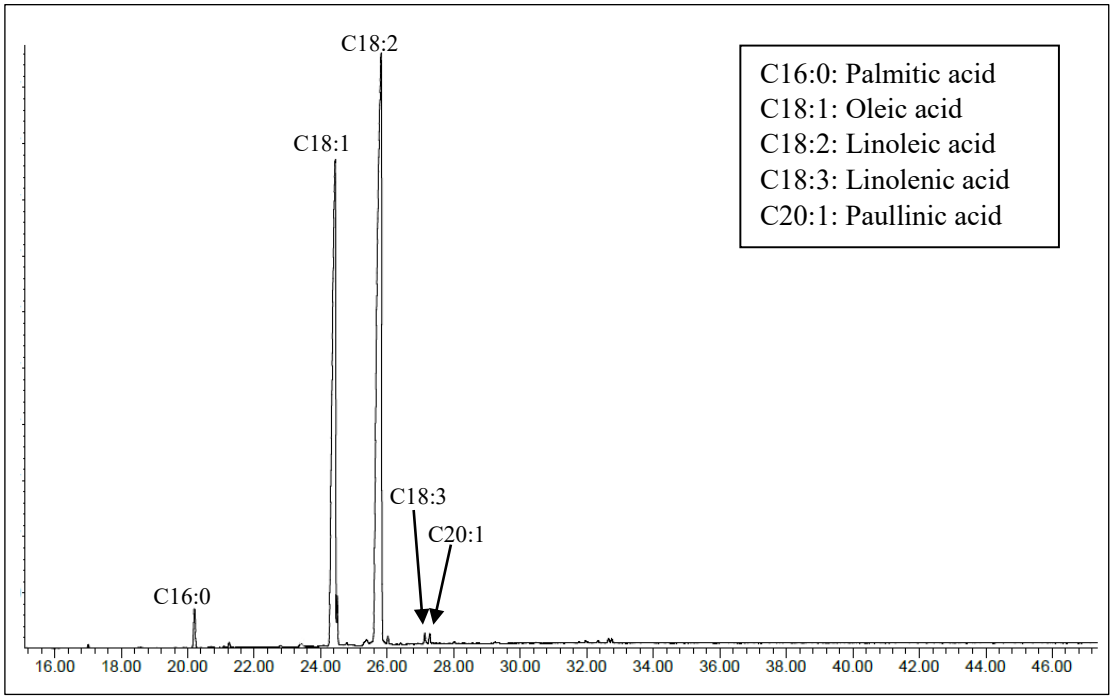


Figure 4.22 GC-MS Chromatogram of Fatty Acids Composition in SFOUFA

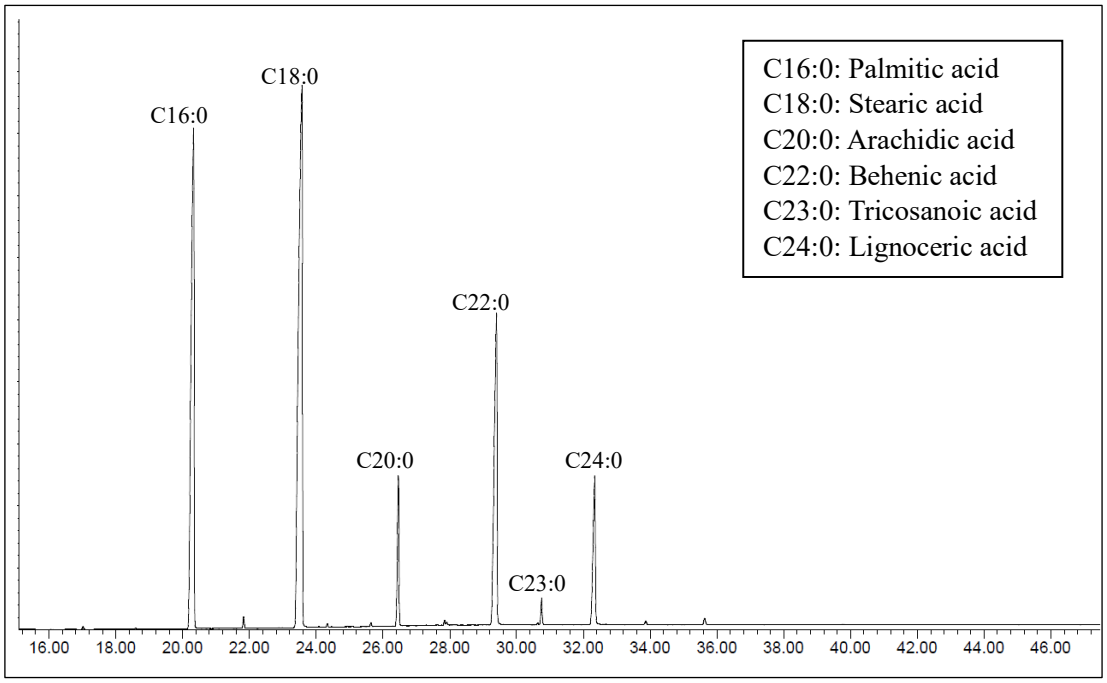


Figure 4.23 GC-MS Chromatogram of Fatty Acids Composition in SFOSFA

Table 4.21
Fatty Acids Composition in SFOUFA and SFOSFA After Separation

Fatty acids	Structure	Percentage composition (%)	
		SFOUFA	SFOSFA
Palmitic acid	C16:0	1.11	29.28
Stearic acid	C18:0	-	41.24
Oleic acid	C18:1	38.35	-
Linoleic acid	C18:2	59.91	-
Linolenic acid	C18:3	0.34	-
Arachidic acid	C20:0	-	4.55
Paullinic acid	C20:1	0.29	-
Behenic acid	C22:0	-	17.48
Tricosanoic acid	C23:0	-	0.72
Lignoceric acid	C24:0	-	6.73
Saturated fatty acids		1.11	100.00
Unsaturated fatty acids		98.89	-

4.3.2.2 Fourier Transform Infrared Spectroscopy

The Perkin Elmer Model 100 spectrometer, using ATR-FTIR spectroscopy, was utilized to analyze the functional groups present in three samples: SFOFA, SFOUFA and SFOSFA. The FTIR spectra of SFOFA, SFOSFA and SFOUFA were shown on Figure 4.24, revealing distinctive peaks and bands indicative of specific functional

groups. In the FTIR spectra of SFOFA and SFOUFA, a sharp peak was observed at 1710.23 cm^{-1} and 1710.60 cm^{-1}, while in SFOSFA, a similar peak appeared at 1705.39 cm^{-1}. These peaks correspond to the stretching vibration of the carbonyl group (C=O) present in carboxylic acid functional groups. Additionally, a peak at range of 2400 to 3400 cm^{-1} was observed in all three spectra, indicating the presence of hydroxyl groups (OH) associated with the carboxylic acid (COOH) functional groups in the fatty acids. The successful separation of the SFOFA mixture into SFOSFA and SFOUFA was confirmed through the absence of a peak at 3009.18 cm^{-1} and 3010.11 cm^{-1} at spectrum of SFOSFA, which typically attributed to the stretching vibration of sp^2 carbon-hydrogen (C-H) bonds found in alkenes. This absence of the alkene peak supports the efficacy of the separation process. Table 4.22 summarizes the functional groups present in SFOFA, SFOSFA and SFOUFA, along with their corresponding wavenumbers obtained from the FTIR spectra.

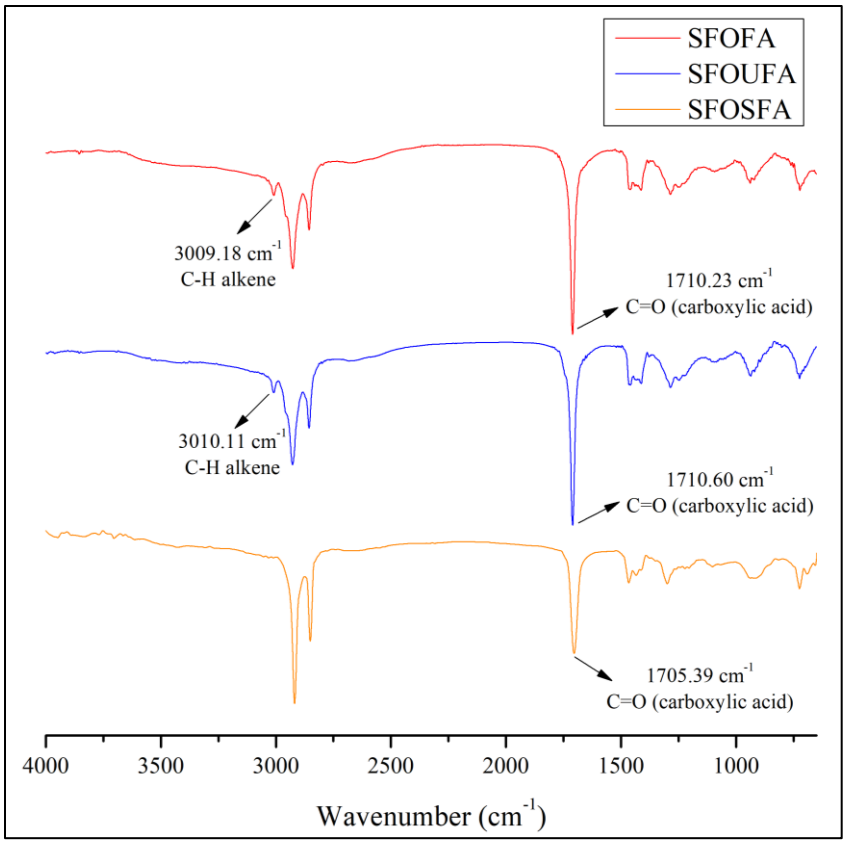


Figure 4.24 FTIR Spectra of SFOFA, SFOUFA and SFOSFA

Table 4.22
Functional Group and Wavenumber for FTIR of SFOFA, SFOUFA and SFOSFA

Functional group	Wavenumber (cm^{-1})		
	SFOFA	SFOUFA	SFOSFA
OH stretching (carboxylic acid)	2400-3400	2400-3400	2400-3400
C-H sp^2 stretching vibration (aliphatic)	3009.18	3010.11	-
C-H sp^3 stretching vibration (aliphatic)	2926.93 and 2856.16	2926.93 and 2856.16	2926.62 and 2857.51
C=O stretching vibration (carboxylic acid)	1710.23	1710.60	1705.39
-C-O stretching vibration (carboxylic acid)	1292.04 and 1249.00	1292.04 and 1249.00	1291.87 and 1248.53

4.3.2.3 Nuclear Magnetic Resonance

Nuclear Magnetic Resonance (NMR) spectroscopy was employed to elucidate the chemical structures of SFOSFA and SFOUFA. The successful separation of SFOFA into SFOSFA and SFOUFA was confirmed based on the observation of specific peaks in the ^{1}H NMR spectra. In the ^{1}H NMR spectra of SFOUFA, a characteristic peak appeared in the chemical shift range of 2.03 to 2.10 ppm, corresponding to the presence of the -CH=C**H**-CH_2- group and this specific peak was absent in the ^{1}H NMR spectra of SFOSFA. Another peak was observed in the chemical shift range of 2.78 to 2.81 ppm in the ^{1}H NMR spectra of SFOUFA, representing the =CH-C**H**$_2$-CH= group. However, this peak was not present in the ^{1}H NMR spectrum of SFOSFA. Furthermore, a distinct peak was identified at the chemical shift range of 5.33 to 5.41 ppm in the ^{1}H NMR spectra of SFOUFA, corresponding to the -C**H**=CH- group. This peak was not observed in the ^{1}H NMR spectra of SFOSFA. The disappeared peak in ^{1}H NMR spectra of SFOSFA confirming the separation and distinguishing between the unsaturated and saturated fatty acids. Both SFOSFA and SFOUFA samples were dissolved in deuterated chloroform ($CDCl_3$) for NMR analysis, resulting in the appearance of the solvent peak at 7.28 ppm, which served as a reference. The ^{1}H NMR spectra of SFOSFA and SFOUFA, along with the associated chemical shifts, are visually represented in Figure 4.25 and summarized in Table 4.23.

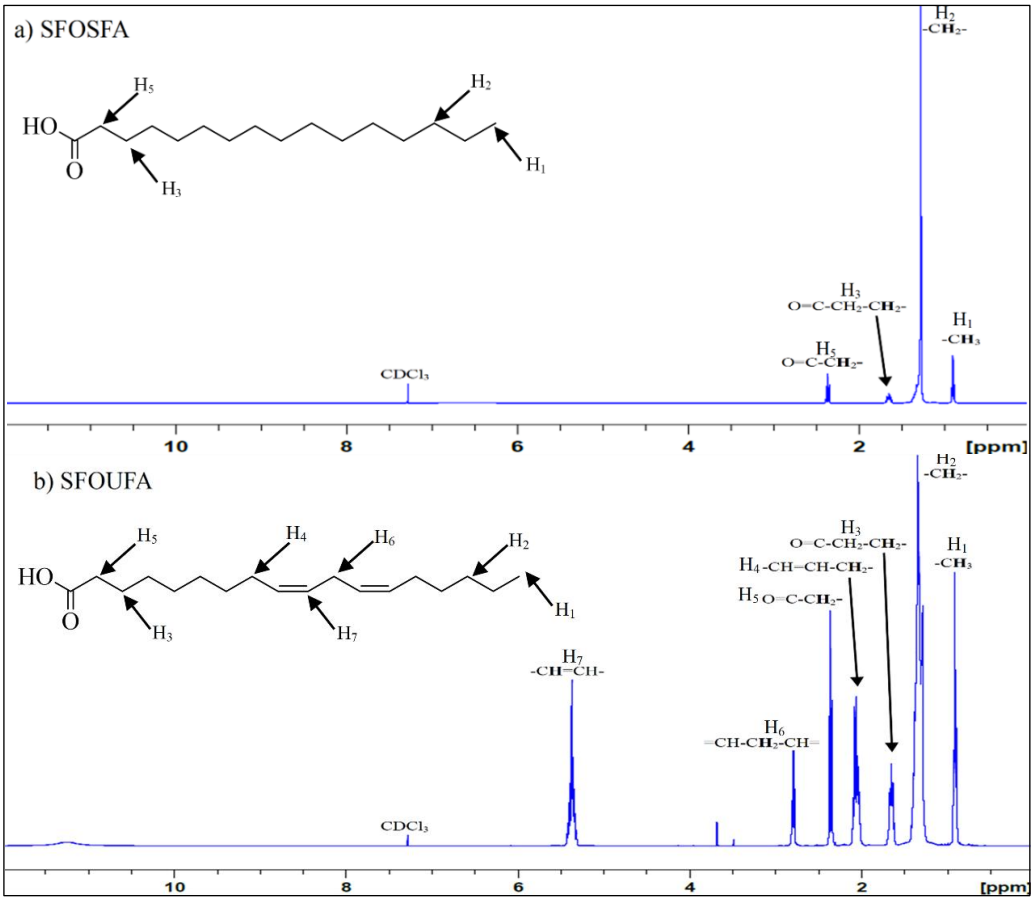


Figure 4.25 ^{1}H NMR Spectra of SFOSFA and SFOUFA

Table 4.23
Type of Proton and Chemical Shift of SFOSFA and SFOUFA

	Type of proton	Chemical shift (ppm)		
		SFOSFA	SFOUFA	Theoretical*
H_1	-C**H**$_3$	0.90-0.92	0.89-0.93	0.70-1.3
H_2	-C**H**$_2$-	1.28-1.34	1.28-1.39	1.2-1.4
H_3	O=C-CH$_2$-C**H**$_2$-	1.62-1.69	1.62-1.67	1.5-2.0
H_4	-CH=CH-C**H**$_2$-	-	2.03-2.10	1.6-2.6
H_5	O=C-C**H**$_2$-	2.3496	2.34-2.38	2.1-2.5
H_6	=CH-C**H**$_2$-CH=	-	2.78-2.81	2.5-3.0
H_7	-CH=C**H**-	-	5.33-5.41	4.5-6.5

Source: *Pavia et al. (2015)

In the ^{13}C NMR spectrum of SFOUFA, a distinctive peak was observed in the chemical shift range of 127.90 to 130.54 ppm, representing the -**C**H=CH- group. This peak was present in the SFOUFA spectrum but absent in the SFOSFA spectrum, serving

as a clear indicator of the successful separation between the two types of fatty acids. Moreover, the ^{13}C NMR spectra revealed the presence of carboxylic acid (**C**OOH) functional groups in both SFOSFA and SFOUFA. These carboxylic acid peaks appeared at chemical shifts of 179.71 and 180.33 ppm, respectively, confirming the presence of this functional group in both types of fatty acids. In the ^{13}C NMR spectra, the solvent peak corresponding to deuterated chloroform ($CDCl_3$) was identified at the chemical shift range of 76.71 to 77.36 ppm, serving as a reference. Figure 4.26 and Table 4.24 present the ^{13}C NMR spectra of SFOSFA and SFOUFA, along with their corresponding chemical shifts. The chemical shifts observed in both the ^{1}H NMR and ^{13}C NMR spectra were found to be in good agreement with the theoretical values, further supporting the accuracy of the NMR analysis.

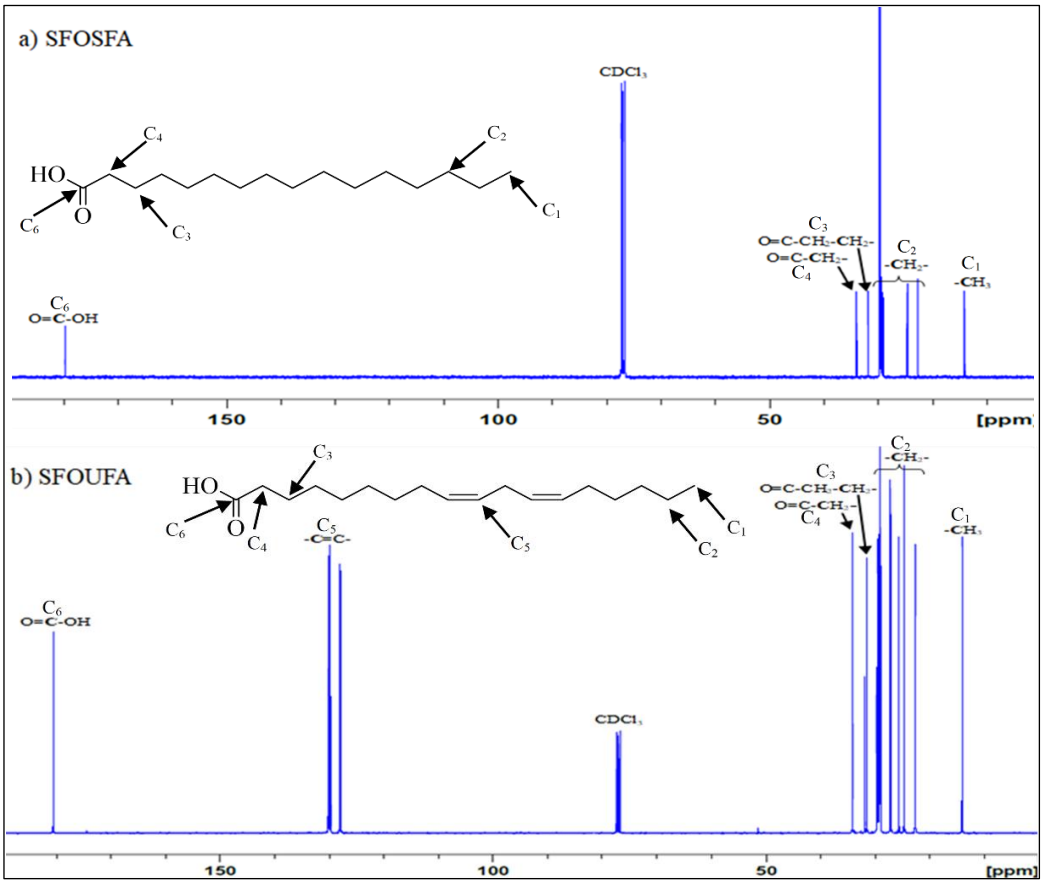


Figure 4.26 ^{13}C NMR of Spectra SFOSFA and SFOUFA

Table 4.24
Type of Carbon and Chemical Shift of SFOSFA and SFOUFA

	Type of carbon	Chemical shift (ppm)		
		SFOSFA	SFOUFA	Theoretical*
C_1	-**C**H_3	14.11	14.03-14.07	8-30
C_2	-**C**H_2-	22.69-29.67	22.39-29.77	15-55
C_3	O=C-CH_2-**C**H_2	31.93	31.36-31.91	15-55
C_4	O=C-**C**H_2	33.99	34.10-34.36	15-55
C_5	-**C**=C-	-	127.90-130.54	100-150
C_6	O=**C**-OH (carboxylic acid)	179.71	180.33	155-185

Source: *Pavia et al. (2015)

4.3.2.4 Iodine Value

The iodine value test was utilized as a measure to assess the level of unsaturation in SFO, SFOFA, SFOUFA and SFOSFA. Figure 4.27 presents the iodine values obtained before (SFO and SFOFA) and after (SFOSFA and SFOUFA) the separation achieved through methanol crystallization. Initially, the iodine value of SFO was found to be 118.01 g I_2/100 g, indicating the degree of unsaturation in the oil. After the hydrolysis process, which yielded SFOFA, the iodine value was 118.69 g I_2/100 g. The separation of SFOFA into SFOSFA and SFOUFA significantly impacted the iodine values. The iodine value of SFOUFA increased to 122.79 g I_2/100 g, demonstrating that this fraction predominantly comprises unsaturated fatty acids. Conversely, the iodine value of SFOSFA dropped drastically to 0.36 g I_2/100 g, signifying the near-complete removal of unsaturated fatty acids from this fraction.

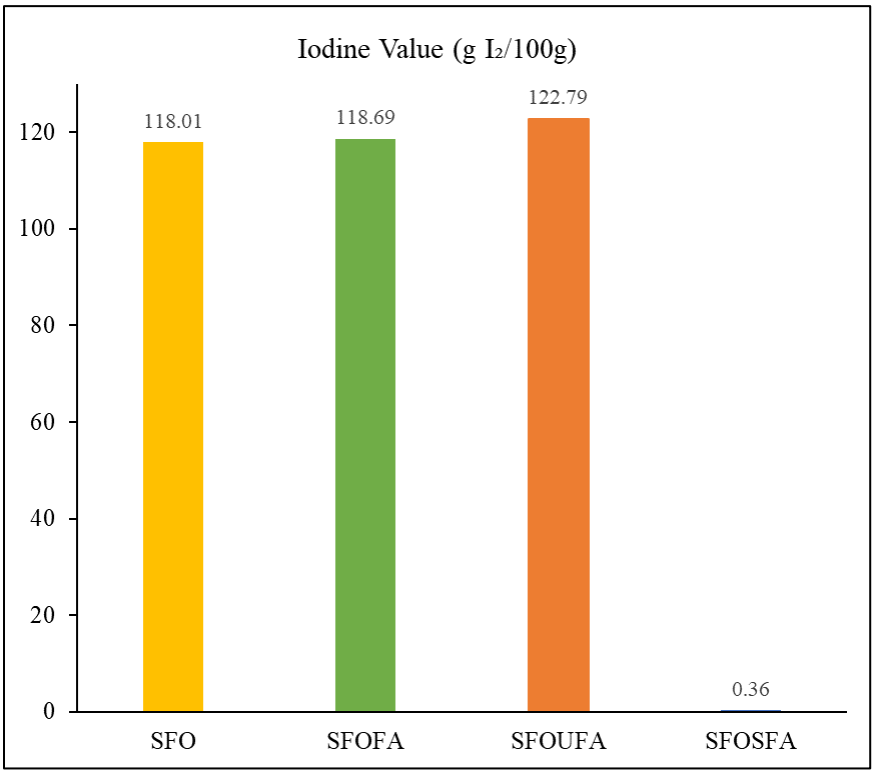


Figure 4.27 Iodine Value Before and After Separation via Methanol Crystallization Method

4.4 Synthesis of Sunflower Oil Unsaturated Fatty Acids Neopentyl Glycol Ester

4.4.1 Esterification of SFOUFA with NPG

The esterification process of SFOUFA with neopentyl glycol (NPG) was carried out to produce sunflower oil unsaturated fatty acids neopentyl glycol ester (SFOUFANPGE). NPG contains two hydroxyl (OH) groups, which react sequentially to form both monoesters and diesters. Figure 4.28 illustrates the esterification reaction scheme between SFOUFA and NPG, while Figure 4.29 presents the mechanism of monoester formation during the esterification of SFOUFA with NPG.

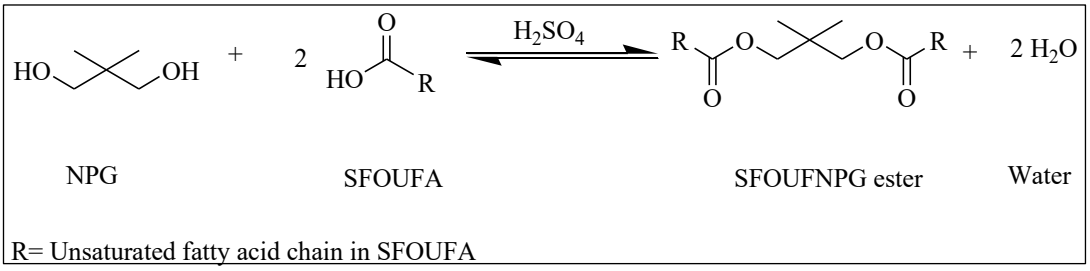


Figure 4.28 Esterification Reaction Scheme of SFOUFA with NPG

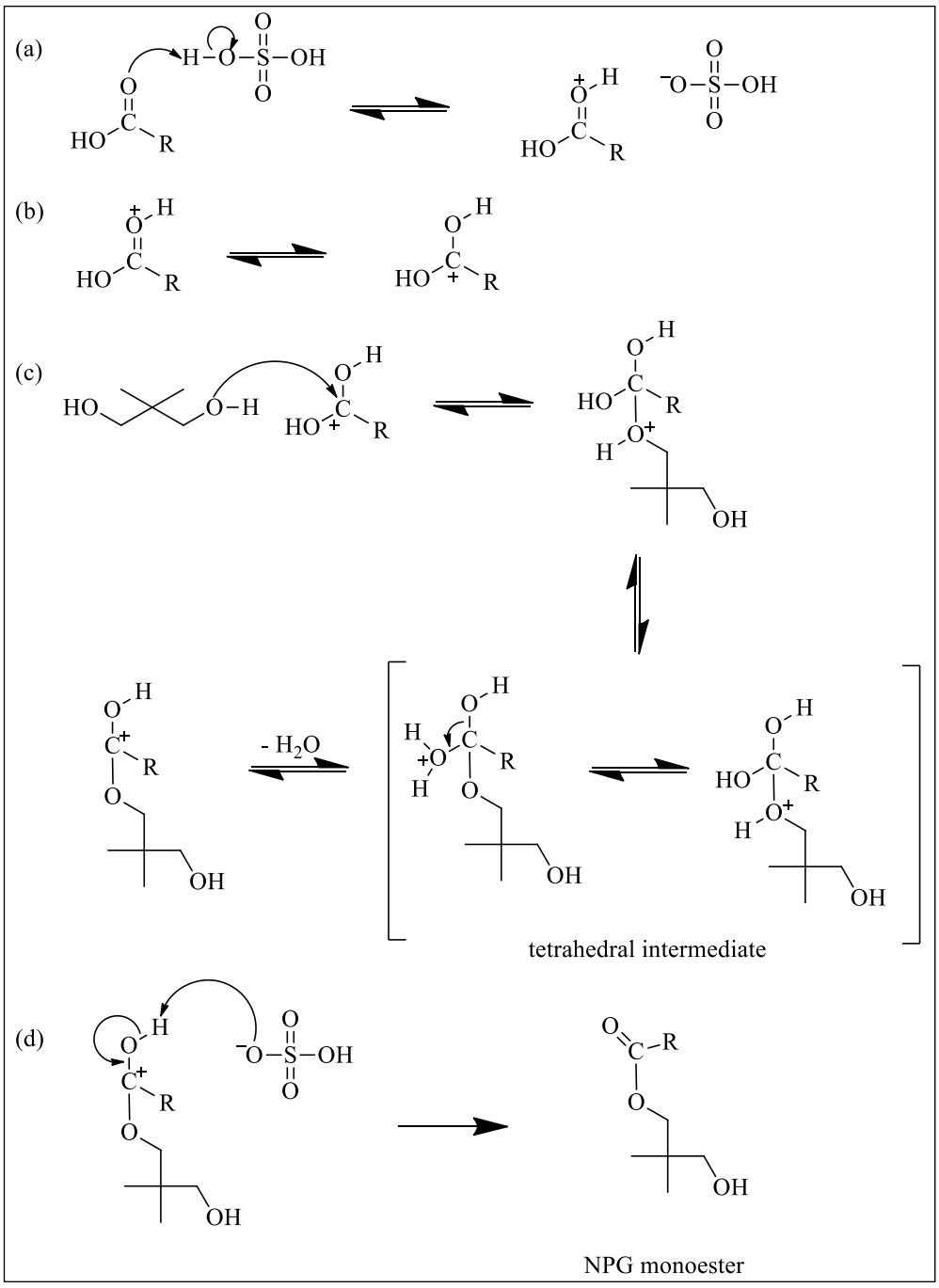


Figure 4.29 Reaction Mechanism Esterification of SFOUFA and NPG for Monoester

4.4.2 Factor Screening Process

Figure 4.30 showed the factor screening for the esterification of SFOUFA with NPG. The factors screened included the molar ratio of SFOUFA to NPG, percentage of catalyst, reaction time and reaction temperature. Based on the percentage yield of SFOUFANPGE, all four factors significantly influenced the esterification process. These factors, molar ratio of SFOUFA (2.0 to 3.5 mole), percentage catalyst (0.5 to 3.0

w/w%), reaction time (2 to 6 h) and reaction temperature (130 to 150 ºC) were used in the optimization process. The range of these factors was displayed in Table 4.25.

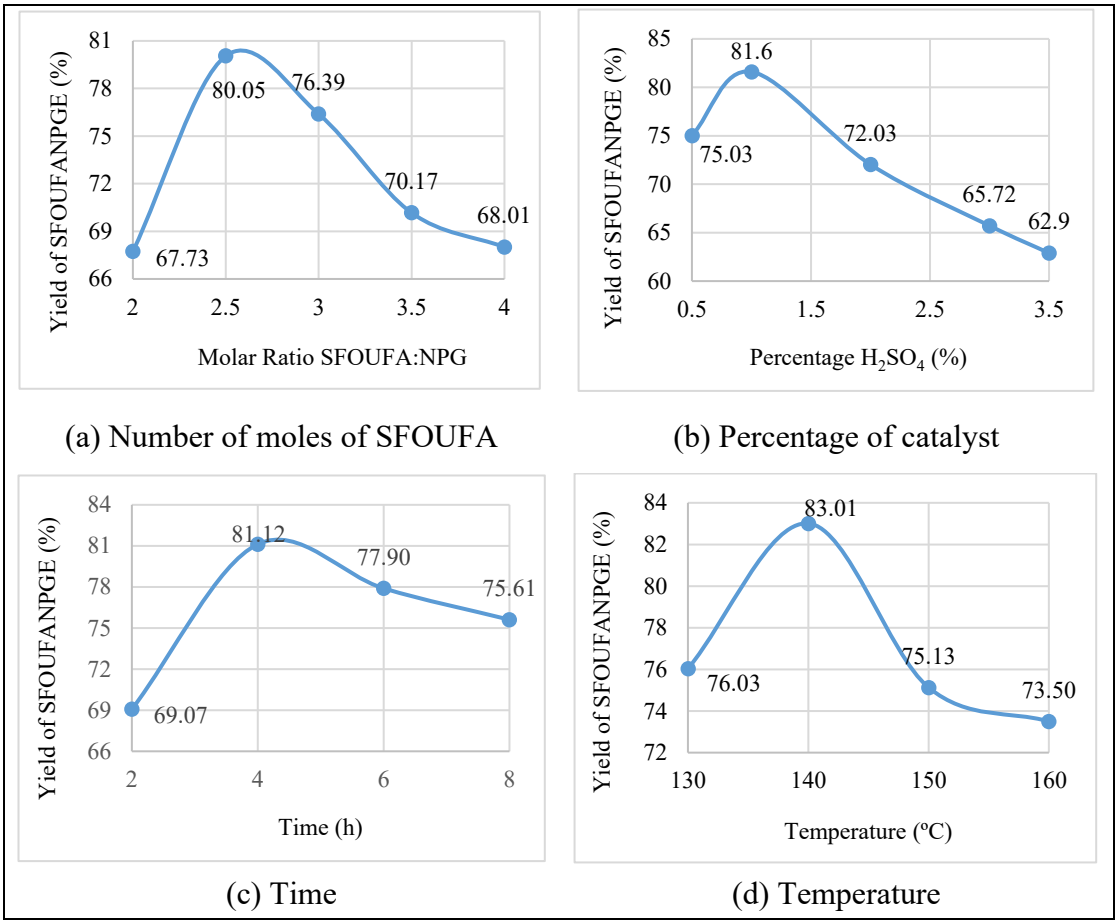


Figure 4.30 The Effect of Factors for Esterification on the Percentage Yield of SFOUFANPGE

Table 4.25
Parameter and Level for D-Optimal Design of Esterification of SFOUFA with NPG

Parameter	Unit	Variable level		
		-1	0	+1
Molar ratio of SFOUFA	mole	2.00	2.75	3.50
Percentage of catalyst	%(w/w)	0.50	1.75	3.00
Time	h	2	4	6
Temperature	°C	130	140	150

4.4.3 Optimization of Esterification of SFOUFA with NPG

The optimization of the esterification process was conducted to examine the effects of various factors, including the molar ratio of SFOUFA to NPG, percentage of

catalyst, temperature and reaction time, on the percentage yield of SFOUFANPGE. A total of 25 experiments were performed to evaluate these factors. Table 4.26 shows the results of the responses, including both the actual values obtained in the experiments and the predicted values.

Table 4.26
Experimental Run, Factors and Response for Percentage Yield of SFOUFANPGE from D-Optimal Design

Run	Factors				Response	
	Molar ratio SFOUFA	Percentage catalyst (%)	Reaction time (h)	Reaction temp. (°C)	Yield (%)	
					Actual	Predicted
1	2.5	2.9	4	130	62.35	63.26
2	2.4	0.5	2	148	72.59	73.10
3	2.6	2.3	2	144	70.0	70.74
4	2.2	0.5	2	130	51.30	50.09
5	2.5	3.0	5	145	69.90	69.59
6	3.5	0.5	5	148	78.56	77.90
7	3.5	2.9	5	130	68.51	67.65
8	2.0	1.7	4	138	77.80	77.05
9	2.9	1.5	4	150	84.09	83.83
10	2.0	3.0	6	130	67.10	67.15
11	2.9	1.7	6	138	79.57	80.89
12	2.5	3.0	5	145	69.70	69.59
13	2.9	1.5	4	150	84.13	83.83
14	2.0	0.5	6	150	76.90	77.35
15	2.4	0.5	5	130	73.67	74.41
16	3.5	3.0	2	130	50.30	50.13
17	2.5	3.0	5	145	69.70	69.59
18	2.0	1.7	4	138	76.30	77.05
19	3.5	1.1	2	131	52.48	53.20
20	3.5	1.8	5	140	79.60	80.46
21	2.0	2.2	6	150	71.0	70.57
22	2.0	3.0	4	150	64.10	64.07
23	3.5	2.9	2	148	75.90	75.25
24	2.9	1.7	6	138	83.19	80.89
25	3.5	3.0	6	150	67.10	68.18

4.4.3.1 Determination of Selected Model

The analysis model were determined based on several analyses, including sequential model sum of squares (Table 4.27), lack of fit tests (Table 4.28), model summary statistics (Table 4.29). The model selection was based on the highest order polynomial where all additional terms are significant and the model was non-aliased. The analysis of sequential model sum of squares revealed that the suitable model to explain the study's variables for the responses was the quadratic model, based on the *F*-value and *p*-value. For the percentage yield of SFOUFANPGE, the *F*-value was 52.95 and the *p*-value was < 0.0001. Table 4.27 shows the sequential model sum of square for percentage yield of SFOUFANPGE. The analysis of sequential model sum of squares for the percentage yield of SFOUFANPGE indicated significance in the quadratic model, with the highest *F*-value and the lowest *p*-value, suggesting the suitability of the model.

Table 4.27
Sequential Model Sum of Squares of Percentage Yield of SFOUFANPGE

Source	Sum of Squares	dF	Mean Square	*F*-value	*p*-value model	
Mean vs Total	126100	1	1.26100			
Linear vs Mean	1070.30	4	267.58	4.89	0.0065	
2FI vs Linear	727.44	6	121.24	4.64	0.0085	
Quadratic vs 2FI	349.64	4	87.41	52.95	< 0.0001	Suggested
Cubic vs Quadratic	8.80	5	1.76	1.14	0.4436	Aliased
Residual	7.70	5	1.54			
Total	128300	25	5132.33			

For the lack of fit for percentage yield of SFOUFAPEE, it shows that it was not significant where the *p*-value was more than 0.05. The *F*-value was 1.14, while the *p*-value was 0.4436. The lack of fit analysis test indicated that the quadratic model was suitable for response based on the non-significant *p*-values of the model. Table 4.28 shows the lack of fit tests for the percentage yield of SFOUFANPGE.

Table 4.28
Lack of Fit Test for Percentage Yield of SFOUFANPGE

Source	Sum of Squares	dF	Mean Square	*F*-value	*p*-value model	
Linear	1085.88	15	72.39	46.98	0.0002	
2FI	358.44	9	39.83	25.85	0.0011	
Quadratic	8.80	5	1.76	1.14	0.4436	Suggested
Cubic	0.0000	0				Aliased
Pure error	7.70	5	1.54			

The model summary statistics for the percentage yield of SFOUFANPGE show satisfactory R^2 values for the quadratic model, as they approach 1. The error was the model can be determined based on the standard deviation values. A low standard deviation value indicates a good model and this value was related to the R^2 and adjusted R^2 values. The standard deviation for the percentage yield of SFOUFANPGE was 1.28. The R^2 value for the percentage yield of SFOUFANPGE was 0.9924 and the adjusted R^2 was 0.9817. The analysis of the model summary statistics for the response shows the smallest value, indicating the selection of the quadratic model. The PRESS for the percentage yield of SFOUFANPGE was 170.20. Table 4.29 shows the model summary statistic for percentage yield of SFOUFANPGE.

Table 4.29
Summary Statistic for Percentage Yield of SFOUFANPGE

Source	Standard deviation	R^2	Adjusted R^2	Predicted R^2	PRESS	
Linear	7.39	0.4946	0.3935	0.1594	1818.98	
2FI	5.11	0.8308	0.7099	0.0489	2058.12	
Quadratic	1.28	0.9924	0.9817	0.9213	170.20	Suggested
Cubic	1.24	0.9964	0.9829			Aliased

4.4.3.2 Identification of Model Accuracy

Several analysis plots, such as the normal probability plot of residuals (Figure 4.31) residual versus predicted plot (Figure 4.32), actual versus predicted (Figure 4.33), residual versus run number plot (Figure 4.34), Cook's Distance plot (Figure 4.35) and Box-Cox plot (Figure 4.36) were used to determine the accuracy of the model. The normal probability plot (Figure 4.31) shows that the residuals were scattered randomly along the straight regression line for the percentage yield of SFOUFANPGE which

shows that the residuals follow a normal distribution, supporting the accuracy of the model. Based on residual versus predicted plot (Figure 4.32), all the test points fall within the defined range of 4.29681 to -4.29681. This indicates that the chosen model was appropriate because all the data points were within the specified range. From the Figure 4.35 for Cook's distance, all points are located below the threshold line of 1 and most points are below 0.2 that indicates the model was accurate in predicting the response variable. The Box-Cox plot (Figure 4.36) gives the best value of lamda which is 1.27 and there was no transformation that proposed for this optimization study.

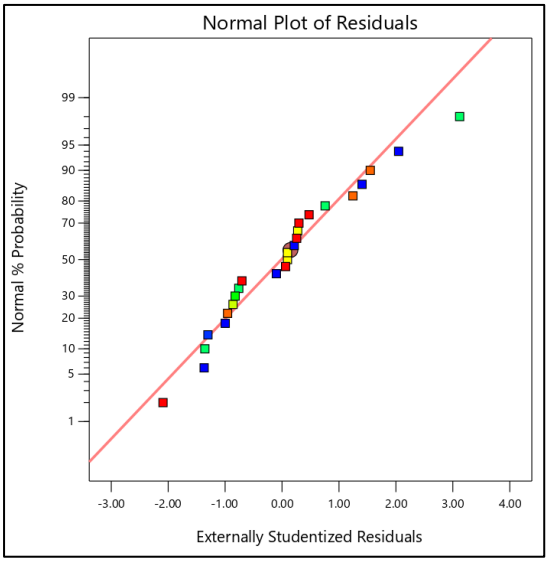


Figure 4.31 Normal Plot of Residual for Percentage Yield of SFOUFANPGE

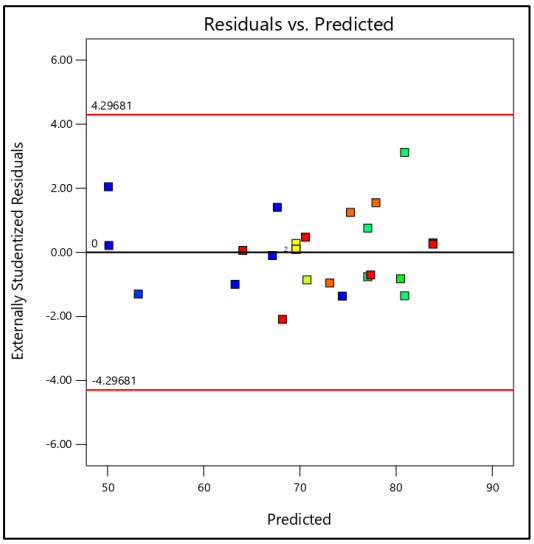


Figure 4.32 Residual versus Predicted Plot for Percentage Yield of SFOUFANPGE

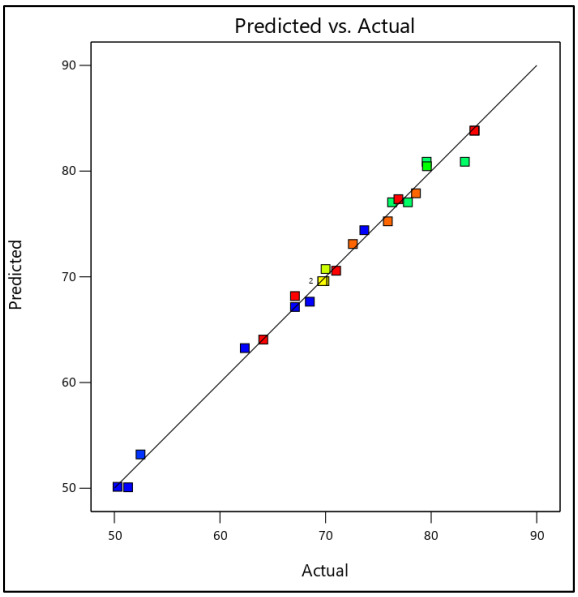


Figure 4.33 Actual versus Predicted for Percentage Yield of SFOUFANPGE

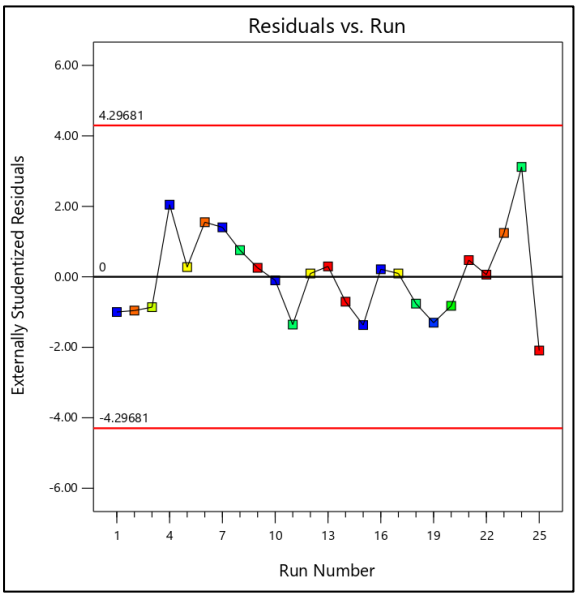


Figure 4.34 Residual versus Run Number for Percentage Yield of SFOUFANPGE

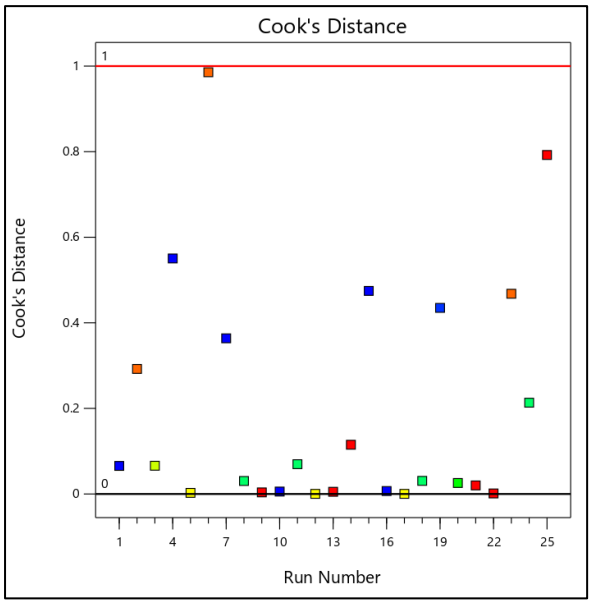


Figure 4.35 Cook's Distance Plot for Percentage Yield of SFOUFANPGE

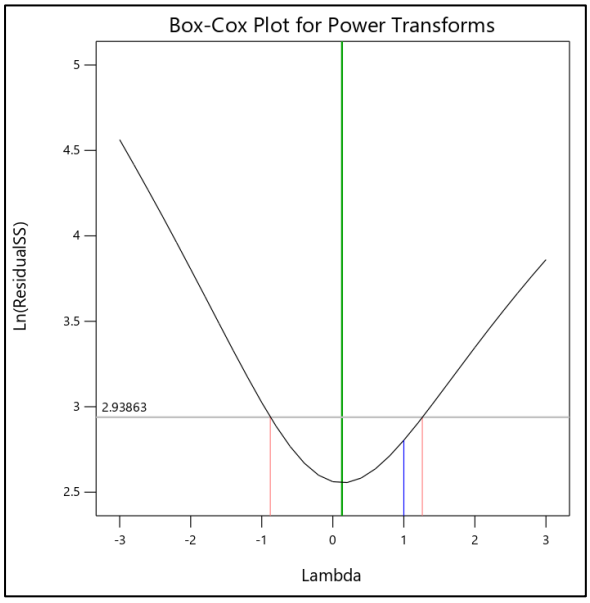


Figure 4.36 Box-Cox Plot for Percentage Yield of SFOUFANPGE

4.4.3.3 Analysis of Variance

The analysis of ANOVA for the percentage yield of SFOUFANPGE has been summarized in Table 4.30. The *p*-value of the percentage yield of SFOUFANPGE was less than 0.0001 and the *p*-value for the lack of fit was more than 0.05. The R^2 value for the percentages yield of SFOUFANPGE was 0.9924.

Table 4.30
Summary of ANOVA Analysis for Percentage Yield of SFOUFANPGE

Source	Percentage yield of SFOUFANPGE
p-value model	< 0.0001
F-value model	92.91
p-value Lack of Fit	0.4436
F-value Lack of Fit	1.14
R^2	0.9924
Adjusted R^2	0.9817
Predicted R^2	0.9213
Standard deviation	1.28
Coefficient of variation (C.V %)	1.81
Adequate precision	33.8995

For the ANOVA for percentage yield of SFOUFAPEE shows all model terms and factors were significant ($p < 0.05$). Table 4.31 shows ANOVA analysis factor for percentage yield of SFOUFANPGE. This further reinforces the screening results, which indicate that all linear terms for the percentage yield of SFOUFANPGE were significant. The regression equations for percentage yield of SFOUFANPGE were shown below:

$$\text{Yield (\%)} = 80.06 + 1.05A - 3.33B + 5.60C + 5.72D + 3.08AB - 1.77AC + 2.13AD - 1.36BC - 1.30BD - 6.25CD - 1.36A^2 - 6.39B^2 - 4.62C^2 - 3.07D^2$$

Table 4.31
ANOVA Analysis Factors for Percentage Yield of SFOUFANPGE

Source	Sum of Squares	dF	Mean Square	*F*-value	*p*-value model	Significance
A-molar ratio SFOUFA	11.11	1	11.11	6.73	0.0268	Significant
B-catalyst	113.30	1	113.30	68.63	< 0.0001	Significant
C-time	349.33	1	349.33	211.60	< 0.0001	Significant
D-temperature	438.03	1	438.03	265.32	< 0.0001	Significant
AB	56.67	1	56.67	34.32	0.0002	Significant
AC	11.23	1	11.23	6.80	0.0261	Significant
AD	33.90	1	33.90	20.54	0.0011	Significant
BC	8.51	1	8.51	5.16	0.0465	Significant
BD	15.25	1	15.25	9.24	0.0125	Significant
CD	243.97	1	243.97	147.78	< 0.0001	Significant
A^2	7.34	1	7.34	4.44	0.0612	Not Significant
B^2	142.04	1	142.04	86.03	< 0.0001	Significant
C^2	65.45	1	65.45	39.64	< 0.0001	Significant
D^2	23.50	1	23.50	14.23	0.0036	Significant

4.4.3.4 Interaction Between Variables

The interaction between variable, molar ratio, percentage of catalyst, time and temperature can be illustrated through a 3-dimentional (3D) response surface plot. Figure 4.39 shows the 3D response surface for the interaction between variables and response.

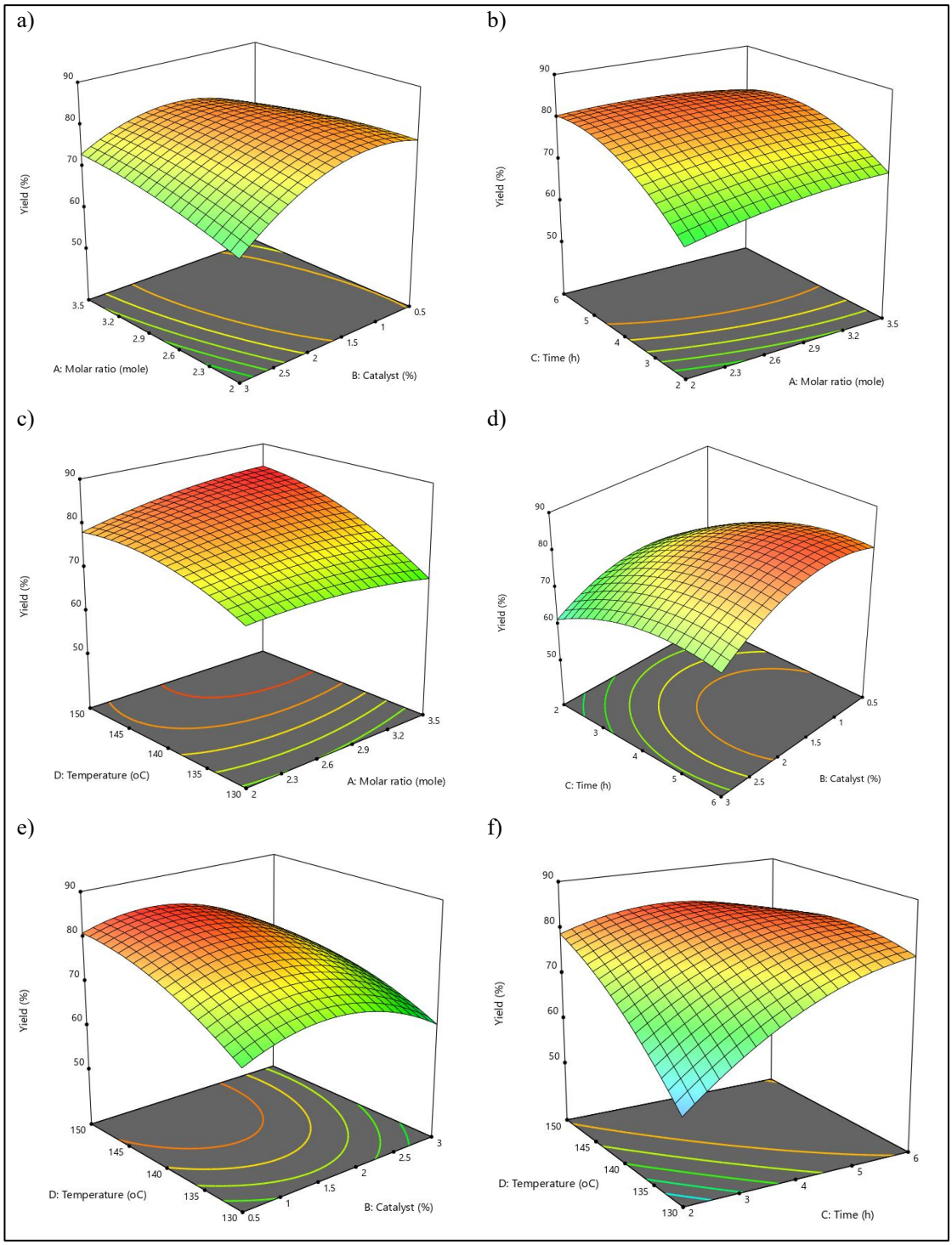


Figure 4.37 3D Surface Plot for a) AB, b) AC, c) AD, d) BC, e) BD and f) CD for Percentage Yield of SFOUFANPGE

Figure 4.37 (a) illustrates the interaction between the SFOUFA:NPG molar ratio and percentage of catalyst on the yield of SFOUFANPGE. An increase in the SFOUFA:NPG ratio from 2.0 to 3.5 resulted in a corresponding increase in ester yield. Similarly, increasing the percentage of catalyst from 0.5% to 1.5% enhanced the yield. However, a further increase in percentage of catalyst beyond 1.5% up to 3.0% led to a

decline in the percentage yield of SFOUFANPGE. Figure 4.37 (b) shows the interaction between the ratio of SFOUFA:NPG and time (AC). The higher the SFOUFA:NPG ratio, the higher the percentage yield of SFOUFANPGE. Similarly, increasing the reaction time from 2 to 6 hours results in an increase in the percentage yield of SFOUFANPGE.

Figure 4.37 (c) shows illustrates the interaction between the SFOUFA: NPG molar ratio and reaction temperature on the yield of SFOUFANPGE. An increase in the SFOUFA:NPG ratio led to a decrease in percentage yield, whereas raising the reaction temperature from 130 to 150 °C resulted in an increase in the yield of SFOUFANPGE. Figure 4.37 (d) shows the interaction between the percentage of catalyst and reaction time (BC). Increasing the catalyst from 0.5 to 1.5 and extending the time from 2 to 4 hours results in an increase in the percentage yield of SFOUFAPEE. However, an increase in the percentage of catalyst from 1.5 to 3.0, coupled with an extension of time from 4 to 6 hours, leads to a decrease in the percentage yield of SFOUFANPGE.

In Figure 4.37 (e), the interaction between the percentage of catalyst and temperature (BD) are shown. It reveals that an increase in the catalyst up to 3% causes a decrease in the percentage yield of SFOUFANPGE. Conversely, increasing the temperature from 130 to 150 °C results in an increase in the percentage yield of SFOUFANPGE. Figure 4.37 (f) shows the interaction between reaction time and temperature on the yield of SFOUFANPGE. Both factors show a positive effect on yield, where extending the reaction time up to 6 hours and increasing the temperature from 130 °C to 150 °C resulted in a progressive increase in the percentage yield of SFOUFANPGE.

An increase in the SFOUFA:NPG molar ratio enhances the availability of SFOUFA, thereby promoting its reactivity with NPG. In contrast, lower molar ratios may lead to incomplete esterification, leaving residual unreacted polyhydric alcohol, which ultimately results in a reduced yield of SFOUFANPGE.

In addition, increasing the percentage of catalyst from 1% to 3% causes a decline in the ester yield. This behavior was attributed to the hygroscopic and dehydrating nature of sulfuric acid, which leads to water absorption from the environment. Excess catalyst increases the water content in the system, potentially shifting the reaction equilibrium towards hydrolysis, thereby reducing ester formation.

Reaction time also plays a vital role in determining the percentage yield of SFOUFANPGE. Yield increases with prolonged reaction time; however, beyond 4 to 6 hours, a decrease was observed. This decline may result from hydrolysis of the ester

bond, where prolonged exposure to heat and moisture leads to cleavage of the ester linkage, reverting the product back to its original reactants.

Furthermore, raising the reaction temperature from 130 to 150 °C significantly enhances the yield of SFOUFANPGE. The elevated temperature increases the reaction kinetics, thereby accelerating the esterification process and promoting higher production of the diester.

4.4.3.5 Verification Model

The optimal conditions for the esterification of SFOUFA with NPG was conducted through numerical optimization. The parameters A, B, C and D were set within a specific range to achieve the highest percentage yield of SFOUFANPGE as shown in Table 4.32 that provides a summary of the applied constraints to determine the optimum condition, aiming for higher percentage yield of SFOUFANPGE. The parameters A, B, C and D were set in range while the response, percentage yield of SFOUFANPGE was set to the maximum values. The desirability of the predicted model was equal to 1.00, indicating that the model provides the ideal value. Figure 4.38 illustrates the predicted outcomes obtained from the numerical optimization model for the esterification reaction.

Table 4.32
Restraints for Optimization of Esterification of SFOUFA with NPG Parameter and Response for D-Optimal Design

Parameter and responses	Goal	Lower limit	Upper limit	Weight	Importance
A: Molar ratio of SFOUFA	in range	2.0	3.5	1	3
B: Catalyst	in range	0.5	3.0	1	3
C: Time	in range	2	6	1	3
D: Temperature	in range	130	150	1	3
Yield of SFOUFANPGE	maximize	50.30	84.13	1	3

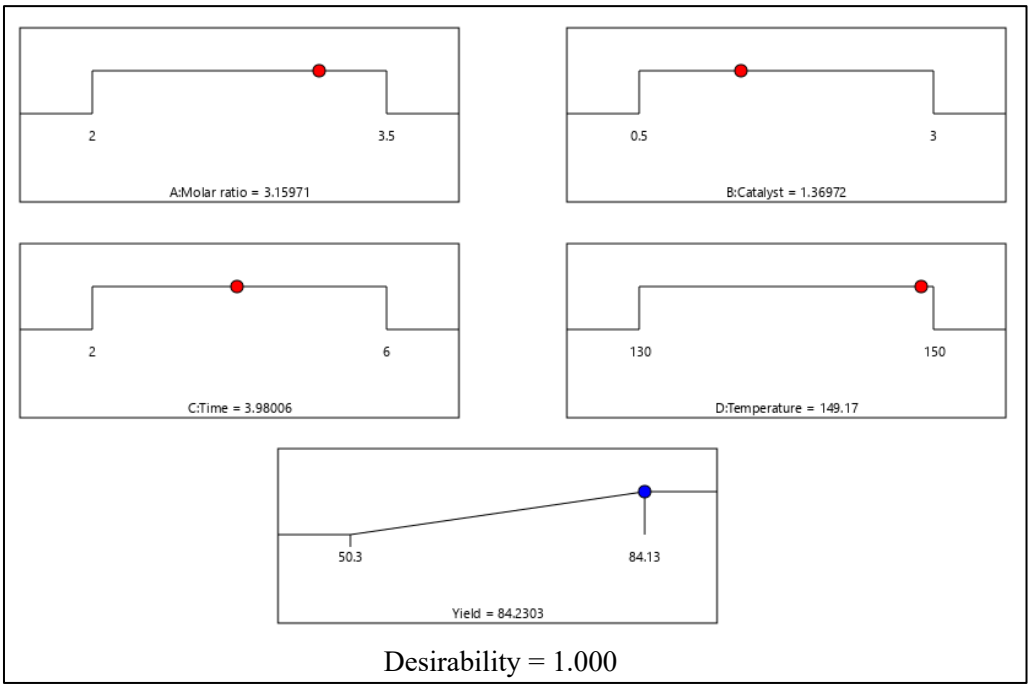


Figure 4.38 D-Optimal Predicted Model at Optimum Condition for Esterification of SFOUFA with NPG

The accuracy of the model generated through D-optimal design was verified by conducting the esterification reaction using three randomly chosen sets of reaction conditions. The actual and predicted values were compared by calculating the RSE for each experiment. Only those experiments with RSE values below 5% were considered acceptable. The results presented in Table 4.33 demonstrate that all RSE values were less than 5%, indicating the model's suitability.

Table 4.33
Actual and Predicted Data for Verification Model for Percentage Yield of SFOUFANPGE

Molar ratio	Catalyst (%)	Reaction time (h)	Reaction temperature (°C)	Yield SFOUFANPGE (%)		
				Actual	Predicted	RSE
2.5	1.0	2.5	140	73.51	72.32	1.65
3.0	2.5	3.0	130	60.15	61.47	2.15
2.9	3.0	3.5	140	48.60	49.47	1.76

4.4.3.6 Optimum Condition of Esterification Reaction

The D-optimal design successfully provided the predicted optimal conditions for the esterification of SFOUFA and NPG. The optimal conditions include a 3.2 for

molar ratio SFOUFA with NPG, 1.37 % for percentage catalyst, a reaction time of 4 hours and a reaction temperature of 149 °C. Using these conditions, percentage yield of SFOFUNPGE ester of 83.75% was obtained. Table 4.34 presents both the actual and predicted data for the optimum condition. The validation of the optimum condition was performed by calculating the RSE, which confirmed that the values below 5% for percentage yield of SFOUFANPGE. Figure 4.39 shows the esterification product which sunflower oil unsaturated fatty acids neopentyl glycol ester (SFOUFANPGE).

Table 4.34
Actual and Predicted Data for Optimum Condition for Percentage Yield of SFOUFANPGE

Molar ratio	Catalyst (%)	Reaction time (h)	Reaction temperature (°C)	Yield SFOUFANPGE (%)		
				Actual	Predicted	RSE
3.2	1.37	4	149	83.75	84.23	0.57



Figure 4.39 Sunflower Oil Unsaturated Fatty Acids Neopentyl Glycol Ester (SFOUFANPGE)

4.4.4 Characterization of SFOUFANPGE

4.4.4.1 Gas Chromatography

The ester composition of SFOUFANPGE was analyzed using GC-FID equipped with a high-temperature column (DB-5HT) by comparison with a reference standard. Due to the unavailability of a specific standard for SFOUFANPGE, a commercial dioleate neopentyl glycol ester was used as the reference standard. In the synthesis of SFOUFANPGE, monoester was initially formed as an intermediate before further esterification produces the diester. Based on the reference standard, the retention time

for the diester was identified in the range of 28 to 36 minutes and was used as a reference region for the identification of diester in the sample. The chromatogram of SFOUFANPGE (Figure 4.40) showed a dominant peak within the retention time range of 30 to 35 minutes, with no observable peaks corresponding to monoester or unreacted fatty acids. This indicates that the esterification of SFOUFA with NPG successfully produced 100% diester. The result shows that all hydroxyl (OH) groups of NPG were fully esterified with SFOUFA, confirming the completion of the esterification reaction.

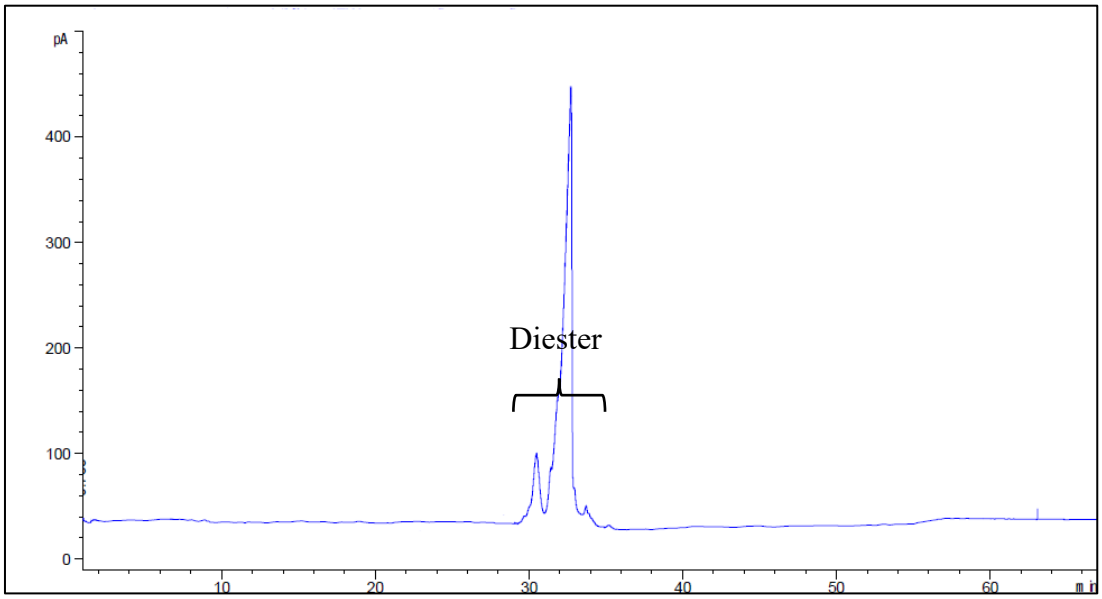


Figure 4.40 GC-FID Chromatogram of Ester Composition in SFOUFANPGE

4.4.4.2 Fourier Transform Infrared Spectroscopy

The FTIR analysis confirms the successful esterification of SFOUFA with NPG to produce SFOUFANPGE. Before esterification, characteristic peaks of carboxylic acid groups were observed, including the C=O stretch at 1708.15 cm^{-1}, C-O stretches at 1248.00 and 1290.14 cm^{-1} and a O-H stretch between 2400-3400 cm^{-1}. After esterification, these carboxylic acid peaks disappear and new peaks associated with esters emerge, such as the C=O stretch at 1740.51 cm^{-1} and C-O stretches at 1160.56 cm^{-1} and 1239.03 cm^{-1}. This shift in the functional groups, from carboxylic acids to esters, confirms the successful conversion of unsaturated fatty acids into esters. Figure 4.41 shows the FTIR spectra of SFOUFA and SFOUFANPGE while Table 4.35 shows the functional group and wavenumber for FTIR spectra of SFOUFA and SFOUFANPGE.

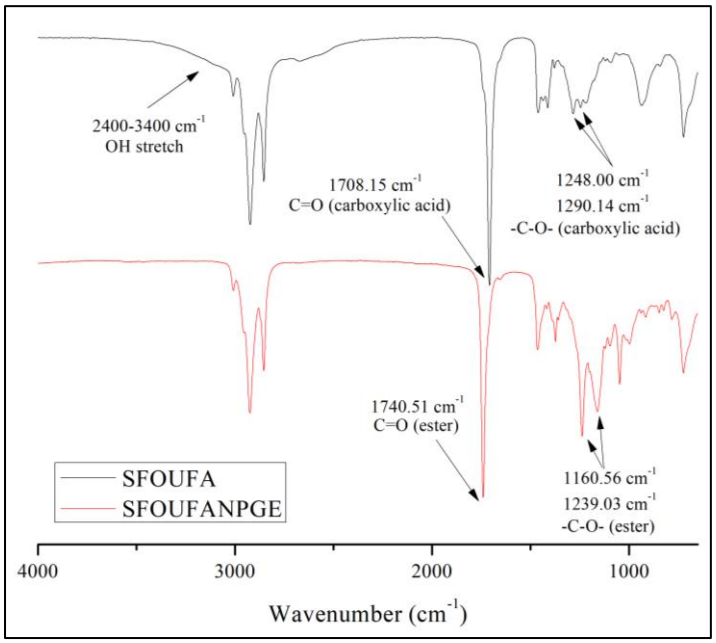


Figure 4.41 FTIR Spectra of SFOUFA and SFOUFANPGE

Table 4.35
Functional Group and Wavenumber for FTIR Spectra of SFOUFA and SFOUFANPGE

Functional group	Wavenumber (cm^{-1})	
	SFOUFA	SFOUFANPGE
OH stretching (carboxylic acid)	2400-3400	-
C=C bending vibration (aliphatic)	3008.11	3008.26
C-H stretching vibration (aliphatic)	2923.82 and 2854.19	2923.27 and 2854.51
C=O stretching vibration (ester)	-	1740.51
C=O stretching vibration (carboxylic acid)	1708.15	-
-C-O stretching vibration (ester)	-	1239.03 and 1160.56
-C-O stretching vibration (carboxylic acid)	1290.14 and 1248.00	-

4.4.4.3 Nuclear Magnetic Resonance

^{1}H and ^{13}C NMR spectroscopy were employed to confirm the formation of ester products in the esterification reaction. In the ^{1}H-NMR spectrum of SFOUFANPGE (Figure 4.42), characteristic peaks were observed at specific chemical shifts, indicating the presence of various proton environments. These included peaks at 0.86 to 0.90 ppm for -C**H**$_3$, 1.23 to 1.37 ppm for -C**H**$_2$-, 1.58 to 1.62 ppm for O=C-CH$_2$-C**H**$_2$-, 2.00 to 2.07 ppm for -CH=CH-C**H**$_2$-, 2.28 to 2.32 ppm for O=C-C**H**$_2$-, 2.75 to 2.78 ppm for =CH-C**H**$_2$-CH=, 5.32 to 5.38 ppm for -CH=CH- and 7.28 ppm for $CDCl_3$ (solvent). The appearance of a peak at 4.00 to 4.14 ppm (C**H**$_2$-O) confirmed the presence of neopentyl

glycol in the SFOUFANPGE mixture. Notably, the absence of a peak in the chemical shift range of 10 to 12 ppm indicated the successful conversion of SFOUFA to SFOUFANPGE, as the -O**H** group from SFOUFA was no longer present. Table 4.36 shows the chemical shift for ^{1}H NMR spectra for SFOUFA and SFOUFANPGE.

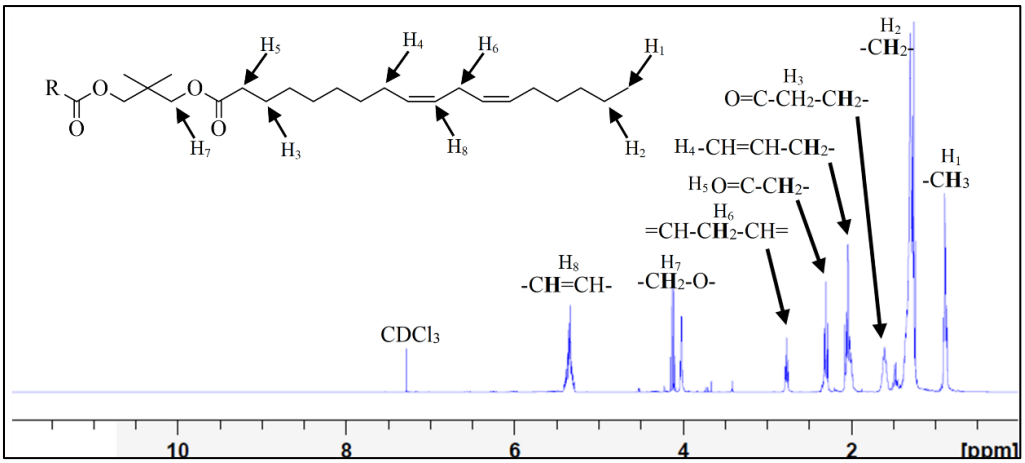


Figure 4.42 ^{1}H NMR Spectrum for SFOUFANPGE

Table 4.36
Type of Proton and Chemical Shift of SFOUFA and SFOUFANPGE

	Type of proton	Chemical shift (ppm)		
		SFOUFA	SFOUFANPGE	Theoretical*
H_1	-C**H**$_3$	0.89-0.93	0.86-0.90	0.70-1.3
H_2	-C**H**$_2$-	1.28-1.39	1.23-1.37	1.2-1.4
H_3	O=C-CH$_2$-C**H**$_2$-	1.62-1.67	1.58-1.62	1.5-2.0
H_4	-CH=CH-C**H**$_2$-	2.03-2.10	2.00-2.07	1.6-2.6
H_5	O=C-C**H**$_2$-	2.34-2.38	2.27-2.32	2.1-2.5
H_6	=CH-C**H**$_2$-CH=	2.78-2.81	2.75-2.78	2.5-3.0
H_7	-C**H**$_2$-O- (neopentyl glycol)	-	4.00-4.14	4.0-4.5
H_8	-CH=C**H**-	5.33-5.41	5.32-5.38	4.5-6.5
-	COO**H**	11.55	-	10-12

Source: *Pavia et al. (2015)

In the ^{13}C-NMR spectrum of SFOUFANPGE (Figure 4.43), carbon peaks appeared at specific chemical shifts, revealing different carbon environments. These included peaks at 8.12 ppm (from NPG) and 14.04 to 14.16 ppm for -**C**H$_3$, 22.50 to 31.89 ppm for -**C**H$_2$-, 33.80 to 34.24 ppm for O=C-**C**H$_2$-, 40.59 ppm for -**C**- (from NPG), 63.68 ppm for C**H**$_2$-O (from NPG), 77.06 to 77.38 ppm for CDCl$_3$ (solvent) and

127.66 to 130.17 ppm for -**C**H=CH-. The observation of the peak corresponding to the carboxylic acid carbonyl group (**C**=O) at 180.33 ppm shifting to 173.45 ppm in the upfield region confirmed the successful conversion of SFOUFA to the SFOUFANPGE. The carboxylic acid carbonyl appears at a more downfield chemical shift because the adjacent hydroxyl (-OH) group causes greater deshielding. After esterification, the hydroxyl group is replaced by an alkoxy (-OR) group, resulting in less deshielding and causing the carbonyl carbon to shift upfield, which is consistent with the characteristic chemical shift ranges reported by Pavia et al. (2015). Table 4.37 shows the chemical shift for ^{13}C NMR spectra for SFOUFA and SFOUFANPGE.

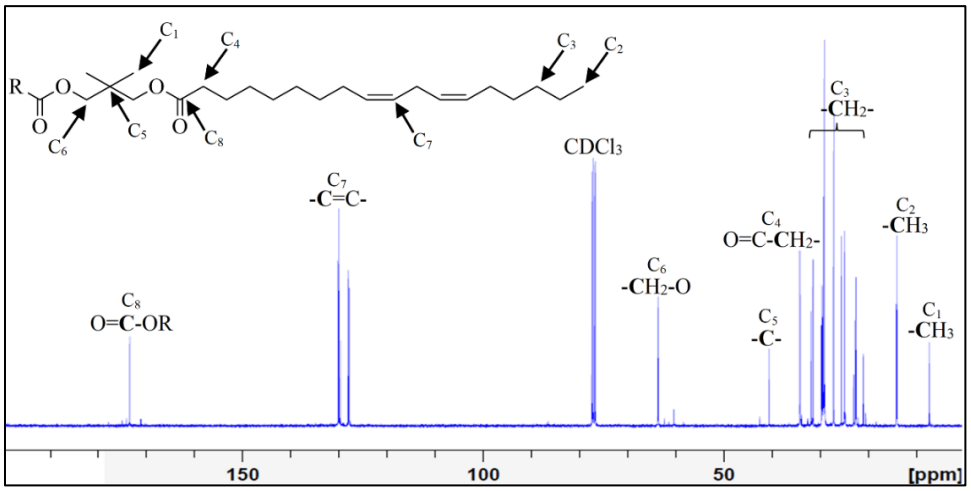


Figure 4.43 ^{13}C NMR Spectrum for SFOUFANPGE

Table 4.37
Type of Carbon and Chemical Shift for SFOUFA and SFOUFANPGE

	Type of carbon	Chemical shift (ppm)		
		SFOUFA	SFOUFANPGE	Theoretical*
C_1	-**C**H$_3$ (neopentyl glycol)	-	8.12	8-30
C_2	-**C**H$_3$	14.03-14.07	14.04-14.16	8-30
C_3	-**C**H$_2$-	22.39-29.77	22.50-31.89	15-55
C_4	O=C-**C**H$_2$	34.10-34.36	33.80-34.24	15-55
C_5	-**C**- (neopentyl glycol)	-	40.59	20-60
C_6	-**C**H$_2$-O- (neopentyl glycol)	-	63.68	40-80
C_7	-**C**=C-	127.90-130.54	127.66-130.17	100-150
-	O=**C**-OH (carboxylic acid)	180.33	-	155-185
C_8	O=**C**-OR (ester)	-	173.45	155-185

Source: *Pavia et al. (2015)

4.4.5 Physicochemical Properties of SFOUFANPGE

The physicochemical properties of SFOUFANPGE were evaluated based on pour point, flash point, kinematic viscosity, viscosity index, oxidative stability and rheology. The physicochemical properties of SFOUFANPGE were compared with NPG ester (NPGE derived from different plant oil, which were palm cooking oil (NPGE A), soybean oil (NPGE B) and palm oil (NPGE C)), as shown in Table 4.38.

Table 4.38
Physicochemical Properties of SFOUFANPGE and Others NPGE

Physicochemical properties	SFOUFANPGE	NPGE A	NPGE B	NPGE C
Pour point (°C)	-15	10	-3	7
Flash point (°C)	268.0	174.2	N/A	245.0
Viscosity at 40°C (cSt)	21.24	7.40	10.50	50.10
Viscosity at 100°C (cSt)	5.35	2.50	3.20	15.20
Viscosity Index	174.5	183.3	198.0	190.0
Oxidative stability (min)	22.4	N/A	24.0	N/A
Rheology	Newtonian	N/A	N/A	Newtonian

Source: NPGE A: Hambali and Raof (2026); NPGE B: Aguieiras et al. (2020); NPGE C: Nor et al. (2022b)

From this study, the pour point of SFOUFANPGE (-15 °C) was significantly lower than NPGE A (10 °C) and NPGE C (7 °C) and slightly lower than NPGE B (-3 °C), indicating better low-temperature fluidity. This lower pour point may be attributed to the higher unsaturated fatty acid content in the SFOUFANPGE, which reduces molecular packing and improves flow properties at low temperatures.

In terms of flash point, SFOUFANPGE exhibited a much higher value (268 °C) compared to NPGE A (174.2 °C) and NPGE C (245 °C), indicating better thermal stability and lower volatility. This difference was mainly attributed to variations in fatty acid chain length and degree of unsaturation in the feedstock oil. For the kinematic viscosity, SFOUFANPGE showed moderate viscosity values of 21.24 cSt at 40 °C and 5.35 cSt at 100 °C, which were higher than NPGE A and NPGE B but lower than NPGE C. This suggests that the viscosity of the ester was influenced by the fatty acids composition of the feedstock oil.

The viscosity index of SFOUFANPGE (174.5) was slightly lower than NPGE A, NPGE B and NPGE C but still indicates good viscosity to temperature behaviour. In addition, SFOUFANPGE showed oxidative stability of 22.4 minutes, which is comparable to NPGE B (24.0 minutes) and exhibited Newtonian rheological behaviour similar to NPGE C. However, the oxidative stability of SFOUFANPGE was relatively lower due to the use of sunflower oil unsaturated fatty acids as the starting material. The high content of unsaturated fatty acids containing multiple double bonds increases the susceptibility of the ester to oxidation. Overall, the results demonstrate that SFOUFANPGE possesses comparable physicochemical properties relative to NPGE derived from other plant oil sources.

4.5 Synthesis of Sunflower Oil Unsaturated Fatty Acids Trimethylolpropane Ester

4.5.1 Esterification of SFOUFA with TMP

The production of sunflower oil unsaturated fatty acids trimethylolpropane ester (SFOUFATMPE) were carried out via esterification process of SFOUFA with trimethylolpropane (TMP). TMP contains three hydroxyl (OH) groups, which react sequentially to form monoesters, diesters and triesters. Figure 4.44 illustrates the esterification reaction scheme between SFOUFA and TMP, while Figure 4.45 presents the mechanism of monoester formation during the esterification of SFOUFA with TMP.

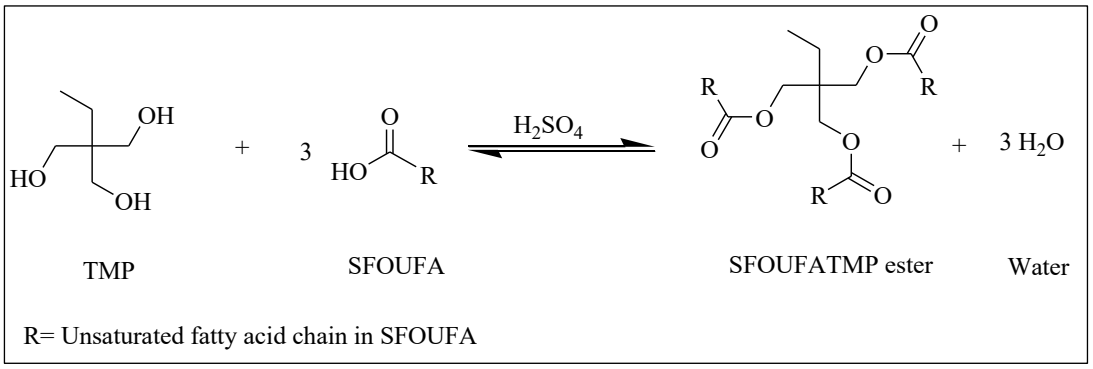


Figure 4.44 Esterification Reaction Scheme of SFOUFA and TMP

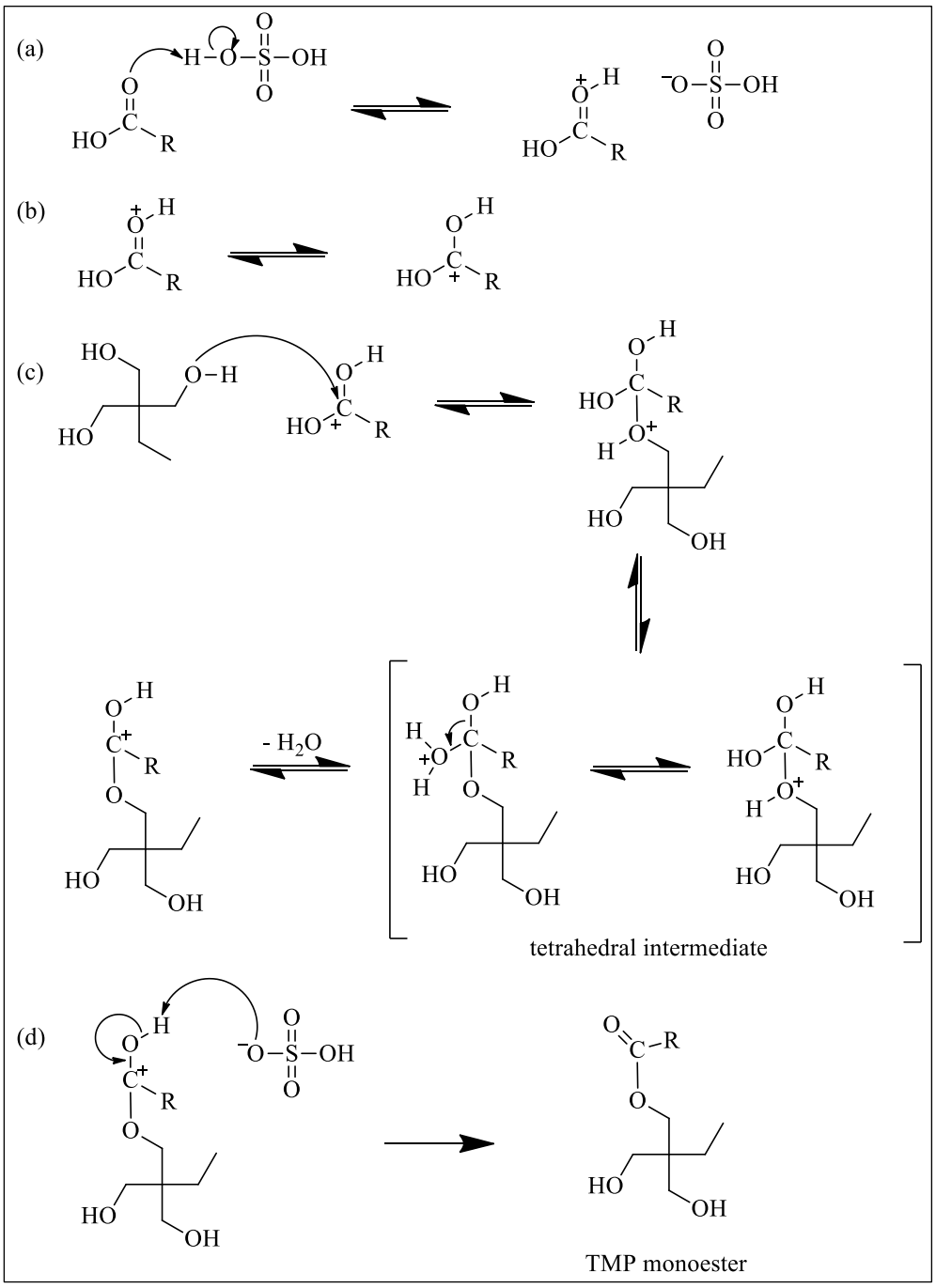


Figure 4.45 Reaction Mechanism Esterification of SFOUFA and TMP for Monoester

4.5.2 Factor Screening Process

Figure 4.46 illustrates the factor screening conducted for the esterification of SFOUFA with TMP. The factors examined included the molar ratio of SFOUFA to TMP, percentage of catalyst, reaction time and reaction temperature. All four variables were found to have a significant impact on the esterification process, as indicated by the percentage yield of SFOUFATMPE. These factors, molar ratio of SFOFA (3.0 to

4.5 mole), percentage catalyst (0.5 to 3.0 w/w%), reaction time (3 to 7 h) and reaction temperature (130 to 170 ºC) were subsequently employed in the optimization study. The specific ranges for each factor were detailed in Table 4.39.

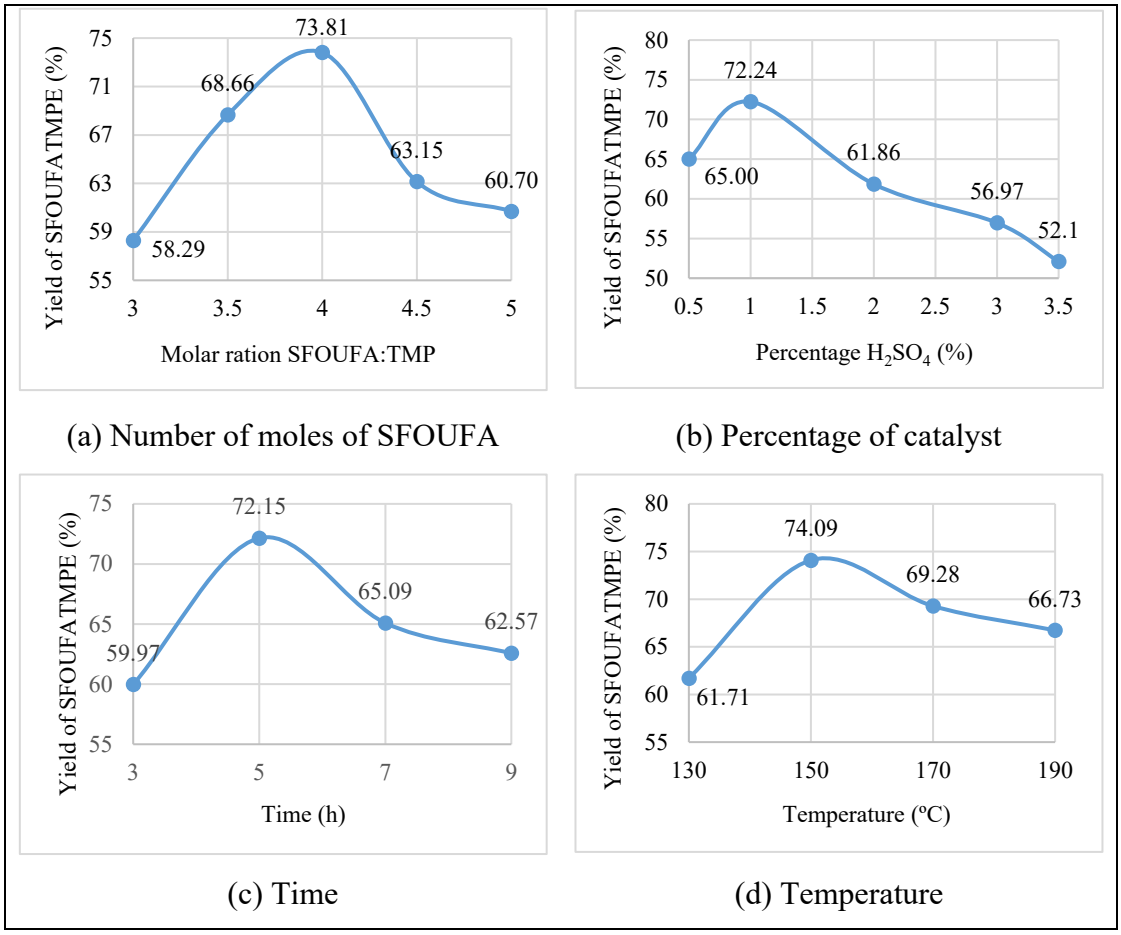


Figure 4.46 The Effect of Factors for Esterification on the Percentage Yield of SFOUFATMPE

Table 4.39
Parameter and Level for D-Optimal Design of Esterification of SFOUFA with TMP

Parameter	Unit	Variable level		
		-1	0	+1
Molar ratio of SFOUFA	mole	3.00	3.75	4.50
Percentage of catalyst	%(w/w)	0.50	1.75	3.00
Time	h	3	5	7
Temperature	°C	130	150	170

4.5.3 Optimization of Esterification of SFOUFA with TMP

The optimization of the esterification process was conducted to examine the effects of various factors, including the molar ratio of SFOUFA to TMP, percentage of catalyst, temperature and reaction time, on the percentage yield of SFOUFATMPE. A total of 25 experiments were performed to evaluate these factors and shown in Table 4.40.

Table 4.40
Experimental Runs, Factors and Response for Percentage Yield of SFOUFATMPE From D-Optimal Design

Run	Factors				Response	
	Molar ratio SFOUFA	Percentage catalyst (%)	Reaction time (h)	Reaction temp. (°C)	Yield (%)	
					Actual	Predicted
1	3.0	1.3	3	130	53.31	53.99
2	3.5	1.8	5	153	76.40	77.95
3	3.5	3.0	3	130	60.00	60.53
4	4.5	2.5	3	130	47.00	47.16
5	3.5	0.5	5	130	56.81	56.24
6	3.9	0.5	7	170	71.39	71.28
7	3.5	2.5	3	130	59.78	59.38
8	3.0	0.7	3	170	54.50	54.22
9	3.5	3.0	3	130	61.00	60.53
10	3.0	0.7	7	130	59.00	58.03
11	3.9	2.5	7	170	76.00	76.99
12	3.0	3.0	7	130	50.00	50.09
13	3.9	1.8	3	153	72.00	70.20
14	3.9	2.5	7	170	78.50	76.99
15	3.9	2.5	3	170	60.50	61.90
16	3.5	1.3	5	154	79.10	78.35
17	3.0	0.5	7	170	52.00	52.40
18	3.5	2.5	5	153	75.96	75.62
19	3.0	0.7	3	170	54.50	54.22
20	3.5	2.5	7	153	75.38	75.66
21	3.9	0.5	7	170	71.38	71.28
22	3.5	0.5	7	130	55.00	55.91
23	3.5	3.0	3	170	40.60	40.11
24	3.5	0.7	3	153	67.90	68.84
25	4.5	1.8	5	153	78.00	78.10

4.5.3.1 Determination of Selected Model

The selected model were determined based on the sequential model sun of squere (Table 4.41), lack of fit test (Table 4.42) and model summary statistic (Table 4.43). The analysis of sequential model sum of square for percentage yield of SFOUFATMPE was quadratic model with *F*-value 215.58 and < 0.001 for *p*-value.

Table 4.41
Sequential Model Sum of Square of Percentage Yield of SFOUFATMPE

Source	Sum of Squares	dF	Mean Square	*F*-value	*p*-value model	
Mean vs Total	1.006E+05	1	1.006E+05			
Linear vs Mean	979.08	4	244.77	2.34	0.0899	
2FI vs Linear	665.42	6	110.90	1.09	0.4147	
Quadratic vs 2FI	1408.28	4	352.07	215.58	< 0.0001	Suggested
Cubic vs Quadratic	12.71	6	2.12	2.34	0.2154	Aliased
Residual	3.63	4	0.9063			
Total	1.037E+05	25	4147.45			

Lack of fit test for the percentage yield of SFOUFATMPE from Table 4.42 shows not significant with the *F*-value was 2.34 (lower value) and *p*-value 0.2154 (more than 0.05).

Table 4.42
Lack of Fit Test for Percentage Yield of SFOUFATMPE

Source	Sum of Squares	dF	Mean Square	*F*-value	*p*-value model	
Linear	2086.40	16	130.40	143.89	0.0001	
2FI	1420.98	10	142.10	156.80	< 0.0001	
Quadratic	12.71	6	2.12	2.34	0.2154	Suggested
Cubic	0.0000	0				Aliased
Pure error	3.63	4	0.9063			

Model summary statistic for percentage yield of SFOUFATMPE from Table 4.43 the R^2 was 0.9947 which was near to 1 with standard deviation was 1.28. The adjusted R^2 was 0.9872 and the predicted R^2 was 0.9449. The PRESS value for

percentage yield of SFOUFANTMPE was 168.96. Table 4.43 shows the model summary statistic for percentage yield of SFOUFATMPE.

Table 4.43
Model Summary Statistic for Percentage Yield of SFOUFATMPE

Source	Standard Deviation	R^2	Adjusted R^2	Predicted R^2	PRESS	
Linear	10.22	0.3190	0.1828	-0.1540	3541.71	
2FI	10.09	0.5358	0.2043	-2.9316	12066.56	
Quadratic	1.28	0.9947	0.9872	0.9449	168.96	Suggested
Cubic	0.9520	0.9988	0.9929			Aliased

4.5.3.2 Identification of Model Accuracy

The identification of the model accuracy for the percentage yield SFOUFATMPE were determined based on the analysis plot from normal probability plot of residuals (Figure 4.47), residual versus predicted plot (Figure 4.48), actual versus predicted (Figure 4.49), residual versus run number plot (Figure 4.50), Cook's Distance plot (Figure 4.51) and Box-Cox plot (Figure 4.52). Based on the plot, it shows that the model was accurate and can be used for the optimization studies.

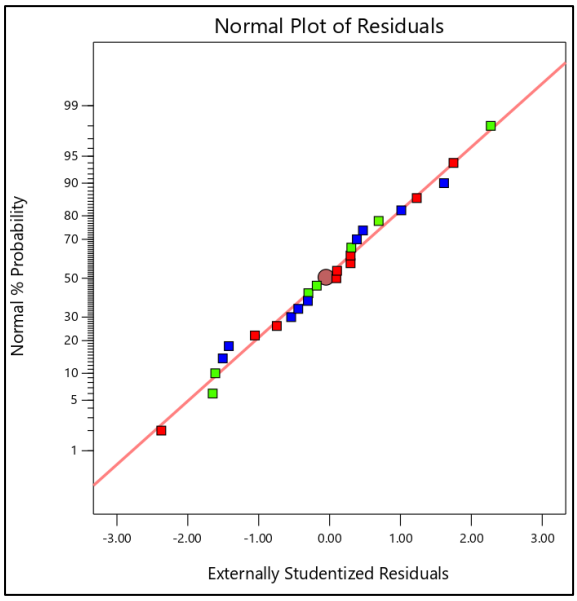


Figure 4.47 Normal Plot of Residual for Percentage Yield of SFOUFATMPE

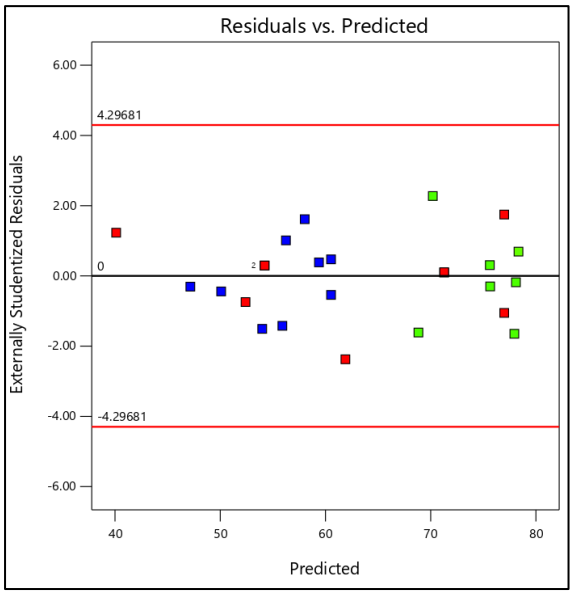


Figure 4.48 Residual versus Predicted Plot for Percentage Yield of SFOUFATMPE

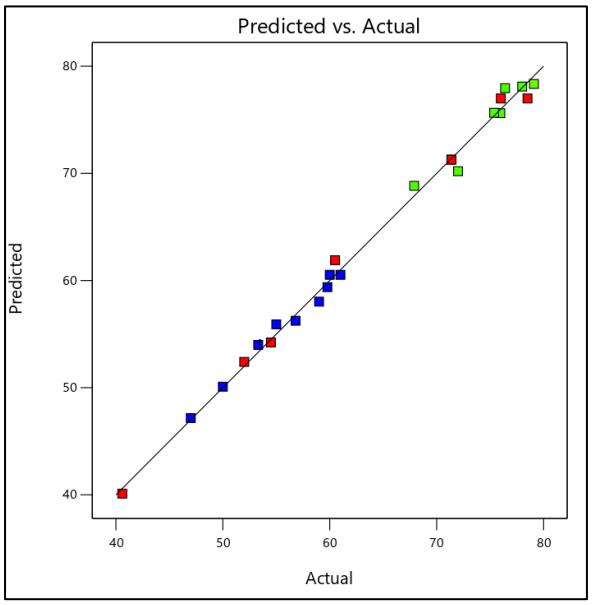


Figure 4.49 Actual versus Predicted for Percentage Yield of SFOUFATMPE

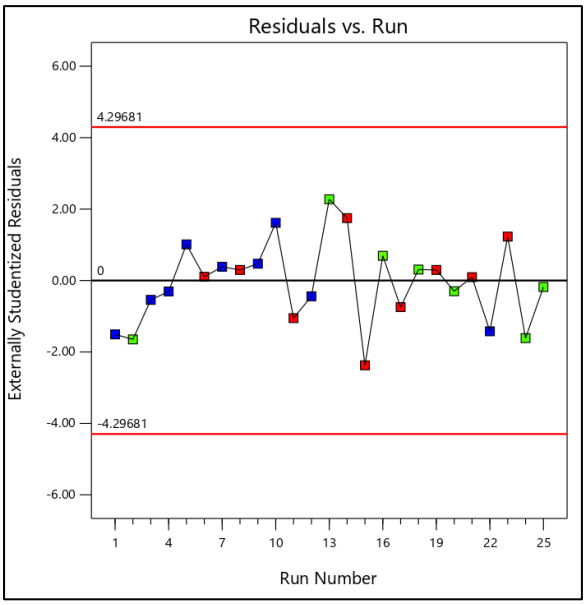


Figure 4.50 Residual versus Run Number for Percentage Yield of SFOUFATMPE

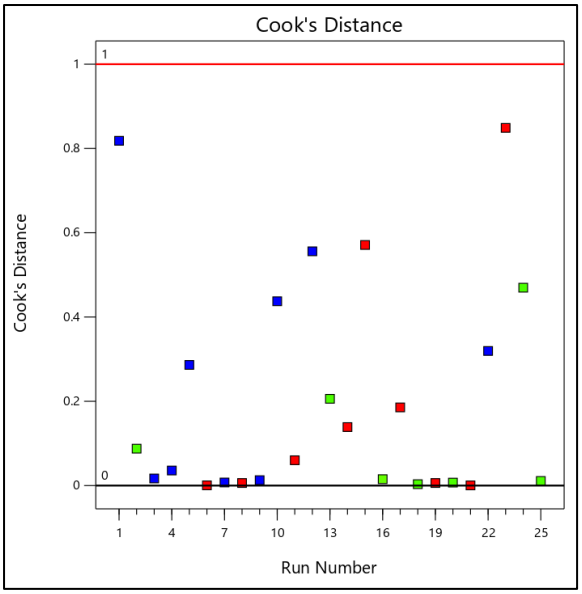


Figure 4.51 Cook's Distance Plot for Percentage Yield of SFOUFATMPE

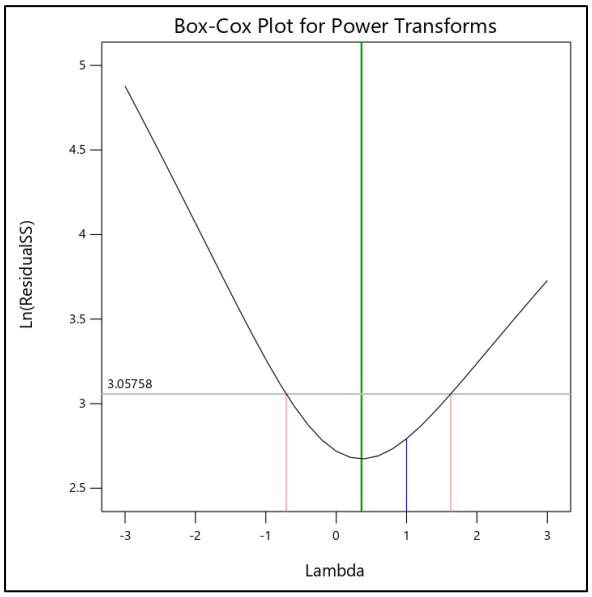


Figure 4.52 Box-Cox Plot for Percentage Yield of SFOUFATMPE

4.5.3.3 Analysis of Variance

ANOVA analysis of the percentage yield of SFOUFATMPE was summarized and presented in Table 4.44. The *p*-value model was significant (< 0.001) with *F*-value was 133.52. The lack of fit was not significant with *p*-value 0.2154 and *F*-value 2.34. The R^2 for the percentage yield of SFOUFATMPE was 0.9947.

Table 4.44
Summary of ANOVA Analysis for Percentage Yield of SFOUFATMPE

Source	Percentage yield of SFOUFAPEE
p-value model	< 0.0001
F-value model	133.52
p-value Lack of Fit	0.2154
F-value Lack of Fit	2.34
R^2	0.9947
Adjusted R^2	0.9872
Predicted R^2	0.9449
Standard deviation	1.28
Coefficient of variation (C.V %)	2.01
Adequate precision	38.6245

ANOVA analysis of percentage yield of SFOUFATMPE shows all the model and factors were significant which was *p*-value less than 0.05. Table 4.45 shows

ANOVA analysis factor for the percentage yield of SFOUFATMPE. The regression equation for the percentage yield of SFOUFATMPE was shown below:

$$\text{Yield (\%)} = 82.44 + 6.68A + 6.43B + 7.14C + 2.23D + 21.69AB + 6.44AC + 13.03AD + 1.52BC - 9.89BD - 1.79CD - 14.09A^2 - 2.94B^2 - 5.60C^2 - 12.47D^2$$

Table 4.45
ANOVA Analysis Factors for Percentage Yield of SFOUFATMPE

Source	Sum of Squares	dF	Mean Square	*F*-value	*p*-value model	Significance
A-molar ratio SFOUFA	11.11	1	11.11	6.73	< 0.0001	Significant
B-catalyst	113.30	1	113.30	68.63	< 0.0001	Significant
C-time	349.33	1	349.33	211.60	< 0.0001	Significant
D-temperature	438.03	1	438.03	265.32	0.0016	Significant
AB	56.67	1	56.67	34.32	< 0.0001	Significant
AC	11.23	1	11.23	6.80	< 0.0001	Significant
AD	33.90	1	33.90	20.54	< 0.0001	Significant
BC	8.51	1	8.51	5.16	0.0158	Significant
BD	15.25	1	15.25	9.24	< 0.0001	Significant
CD	243.97	1	243.97	147.78	0.0063	Significant
A^2	7.34	1	7.34	4.44	< 0.0001	Significant
B^2	142.04	1	142.04	86.03	0.0695	Not Significant
C^2	65.45	1	65.45	39.64	< 0.0001	Significant
D^2	23.50	1	23.50	14.23	< 0.0001	Significant

4.5.3.4 Interaction Between Variables

The interaction between variables (molar ratio, percentage catalyst, time and temperature) can be illustrated through the 3-dimentional (3D) response surface plot. Figure 4.53 shows the 3D response surface for the interaction between variables with the response (percentage yield of SFOUFATMPE).

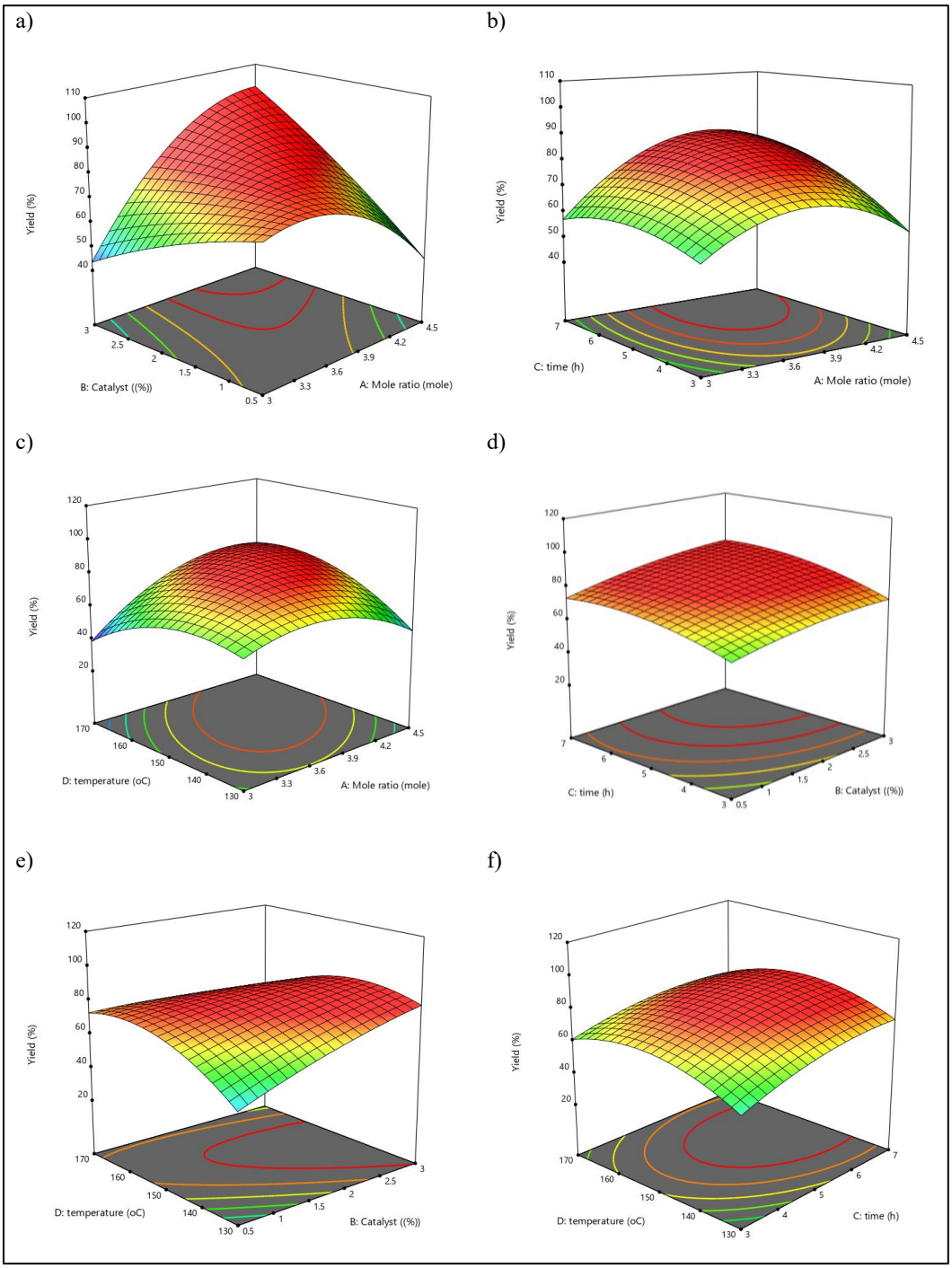


Figure 4.53 3D Surface Plot for a) AB, b) AC, c) AD, d) BC, e) BD and f) CD for Percentage Yield of SFOUFATMPE

Figure 4.53 (a) displays the interaction between the SFOUFA:TMP molar ratio and percentage of catalyst on the yield of SFOUFATMPE. An increase in the molar ratio from 3.0 to 4.0 led to a corresponding rise in ester yield, likely due to improved availability of unsaturated fatty acids for the reaction. However, further increasing the ratio from 4.0 to 4.5 resulted in a decline in yield, which may be attributed to excess fatty acids causing imbalance in the stoichiometry or potential side reactions.

Additionally, increasing the percentage of catalyst from 0.5% to 3.0% contributed to a higher yield, suggesting enhanced catalytic activity within this range. Figure 4.53 (b) shows the interaction between the SFOUFA:TMP molar ratio and reaction time on the yield of SFOUFATMPE. An increase in the molar ratio from 3.0 to 4.0 led to a higher percentage yield, while a further increase from 4.0 to 4.5 resulted in a decrease in yield. Similarly, extending the reaction time from 3 to 6 hours increased the yield, whereas a further increase from 6 to 7 hours caused a reduction in the percentage yield of SFOUFATMPE.

Figure 4.53 (c) shows the interaction between the SFOUFA:TMP molar ratio and reaction temperature (AD) on the yield of SFOUFATMPE. An increase in the molar ratio from 3.0 to 4.0 resulted in a higher yield, while a further increase from 4.0 to 4.5 led to a decrease in yield. Similarly, increasing the temperature from 130 to 150 °C improved the yield, whereas a further increase from 150 to 170 °C resulted in a reduction in the yield of SFOUFATMPE. Figure 4.53 (d) shows the interaction between the percentage of catalyst and reaction time (BC). Increasing the catalyst from 0.5 to 1.5 and extending the time from 3 to 5 hours results in an increase in the percentage yield of SFOUFATMPE. However, an increase in the percentage of catalyst from 1.5 to 3.0, coupled with an extension of time from 5 to 7 hours, leads to a decrease in the percentage yield of SFOUFATMPE.

In Figure 4.53 (e), the interaction between the percentage of catalyst and temperature (BD) were shown. It reveals that an increase in the catalyst up to 3% causes a increase in the percentage yield of SFOUFATMPE. Conversely, increasing the temperature from 130 to 150 °C results in an increase in the percentage yield of SFOUFATMPE while 150 to 170 °C resulting in decreasing for the percentage yield. Figure 4.53 (f) shows the interaction between reaction time and temperature on the yield of SFOUFATMPE. Both factors show a positive effect on yield, where extending the reaction time up to 7 hours and increasing the temperature from 130 to 150 °C resulted in a progressive increase while 150 to 170 °C resulting in decrease in the percentage yield of SFOUFATMPE.

An increase in the SFOUFA:TMP molar ratio improves the availability of SFOUFA, leading to a higher yield of SFOUFATMPE, while lower ratios may leave unreacted alcohol and reduce the yield. Increasing the percentage of catalyst from 1% to 3% decreases the yield due to excess sulfuric acid absorbing water and promoting hydrolysis. The reaction time also affects the yield where longer times up to 3 to 6 hours

improve it, but further extension can cause ester breakdown. Additionally, raising the reaction temperature from 130 to 150 °C increases the yield of SFOUFATMPE by accelerating the esterification process.

4.5.3.5 Model Verification

The optimal condition for the esterification reaction of SFOUFA with TMP was determined using numerical optimization. The parameter which A, B, C and D were set within the range while the response was set at maximum. Table 4.46 shows the restraints for optimization of esterification applied to the parameter and response. The desirability of the predicted model was equal to 1.00. Figure 4.54 shows the predicted outcome obtained from the numerical optimization model for the esterification reaction between SFOUFA with TMP.

Table 4.46
Restraints for Optimization of Esterification of SFOUFA with TMP Parameter and Response for D-Optimal Design

Parameter and responses	Goal	Lower limit	Upper limit	Weight	Importance
A: Molar ratio SFOUFA	in range	3.0	4.5	1	3
B: Catalyst	in range	0.5	3.0	1	3
C: Time	in range	3	7	1	3
D: Temperature	in range	130	170	1	3
Yield of SFOUFATMPE	maximize	40.6	79.1	1	3

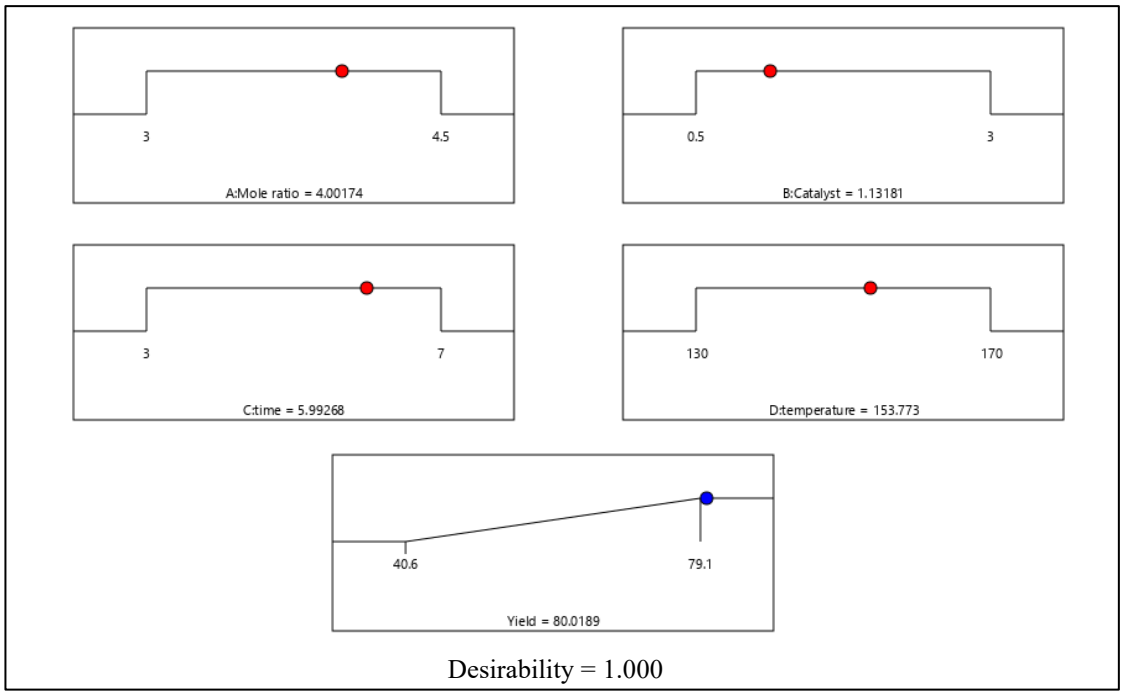


Figure 4.54 D-Optimal Predicted Model at Optimum Condition for Esterification of SFOUFA with TMP

The accuracy of the model that generated by D-optimal design was verified by conducting the esterification reaction using random set of reaction condition. Table 4.47 shows that all the RSE values were less than 5% indicating the model was accurate.

Table 4.47
Actual and Predicted Data for Verification Model for Percentage Yield of SFOUFATMPE

Molar ratio	Catalyst (%)	Reaction time (h)	Reaction temperature (°C)	Yield SFOUFATMPE (%)		
				Actual	Predicted	RSE
3.5	1.5	6	159	75.9	77.10	1.56
4.5	3.0	3	170	74.83	74.20	0.85
3.0	3.0	7	130	51.16	50.09	2.14

4.5.3.6 Optimum Condition of Esterification Reaction

The D-optimal design successfully provided the predicted optimal condition for the esterification of SFOUFA with TMP. The optimal conditions were 4.0 for molar ratio SFOUFA to TMP, 1.13% for percentage catalyst (H_2SO_4), a reaction time of 6 hours and at reaction temperature of 154 °C. The percentage yield of SFOUFATMPE obtained from this condition was 79.41%. The validation of the optimum condition also

conducted based on the calculation of RSE. Table 4.48 shows the result of actual and predicted for the esterification reaction was 0.76% which below than 5%. Figure 4.55 shows the esterification product which sunflower oil unsaturated fatty acids trimethylolpropane ester (SFOUFATMPE).

Table 4.48
Actual and Predicted Data for Optimum Condition for Percentage Yield of SFOUFATMPE

Molar ratio	Catalyst (%)	Reaction time (h)	Reaction temperature (°C)	Yield SFOUFATMPE (%)		
				Actual	Predicted	RSE
4.0	1.13	6	154	79.41	80.02	0.76



Figure 4.55 Sunflower Oil Unsaturated Fatty Acids Trimethylolpropane Ester (SFOUFATMPE)

4.5.4 Characterization of SFOUFATMPE

4.5.4.1 Gas Chromatography

The ester composition of SFOUFATMPE was analyzed using GC-FID equipped with a high-temperature column (DB-5HT) by comparison with a reference standard. Due to the unavailability of a specific standard for SFOUFATMPE, a commercial trioleate trimethylolpropane ester was used as the reference standard. In the synthesis of SFOUFATMPE, monoester and diester are initially formed as intermediates before further esterification produces the triester. Based on the reference standard, the retention time for the triester was identified in the range of 42 to 48 minutes and was used as the reference region for the identification of triester in the sample. The chromatogram of

SFOUFATMPE (Figure 4.56) showed a dominant peak within the retention time range of 44 to 47 minutes, with no observable peaks corresponding to monoester, diester, or unreacted fatty acids. This indicates that the esterification of SFOUFA with TMP successfully produced 100% triester. The result suggests that all hydroxyl (-OH) groups of TMP were fully esterified with SFOUFA, confirming the completion of the esterification reaction.

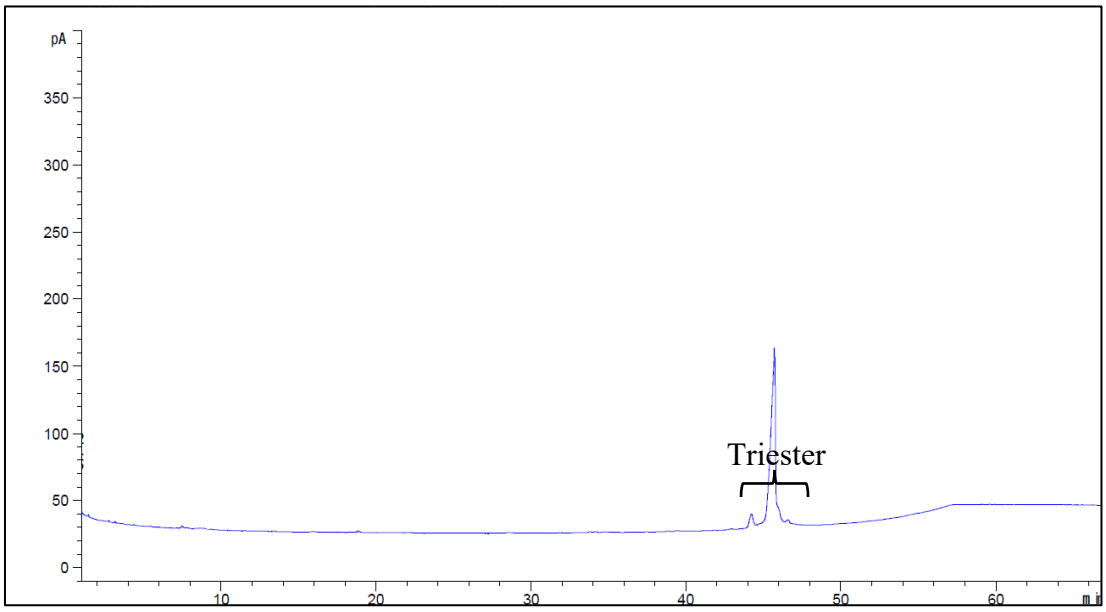


Figure 4.56 GC-FID Chromatogram of Ester Composition in SFOUFATMPE

4.5.4.2 Fourier Transform Infrared Spectroscopy

The functional groups in SFOUFATMPE were identified using FTIR analysis. The spectrum before esterification (SFOUFA) exhibited peaks at 1708 cm^{-1}, corresponding to the C=O stretch of carboxylic acids and at 1248.00 cm^{-1} and 1290.19 cm^{-1}, indicating the C-O stretches of carboxylic acids. After esterification (SFOUFATMPE), these peaks disappeared and new peaks emerged at 1740.35 cm^{-1}, representing the C=O stretch of esters, along with peaks at 1160.57 cm^{-1} and 1238.16 cm^{-1}, corresponding to the C-O stretches of esters. Additionally, the disappearance of the O-H peak in the spectrum confirmed the successful conversion of fatty acids into esters. Figure 4.57 shows the FTIR spectra and Table 4.49 shows the functional group and wavenumber of SFOUFA and SFOUFATMPE.

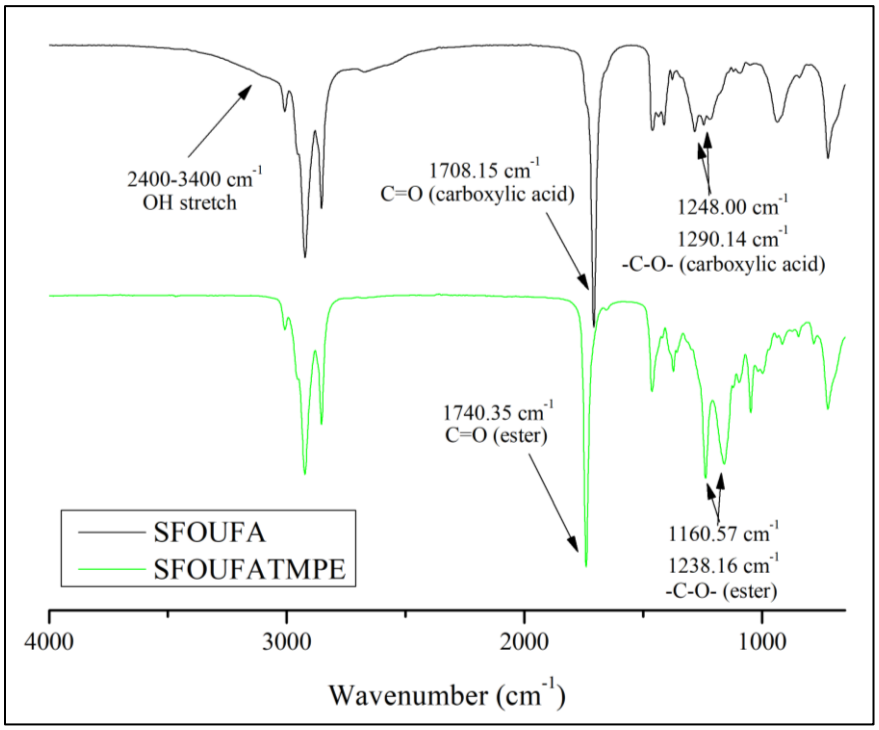


Figure 4.57 FTIR Spectra of SFOUFA and SFOUFATMPE

Table 4.49
Functional Group and Wavenumber for FTIR Spectra of SFOUFA and SFOUFATMPE

Functional group	Wavenumber (cm^{-1})	
	SFOUFA	SFOUFATMPE
OH stretching (carboxylic acid)	2400-3400	-
C=C bending vibration (aliphatic)	3008.11	3008.22
C-H stretching vibration (aliphatic)	2923.82 and 2854.19	2923 and 2854
C=O stretching vibration (ester)	-	1740.35
C=O stretching vibration (carboxylic acid)	1708.15	-
-C-O stretching vibration (ester)	-	1238.16 and 1160.57
-C-O stretching vibration (carboxylic acid)	1290.19 and 1248.00	-

4.5.4.3 Nuclear Magnetic Resonance

The success of the esterification reaction was determined from the ^{1}H and ^{13}C NMR, as depicted in Figure 4.58 and Figure 4.59, respectively. In the ^{1}H NMR spectrum of SFOUFATMPE, characteristic peaks were observed at specific chemical shifts, indicating the presence of various proton environments. These included peaks at 0.86 to 0.90 ppm for -C**H**$_3$, 1.23 to 1.36 ppm for -C**H**$_2$-, 1.58 to 1.61 ppm for O=C-CH$_2$-C**H**$_2$, 1.98 to 2.07 ppm for -CH=CH-C**H**$_2$-, 2.27 to 2.31 ppm for O=C-C**H**$_2$-, 2.75 to 2.78 ppm

for =CH-C**H**$_2$-CH=, 5.30 to 5.38 ppm for -CH=CH- and 7.28 ppm for $CDCl_3$ (solvent). The appearance of a peak at 4.12 to 4.14 ppm (C**H**$_2$-O) confirmed the presence of trimethylolpropane as a backbone in the mixture of SFOUFATMPE. Notably, the absence of a peak in the chemical shift range of 10 to 12 ppm indicated the successful conversion of SFOUFA to SFOUFATMPE, as the -O**H** group from SFOUFA was no longer present. Table 4.50 shows the chemical shift for ^{1}H NMR spectra for SFOUFA and SFOUFATMPE.

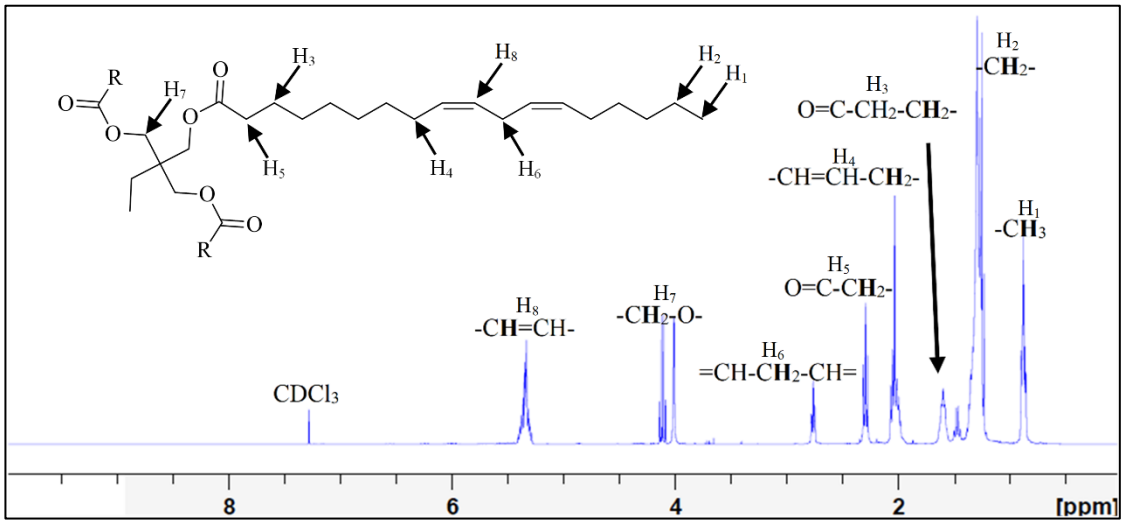


Figure 4.58 ^{1}H NMR Spectrum for SFOUFATMPE

Table 4.50
Type of Proton and Chemical Shift for SFOUFA and SFOUFATMPE

	Type of proton	Chemical shift (ppm)		
		SFOUFA	SFOUFATMPE	Theoretical*
H_1	-C**H**$_3$	0.89-0.93	0.86-0.90	0.70-1.3
H_2	-C**H**$_2$-	1.28-1.39	1.23-1.36	1.2-1.4
H_3	O=C-CH$_2$-C**H**$_2$-	1.62-1.67	1.58-1.61	1.5-2.0
H_4	-CH=CH-C**H**$_2$-	2.03-2.10	1.98-2.07	1.6-2.6
H_5	O=C-C**H**$_2$-	2.34-2.38	2.27-2.31	2.1-2.5
H_6	=CH-C**H**$_2$-CH=	2.78-2.81	2.75-2.78	2.5-3.0
H_7	-C**H**$_2$-O- (trimethylolpropane)	-	4.12-4.14	4.0-4.5
H_8	-CH=C**H**-	5.33-5.41	5.30-5.38	4.5-6.5
-	COO**H**	11.55	-	10-12

Source: *Pavia et al. (2015)

In the ^{13}C-NMR spectrum of SFOUFATMPE, carbon peaks appeared at specific chemical shifts, revealing different carbon environments. These included peaks at 8.12

ppm (from TMP) and 14.02 to 14.15 ppm for -**C**H_3, 20.96 to 31.88 ppm for -**C**H_2-, 34.17 ppm for O=C-**C**H_2-, 40.59 ppm for -**C**- (from TMP), 63.67 ppm for C**H**$_2$-O (from TMP), 76.74 to 77.38 ppm for $CDCl_3$ (solvent) and 127.89 to 130.16 ppm for -**C**H=CH. The observation of the peak corresponding to the carboxylic acid carbonyl group (**C**=O) at 180.33 ppm shifting to 173.42 ppm (**C**=O ester) in the upfield region confirmed the successful conversion of SFOUFA to the SFOUFANTMPE. Table 4.51 shows the chemical shift for ^{13}C NMR spectra for SFOUFA and SFOUFATMPE.

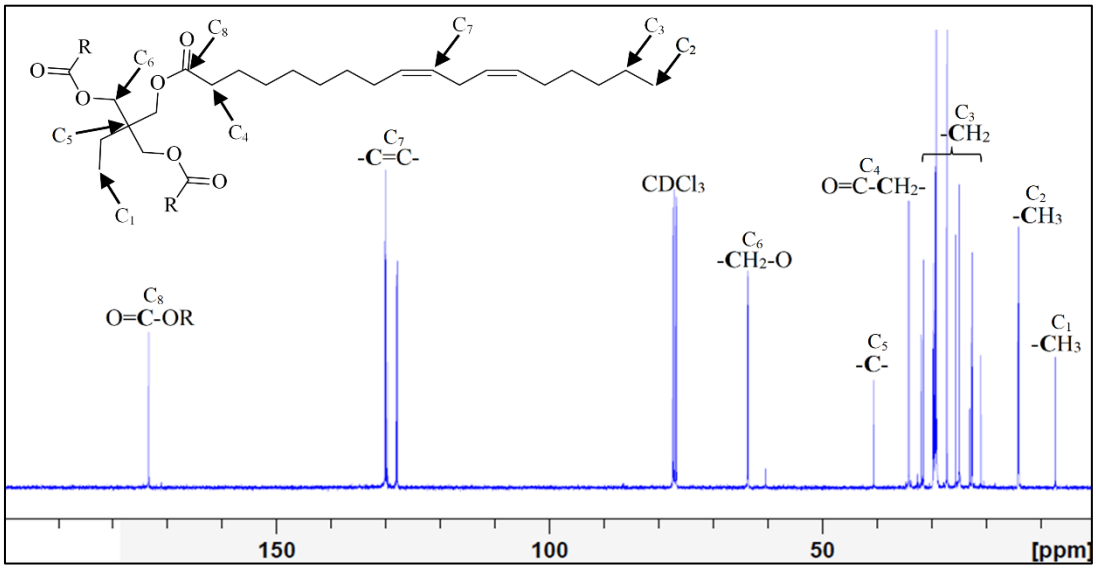


Figure 4.59 ^{13}C NMR spectrum for SFOUFATMPE

Table 4.51
Type of Carbon and Chemical Shift for SFOUFA and SFOUFATMPE

	Type of carbon	Chemical shift (ppm)		
		SFOUFA	SFOUFATMPE	Theoretical*
C_1	-**C**H_3 (trimethylolpropane)	-	8.12	8-30
C_2	-**C**H_3	14.03-14.07	14.02-14.15	8-30
C_3	-**C**H_2-	22.39-29.77	20.96-31.88	15-55
C_4	O=C-**C**H_2	34.10-34.36	33.8-34.24	15-55
C_5	-**C**- (trimethylolpropane)	-	40.59	20-60
C_6	-**C**H_2-O- (trimethylolpropane)	-	63.67	40-80
C_7	-**C**=C-	127.90-130.54	127.88-130.15	100-150
-	O=**C**-OH (carboxylic acid)	180.33	-	155-185
C_8	O=**C**-OR (ester)	-	173.42	155-185

Source: *Pavia et al. (2015)

4.5.5 Physicochemical Properties of SFOUFATMPE

The physicochemical properties of SFOUFATMPE were evaluated based on pour point, flash point, kinematic viscosity, viscosity index, oxidative stability and rheology. The physicochemical properties of SFOUFATMPE were compared with TMP ester (TMPE) derived from different plant oil, which were sunflower oil (TMPE A), palm kernel oil (TMPE B) and palm oil (TMPE C), as shown in Table 4.52.

Table 4.52
Physicochemical Properties of SFOUFATMPE and Others TMPE

Physicochemical properties	SFOUFATMPE	TMPE A	TMPE B	TMPE C
Pour point (°C)	-18	-37	10	8
Flash point (°C)	290	>330	320	300
Viscosity at 40 °C (cSt)	32.47	39.52	41.76	61.79
Viscosity at 100 °C (cSt)	7.21	8.83	8.73	14.00
Viscosity Index	157.48	213.00	154.80	158.00
Oxidative stability (min)	24	36	N/A	N/A
Rheology	Newtonian	N/A	Newtonian	N/A

Source: TMPE A: Esipovich et al. (2025); TMPE B: Bahadi et al. (2022); Nor et al. (2019a)

Form the study, it shows that the pour point of SFOUFATMPE (-18 °C) was higher than TMPE A (-37 °C) but significantly lower than TMPE B (10 °C) and TMPE C (8 °C), indicating good low-temperature fluidity compared to esters derived from palm-based oils. The variation in pour point was mainly influenced by the fatty acid composition of the feedstock, where higher unsaturated fatty acid content contributes to lower pour point values.

In terms of flash point, SFOUFATMPE exhibited a flash point of 290 °C, which was slightly lower than TMPE A (>330 °C) and TMPE B (320 °C) but comparable to TMPE C (300 °C), indicating good thermal stability and low volatility. The kinematic viscosity of SFOUFATMPE was 32.47 cSt at 40 °C and 7.21 cSt at 100 °C, which were lower than all compared TMPE samples, suggesting lower resistance to flow. This difference was likely due to the higher unsaturated fatty acid content in the SFOUFATMPE compared to palm-based oils, which generally increases fluidity. The viscosity index of SFOUFATMPE (157.48) was comparable to TMPE B (154.80) and

TMPE C (158.00) but lower than TMPE A (213.00), indicating acceptable viscosity–temperature behaviour.

In addition, SFOUFATMPE showed an oxidative stability of 24 minutes, which is lower than TMPE A (36 minutes). This lower oxidative stability was attributed to the use of sunflower oil unsaturated fatty acids, which contain a high number of double bonds that are more prone to oxidation. The rheological behaviour of SFOUFATMPE was Newtonian, similar to TMPE B. Overall, the results indicate that SFOUFATMPE exhibits comparable physicochemical properties with TMPE derived from other plant oils, although its oxidative stability was influenced by the higher degree of unsaturation in sunflower oil fatty acids.

4.6 Synthesis of Sunflower Oil Unsaturated Fatty Acids Pentaerythritol Ester

4.6.1 Esterification of SFOUFA with PE

After the separation process was carried out, the esterification process between SFOUFA and pentaerythritol (PE) was done to produce a polyol ester called sunflower oil unsaturated fatty acids pentaerythritol ester (SFOUFAPEE). PE has four hydroxyl groups (OH) which when reacted produce monoester, diester, triester and tetraester in stages. The Figure 4.60 shows the reaction scheme of SFOUFA esterification with PE, while the Figure 4.61 shows the reaction mechanism esterification of monoester from SFOUFA with PE.

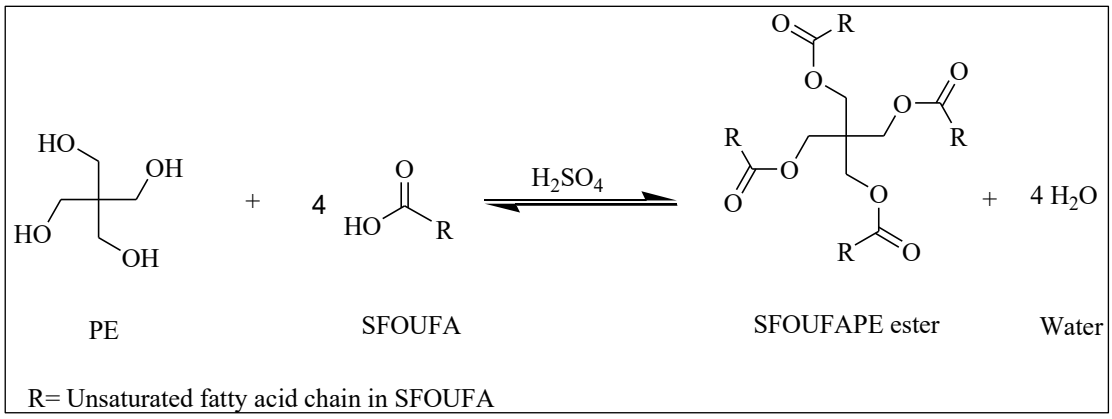


Figure 4.60 Esterification Reaction Scheme of SFOUFA with PE

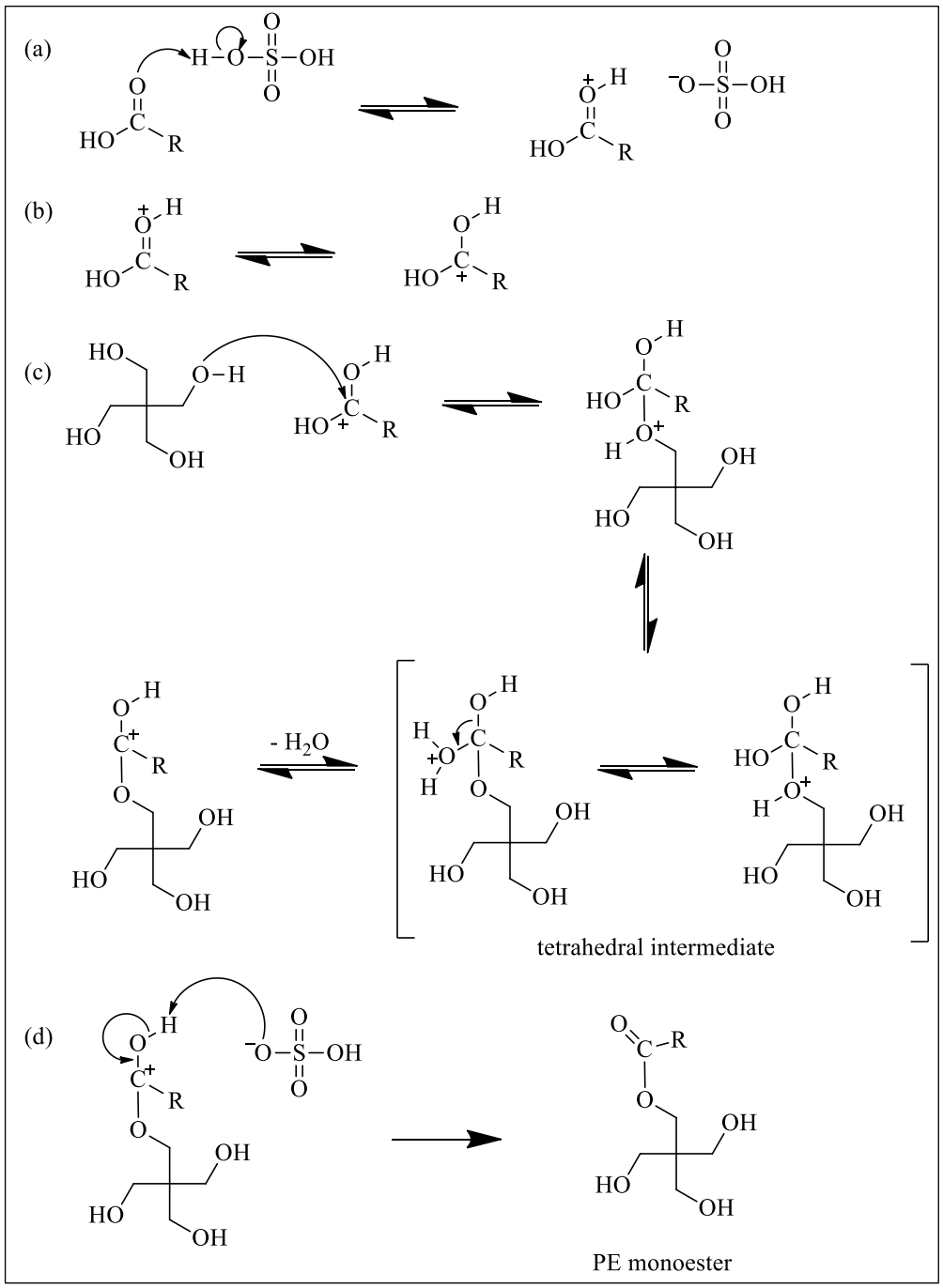


Figure 4.61 Reaction Mechanism Esterification of SFOUFA with PE for Monoester

4.6.2 Screening Factor Process

The factor screening process can be referred in Figure 4.62. Based on the change in percentage yield of SFOUFAPEE, it can be seen that all four factors have an effect on esterification and all factors have been used in process optimization. These factors, molar ratio of SFOFA (4.0 to 5.5 mole), percentage catalyst (0.5 to 3.0 w/w%), reaction

time (4 to 10 h) and reaction temperature (140 to 180 ºC) were used in the optimization process. The range of identified factors was shown in Table 4.53.

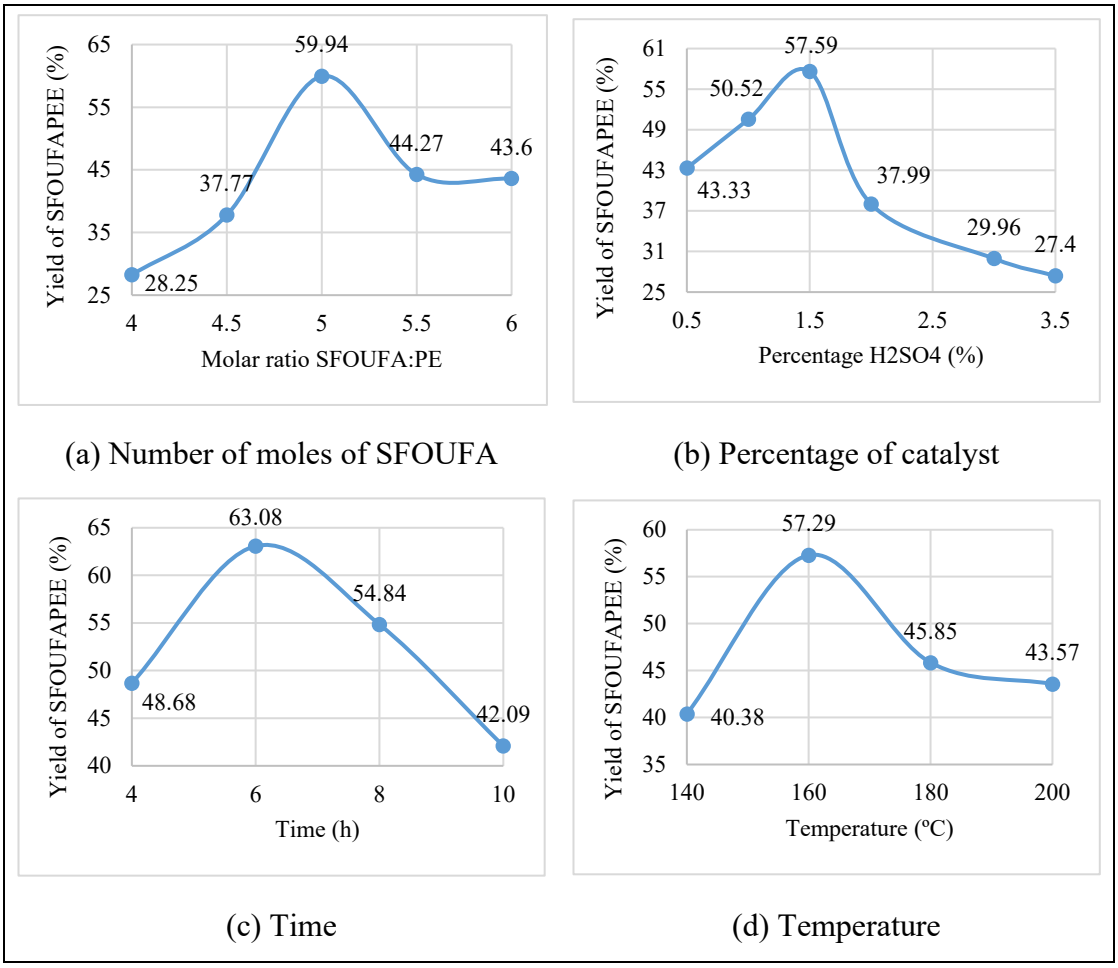


Figure 4.62 The Effect of Factor for Esterification on the Percentage Yield of SFOUFAPEE

Table 4.53
Parameter and Level for D-Optimal Design of Esterification of SFOUFA with PE

Parameter	Unit	Variable level		
		-1	0	+1
Molar ratio of SFOUFA	mole	4.00	4.75	5.50
Percentage of catalyst	%(w/w)	0.50	1.75	3.00
Time	h	4	7	10
Temperature	°C	140	160	180

4.6.3 Optimization of Esterification of SFOUFA with PE

The optimization for esterification involved conducting 25 experiments to examine the impact of factors such as molar ratio of SFOUFA, percentage of catalyst, temperature and reaction time on the response variables: the percentage yield of SFOUFAPEE. The results of the response, including both the actual values obtained in the experiments and the predicted values, were presented in Table 4.54.

Table 4.54
Experimental Run, Factors and Response for Percentage Yield of SFOUFAPEE from D-Optimal Design

Run	Factors				Response	
	Molar ratio SFOUFA	Percentage catalyst (%)	Reaction time (h)	Reaction temp. (°C)	Yield (%)	
					Actual	Predicted
1	5.5	1.1	4	140	22.79	22.60
2	4.0	0.5	10	180	41.8	41.68
3	4.9	1.7	6	180	58.16	59.07
4	4.9	1.7	10	156	49.06	49.93
5	4.5	2.9	4	140	18.59	18.40
6	4.0	3.0	10	140	22.08	22.15
7	4.6	2.3	4	164	40.76	40.57
8	5.5	3.0	4	140	15.73	16.23
9	4.0	1.7	6	156	45.83	46.40
10	5.5	2.9	8	140	28.03	27.69
11	4.9	1.7	10	156	50.66	49.93
12	5.5	0.5	8	170	52.49	52.46
13	4.5	3.0	8	166	34.63	34.13
14	4.4	0.5	8	140	36.97	37.00
15	5.5	1.8	7	158	54.05	54.28
16	4.0	3.0	4	180	18.12	18.23
17	4.9	1.7	6	180	59.89	59.07
18	4.0	2.2	10	180	35.69	35.66
19	4.5	3.0	8	166	33.73	34.13
20	5.5	2.9	4	168	38.4	38.16
21	4.2	0.5	4	140	15.83	15.88
22	4.0	1.7	6	156	46.99	46.40
23	5.5	3.0	10	180	31.15	31.17
24	4.5	3.0	8	166	34.01	34.13
25	4.4	0.5	4	170	34.99	35.08

4.6.3.1 Determination of Selected Model

The analysis model were determined based on several analyses, including sequential model sum of squares (Table 4.55), lack of fit tests (Table 4.56) and model summary statistics (Table 4.57). The model selection was based on the highest order polynomial where all additional terms were significant and the model was non-aliased. The analysis of sequential model sum of squares revealed that the suitable model to explain the study's variables for the responses was the quadratic model, based on the *F*-value and *p*-value. For the Percentage yield of SFOUFAPEE, the *F*-value was 872.63 and the *p*-value was < 0.0001. Table 4.55 shows the sequential model sum of square for percentage yield of SFOUFAPEE. The analysis of sequential model sum of squares for the percentage yield of SFOUFAPEE indicated significance in the quadratic model, with the highest *F*-value and the lowest *p*-value, suggesting the suitability of the model.

Table 4.55
Sequential Model Sum of Squares of Percentage Yield of SFOUFAPEE

Source	Sum of Squares	dF	Mean Square	*F*-value	*p*-value model	
Mean vs Total	33887.66	1	33887.66			
Linear vs Mean	1956.35	4	489.09	4.33	0.0110	
2FI vs Linear	678.16	6	113.03	1.00	0.4627	
Quadratic vs 2FI	1577.60	4	394.40	872.63	< 0.0001	Suggested
Cubic vs Quadratic	06.6461	5	0.1292	0.1668	0.9643	Aliased
Residual	3.87	5				
Total	38104.29	25				

For the lack of fit for percentage yield of SFOUFAPEE, it shows that it was not significant where the *F*-value was 0.1668, while the *p*-value was 0.9643. The lack of fit analysis test indicated that the quadratic model was suitable for response based on the non-significant *p*-values of the model. Table 4.56 shows the lack of fit tests for the percentage yield of SFOUFAPEE.

Table 4.56
Lack of Fit Test of Percentage Yield of SFOUFAPEE

Source	Sum of Squares	dF	Mean Square	*F*-value	*p*-value model	
Linear	2256.41	15	150.43	194.17	< 0.0001	
2FI	157825	9	175.36	226.36	< 0.0001	
Quadratic	0.6461	5	0.1292	0.1668	0.9643	Suggested
Cubic	0.0000	0				Aliased
Pure error	3.87	5	0.7747			

The model summary statistics for the percentage yield of SFOUFAPEE show satisfactory R^2 values for the quadratic model, as they approach 1. The errors in the model can be determined based on the standard deviation values. A low standard deviation value indicates a good model and this value was related to the R^2 and adjusted R^2 values. The standard deviation for the percentage yield of SFOUFAPEE was 0.6723. The R^2 value for the percentage yield of SFOUFAPEE was 0.9989 and the adjusted R^2 was 0.9974. The analysis of the model summary statistics for the response shows the smallest value, indicating the selection of the quadratic model. The PRESS for the percentage yield of SFOUFAPEE was 28.61. Table 4.57 shows the model summary statistic for percentage yield of SFOUFAPEE.

Table 4.57
Model Summary Statistic for Percentage Yield of SFOUFAPEE

Source	Standard Deviation	R^2	Adjusted R^2	Predicted R^2	PRESS	
Linear	10.63	0.4640	0.3568	0.1352	3646.41	
2FI	10.63	0.6248	0.3568	-2.0065	12677.21	
Quadratic	0.6723	0.9989	0.9974	0.9932	28.61	Suggested
Cubic	0.8802	0.9991	0.9956			Aliased

4.6.3.2 Identification of Model Accuracy

Several analysis plots, such as the normal probability plot of residuals (Figure 4.63) residual versus predicted plot (Figure 4.64), actual versus predicted (Figure 4.65), residual versus run number plot (Figure 4.66), Cook's Distance plot (Figure 4.67) and Box-Cox plot (Figure 4.68) were used to determine the accuracy of the model. The

normal probability plot (Figure 4.63) shows that the residuals were scattered randomly along the straight regression line for the percentage yield of SFOUFAPEE which shows that the residuals follow a normal distribution, supporting the accuracy of the model. Based on residual versus predicted plot (Figure 4.64), all the test points fall within the defined range of 4.29681 to -4.29681. This indicates that the chosen model was appropriate because all the data points were within the specified range. From the Figure 4.67 for Cook's distance, all points were located below the threshold line of 1 and most points were below 0.2 that indicates the model was accurate in predicting the response variable. The Box-Cox plot (Figure 4.68) gives the best value of lamda which is 1.04 and there is no transformation that proposed for this optimization study.

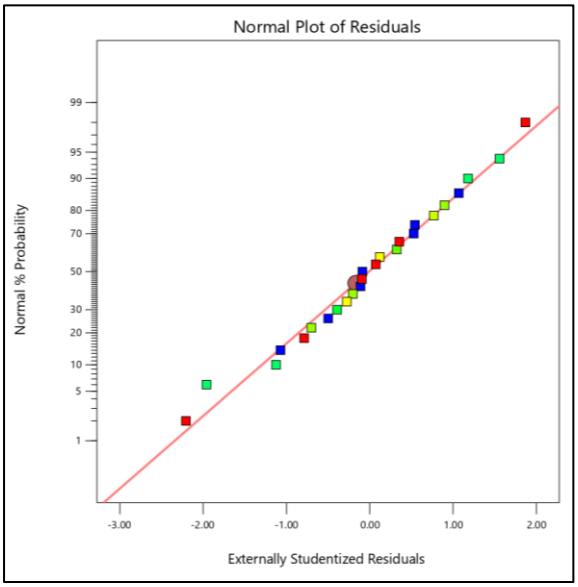


Figure 4.63 Normal Plot of Residual for Percentage Yield of SFOUFAPEE

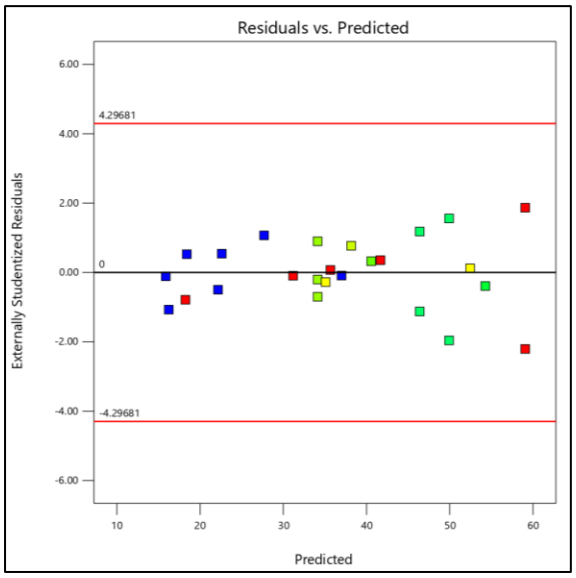


Figure 4.64 Residual versus Predicted Plot for Percentage Yield of SFOUFAPEE

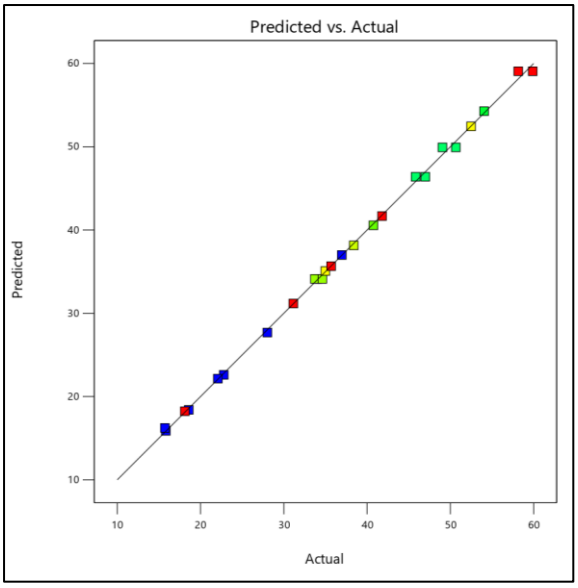


Figure 4.65 Actual versus Predicted for Percentage Yield of SFOUFAPEE

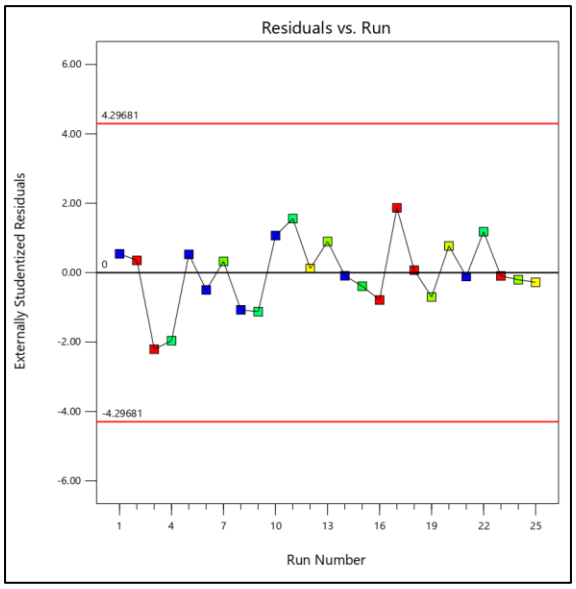


Figure 4.66 Residual versus Run Number for Percentage Yield of SFOUFAPEE

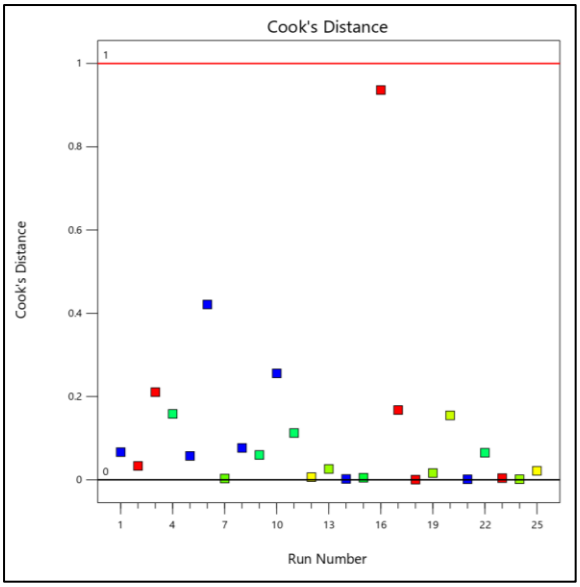


Figure 4.67 Cook's Distance Plot for Percentage Yield of SFOUFAPEE

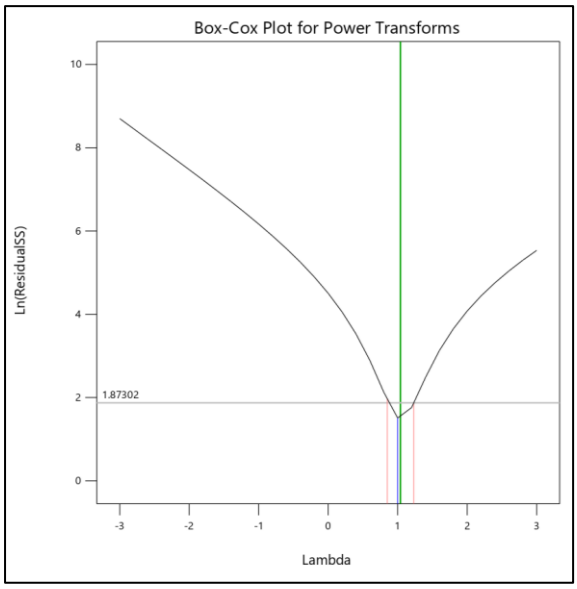


Figure 4.68 Box-Cox Plot for Percentage Yield of SFOUFAPEE

4.6.3.3 Analysis of Variance

Analysis of the ANOVA for the percentage yield of SFOUFAPEE has been summarized in Table 4.58. The *p*-value for the percentage yield of SFOUFAPEE was less than 0.0001 and the *p*-value for the lack of fit was over 0.05. The R^2 value for the percentage yield of SFOUFAPEE was 0.9989.

Table 4.58
Summary of ANOVA Analysis for Percentage Yield of SFOUFAPEE

Source	Percentage yield of SFOUFAPEE
p-value model	< 0.0001
F-value model	665.06
p-value Lack of Fit	0.9643
F-value Lack of Fit	0.1668
R^2	0.9989
Adjusted R^2	0.9974
Predicted R^2	0.9932
Standard deviation	0.6723
Coefficient of variation (C.V %)	1.83
Adequate precision	82.9479

For the ANOVA for percentage yield of SFOUFAPEE shows all model terms and factors were significant ($p < 0.05$). Table 4.59 shows ANOVA analysis factor for percentage yield of SFOUFAPEE. This further reinforces the screening results, which indicate that all linear terms for the percentage yield of SFOUFAPEE were significant. The regression equation for percentage yield of SFOUFAPEE was shown below:

$$\text{Yield (\%)} = 55.23 + 3.04A - 5.38B + 3.36C + 7.02D + 1.67AB - 1.51AC + 4.55AD - 3.20BC - 2.75BD - 2.94CD - 2.63A^2 - 13.37B^2 - 8.00C^2 - 3.90D^2$$

Table 4.59
ANOVA Analysis Factors for Percentage Yield of SFOUFAPEE

Source	Sum of Squares	dF	Mean Square	*F*-value	*p*-value model	Significance
A-molar ratio SFOUFA	113.02	1	113.02	250.06	< 0.0001	Significant
B-catalyst	365.29	1	365.29	808.22	< 0.0001	Significant
C-time	133.13	1	133.13	294.55	< 0.0001	Significant
D-temperature	568.39	1	568.39	1257.60	< 0.0001	Significant
AB	20.77	1	20.77	45.96	< 0.0001	Significant
AC	15.95	1	15.95	35.29	0.0001	Significant
AD	145.70	1	145.70	322.38	< 0.0001	Significant
BC	76.46	1	76.46	169.17	< 0.0001	Significant
BD	59.19	1	59.19	130.95	< 0.0001	Significant
CD	64.24	1	64.24	142.13	< 0.0001	Significant
A^2	28.89	1	28.89	63.93	< 0.0001	Significant
B^2	763.20	1	763.20	1688.62	< 0.0001	Significant
C^2	264.68	1	264.68	585.62	< 0.0001	Significant
D^2	60.74	1	60.74	134.38	< 0.0001	Significant

4.6.3.4 Interaction Between Variables

The interaction between variables can be illustrated through a 3-dimensional (3D) response surface plot. Figure 4.69 shows the 3D response surface for the interaction between variables and response.

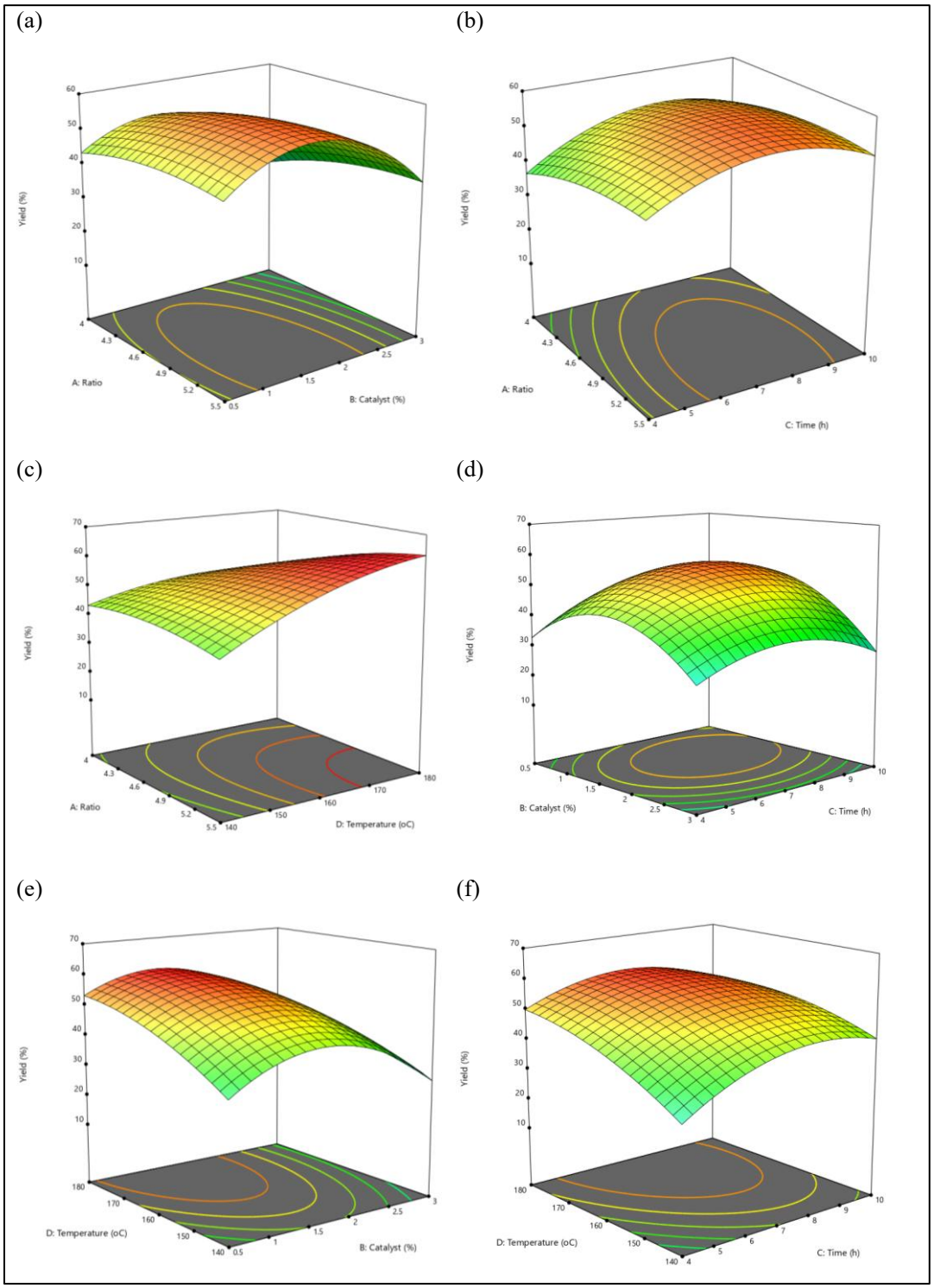


Figure 4.69 3D Surface Plot for a) AB, b) AC, c) AD, d) BC, e) BC and f) CD for Percentage Yield of SFOUFAPEE

Figure 4.69 (a) shows the interaction between the ratio of SFOUFA and the percentage of catalyst (AB). Increasing the SFOUFA ratio from 4.0 to 5.5 results in an increase in the percentage yield of SFOUFAPEE. Additionally, an increase in the percentage of catalyst from 0.5 to 1.5% leads to an increase in the percentage yield of

SFOUFAPEE. However, increasing the percentage of catalyst from 1.5 to 3% results in a decrease in the percentage yield of SFOUFAPEE. Figure 4.69 (b) shows the interaction between the ratio of SFOUFA and time (AC). The higher the SFOUFA ratio, the higher the percentage yield of SFOUFAPEE. Additionally, increasing the time from 4 to 7 hours results in an increase in the percentage yield, whereas the extended time frame of 7 to 10 hours leads to a decrease in the percentage yield of SFOUFAPEE.

Figure 4.69 (c) shows the interaction between the SFOUFA ratio and temperature (AD). It demonstrates that the higher the SFOUFA ratio and the temperature within the range of 140 to 180 °C, the higher the percentage yield of SFOUFAPEE. Figure 4.69 (d) shows the interaction between the percentage of catalyst and time (BC). Increasing the catalyst from 0.5 to 1.5 and extending the time from 4 to 7 hours results in an increase in the percentage yield of SFOUFAPEE. However, an increase in the percentage of catalyst from 1.5 to 3.0, coupled with an extension of time from 7 to 10 hours, leads to a decrease in the percentage yield of SFOUFAPEE.

In Figure 4.69 (e), the interaction between the percentage of catalyst and temperature (BD) were shown. It reveals that an increase in the catalyst up to 3% causes a decrease in the percentage yield of SFOUFAPEE. Conversely, increasing the temperature from 140 to 180 °C results in an increase in the percentage yield of SFOUFAPEE. Figure 4.69 (f) shows the interaction between time and temperature (CD). As the time increases up to 10 hours, there was a decrease in the percentage yield of SFOUFAPEE. Conversely, as the temperature rises from 140 to 180 °C, the percentage yield of SFOUFAPEE increases.

Increasing in ratio of SFOUFA was attributed to the higher availability of SFOUFA, encouraging its reaction with PE. Lower molar ratios lead to incomplete reactions, leaving unreacted polyhydric alcohol which lead to decreasing in percentage yield of SFOUFAPEE. Increasing the catalyst percentage from 1 to 3% leads to a decrease in the percentage yield of SFOUFAPEE. This phenomenon arises from the hygroscopic and dehydrating properties of sulfuric acid, causing it to absorb water. Excessive catalyst usage results in increased water content in the reaction mixture, triggering a reverse reaction.

The reaction time plays a crucial role in the percentage yield of SFOUFAPEE. As the reaction time increases, the percentage yield of the ester also rises. However, between 8 to 10 hours, a decrease in yield occurs. This was likely due to excessively long reaction times leading to ester hydrolysis, breaking the bond between SFOUFA

and PE, effectively reverting the compound to its starting material. Increasing the temperature from 140 to 180 °C leads to a significant boost in the percentage yield of SFOUFAPEE. This temperature increase accelerates the chemical reaction rate for the esterification reaction, facilitating higher yields of the desired product.

4.6.3.5 Verification Model

Numerical optimization was conducted to find the optimal conditions for the esterification of SFOUFA with PE. The parameters A, B, C and D were set within a specific range to achieve the highest percentage yield of SFOUFAPEE. Table 4.60 provides a summary of the applied constraints to determine the optimum condition, aiming for higher percentage yield of SFOUFAPEE. The parameters A, B, C and D were varied while the response, percentage yield of SFOUFAPEE was set to the maximum values. The desirability of the predicted model was equal to 1.00, indicating that the model provides the ideal value. Figure 4.70 illustrates the predicted outcomes obtained from the numerical optimization model for the esterification reaction.

Table 4.60
Restraints for Optimization of Esterification of SFOUFA with PE Parameter and Response for D-Optimal Design.

Parameter and responses	Goal	Lower limit	Upper limit	Weight	Importance
A: Molar ratio SFOUFA	in range	4.0	5.5	1	3
B: Catalyst	in range	0.5	3.0	1	3
C: Time	in range	4	10	1	3
D: Temperature	in range	140	180	1	3
Yield of SFOUFAPEE	maximize	15.73	59.89	1	3

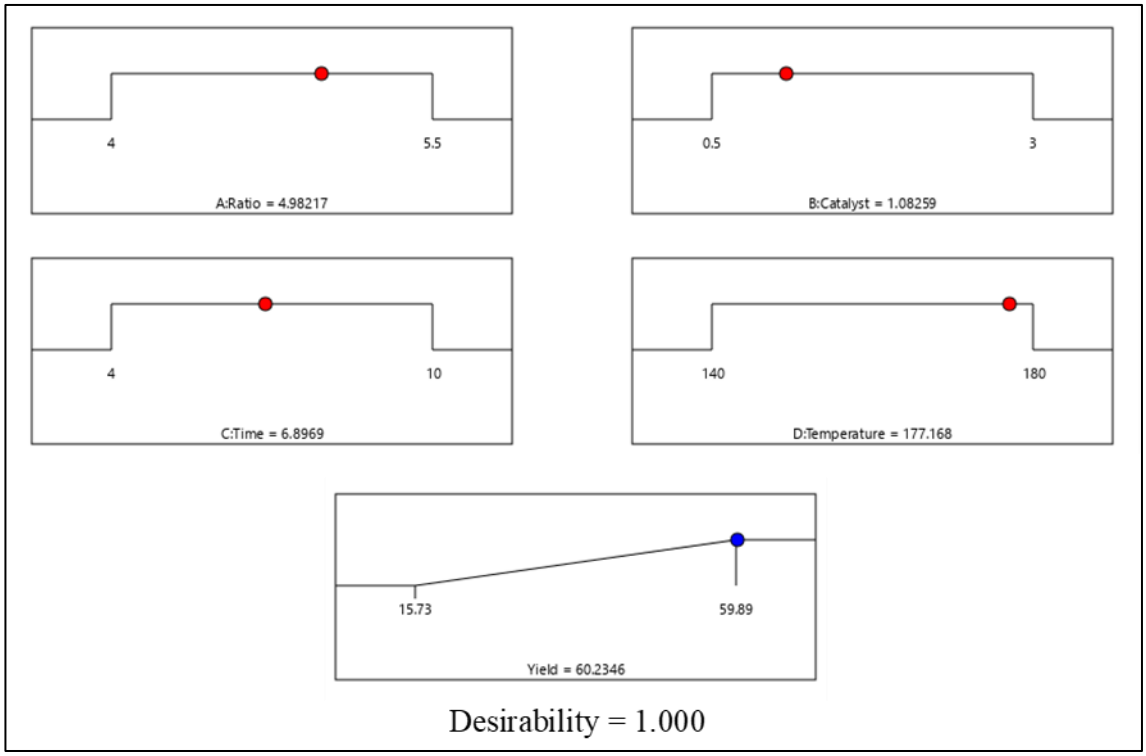


Figure 4.70 D-Optimal Predicted Model at Optimum Condition for Esterification of SFOUFA with PE

The accuracy of the model generated through D-optimal design was verified by conducting the esterification reaction using three randomly chosen sets of reaction conditions. The actual and predicted values were compared by calculating the RSE for each experiment. Only those experiments with RSE values below 5% were considered acceptable. The results presented in Table 4.61 demonstrate that all RSE values were less than 5%, indicating the model's suitability.

Table 4.61
Actual and Predicted Data for Verification Model for Percentage Yield of SFOUFAPEE

Molar ratio	Catalyst (%)	Reaction time (h)	Reaction temperature (°C)	Yield SFOUFAPEE (%)		
				Actual	Predicted	RSE
4.5	1.0	4	160	38.59	39.87	3.21
5.5	2.0	4	170	48.97	49.65	1.37
5.0	3.0	8	150	34.15	33.37	2.34

4.6.3.6 Optimum Condition of Esterification Reaction

The D-optimal design successfully provided the predicted optimal conditions for the esterification of SFOUFA and PE. The optimal conditions include a 5 for molar ratio SFOUFA with PE, 1.08% for percentage catalyst, a reaction time of 6.9 hours and a reaction temperature of 177 °C. Using these conditions, percentage yield of SFOFUFAPE ester of 59.73% was obtained. Table 4.62 presents both the actual and predicted data for the optimum condition. The validation of the optimum condition was performed by calculating the RSE, which confirmed that the values below 5% for percentage yield of SFOUFAPEE. Figure 4.71 shows the esterification product which sunflower oil unsaturated fatty acids pentaerythritol ester (SFOUFAPEE).

Table 4.62
Actual and Predicted Data for Optimum Condition for Percentage Yield of SFOUFAPEE

Molar ratio	Catalyst (%)	Reaction time (h)	Reaction temperature (°C)	Yield SFOUFAPEE (%)		
				Actual	Predicted	RSE
5	1.08	6.9	177	59.73	60.23	0.83



Figure 4.71 Sunflower Oil Unsaturated Fatty Acids Pentaerythritol Ester (SFOUFAPEE)

4.6.4 Characterization of SFOUFAPEE

4.6.4.1 Gas Chromatography

The ester composition of SFOUFAPEE was analyzed using GC-FID equipped with a high temperature column (DB-5HT) by comparison with a reference standard.

Due to the unavailability of a specific standard for SFOUFAPEE, a commercial tetraoleate pentaerythritol ester was used as the reference standard. In the synthesis of SFOUFAPEE, monoester, diester and triester are initially formed as intermediates before further esterification produces the tetraester as the main product. Based on the reference standard, the retention time for the tetraester was identified in the range of 52 to 56 minutes and was used as the reference region for the identification of tetraester in the sample. The chromatogram of SFOUFAPEE (Figure 4.72) showed a dominant peak within the retention time range of 53 to 55 minutes corresponding to the tetraester, along with a small peak at range of 45 to 47 minutes attributed to the triester. The ester composition consisted of approximately 94.6% tetraester and 5.4% triester, with no detectable peaks for monoester, diester, or unreacted fatty acids. The result suggests that most hydroxyl (OH) groups of PE were successfully esterified with SFOUFA, confirming the high conversion of the esterification reaction.

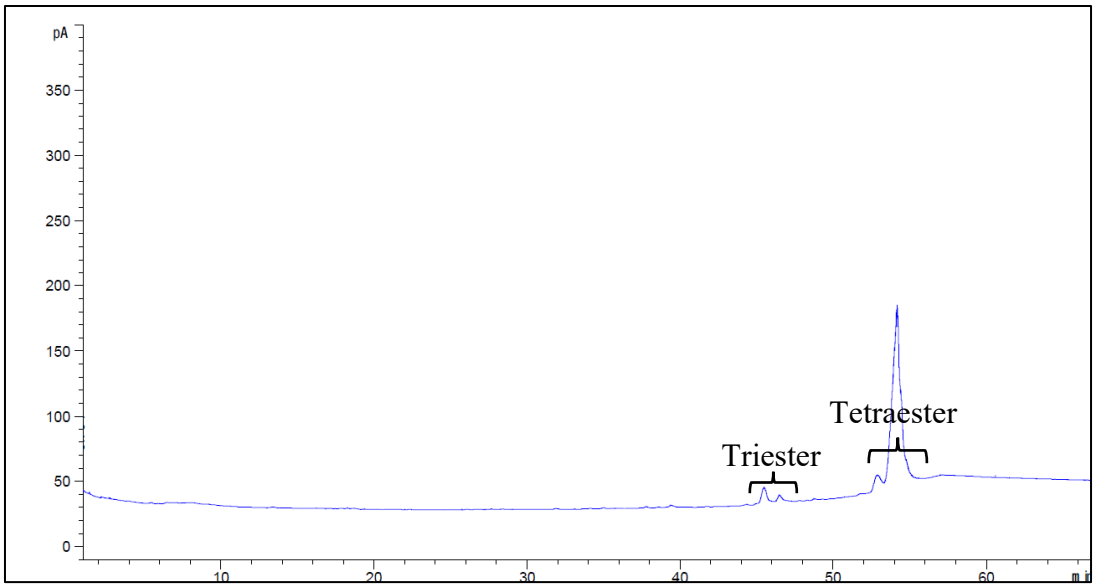


Figure 4.72 GC-FID Chromatogram of Ester Composition in SFOUFAPEE

4.6.4.2 Fourier Transform Infrared Spectroscopy

FTIR analysis was employed to determine the presence of specific functional groups within SFOUFAPEE. A comparative assessment was conducted by analyzing both spectra before (SFOUFA) and after (SFOUFAPEE) the esterification process, as shown in Figure 4.73. In the initial spectrum (SFOUFA) prior to esterification, distinct features were observed, including a C=O carboxylic acid stretch at a wavenumber of

1710.60 cm^{-1}, as well as C-O carboxylic acid stretches at 1292.04 and 1249.00 cm^{-1}. Additionally, OH stretching was evident within the range of 2400-3400 cm^{-1}. Subsequent to the completion of the esterification reaction, notable changes in the spectra were noted. Specifically, the C=O carboxylic acid peak disappeared, giving way to the emergence of a C=O ester peak at a wavenumber of 1742.32 cm^{-1} and the C-O ester stretches at 1239.03 and 1162.02 cm^{-1}. The absence of OH stretching in the post-reaction spectrum serves as evidence indicating the successful occurrence of the esterification reaction, ultimately yielding SFOUFAPEE. Table 4.63 summarizes the functional groups present in SFOUFAPEE.

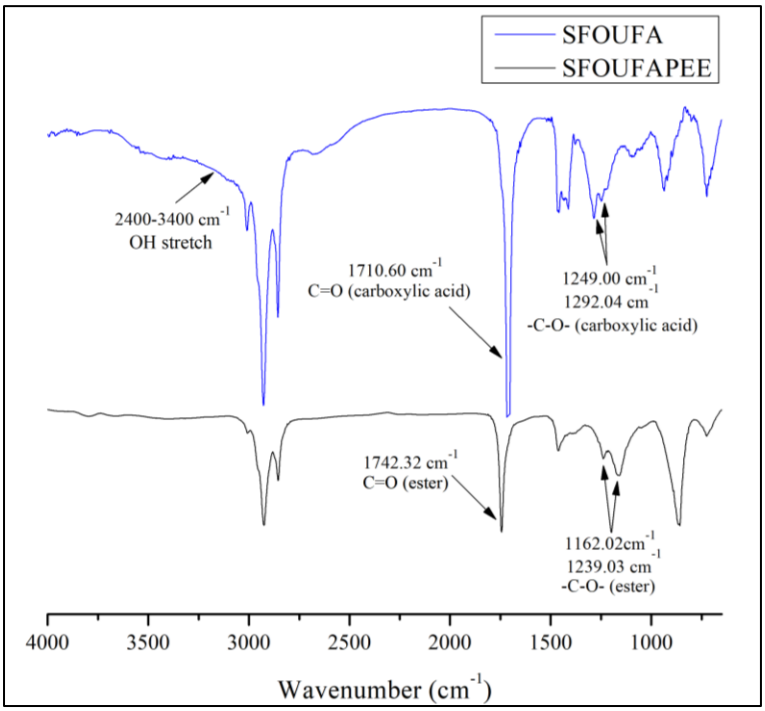


Figure 4.73 FTIR Spectra of SFOUFA and SFOUFAPEE

Table 4.63
Functional Group and Wavenumber of SFOUFA and SFOUFAPEE

Functional group	Wavenumber (cm^{-1})	
	SFOUFA	SFOUFAPEE
OH stretching (carboxylic acid)	2400-3400	-
C=C bending vibration (aliphatic)	3010.11	3008.48
C-H stretching vibration (aliphatic)	2926.93 and 2856.16	2925.96 and 2854.51
C=O stretching vibration (ester)	-	1742.32
C=O stretching vibration (carboxylic acid)	1710.60	-
-C-O stretching vibration (ester)	-	1239.03, 1162.02
-C-O stretching vibration (carboxylic acid)	1292.04 and 1249.00	-

4.6.4.3 Nuclear Magnetic Resonance

The success of the esterification reaction was assessed through the analysis of ^{1}H and ^{13}C-NMR, as depicted in Figure 4.74 and Figure 4.75, respectively. In the ^{1}H-NMR spectrum of SFOUFAPEE, characteristic peaks were observed at specific chemical shifts, indicating the presence of various proton environments. These included peaks at 0.88 to 0.93 ppm for -C**H**$_3$, 1.26 to 1.39 ppm for -C**H**$_2$-, 1.60 to 1.62 ppm for O=C-CH$_2$-C**H**$_2$-, 2.00 to 2.09 ppm for -CH=CH-C**H**$_2$-, 2.29 to 2.37 ppm for O=C-C**H**$_2$-, 2.77 to 2.80 ppm for =CH-C**H**$_2$-CH=, 5.31 to 5.34 ppm for -CH=CH- and 7.28 ppm for $CDCl_3$ (solvent). The appearance of a peak at 4.10 to 4.15 ppm (C**H**$_2$-O) confirmed the presence of pentaerythritol in the reaction mixture. Notably, the absence of a peak in the chemical shift range of 10 to 12 ppm indicated the successful conversion of SFOUFA to SFOUFAPEE, as the -O**H** group from SFOUFA was no longer present. Table 4.64 shows the chemical shift for ^{1}H NMR spectra for SFOUFA and SFOUFAPEE.

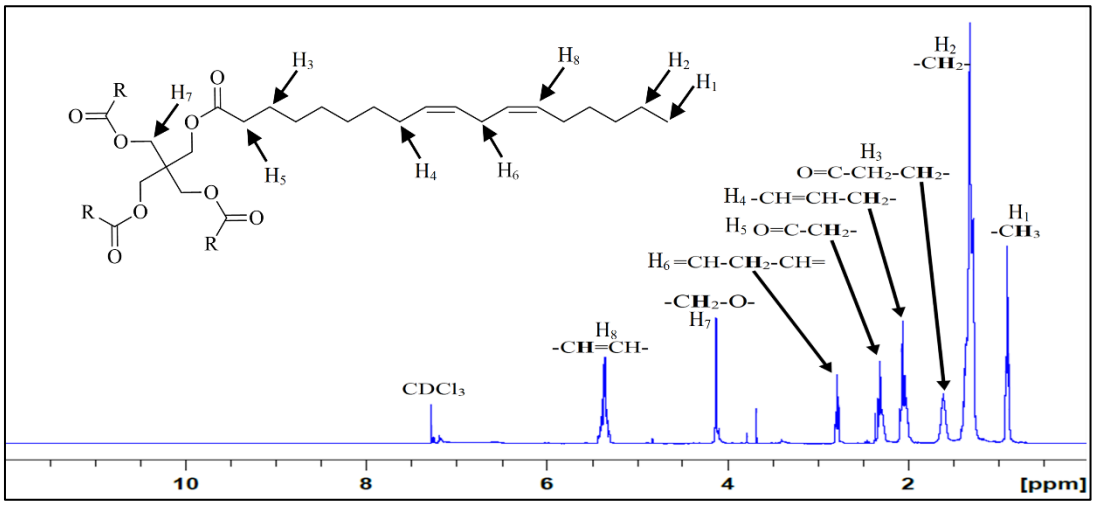


Figure 4.74 ^{1}H NMR Spectrum for SFOUFAPEE

Table 4.64
Type of Proton and Chemical Shift for SFOUFA and SFOUFAPEE

	Type of proton	Chemical shift (ppm)		
		SFOUFA	SFOUFAPEE	Theoretical*
H_1	-C**H**$_3$	0.89-0.93	0.88-0.93	0.70-1.3
H_2	-C**H**$_2$-	1.28-1.39	1.26-1.39	1.2-1.4
H_3	O=C-CH$_2$-C**H**$_2$-	1.62-1.67	1.60-1.62	1.5-2.0
H_4	-CH=CH-C**H**$_2$-	2.03-2.10	2.00-2.09	1.6-2.6
H_5	O=C-C**H**$_2$-	2.34-2.38	2.29-2.37	2.1-2.5
H_6	=CH-C**H**$_2$-CH=	2.78-2.81	2.77-2.80	2.5-3.0
H_7	-C**H**$_2$-O- (pentaerythritol)	-	4.10-4.15	4.0-4.5
H_8	-C**H**=CH-	5.33-5.41	5.31-5.34	4.5-6.5
-	COO**H**	11.55	-	10-12

Source: *Pavia et al. (2015)

In the ^{13}C-NMR spectrum of SFOUFAPEE, carbon peaks appeared at specific chemical shifts, revealing different carbon environments. These included peaks at 14.05 ppm for -**C**H$_3$, 25.09 to 31.91 ppm for -**C**H$_2$-, 34.07 ppm for O=C-**C**H$_2$-, 41.86 ppm for -**C**- (from PE), 62.14 ppm for **C**H$_2$-O (from PE), 76.71 to 77.35 ppm for CDCl$_3$ (solvent) and 127.91 to 130.20 ppm for -**C**H=CH-. The observation of the peak corresponding to the carboxylic acid carbonyl group (**C**=O) at 180.33 ppm shifting to 173.21 ppm in the upfield region confirmed the successful conversion of SFOUFA to the SFOUFAPEE. Table 4.65 shows the chemical shift for ^{13}C NMR spectra for SFOUFA and SFOUFAPEE.

The chemical shifts of the peaks obtained from both ^{1}H and ^{13}C NMR spectra were found to be consistent with the theoretical values, further supporting the successful formation of the desired SFOUFAPEE. These findings from the NMR analysis provide valuable evidence of the completion of the esterification reaction.

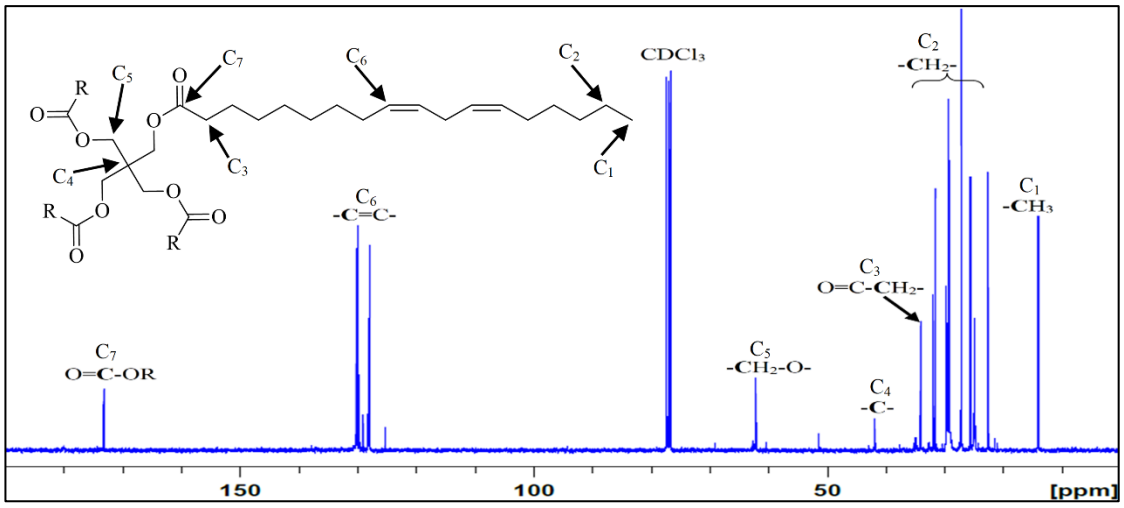


Figure 4.75 ^{13}C NMR Spectrum for SFOUFAPEE

Table 4.65
Type of Carbon and Chemical Shift for SFOUFA and SFOUFAPEE

	Type of carbon	Chemical shift (ppm)		
		SFOUFA	SFOUFAPEE	Theoretical*
C_1	-**C**H$_3$	14.03-14.07	14.05	8-30
C_2	-**C**H$_2$-	22.39-29.77	25.09-31.91	15-55
C_3	O=C-**C**H$_2$	34.10-34.36	34.07	15-55
C_4	-**C**- (pentaerythritol)	-	41.86	20-60
C_5	-**C**H$_2$-O- (pentaerythritol)	-	62.14	40-80
C_6	-**C**=C-	127.90-130.54	127.91-130.20	100-150
-	O=**C**-OH (carboxylic acid)	180.33	-	155-185
C_7	O=**C**-OR (ester)	-	173.21	155-185

Source: *Pavia et al. (2015)

4.6.5 Physicochemical Properties of SFOUFAPEE

The physicochemical properties of SFOUFAPEE were evaluated based on pour point, flash point, kinematic viscosity, viscosity index, oxidative stability and rheology. The physicochemical properties of SFOUFAPEE were compared with PE ester (PEE) derived from different plant oil, which were palm kernel oil (PEE A) and palm oil (PEE B and PEE C), as shown in Table 4.66.

Table 4.66
Physicochemical Properties of SFOUFAPEE and Others PEE

Physicochemical properties	SFOUFAPEE	PEE A	PEE B	PEE C
Pour point (°C)	-21	-8	-20	17
Flash point (°C)	302	320	302	300
Viscosity at 40 °C (cSt)	80.49	87.06	68.40	57.47
Viscosity at 100 °C (cSt)	14.66	14.55	12.70	10.87
Viscosity Index	145.93	140.86	N/A	147.00
Oxidative stability (min)	19.0	N/A	N/A	N/A
Rheology	Newtonian	Newtonian	N/A	N/A

Source: PEE A: Bahadi et al. (2022); PEE B: Aziz et al. (2014); PEE C: Nor and Salimon, (2023)

From this study, it shows that the pour point of SFOUFAPEE was -21 °C, which was lower than PEE A (-8 °C) and PEE C (17 °C) and slightly lower than PEE B (-20 °C). The lower pour point of SFOUFAPEE indicates better low-temperature fluidity and can be attributed to the higher unsaturated fatty acid content in the SFOUFAPEE, which reduces crystallization at low temperatures.

In terms of flash point, SFOUFAPEE exhibited a flash point of 302 °C, which was comparable to PEE B (302 °C) and PEE C (300 °C) but slightly lower than PEE A (320 °C), indicating good thermal stability and low volatility. The kinematic viscosity of SFOUFAPEE was 80.49 cSt at 40 °C and 14.66 cSt at 100 °C, which were slightly lower than PEE A but higher than PEE B and PEE C. This variation was influenced by differences in fatty acid composition and degree of unsaturation among the feedstocks. The viscosity index of SFOUFAPEE (145.93) was comparable to PEE A (140.86) and PEE C (147.00), indicating acceptable viscosity to temperature behaviour.

SFOUFAPEE exhibited an oxidative stability of 19.0 minutes, which was low and can be attributed to the high content of unsaturated fatty acids, particularly linoleic and oleic acids that contain double bonds susceptible to oxidation. The rheological behaviour of SFOUFAPEE was Newtonian, similar to PEE A. Overall, SFOUFAPEE shows comparable physicochemical properties with PEE derived from palm-based oils, with improved low temperature properties but lower oxidative stability due to the higher degree of unsaturation.

4.7 Comparison of Esterification Yield and Physicochemical properties of SFOUFANPGE, SFOUFATMPE and SFOUFAPEE

The percentage yield, physicochemical and rheological properties of polyol ester were evaluated to assess the suitability of the polyol ester as a potential biolubricant base stock. The percentage yield of SFOUFANPGE, SFOUFATMPE and SFOUFAPEE were compared to determine the effect of polyhydric alcohol structure on esterification efficiency while the physicochemical properties were evaluated and compared to determine how the biolubricant performs under real operating conditions. The pour point indicates the lowest temperature at which the biolubricant can still flow, while the flash point reflects its safety when exposed to high temperatures. Kinematic viscosity and viscosity index determine the biolubricant ability to maintain a stable lubricating film across different temperatures, which directly affects friction and component wear. Oxidative stability shows the biolubricant resistance to degradation when subjected to heat and oxygen, influencing its durability and service life. In addition, assessing the rheological behaviour of polyol ester, whether the oil exhibits Newtonian or non-Newtonian characteristics which helps to understand how the polyol ester flows under stress and shear, which is crucial for ensuring that the polyol ester is suitable for lubrication applications that require consistent flow behaviour. Table 4.67 shows the comparison of physicochemical and rheological properties of the polyol ester.

Table 4.67
Percentage Yield and Physicochemical Properties of SFOUFANPGE, SFOUFATMPE and SFOUFAPEE

Properties	SFO	SFOUFANPGE	SFOUFATMPE	SFOUFAPEE
Yield (%)	-	83.75	79.41	59.73
Pour point (°C)	-13	-15	-18	-21
Flash point (°C)	280	268	290	302
Viscosity at 40 °C (cSt)	30.54	21.24	32.47	80.49
Viscosity at 100 °C (cSt)	7.22	5.35	7.21	14.66
Viscosity Index	163.59	174.50	157.48	145.93
Oxidative stability (min)	22.0	22.4	24.0	19.0
ISO viscosity grade	32	22	32	68
Rheology	Newtonian	Newtonian	Newtonian	Newtonian

4.7.1 Esterification Yield

The esterification yields of SFOUFANPGE (diester, 83.75%), SFOUFATMPE (triester, 79.41%) and SFOUFAPEE (tetraester, 59.73%) showed a decreasing trend as the number of hydroxyl groups in the polyhydric alcohol increased. This reduction was mainly attributed to the increasing steric hindrance, which reduced the accessibility of the remaining hydroxyl groups as esterification progressed, thereby lowering the esterification rate and making complete esterification more difficult. This observation was further supported by the ester composition analysis, where SFOUFANPGE and SFOUFATMPE consisted of 100% diester and triester, respectively whereas SFOUFAPEE contained 94.6% tetraester and 5.4% triester, indicating incomplete esterification. Consequently, NPG (2 OH) produced the highest yield, followed by TMP (3 OH), while PE (4 OH) exhibited the lowest yield due to the greater steric hindrance surrounding its four hydroxyl groups. Padmaja et al. (2012) demonstrated that increasing polyol functionality reduced esterification efficiency because of steric hindrance around the remaining hydroxyl groups. Likewise, Jumaah et al. (2024) reported that polyhydric alcohols with lower steric hindrance produced higher ester yields owing to enhanced esterification rates. Suemanotham et al. (2026) also reported that NPG exhibited higher esterification reactivity than TMP because of its lower steric hindrance and greater hydroxyl accessibility. Therefore, the lower yield of SFOUFAPEE was attributed to the increased steric hindrance and the greater difficulty in achieving complete tetraester formation.

4.7.2 Pour Point

The pour point is the lowest temperature that the lubricant can flow with only gravity (Owuna, 2020; Salimon and Salih, 2023). The results of pour point show a clear improvement in low-temperature behaviour for all three synthesized polyol esters. SFOUFANPGE recorded -15 °C, SFOUFATMPE -18 °C and SFOUFAPEE reached the lowest value at -21 °C, compared with SFO which solidified at -13 °C. This improvement mainly comes from the use of unsaturated fatty acids (SFOUFA) in producing the esters. The double bonds in unsaturated fatty acids create bends along the carbon chain and these bends prevent the molecules from packing closely together. As

a result, the esters do not form solid waxy structures easily when the temperature drops (Nor et al., 2018a).

Among the polyol ester, SFOUFAPEE shows the best low temperature performance. Its structure has more branching and a higher number of unsaturated fatty acids, which increases molecular irregularity and further disrupts packing. SFOUFATMPE and SFOUFANPGE also show better pour points than SFO, with their improvements linked to the degree of unsaturation and the complexity of their structures. In contrast, SFO contains both saturated and unsaturated fatty acids, where the saturated fractions promote tighter molecular packing at low temperatures, resulting in a higher pour point. For the international standard for paraffin oil-based lubricant in the market were from -7 to -18 °C (Rudnick, 2020)

Overall, these results emphasize that increasing the proportion of unsaturated fatty acids and structural branching in polyol esters is an effective strategy to improve low-temperature performance, which is essential for ensuring reliable flow properties of potential biolubricants in cold-climate applications.

4.7.3 Flash Point

Flash point is the lowest temperature at which a lubricant begins to vaporize and can be ignited by an external ignition source (Owuna et al., 2020). It is commonly used as a descriptive characteristic for both fuel oils and non-fuel oils such as lubricants, as it distinguishes between flammable and combustible materials. Oils with flash points below 43 °C were classified as flammable, whereas those with flash points above this temperature were considered combustible (Salimon et al, 2011; Nor et al., 2017). The flash point results of the synthesized polyol esters show a clear increasing trend from SFOUFANPGE to SFOUFAPEE, indicating that structural modification through esterification significantly enhances thermal safety. Among the three esters, SFOUFANPGE recorded the lowest flash point at 268 °C, followed by SFOUFATMPE at 290 °C, while SFOUFAPEE exhibited the highest flash point at 302 °C, which is also higher than that of SFO (280 °C). This increasing trend can be attributed to the rise in molecular weight and structural complexity of the esters formed with different polyols. As molecular weight increases, greater energy is required for molecular vaporization, resulting in a higher flash point.

The increase in flash point is also influenced by the number of ester branches and the length of the carbon chain in each polyol ester (Soodoo et al., 2023). SFOUFANPGE, which contains fewer branching points, has a lower molecular weight and therefore requires less energy to reach vaporization, resulting in a comparatively lower flash point. In contrast, SFOUFATMPE and especially SFOUFAPEE possess more branched and bulkier molecular structures, which contribute to stronger intermolecular interactions. These stronger interactions limit the volatility of the ester molecules, meaning they require more heat to overcome the molecular forces and form vapour that can ignite. This explains why SFOUFAPEE shows the highest flash point among the three esters.

The increase in polarity from multiple ester linkages also plays an important role. More ester groups promote stronger dipole-dipole interactions, further reducing volatility and enhancing thermal resistance (Fox and Stachowiak 2007). Overall, the higher flash point of these polyol esters, particularly SFOUFATMPE and SFOUFAPEE, demonstrates improved thermal stability, which is an important characteristic for safe and reliable operation in high-temperature lubrication applications. This enhancement confirms that esterification not only improves the performance of sunflower oil but also makes the resulting polyol esters more suitable as potential biolubricants in demanding industrial environments.

4.7.4 Kinematic Viscosity and Viscosity Index

The viscosity results show clear differences among the synthesized polyol esters. At 40 °C, SFOUFANPGE recorded the lowest viscosity (21.24 cSt), followed by SFOUFATMPE (32.47 cSt), while SFOUFAPEE exhibited the highest value (80.49 cSt). A similar trend was observed at 100 °C, where the viscosities decreased to 5.35 cSt, 7.21 cSt and 14.66 cSt, respectively. These reductions with increasing temperature were typical for liquid lubricants because higher thermal energy weakens intermolecular interactions, allowing the molecules to flow more easily. The differences in viscosity among the three polyol esters were mainly due to variations in molecular weight, branching and polarity. SFOUFAPEE has the largest molecular structure and the highest number of ester linkages, which contribute to stronger intermolecular attraction and result in higher viscosity at both temperatures. SFOUFATMPE, with a

moderately branched structure, falls in the middle, while SFOUFANPGE, having the smallest molecular size among the three, shows the lowest viscosity values.

These viscosity differences were also reflected in their ISO VG grades. SFOUFANPGE corresponds to ISO VG 22, which is typically used in light-duty hydraulic systems and precision instruments where lower viscosity ensures efficient flow and reduced energy loss. SFOUFATMPE corresponds to ISO VG 32, commonly applied in general-purpose hydraulic fluids, compressors and automotive lubrication requiring moderate viscosity for balanced film strength and flowability. SFOUFAPEE corresponds to ISO VG 68, which suits heavier-duty industrial machinery, gear oils and high-load lubrication where higher viscosity is needed to maintain a protective film under stress.

The viscosity index (VI) of the polyol esters also provides insight into their resistance to viscosity changes with temperature (Dabai et al., 2018; Owuna et al., 2020). SFOUFANPGE shows the highest VI (174.50), followed by SFOUFATMPE (157.48), while SFOUFAPEE records the lowest VI (145.93). A higher VI suggests better stability in viscosity across temperature changes, meaning the lubricant can maintain its film strength under varying operating conditions. The lower VI of SFOUFAPEE is likely due to the higher degree of unsaturation in its structure, which makes it more susceptible to thermal and oxidative effects that influence viscosity behaviour. Meanwhile, the higher VI of SFOUFANPGE indicates that its molecular structure provides more stable flow characteristics with less sensitivity to temperature.

Overall, the viscosity and viscosity index trends highlight the influence of molecular size, branching and unsaturation on the flow behaviour of these polyol esters. SFOUFAPEE, with its larger and more polar structure, offers higher viscosity suitable for heavier applications, while SFOUFANPGE and SFOUFATMPE provide lower viscosities with better temperature stability. These characteristics support their potential use as biolubricants for different lubrication requirements.

4.7.5 Oxidative Stability

The oxidative stability test results show that SFOUFAPEE has the lowest induction time of 19.0 minutes, indicating lower oxidative stability compared to SFO and the other polyol esters. SFOUFATMPE exhibits the highest induction time of 24.0 minutes, while SFOUFANPGE and SFO show similar values of 22.4 minutes and 22.0

minutes, respectively. This difference in oxidative stability can be explained by the structural variations among the samples. SFO contains beta hydrogen atoms, which influence its oxidation behaviour and contribute to its relatively good oxidative stability. In contrast, SFOUFAPEE (19.0 minutes) lacks beta hydrogens but has a higher concentration of unsaturated fatty acids with multiple double bonds. These double bonds increase the presence of bis-allylic protons, which were particularly vulnerable to free radical attacks. As a result, SFOUFAPEE undergoes faster oxidative degradation, leading to the formation of hydroperoxides and accelerating the oxidation process (Nor et al., 2018b).

SFOUFANPGE and SFOUFATMPE show better oxidative stability than SFOUFAPEE because their molecular structures contain fewer double bonds or less unsaturation, making them less prone to oxidative breakdown. The higher degree of unsaturation in SFOUFAPEE, while beneficial for properties like pour point and viscosity, negatively impacts its oxidative resistance, resulting in the shortest induction time. SFOUFATMPE exhibited the best oxidative stability compared to SFOUFAPEE and SFOUFANPGE.

Overall, the oxidative stability results highlight the trade-off between unsaturation and stability in polyol esters. While increased unsaturation improves certain physical properties, it also makes the ester more susceptible to oxidation, which must be considered when developing biolubricants for practical applications.

4.7.6 Rheology

The rheological test of SFOUFANPGE, SFOUFATMPE and SFOUFAPEE shows a similar result to SFO, indicating a Newtonian fluid where the viscosity remained constant regardless of the applied shear rate. This behavior demonstrates that these polyol esters and SFO possess a stable and uniform flow profile, making them suitable as potential biolubricants that require consistent film formation under varying operating conditions. This also shows that the shear stress of SFOUFANPGE (a), SFOUFATMPE (b) and SFOUFAPEE (c) increased proportionally with the shear rate, as presented in Figure Figure 4.76, which is a key characteristic of Newtonian fluids.

The viscosity versus shear rate (Figure 4.77) relationship further supports this observation. For SFOUFANPGE, the viscosity remained essentially constant and did not show meaningful changes within the shear-rate range of 30 to 100 s^{-1}, confirming

its stable flow behavior under applied shear. A similar trend was observed for SFOUFATMPE, where its viscosity also remained steady across 30 to 100 s^{-1} indicating that its molecular structure does not undergo significant alignment or deformation when subjected to shear forces. Meanwhile, SFOUFAPEE showed a constant viscosity over a slightly broader shear rate range of 20 to 100 s^{-1} reaffirming its Newtonian characteristics.

The consistency in viscosity across increasing shear rates for all three synthesized polyol esters (SFOUFANPGE, SFOUFATMPE and SFOUFAPEE) indicates that the esterification process did not disrupt the flow stability of the base oil but instead maintained or even enhanced desirable rheological properties. This predictable and uniform flow behavior is advantageous for applications as potential biolubricants.

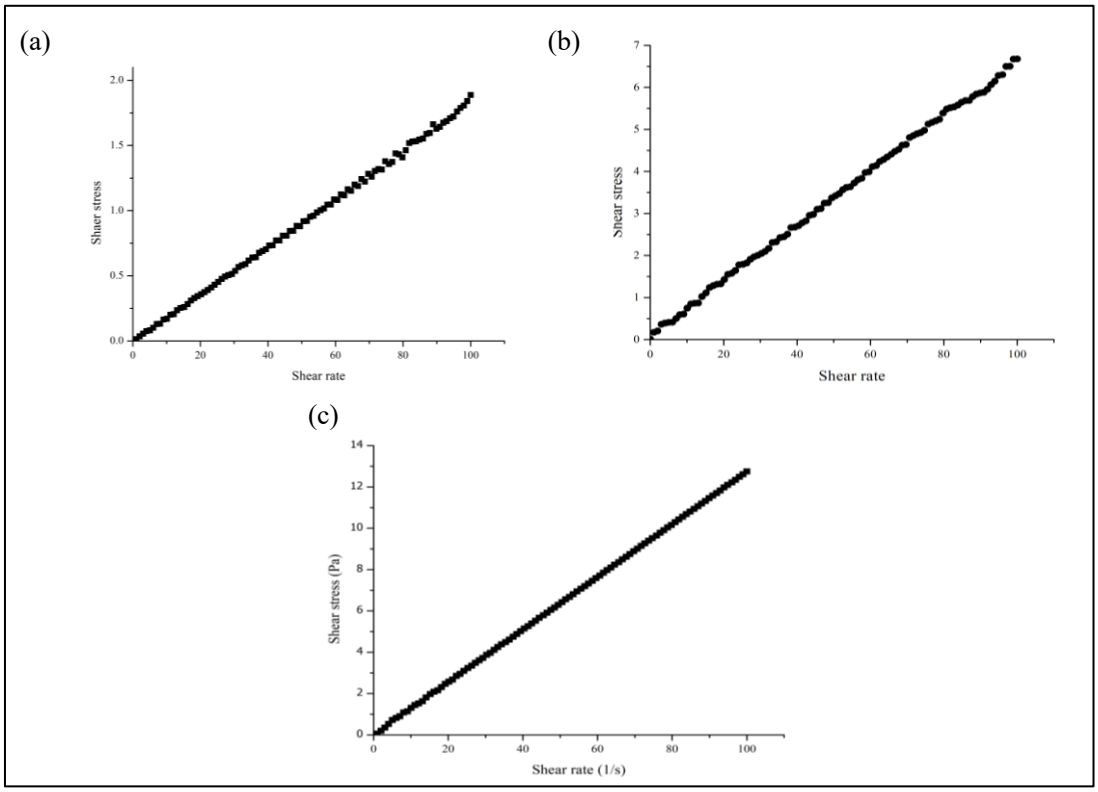


Figure 4.76 Rheological Properties Shear Stress versus Shear Rate of (a) SFOUFANPGE, (b) SFOUFATMPE and (c) SFOUFAPEE

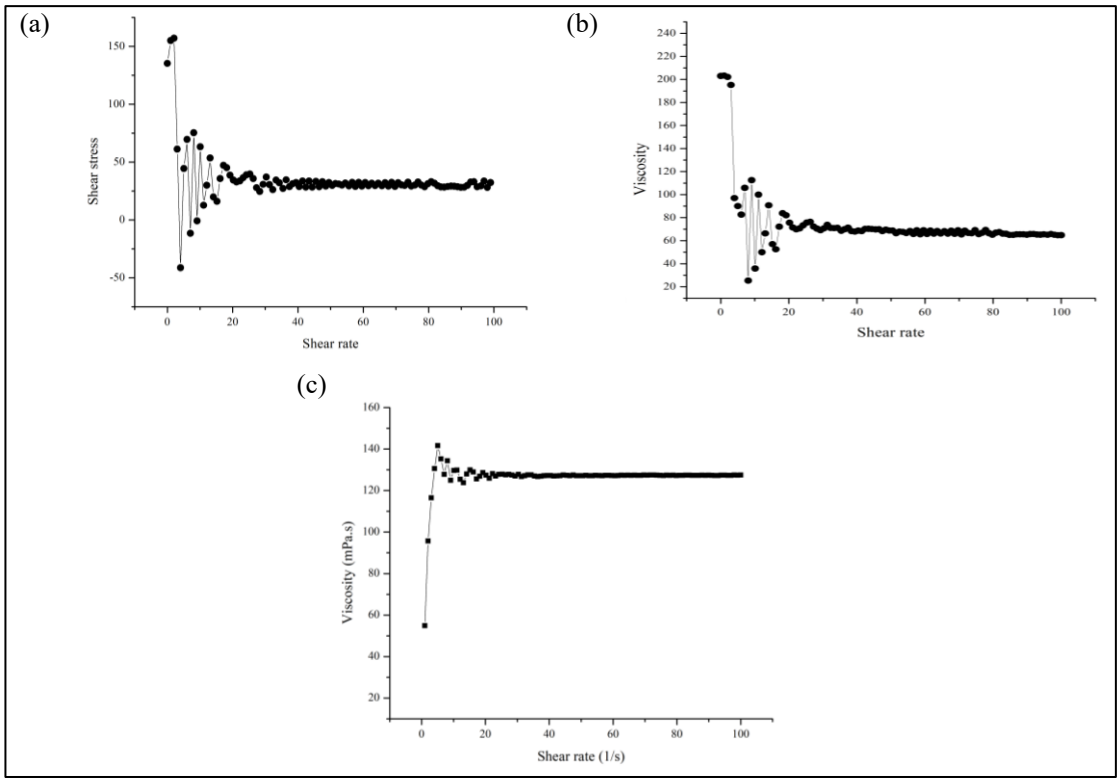


Figure 4.77 Rheological Properties Viscosity versus Shear Rate of (a) SFOUFANPGE, (b) SFOUFATMPE and (c) SFOUFAPEE

4.7.7 Determination of Polyol Ester for Further Reaction

Based on the evaluation of oxidative stability and other important physicochemical properties, SFOUFATMPE was selected for further epoxidation. It demonstrated a high oxidative stability with an induction time of 24.0 minutes, which was slightly higher than SFO and another polyol ester. This resistance to oxidation suggests better thermal durability, essential for practical lubricant applications. Additionally, SFOUFATMPE mimics SFO closely because it contains the same number of ester groups, resulting in viscosity values (32.47 cSt at 40 °C and 7.21 cSt at 100 °C) that were nearly similar to those of SFO. Its ISO VG grade of 32 suits general-purpose hydraulic and machinery lubrication, while its viscosity index of 157.48 indicates good stability across temperature variations. The pour point of -18 °C also reflects favorable low-temperature flow properties. Taken together, these characteristics provide an optimal balance between oxidative stability, viscosity behavior and low-temperature performance. Therefore, SFOUFATMPE stands out as the most suitable candidate for epoxidation and ring opening reaction to further improve its lubrication performance and stability.

4.8 Synthesis of Epoxidized Sunflower Oil Unsaturated Fatty Acids Trimethylolpropane Ester

4.8.1 Epoxidation of SFOUFATMPE

The epoxidation reaction of SFOUFATMPE was carried out to produce epoxidized sunflower oil unsaturated fatty acids trimethylolpropane ester (ESFOUFATMPE). In this study, the epoxidation reaction was carried out using peracids through an in-situ process. To produce performic acid, formic acid (HCOOH) reacts in-situ with hydrogen peroxide (H_2O_2), where H_2O_2 serves as the oxygen donor while HCOOH acts as the oxygen carrier. During this reaction, the oxygen atom from H_2O_2 is transferred to HCOOH, resulting in the formation of performic acid. In addition, H_2SO_4 is added as a catalyst to accelerate and promote the formation of performic acid. Figure 4.78 shows the formation of performic acid.

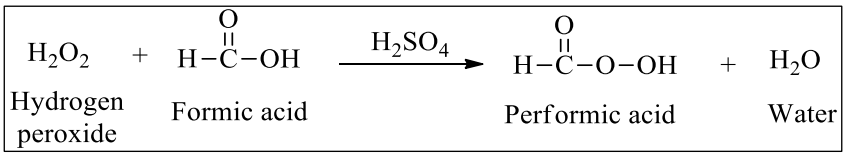


Figure 4.78 Formation of Perfomic Acid

During the epoxidation mechanism, several changes happen in one continuous step. The C=C in the SFOUFATMPE acts as a nucleophile, while the oxygen in the performic acid behaves as the electrophile. The C=C attacks the positively charged oxygen, causing the weak O-O bond in the performic acid to break. When this bond breaks, a carbonyl group is formed and the oxygen is rearranged. This rearrangement then releases an electrophilic oxygen atom, which attaches to the C=C and forms the epoxide ring. Figure 4.79 shows the mechanism of epoxidation reaction and Figure 4.80 shows the epoxidation of SFOUFATMPE.

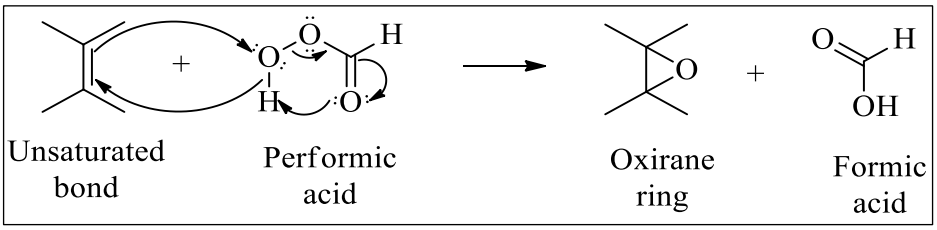


Figure 4.79 Mechanism of Epoxidation Reaction

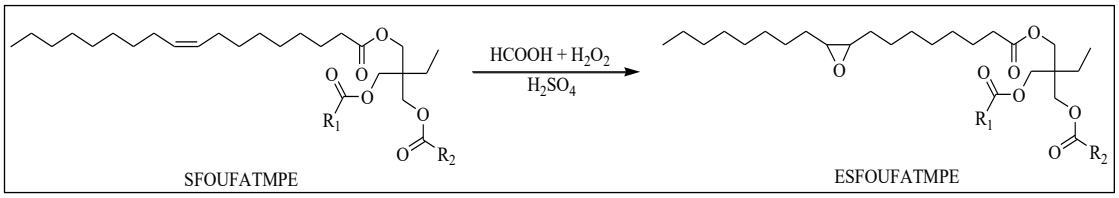


Figure 4.80 Epoxidation of SFOUFATMPE

4.8.2 Factor Screening Process

The factor screening results, as shown in Figure 4.81, clearly shows that all five parameters, which include the moles of formic acid, the moles of hydrogen peroxide, the reaction time, the reaction temperature and the catalyst percentage, play a significant role in influencing the percentage yield of ESFOUFATMPE. Since each factor demonstrated a significant effect on the epoxidation reaction, all five parameter, molar ratio of HCOOH (3 to 9 mole), molar ratio H_2O_2 (1 to 4 mole), percentage catalyst (1 to 3 w/w%), reaction time (2 to 4 h) and reaction temperature (40 to 60 ºC) were selected for the optimization process. Table 4.68 shows the range of identified factors for the optimization using D-optimal design.

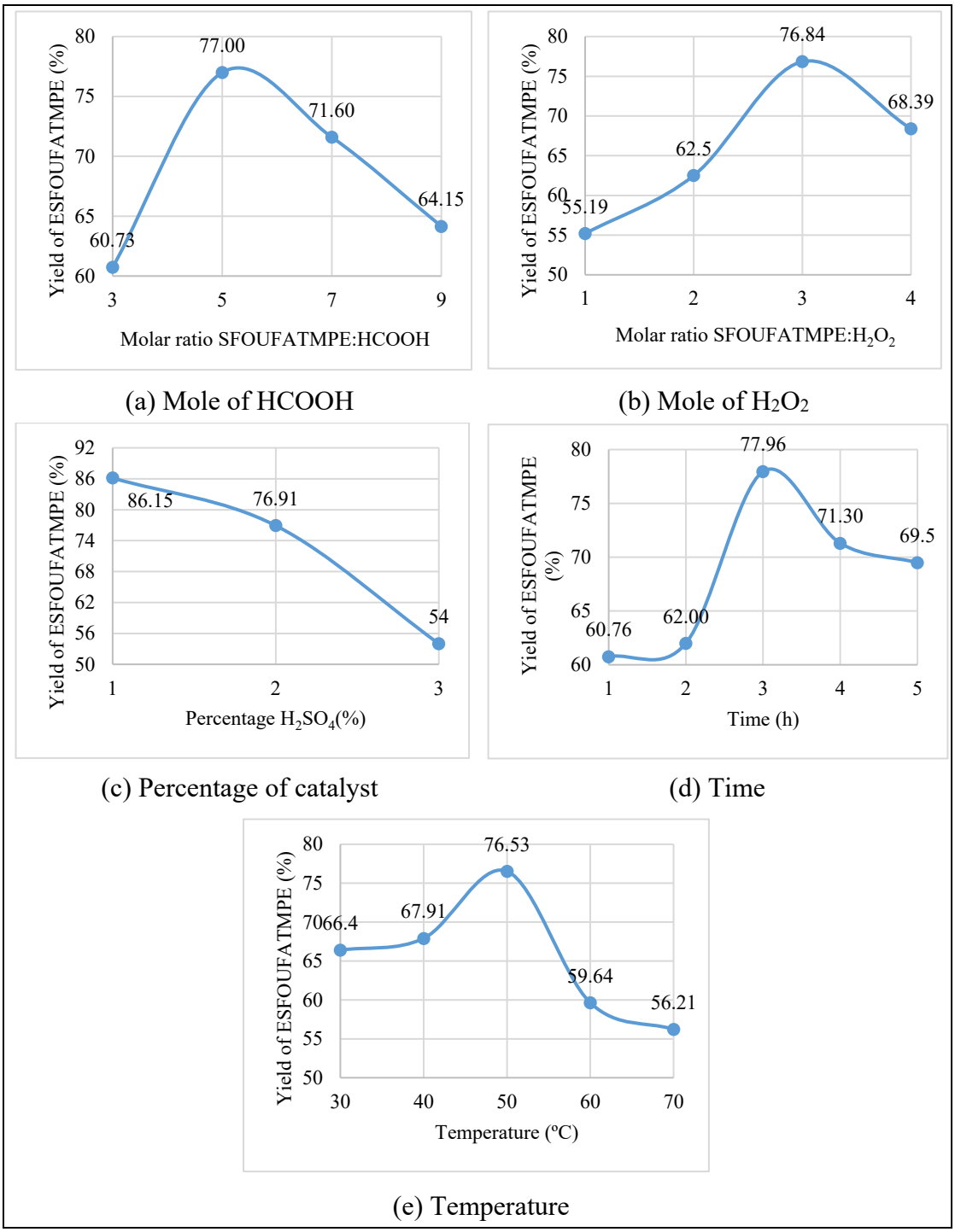


Figure 4.81 The Effect of Factor for Epoxidation Reaction on the Percentage Yield of ESFOUFATMPE

Table 4.68
Parameter and Level for D-Optimal Design of Epoxidation Reaction of SFOUFATMPE

Parameter	Unit	Variable level		
		-1	0	+1
Molar ratio of HCOOH	mole	3.0	6.0	9.0
Molar ratio of H_2O_2	mole	1.0	2.5	4.0
Percentage of catalyst	%(w/w)	1.0	2.0	3.0
Time	h	2	3	4
Temperature	°C	40	50	60

4.8.3 Optimization of Epoxidation of SFOUFATMPE

The optimization of the epoxidation reaction was carried out by performing 31 experimental runs designed that suggested by the RSM to evaluate how several key factors, including the molar ratio of HCOOH, molar ratio of H_2O_2, percentage of catalyst, reaction temperature and reaction time, that influenced the responses which were percentage yield of ESFOUFATMPE (yield), percentage of oxirane oxygen content (OOC) and iodine value (IV). These experiments produced both actual response values and model-predicted values for each response, which were summarised in Table 4.69, Table 4.70 and Table 4.71. A comparison of these values shows that the predicted results closely match the experimental outcomes, indicating that the model used to estimate the percentage yield, percentage OOC and IV were reliable.

Table 4.69
Experimental Run, Factors and Response for Percentage Yield of ESFOUFATMPE

Run	Factors					Response	
	Molar ratio HCOOH	Molar ratio H_2O_2	Catalyst (%)	Reaction time (h)	Reaction temp. (°C)	Yield (%)	
						Actual	Predicted
1	9	4	2	3	50	72.3	71.95
2	5	4	3	2	59	74.2	74.18
3	6	1	2	3	40	83.5	83.41
4	9	1	2	3	53	69.5	69.43
5	3	4	1	4	60	69.0	69.03
6	7	3	3	3	41	68.2	68.40
7	3	2	1	3	54	65.1	65.35
8	7	2	3	4	60	74.0	73.99
9	3	4	3	4	44	48.4	48.38
10	9	1	1	4	56	61.3	61.35
11	9	4	3	2	40	64.92	64.82
12	3	1	2	4	50	65.2	65.35
13	3	1	1	2	40	78.6	78.63
14	9	1	3	2	60	69.3	69.36
15	6	3	2	2	50	79.5	79.42
16	6	3	1	4	40	82.5	82.50
17	5	3	2	4	51	77.5	77.34
18	3	2	2	3	40	65.0	64.61
19	4	4	1	2	60	67.0	67.11
20	9	2	1	2	41	79.38	79.43
21	3	4	1	2	40	62.3	62.27
22	3	2	2	3	40	64.2	64.61
23	3	2	1	3	54	65.73	65.35
24	6	3	2	2	50	79.3	79.42
25	3	1	3	2	60	51.0	50.96
26	9	4	2	3	50	71.5	71.95
27	6	1	3	3	47	72.0	71.78
28	9	1	3	4	40	64.0	63.96
29	9	4	1	2	60	67.0	66.91
30	6	1	2	3	60	71.5	71.51
31	6	1	3	3	47	71.59	71.78

Table 4.70
Experimental Run, Factors and Response for Percentage of OOC of ESFOUFATMPE

Run	Factors					Response	
	Molar ratio HCOOH	Molar ratio H_2O_2	Catalyst (%)	Reaction time (h)	Reaction temp. (°C)	OOC (%)	
						Actual	Predicted
1	9	4	2	3	50	93.83	92.35
2	5	4	3	2	59	95.02	95.07
3	6	1	2	3	40	99.12	99.25
4	9	1	2	3	53	90.15	89.64
5	3	4	1	4	60	87.90	87.77
6	7	3	3	3	41	88.16	88.17
7	3	2	1	3	54	84.88	85.48
8	7	2	3	4	60	94.12	93.93
9	3	4	3	4	44	77.20	77.11
10	9	1	1	4	56	81.00	81.15
11	9	4	3	2	40	83.71	83.66
12	3	1	2	4	50	85.42	85.35
13	3	1	1	2	40	96.87	96.79
14	9	1	3	2	60	89.52	89.74
15	6	3	2	2	50	98.45	97.65
16	6	3	1	4	40	97.92	97.64
17	5	3	2	4	51	95.46	96.02
18	3	2	2	3	40	84.15	83.36
19	4	4	1	2	60	86.77	86.79
20	9	2	1	2	41	99.49	99.64
21	3	4	1	2	40	81.42	81.53
22	3	2	2	3	40	82.55	83.36
23	3	2	1	3	54	85.99	85.48
24	6	3	2	2	50	97.21	97.65
25	3	1	3	2	60	79.88	79.85
26	9	4	2	3	50	90.73	92.35
27	6	1	3	3	47	93.27	92.67
28	9	1	3	4	40	81.96	82.00
29	9	4	1	2	60	87.34	87.30
30	6	1	2	3	60	91.68	91.76
31	6	1	3	3	47	92.04	92.67

Table 4.71
Experimental Run, Factors and Response for Iodine Value of ESFOUFATMPE

Run	Factors					Response	
	Molar ratio HCOOH	Molar ratio H_2O_2	Catalyst (%)	Reaction time (h)	Reaction temp. (°C)	IV	
						Actual	Predicted
1	9	4	2	3	50	1.05	1.26
2	5	4	3	2	59	0.84	0.83
3	6	1	2	3	40	0.20	0.19
4	9	1	2	3	53	1.66	1.75
5	3	4	1	4	60	1.82	1.85
6	7	3	3	3	41	1.89	1.85
7	3	2	1	3	54	2.41	2.33
8	7	2	3	4	60	0.94	0.99
9	3	4	3	4	44	3.30	3.33
10	9	1	1	4	56	3.01	2.98
11	9	4	3	2	40	2.64	2.66
12	3	1	2	4	50	2.34	2.33
13	3	1	1	2	40	0.54	0.54
14	9	1	3	2	60	1.74	1.69
15	6	3	2	2	50	0.24	0.39
16	6	3	1	4	40	0.18	0.23
17	5	3	2	4	51	0.68	0.54
18	3	2	2	3	40	2.59	2.67
19	4	4	1	2	60	2.08	2.05
20	9	2	1	2	41	0.16	0.12
21	3	4	1	2	40	2.93	2.91
22	3	2	2	3	40	2.75	2.67
23	3	2	1	3	54	2.25	2.33
24	6	3	2	2	50	0.44	0.39
25	3	1	3	2	60	3.09	3.10
26	9	4	2	3	50	1.50	1.26
27	6	1	3	3	47	1.11	1.18
28	9	1	3	4	40	2.87	2.88
29	9	4	1	2	60	1.97	1.99
30	6	1	2	3	60	1.33	1.32
31	6	1	3	3	47	1.25	1.18

4.8.3.1 Determination of Selected Model

The selection of the analysis model was based on several statistical evaluations, including the sequential model sum of squares, lack-of-fit tests, model summary statistics and fit summary analysis, with the chosen model corresponding to the highest-order polynomial in which all additional terms were significant and non-aliased. The sequential model sum of squares analysis identified the quadratic model as the most suitable for describing the relationship between the process variables and the responses, as indicated by its high *F*-values and very low *p*-values. For the percentage yield of ESFOUFATMPE, the quadratic model showed an *F*-value of 1435.56 with a *p*-value of < 0.0001 (Table 4.72). In addition, the quadratic model was also highly significant for the percentage oxirane oxygen content (OOC) (Table 4.73) and iodine value (IV) (Table 4.74), with *p*-values of < 0.0001 and *F*-values of 111.11 and 124.37, respectively, demonstrating the suitability and reliability of the model for all studied responses.

Table 4.72
Sequential Model Sum of Squares of Percentage Yield of ESFOUFATMPE

Source	Sum of Squares	dF	Mean Square	*F*-value	*p*-value model	
Mean vs Total	149700	1	149700			
Linear vs Mean	357.09	5	71.42	1.12	0.3738	
2FI vs Linear	794.03	10	79.40	1.50	0.2326	
Quadratic vs 2FI	794.69	5	158.94	1435.56	< 0.0001	Suggested
Cubic vs Quadratic	0.1646	5	0.0329	0.1747	0.9608	Aliased
Residual	0.9425	5	0.1885			
Total	151700	31	4893.14			

Table 4.73
Sequential Model Sum of Squares of Percentage OOC of ESFOUFATMPE

Source	Sum of Squares	dF	Mean Square	*F*-value	*p*-value model	
Mean vs Total	248100	1	248100			
Linear vs Mean	148.73	5	29.75	0.7034	0.6262	
2FI vs Linear	538.61	10	53.86	1.56	0.2120	
Quadratic vs 2FI	509.44	5	101.89	111.11	< 0.0001	Suggested
Cubic vs Quadratic	0.9435	5	0.1887	0.1147	0.9835	Aliased
Residual	8.23	5	1.65			
Total	249300	31	8041.70			

Table 4.74
Sequential Model Sum of Squares of Iodine Value of ESFOUFATMPE

Source	Sum of Squares	dF	Mean Square	*F*-value	*p*-value model	
Mean vs Total	86.56	1	86.56			
Linear vs Mean	2.85	5	0.5704	0.5488	0.7377	
2FI vs Linear	12.96	10	1.30	1.49	0.2340	
Quadratic vs 2FI	12.82	5	2.56	124.37	< 0.0001	Suggested
Cubic vs Quadratic	0.0494	5	0.0099	0.3156	0.8843	Aliased
Residual	0.1566	5	0.0313			
Total	115.39	31	3.72			

The lack-of-fit analysis for the percentage yield (Table 4.75), percentage OOC (Table 4.76) and IV (Table 4.77) indicated that the lack of fit tests were not statistically significant, as the *p*-value was greater than 0.05, confirming the adequacy of the quadratic model. Specifically, the percentage yield showed a *p*-value of 0.9608 with an *F*-value of 0.1747. Similarly, the lack-of-fit tests for percentage oxirane oxygen content (OOC) and iodine value (IV) were also non-significant, with *p*-values of 0.9835 and 0.8843 and corresponding *F*-values of 0.1147 and 0.3156, respectively. These non-significant results demonstrate that the quadratic model adequately represents the experimental data without systematic error.

Table 4.75
Lack of Fit Test for Percentage Yield of ESFOUFATMPE

Source	Sum of Squares	dF	Mean Square	*F*-value	*p*-value model	
Linear	1588.88	20	79.44	421.45	< 0.0001	
2FI	794.85	10	79.49	421.67	< 0.0001	
Quadratic	0.1646	5	0.0329	0.1747	0.9608	Suggested
Cubic	0.0000	0				Aliased
Pure error	0.9425	5	0.1885			

Table 4.76
Lack of Fit Test for Percentage OOC of ESFOUFATMPE

Source	Sum of Squares	dF	Mean Square	*F*-value	*p*-value model	
Linear	1048.99	20	52.45	31.88	0.0006	
2FI	510.39	10	51.04	31.02	0.0007	
Quadratic	0.9435	5	0.1887	0.1147	0.9835	Suggested
Cubic	0.0000	0				Aliased
Pure error	8.23	5	1.65			

Table 4.77
Lack of Fit Test for Iodine Value of ESFOUFATMPE

Source	Sum of Squares	dF	Mean Square	*F*-value	*p*-value model	
Linear	25.83	20	1.29	41.21	0.0003	
2FI	12.87	10	1.29	41.06	0.0004	
Quadratic	0.0494	5	0.0099	0.3156	0.8843	Suggested
Cubic	0.0000	0				Aliased
Pure error	0.1567	5	0.0313			

The model summary statistics from Table 4.78, Table 4.79 and Table 4.80 indicate that the quadratic model provides an excellent fit for all studied responses, as reflected by the high R^2 and adjusted R^2 values, which were close to unity, along with low standard deviation values. For the percentage yield of ESFOUFATMPE, the model exhibited an R^2 value of 0.9994 and an adjusted R^2 of 0.9983, with a low standard deviation of 0.3327, indicating minimal prediction error and good model reliability. In addition, the PRESS value for percentage yield was 8.87, further confirming the strong predictive capability of the model. Similarly, the percentage oxirane oxygen content (OOC) showed an R^2 of 0.9924 and an adjusted R^2 of 0.9772, with a standard deviation of 0.9576 and a PRESS value of 69.41. The iodine value (IV) also demonstrated a good model fit, with an R^2 of 0.9929 and an adjusted R^2 of 0.9674, a low standard deviation of 0.1436 and a PRESS value of 2.83. Overall, the small standard deviation and PRESS values, together with the high R^2 and adjusted R^2 values, support the suitability of the quadratic model for predicting all response variables.

Table 4.78
Model Summary Statistic for Percentage Yield of ESFOUFATMPE

Source	Standard Deviation	R^2	Adjusted R^2	Predicted R^2	PRESS	
Linear	7.97	0.1834	0.0201	-0.4024	2730.44	
2FI	7.28	0.5913	0.1825	-4.8281	11346.80	
Quadratic	0.3327	0.9994	0.9983	0.9954	8.87	Suggested
Cubic	0.4342	0.9995	0.9971			Aliased

Table 4.79
Model Summary Statistic for Percentage OOC of ESFOUFATMPE

Source	Standard Deviation	R^2	Adjusted R^2	Predicted R^2	PRESS	
Linear	6.50	0.1233	-0.0520	-0.4663	1768.33	
2FI	5.88	0.5700	0.1399	-5.1684	7438.79	
Quadratic	0.9576	0.9924	0.9772	0.9424	69.41	Suggested
Cubic	1.28	0.9932	0.9591			Aliased

Table 4.80
Model Summary Statistic for Iodine Value of ESFOUFATMPE

Source	Standard Deviation	R^2	Adjusted R^2	Predicted R^2	PRESS	
Linear	1.02	0.0989	-0.0813	-0.4906	42.98	
2FI	0.9317	0.5484	0.0967	-5.3065	181.84	
Quadratic	0.1436	0.9929	0.9786	0.9017	2.83	Suggested
Cubic	0.1770	0.9946	0.9674			Aliased

4.8.3.2 Identification of Model Accuracy

Several diagnostic plots were used to evaluate the accuracy and reliability of the developed model, including the normal probability plot of residuals (Figure 4.82), residual versus predicted plot (Figure 4.83), actual versus predicted plot (Figure 4.84), residual versus run number plot (Figure 4.85), Cook's distance plot (Figure 4.86) and Box–Cox plot (Figure 4.87). The normal probability plot (Figure 4.82) shows that the residuals were randomly distributed along the straight regression line, indicating that the residuals follow a normal distribution and confirming the adequacy of the model for predicting the percentage yield of ESFOUFATMPE, Percentage of oxirane oxygen content (OOC) and iodine value (IV). The residual versus predicted plot (Figure 4.83) shows that all data points fall within the acceptable range of −4.29681 to 4.29681, suggesting that the model is appropriate and free from systematic errors. The Cook's distance plot (Figure 4.86) indicates that all data points lie below the threshold value of 1, with most points below 0.2, confirming that no influential outliers affect the model predictions. The Box–Cox plot (Figure 4.87) shows an optimum lambda value of 1.04, indicating that no data transformation is required for this optimization study.

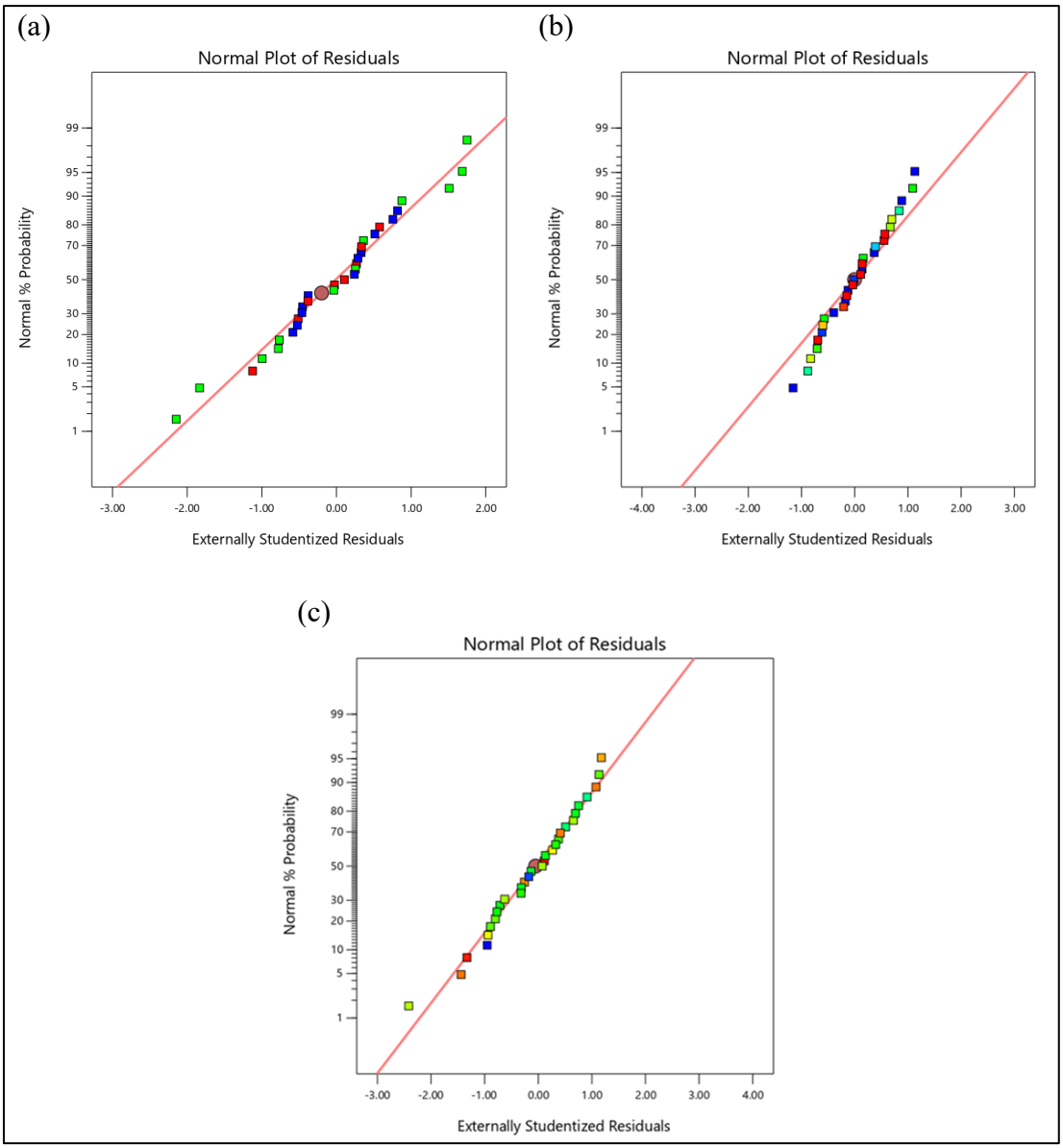


Figure 4.82 Normal Plot of Residual for (a) Percentage Yield, (b) Percentage OOC and (c) Iodine Value of ESFOUFATMPE

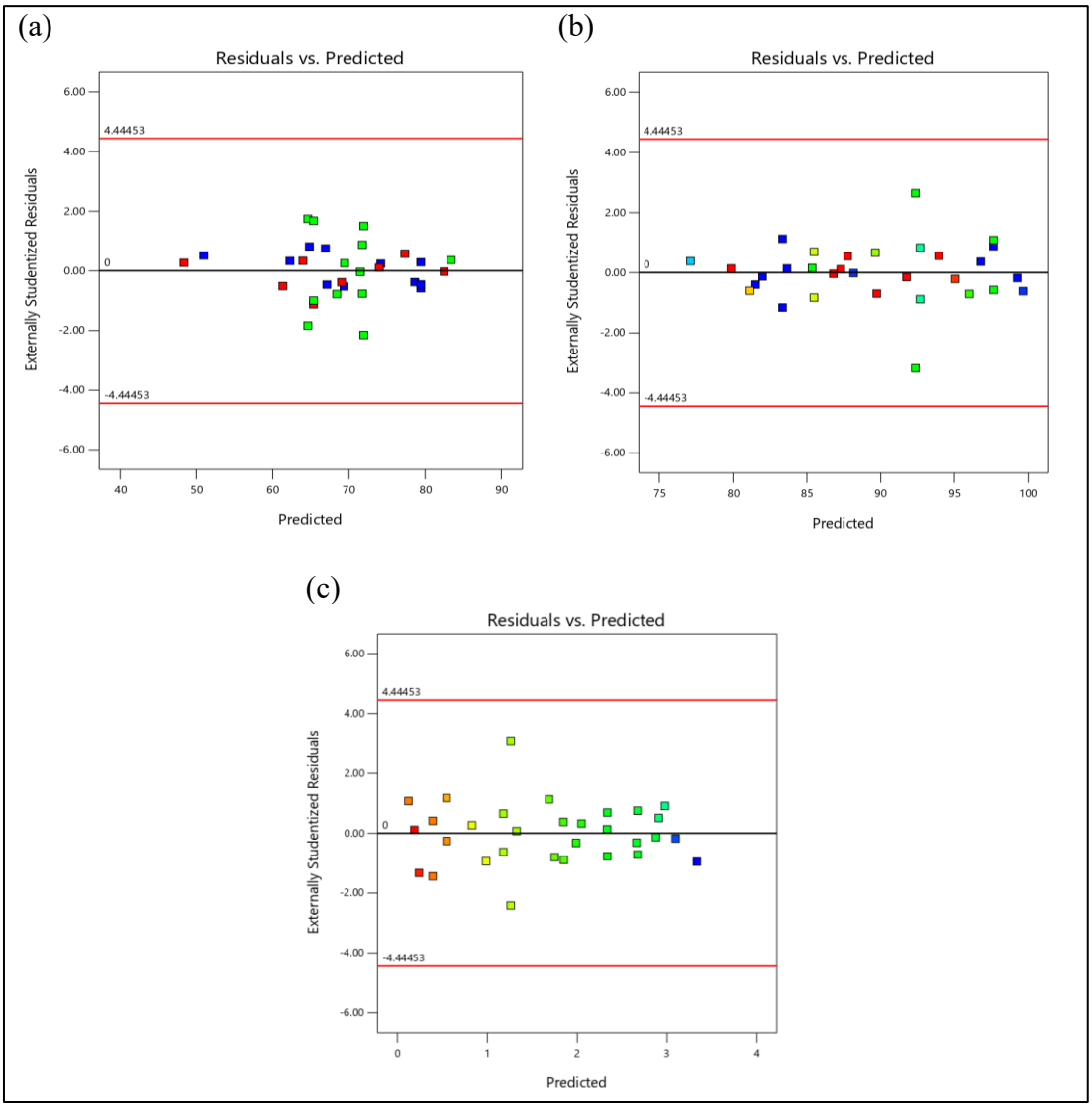


Figure 4.83 Residual versus Predicted Plot for (a) Percentage Yield, (b) Percentage OOC and (c) Iodine Value of ESFOUFATMPE

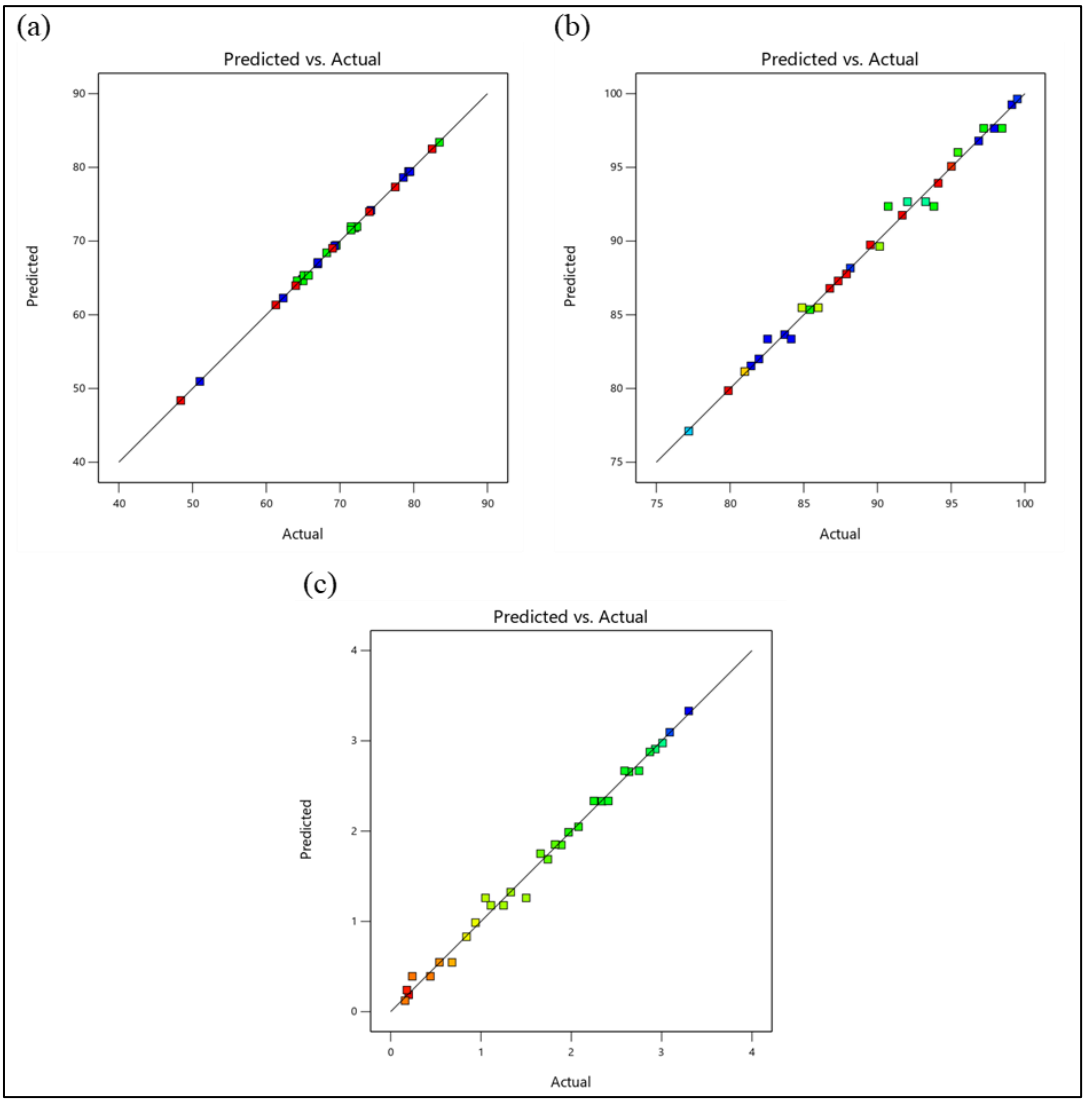


Figure 4.84 Actual versus Predicted for (a) Percentage Yield, (b) Percentage OOC and (c) Iodine Value of ESFOUFATMPE

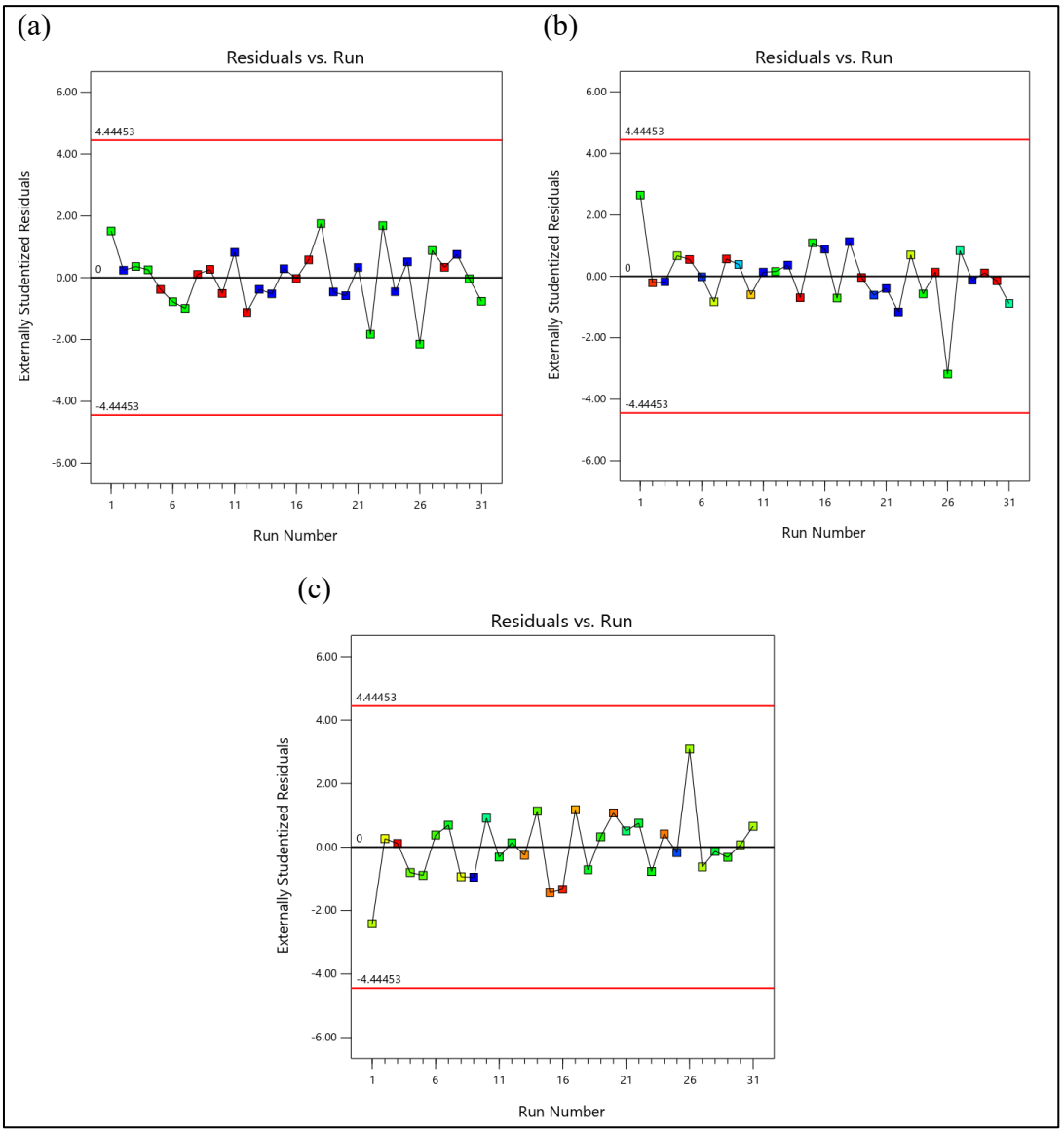


Figure 4.85 Residual versus Run Number for (a) Percentage Yield, (b) Percentage OOC and (c) Iodine Value of ESFOUFATMPE

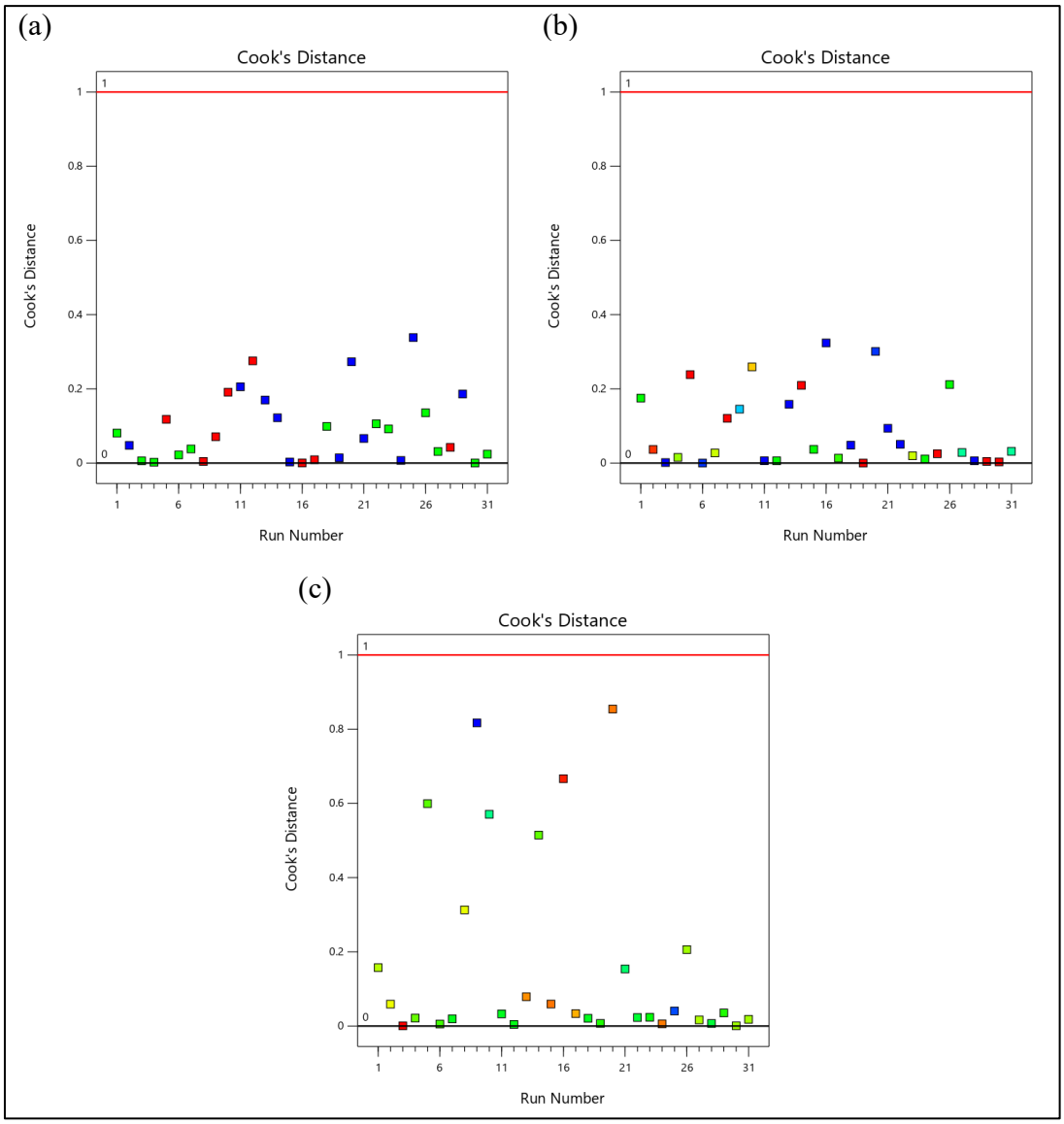


Figure 4.86 Cook's Distance Plot for (a) Percentage Yield, (b) Percentage OOC and (c) Iodine Value of ESFOUFATMPE

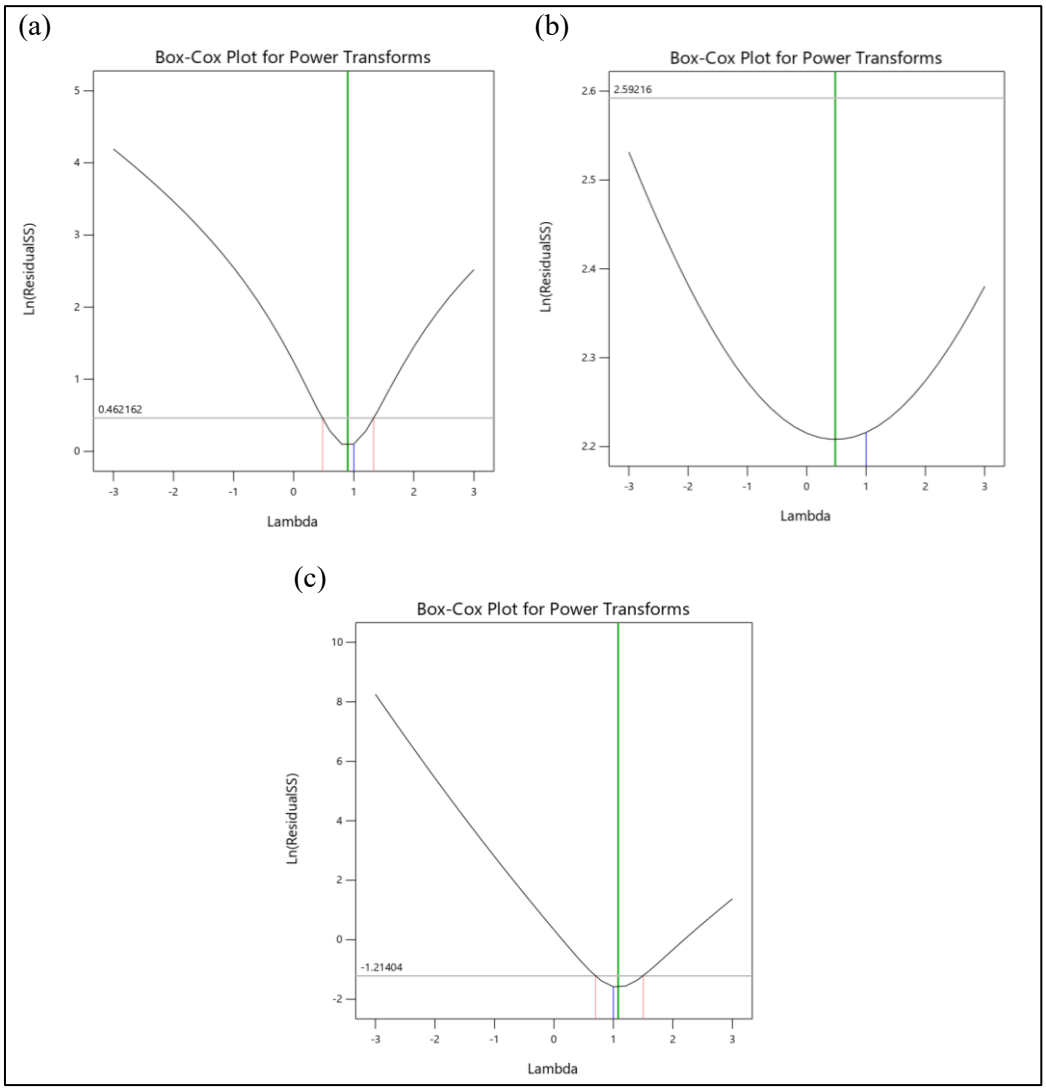


Figure 4.87 Box-Cox Plot for (a) Percentage Yield, (b) Percentage OOC and (c) Iodine Value of ESFOUFATMPE

4.8.3.3 Analysis of Variance

The ANOVA results for the studied responses were presented in Table 4.81 The models show a highly significant effect on all responses, with *p*-values of < 0.0001. For the percentage yield of ESFOUFATMPE, the model exhibited an *F*-value of 878.75 and a high R^2 value of 0.9994, indicating an excellent fit between the predicted and experimental data. Similarly, the percentage OOC showed a significant model with an *F*-value of 65.26 and an R^2 value of 0.9924, while the IV also demonstrated strong model significance with an *F*-value of 69.45 and an R^2 value of 0.9929. These results confirm the reliability and adequacy of the developed models for predicting all response variables.

Table 4.81
Summary of ANOVA Analysis for Percentage Yield, Percentage OOC and Iodine Value of ESFOUFATMPE

Source	Percentage yield	Percentage OOC	IV
p-value model	< 0.0001	< 0.0001	< 0.0001
F-value model	878.75	65.26	69.45
p-value Lack of Fit	0.9608	0.9835	0.8843
F-value Lack of Fit	0.1747	0.1147	0.3156
R^2	0.9994	0.9924	0.9929
Adjusted R^2	0.9983	0.9772	0.9786
Predicted R^2	0.9954	0.9424	0.9017
Standard deviation	0.3327	0.9576	0.1436
Coefficient of variation (C.V %)	0.4788	1.07	8.59
Adequate precision	127.9073	28.5801	27.1538

The ANOVA results indicate that the developed quadratic models were statistically significant for all studied responses, including the percentage yield of ESFOUFATMPE, percentage oxirane oxygen content (OOC) and iodine value (IV). For the percentage yield of ESFOUFATMPE, all major model terms, including linear, interaction and quadratic terms, show *p*-values less than 0.05, demonstrating their significant influence on the response, as presented in Table 4.82. This finding further supports the screening results, which identified these variables as important contributors to the percentage yield. Similarly, the ANOVA analysis for percentage OOC (Table 4.83) reveals that several linear, interaction and quadratic terms were statistically significant, indicating that the process variables have a strong effect on oxirane oxygen formation and confirming the suitability of the quadratic model. In addition, the ANOVA results for IV (Table 4.84) show that key model terms significantly affect the iodine value, reflecting the influence of reaction conditions on the degree of unsaturation. The regression equations for all the responses were shown below:

$$\text{Yield (\%)} = 78.71 + 4.61A - 0.5355B - 3.62C - 0.4067D - 0.9547E + 0.7998AB + 3.63AC - 2.10AD - 0.3428AE + 0.7938BC + 1.05BD + 5.0BE - 0.8369CD + 4.59CE + 1.02DE - 10.99\ A^2 - 0.6397B^2 - 2.71C^2 + 0.9082D^2 - 1.15E^2$$

$$\text{OOC (\%)} = 97.08 + 3.35A - 0.1787B - 2.12C - 0.8036D - 0.0264E + 0.7328AB + 1.56AC - 1.74AD - 0.9818AE + 0.9352BC + 2.06BD + 3.72BE + 0.2880CD + 2.27CE + 0.800DE - 8.94A^2 - 0.2976B^2 - 1.50C^2 + 0.4730D^2 - 2.06E^2$$

$$\text{IV} = 0.4971 - 0.4952A - 0.0047B + 0.3448C + 0.0910D + 0.0204E - 0.1182AB - 0.2102AC + 0.2659AD + 0.1494AE - 0.1419BC - 0.3769BD - 0.5480BE - 0.0609CD - 0.06394CE - 0.0968DE + 1.45A^2 - 0.0700B^2 + 0.2095C^2 - 0.1302D^2 + 0.3241E^2$$

Table 4.82
ANOVA Analysis Factors for Percentage Yield of ESFOUFATMPE

Source	Sum of Squares	dF	Mean Square	*F*-value	*p*-value model	Significance
A-HCOOH	324.42	1	324.42	2930.27	< 0.0001	Significant
B-H_2O_2	4.40	1	4.40	39.77	< 0.0001	Significant
C-H_2SO_4	167.10	1	167.10	1509.26	< 0.0001	Significant
D-Time	2.29	1	2.29	20.68	0.0011	Significant
E-Temperature	12.47	1	12.47	112.60	< 0.0001	Significant
AB	7.20	1	7.20	65.01	< 0.0001	Significant
AC	128.55	1	128.55	1161.07	< 0.0001	Significant
AD	37.69	1	37.69	340.45	< 0.0001	Significant
AE	1.07	1	1.07	9.65	0.0111	Significant
BC	6.29	1	6.29	56.86	< 0.0001	Significant
BD	9.35	1	9.35	84.47	< 0.0001	Significant
BE	226.30	1	226.30	2043.96	< 0.0001	Significant
CD	7.20	1	7.20	64.99	< 0.0001	Significant
CE	149.96	1	149.96	1354.45	< 0.0001	Significant
DE	9.33	1	9.33	84.32	< 0.0001	Significant
A^2	522.97	1	522.97	4723.57	< 0.0001	Significant
B^2	1.56	1	1.56	14.08	0.0038	Significant
C^2	33.82	1	33.82	305.44	< 0.0001	Significant
D^2	3.57	1	3.57	32.21	0.0002	Significant
E^2	5.53	1	5.53	49.96	< 0.0001	Significant

Table 4.83
ANOVA Analysis Factors for Percentage OOC of ESFOUFATMPE

Source	Sum of Squares	dF	Mean Square	*F*-value	*p*-value model	Significance
A-HCOOH	171.60	1	171.60	187.13	< 0.0001	Significant
B-H_2O_2	0.4902	1	0.4902	0.5345	0.4815	Not Significant
C-H_2SO_4	57.21	1	57.21	62.39	< 0.0001	Significant
D-Time	8.94	1	8.94	9.75	0.0108	Significant
E-Temperature	0.0096	1	0.0096	0.0104	0.9207	Not Significant
AB	6.04	1	6.04	6.59	0.0280	Significant
AC	23.91	1	23.91	26.08	0.0005	Significant
AD	25.84	1	25.84	28.18	0.0003	Significant
AE	8.77	1	8.77	9.56	0.0114	Significant
BC	8.74	1	8.74	9.53	0.0115	Significant
BD	35.83	1	35.83	39.08	< 0.0001	Significant
BE	125.49	1	125.49	136.85	< 0.0001	Significant
CD	0.8520	1	0.8520	0.9291	0.3578	Not Significant
CE	129.99	1	129.99	141.75	< 0.0001	Significant
DE	5.75	1	5.75	6.28	0.0312	Significant
A^2	345.70	1	345.70	377.00	< 0.0001	Significant
B^2	0.3407	1	0.3407	0.3715	0.5558	Not Significant
C^2	10.27	1	10.27	11.20	0.0074	Significant
D^2	0.9673	1	0.9673	1.05	0.3286	Not Significant
E^2	17.76	1	17.76	19.37	0.0013	Significant

Table 4.84
ANOVA Analysis Factors for Iodine Value of ESFOUFATMPE

Source	Sum of Squares	dF	Mean Square	*F*-value	*p*-value model	Significance
A-HCOOH	3.74	1	3.74	181.66	< 0.0001	Significant
B-H_2O_2	0.0003	1	0.0003	0.0168	0.8995	Not Significant
C-H_2SO_4	1.51	1	1.51	73.50	< 0.0001	Significant
D-Time	0.1147	1	0.1147	5.57	0.0400	Significant
E-Temperature	0.0057	1	0.0057	0.2775	0.6098	Not Significant
AB	0.1573	1	0.1573	7.63	0.0200	Significant
AC	0.4316	1	0.4316	20.94	0.0010	Significant
AD	0.6017	1	0.6017	29.20	0.0003	Significant
AE	0.2030	1	0.2030	9.85	0.0105	Significant
BC	0.2012	1	0.2012	9.76	0.0108	Significant
BD	1.19	1	1.19	57.94	< 0.0001	Significant
BE	2.72	1	2.72	132.11	< 0.0001	Significant
CD	0.0382	1	0.0382	1.85	0.2035	Not Significant
CE	2.91	1	2.91	141.17	< 0.0001	Significant
DE	0.0843	1	0.0843	4.09	0.0707	Not Significant
A^2	9.11	1	9.11	442.06	< 0.0001	Significant
B^2	0.0189	1	0.0189	0.9155	0.3612	Not Significant
C^2	0.2015	1	0.2015	9.77	0.0108	Significant
D^2	0.0733	1	0.0733	3.56	0.0886	Not Significant
E^2	0.4397	1	0.4397	21.34	0.0010	Significant

4.8.3.4 Interaction Between Variables

The interaction between variables (molar ratio HCOOH (A), molar ratio H_2O_2 (B), percentage catalyst (C), reaction time (D) and reaction temperature (E)) can be illustrated through the 3-dimentional (3D) response surface plot. Figure 4.88, Figure 4.89, Figure 4.90, Figure 4.91, Figure 4.92 and Figure 4.93 show the 3D response surface for the interaction between variables with the three responses (percentage yield of ESFOUFATMPE, percentage of OOC and IV), respectively.

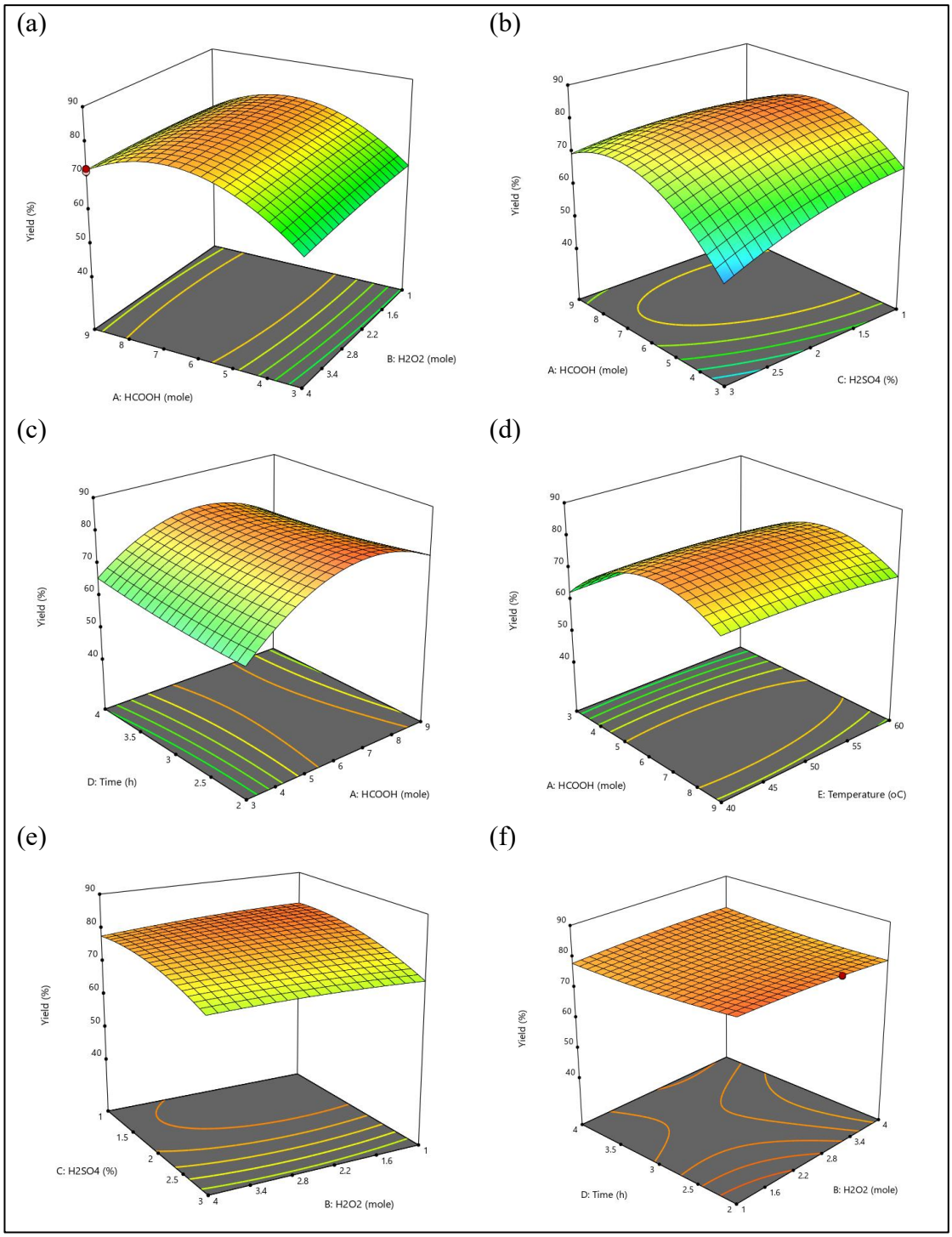


Figure 4.88 3D Surface Plot for a) AB, b) AC, c) AD, d) AE e) BC and f) BD for Percentage Yield of ESFOUFATMPE

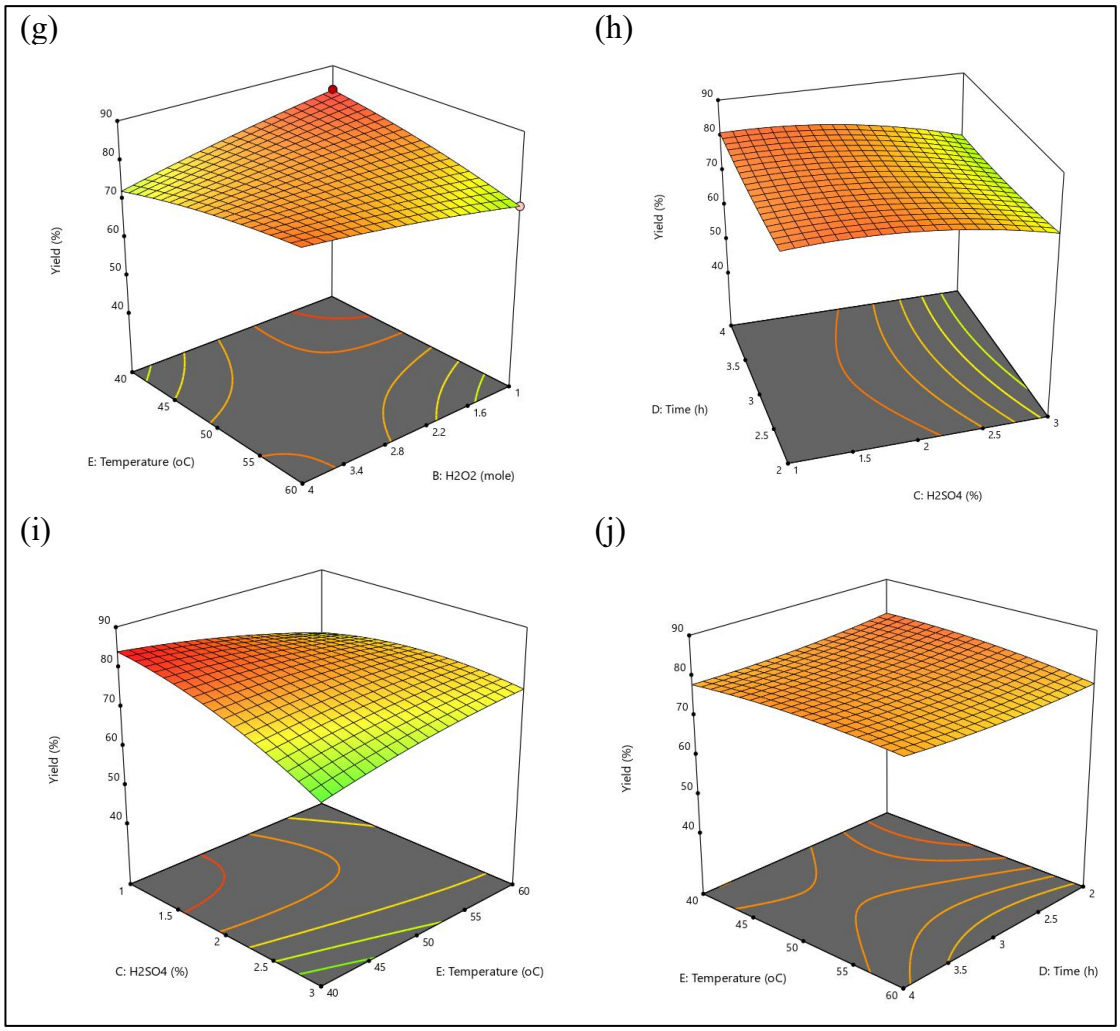


Figure 4.89 3D Surface Plot for g) BE, h) CD, i) CE and j) DE for Percentage Yield of ESFOUFATMPE

Figure 4.88 (a) illustrates the interaction between molar ratio of formic acid (A: HCOOH) and molar ratio of hydrogen peroxide (B: H_2O_2) on the percentage yield of ESFOUFATMPE. Increasing the molar ratio HCOOH amount from the lower level to a moderate level results in an increase in the percentage yield, which can be attributed to enhanced formation of performic acid that promotes effective epoxidation. Similarly, increasing the molar ratio H_2O_2 contributes positively to the yield by providing sufficient oxidizing agent. However, excessive levels of either HCOOH or H_2O_2 lead to a slight reduction in yield, possibly due to over-oxidation or decomposition of the epoxide ring. Figure 4.88 (b) shows the interaction between molar ratio of formic acid (A) and percentage sulfuric acid (C: H_2SO_4). The percentage yield increases with increasing molar ratio HCOOH and moderate percentage H_2SO_4, indicating that sufficient acid catalysis enhances the formation of the epoxidizing species. However, further increases in percentage H_2SO_4 result in a decline in yield, which may be due to

excessive acidity promoting side reactions such as ring opening of the epoxide, thereby reducing the overall yield of ESFOUFATMPE.

Figure 4.88 **(**c) presents the interaction between molar ratio of formic acid (A) and reaction time (D). The percentage yield increases as both molar ratio HCOOH and reaction time were increased to an optimum level, suggesting that longer reaction times allow more complete conversion of unsaturated bonds. Beyond this optimum region, the yield begins to decrease, which may be attributed to prolonged exposure to acidic conditions leading to epoxide degradation or secondary reactions. Figure 4.88 (d) depicts the interaction between molar ratio of formic acid (A) and reaction temperature (E). An increase in temperature from the lower range enhances the percentage yield, especially at moderate HCOOH levels, due to improved reaction kinetics and mass transfer. However, further increases in temperature lead to a reduction in yield, likely caused by thermal instability of the epoxide groups or acceleration of undesired side reactions.

Figure 4.88 (e) illustrates the combined effect of molar ratio of hydrogen peroxide (B) and percentage sulfuric acid (C). Increasing both variables up to their optimal levels leads to a higher percentage yield, indicating a synergistic effect between oxidant availability and acid catalysis. Excessive percentage sulfuric acid, however, results in a decrease in yield, which may be due to increased ring-opening reactions and reduced epoxide stability. Figure 4.88 (f) shows the interaction between molar ratio of hydrogen peroxide (B) and reaction time (D). The percentage yield increases with increasing molar ratio H_2O_2 and longer reaction time up to an optimum, as sufficient oxidant and time promote effective epoxidation. Beyond this region, a decrease in yield is observed, possibly due to oxidative degradation or prolonged acidic exposure affecting the epoxide structure.

Figure 4.89 (g) presents the interaction between molar ratio of hydrogen peroxide (B) and reaction temperature (E). The yield of ESFOUFATMPE increases with increasing temperature and moderate molar ratio H_2O_2, reflecting enhanced reaction rates at elevated temperatures. However, excessive temperature combined with high oxidant concentration leads to a slight decline in yield, which may be attributed to epoxide ring instability or peroxide decomposition. Figure 4.89 (h) shows the interaction between percentage sulfuric acid (C) and reaction time (D). Increasing both variables initially improves the percentage yield due to enhanced catalytic activity and sufficient reaction duration. Nevertheless, higher percentage sulfuric acid combined

with extended reaction time results in a decrease in yield, likely caused by acid-catalyzed ring opening or hydrolysis reactions.

Figure 4.89 (i) illustrates the interaction between percentage sulfuric acid (C) and reaction temperature (E). Increasing the temperature at moderate sulfuric acid levels enhances the yield, suggesting improved catalytic efficiency and reaction kinetics. However, higher percentage sulfuric acid at elevated temperatures reduces the yield, which may be due to excessive acidity accelerating undesired side reactions. Figure 4.89 (j) depicts the interaction between reaction time (D) and reaction temperature (E). The percentage yield increases with increasing reaction time and temperature up to an optimum region, indicating that sufficient thermal energy and time were required for effective epoxidation. Beyond this optimum, further increases lead to a reduction in yield, likely due to thermal degradation or prolonged exposure to acidic conditions.

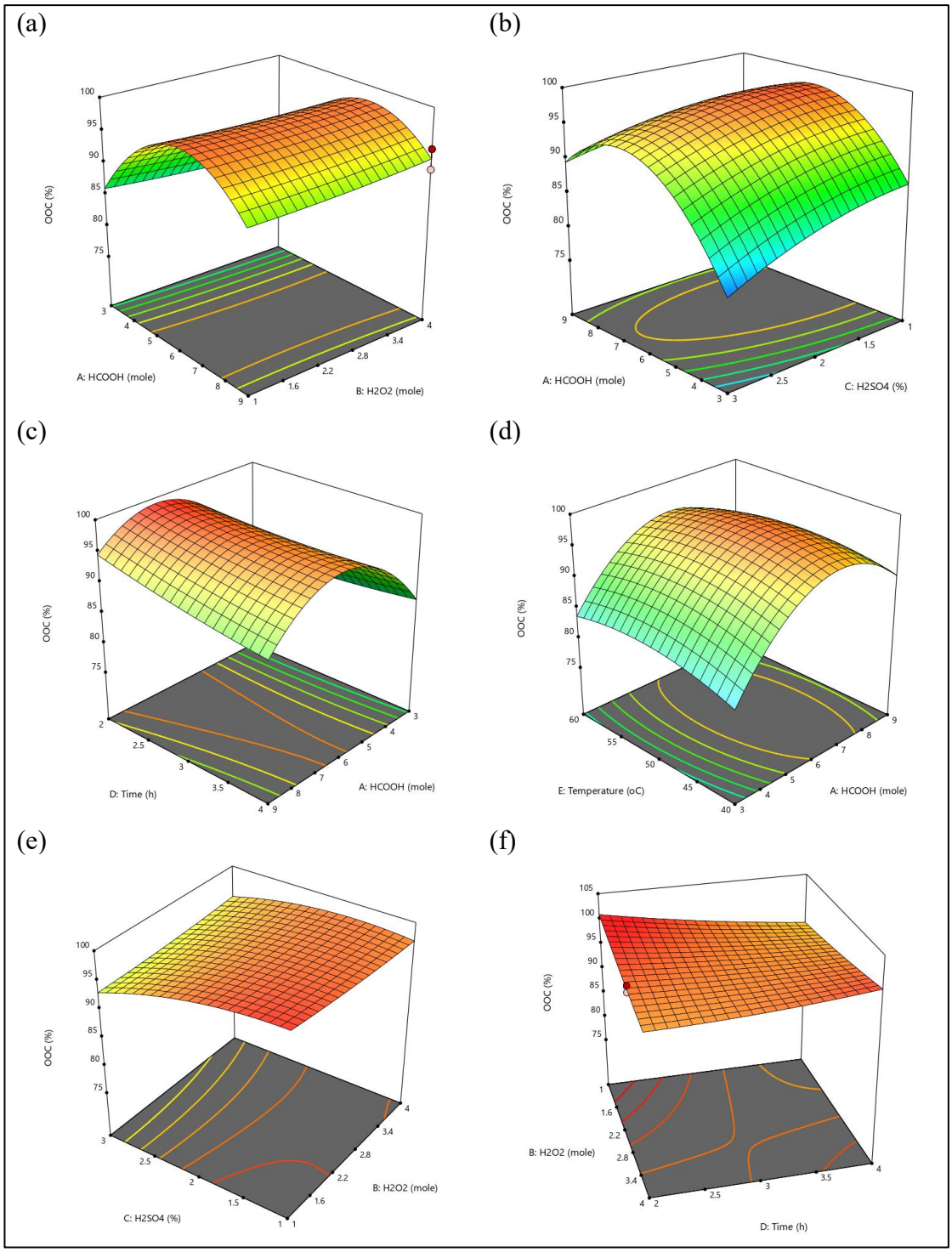


Figure 4.90 3D Surface Plot for a) AB, b) AC, c) AD, d) AE e) BC and f) BD for Percentage OOC of ESFOUFATMPE

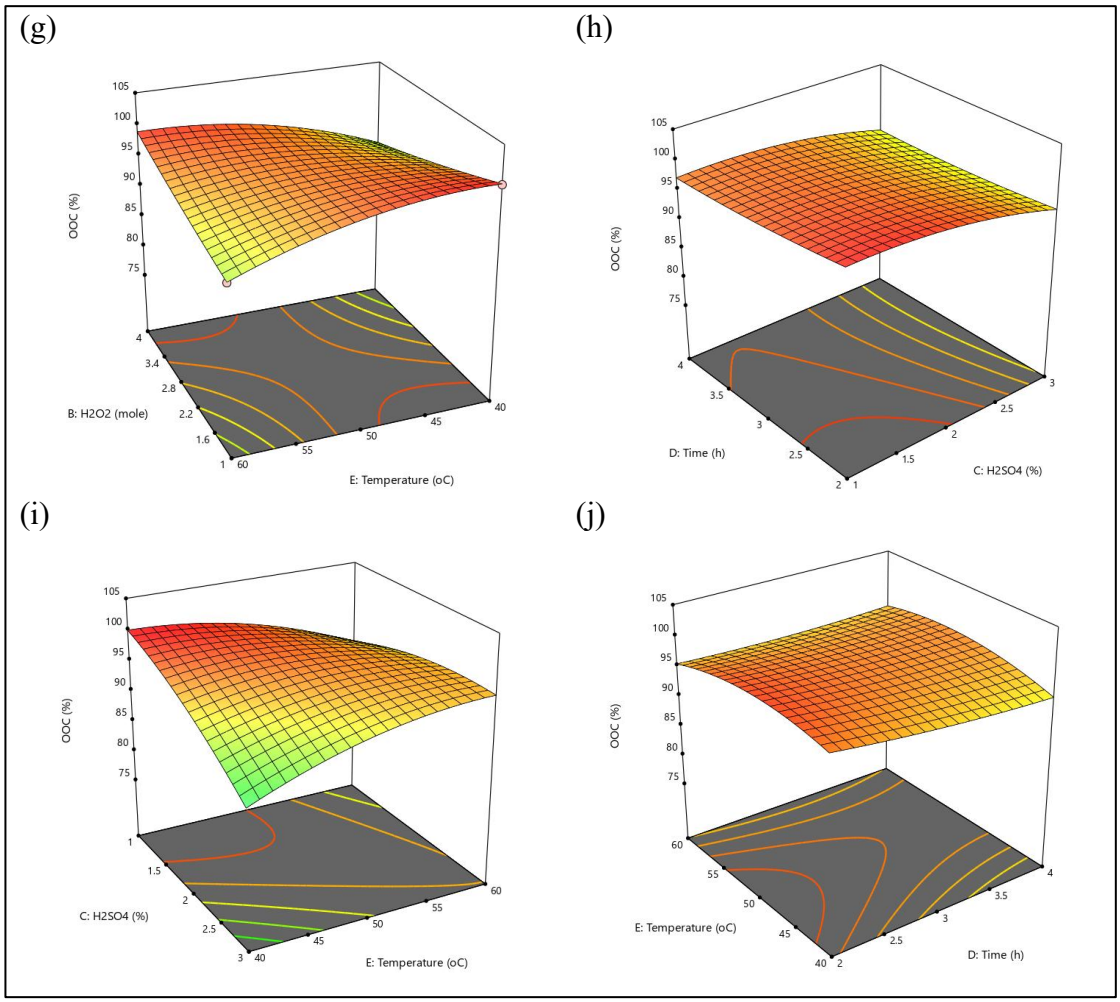


Figure 4.91 3D Surface Plot for g) BE, h) CD, i) CE and j) DE for Percentage OOC of ESFOUFATMPE

Figure 4.90 (a) shows the interaction between molar ratio of formic acid (A: HCOOH) and molar ratio of hydrogen peroxide (B: H_2O_2) on the percentage of OOC. Increasing the molar ratio HCOOH from the lower range to a moderate level results in a noticeable increase in OOC, which can be attributed to enhanced formation of performic acid that promotes epoxidation. Similarly, increasing the molar ratio H_2O_2 improves the OOC due to sufficient availability of the oxidizing agent. However, at higher molar ratio of both HCOOH and H_2O_2, the OOC slightly decreases, possibly due to peroxide decomposition or epoxide ring instability under highly oxidative conditions. Figure 4.90 (b) illustrates the interaction between formic acid (A) and percentage sulfuric acid (C: H_2SO_4). The percentage of OOC increases with increasing molar ratio HCOOH at moderate H_2SO_4 levels, indicating that controlled acid catalysis enhances oxirane formation. Nevertheless, further increasing the percentage sulfuric acid results

in a reduction in OOC, which may be attributed to excessive acidity promoting epoxide ring-opening reactions and reducing oxirane stability.

Figure 4.90 (c) presents the interaction between molar ratio of formic acid (A) and reaction time (D). Increasing both molar ratio HCOOH and reaction time initially leads to higher OOC, as longer reaction times allow more complete conversion of double bonds into oxirane rings. However, excessive reaction time combined with higher molar ratio HCOOH causes a decline in OOC, likely due to prolonged exposure to acidic conditions that favors oxirane degradation. Figure 4.90 (d) shows the interaction between molar ratio HCOOH (A) and reaction temperature (E). An increase in temperature from the lower range enhances the percentage of OOC at moderate molar ratio HCOOH, owing to improved reaction kinetics. However, further increases in temperature result in a decrease in OOC, possibly due to thermal instability of the oxirane rings and acceleration of side reactions.

Figure 4.90 (e) depicts the interaction between molar ratio hydrogen peroxide (B) and percentage sulfuric acid (C). Increasing molar ratio H_2O_2 enhances the OOC, particularly at lower to moderate sulfuric acid levels, indicating effective epoxidation under controlled acidic conditions. Excessive percentage sulfuric acid, however, leads to a reduction in OOC, which may be due to increased ring-opening reactions caused by strong acidity. Figure 4.90 (f) illustrates the interaction between molar ratio hydrogen peroxide (B) and reaction time (D). The percentage of OOC increases with increasing molar ratio H_2O_2 and longer reaction time up to an optimum, as sufficient oxidant and time favor epoxide formation. Beyond this optimum, a decrease in OOC is observed, likely due to oxidative degradation or prolonged acidic exposure affecting oxirane stability.

Figure 4.91 (g) shows the combined effect of molar ratio hydrogen peroxide (B) and reaction temperature (E). Increasing temperature and molar ratio H_2O_2 enhances the OOC up to an optimum region, reflecting improved reaction rates and oxidant efficiency. However, excessive temperature coupled with high oxidant concentration results in a slight decrease in OOC, which may be attributed to peroxide decomposition and epoxide ring instability. Figure 4.91 (h) presents the interaction between percentage sulfuric acid (C) and reaction time (D). Increasing both parameters initially improves the percentage of OOC, indicating enhanced catalytic activity over sufficient reaction duration. Nevertheless, higher percentage sulfuric acid combined with extended

reaction time leads to a reduction in OOC, likely due to acid-catalyzed ring opening and oxirane degradation.

Figure 4.91 (i) illustrates the interaction between percentage sulfuric acid (C) and reaction temperature (E). The percentage of OOC increases with increasing temperature at moderate sulfuric acid levels, suggesting improved catalytic efficiency. However, excessive percentage sulfuric acid at elevated temperatures results in a decline in OOC, which may be attributed to strong acidic and thermal conditions destabilizing the oxirane rings. Figure 4.91 (j) shows the interaction between reaction time (D) and reaction temperature (E). Increasing both reaction time and temperature enhances the percentage of OOC up to an optimum region, indicating favorable conditions for oxirane formation. Beyond this region, further increases result in a slight decrease in OOC, likely due to prolonged thermal exposure and acid-catalyzed degradation of oxirane groups.

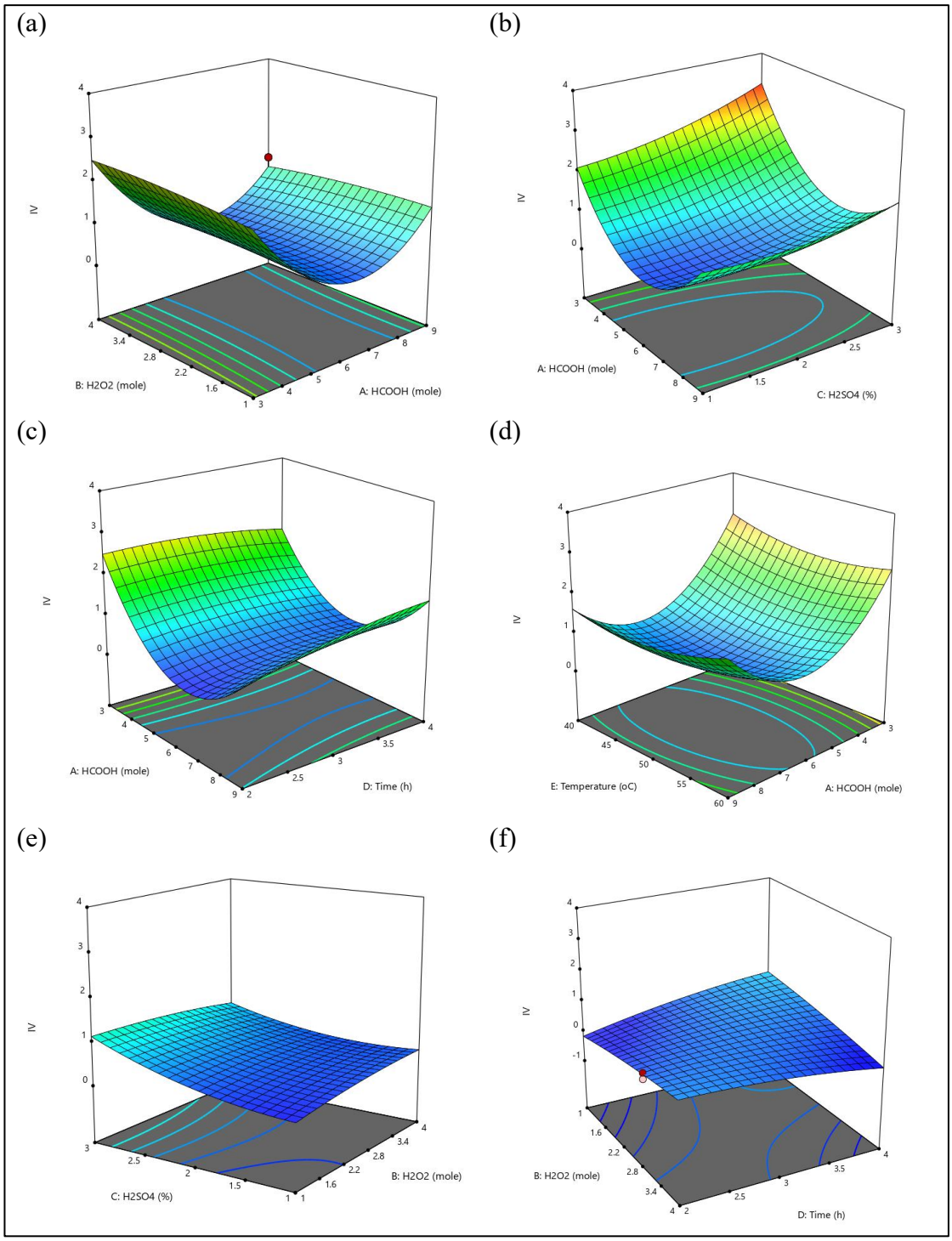


Figure 4.92 3D Surface Plot for a) AB, b) AC, c) AD, d) AE e) BC and f) BD for Iodine Value of ESFOUFATMPE

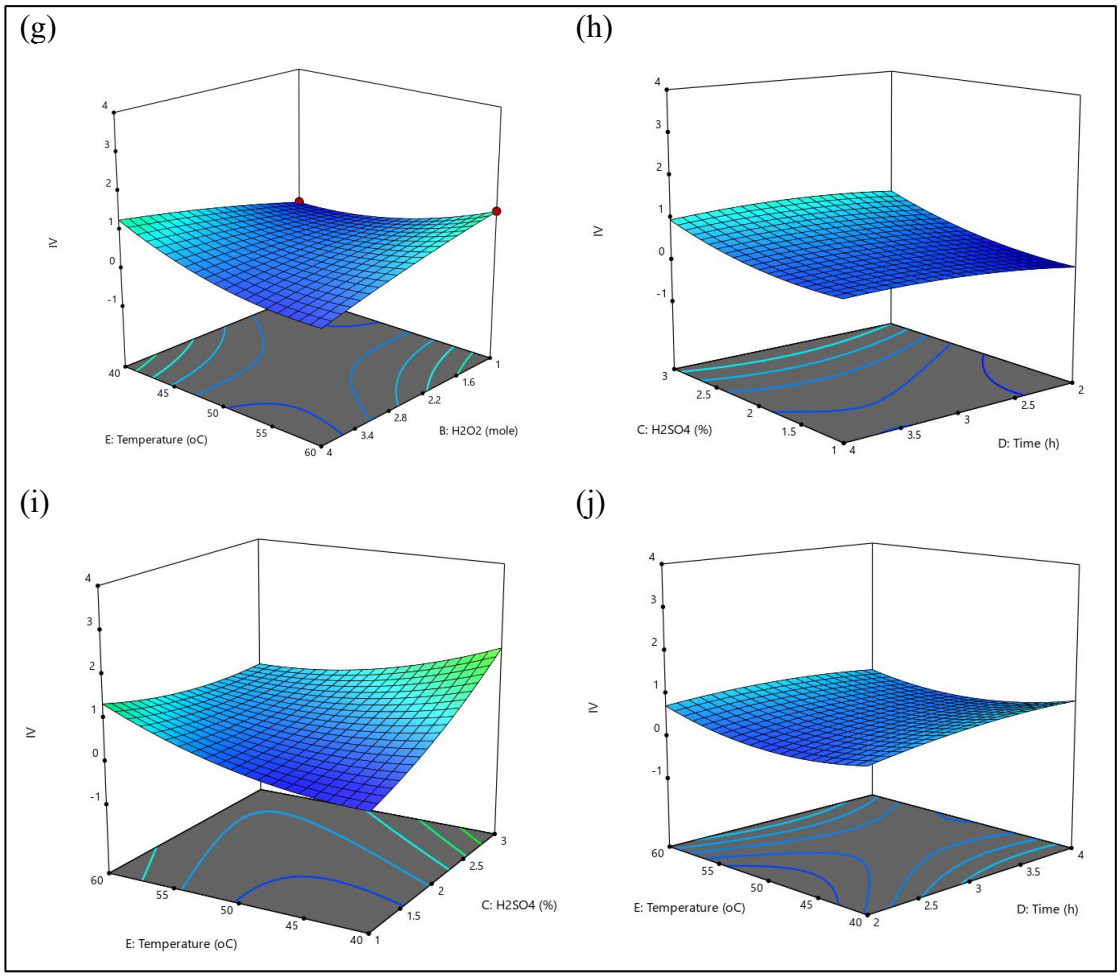


Figure 4.93 3D Surface Plot for g) BE, h) CD, i) CE and j) DE for Iodine Value of ESFOUFATMPE

Figure 4.92 (a) illustrates the interaction between molar ratio formic acid (A: HCOOH) and molar ratio hydrogen peroxide (B: H_2O_2) on the iodine value. Increasing the molar ratio HCOOH leads to a noticeable decrease in IV, indicating effective consumption of carbon-carbon double bonds during the epoxidation process. Similarly, increasing the molar ratio H_2O_2 contributes to a reduction in IV due to enhanced oxidizing capability. However, at higher concentrations of both variables, the decrease in IV becomes less pronounced, suggesting that most reactive double bonds have already been converted. Figure 4.92 (b) shows the interaction between molar ratio formic acid (A) and percentage sulfuric acid (C: H_2SO_4). The iodine value decreases as the molar ratio HCOOH increases, particularly at moderate percentage sulfuric acid levels, indicating improved epoxidation efficiency. Excessive amount of sulfuric acid, results in a less significant reduction in IV, possibly due to side reactions or acid-catalyzed degradation that limits further conversion of unsaturated bonds.

Figure 4.92 (c) presents the interaction between molar ratio formic acid (A) and reaction time (D). Increasing the reaction time from the lower range leads to a reduction in IV, especially at moderate HCOOH levels, as longer reaction duration allows greater conversion of unsaturation. Beyond an optimum time, the IV shows only a slight change, indicating that the reaction approaches completion and further extension offer minimal benefit. Figure 4.92 (d) depicts the interaction between molar ratio formic acid (A) and reaction temperature (E). An increase in reeduction of iodine value is observed with increasing temperature up to an optimum range, particularly at moderate molar ratio HCOOH, due to accelerated reaction kinetics. Further increases in temperature result in a less significant decrease in IV, which may be attributed to thermal degradation or competing side reactions.

Figure 4.92 (e) shows the interaction between molar ratio hydrogen peroxide (B) and percentage sulfuric acid (C). Increasing the molar ratio H_2O_2 leads to a continuous decrease in IV, reflecting improved oxidation of double bonds. The effect of sulfuric acid is less pronounced, although moderate molar ratio enhance the reduction of IV, indicating that sufficient acid catalysis supports efficient epoxidation. Figure 4.92 (f) illustrates the interaction between molar ratio hydrogen peroxide (B) and reaction time (D). The iodine value decreases with increasing reaction time and molar ratio H_2O_2, confirming that sufficient oxidant and reaction duration were required for effective conversion of unsaturated bonds. At higher levels, the change in IV becomes gradual, suggesting that most double bonds have already reacted.

Figure 4.93 (g) presents the interaction between molar ratio hydrogen peroxide (B) and reaction temperature (E). Increasing temperature enhances the reduction in IV, particularly at moderate molar ratio H_2O_2, due to faster reaction rates. However, excessive temperature does not significantly improve the reduction of IV, indicating that the epoxidation reaction has reached a limiting stage.

Figure 4.93 (h) shows the interaction between percentage sulfuric acid (C) and reaction time (D). Increasing both parameters results in a gradual decrease in IV, suggesting improved catalytic efficiency and reaction completeness. Nevertheless, excessive percentage sulfuric acid combined with longer reaction time shows minimal additional reduction, likely due to saturation of the reaction system.

Figure 4.93 (i) illustrates the interaction between percentage sulfuric acid (C) and reaction temperature (E). The iodine value decreases with increasing temperature at moderate sulfuric acid levels, indicating enhanced reaction kinetics. At higher

percentage sulfuric acid, the reduction in IV becomes less significant, which may be associated with competing acid-catalyzed side reactions.

Figure 4.93 (j) depicts the interaction between reaction time (D) and reaction temperature (E). Increasing both variables results in a reduction in iodine value up to an optimum region, demonstrating that sufficient thermal energy and reaction duration promote effective epoxidation. Beyond this region, further increases lead to only minor changes in IV, suggesting that most unsaturated bonds have been converted.

4.8.3.5 Verification Model

Numerical optimization was performed to determine the optimum conditions for the reaction by simultaneously evaluating the effects of formic acid (A, HCOOH), hydrogen peroxide (B, H_2O_2), catalyst percentage (C), reaction time (D) and reaction temperature (E). Each parameter was varied within its specified experimental range, while the responses, namely percentage yield, oxirane oxygen content (OOC) and iodine value (IV), were optimized according to the defined criteria. Table 4.85 summarizes the constraints applied in the optimization process to achieve a high percentage yield and OOC while minimizing the iodine value. The optimization results show that the predicted model achieved a desirability value of 1.00, indicating that the selected conditions represent an ideal solution within the studied design space. Figure 4.94 presents the predicted response values obtained from the numerical optimization of the reaction system.

Table 4.85
Restraints for Optimization of Epoxidation of SFOUFATMPE Parameter and Response for D-Optimal Design

Parameter and responses	Goal	Lower limit	Upper limit	Weight	Importance
A: HCOOH	is in range	3	9	1	1
B: H_2O_2	is in range	1	4	1	1
C: Percentage catalyst	is in range	1	3	1	1
D: Time	is in range	2	4	1	1
E: Temperature	is in range	40	60	1	1
Yield	maximize	48.4	83.5	1	1
OOC	maximize	77.20	99.49	1	1
IV	minimize	0.16	3.30	1	1

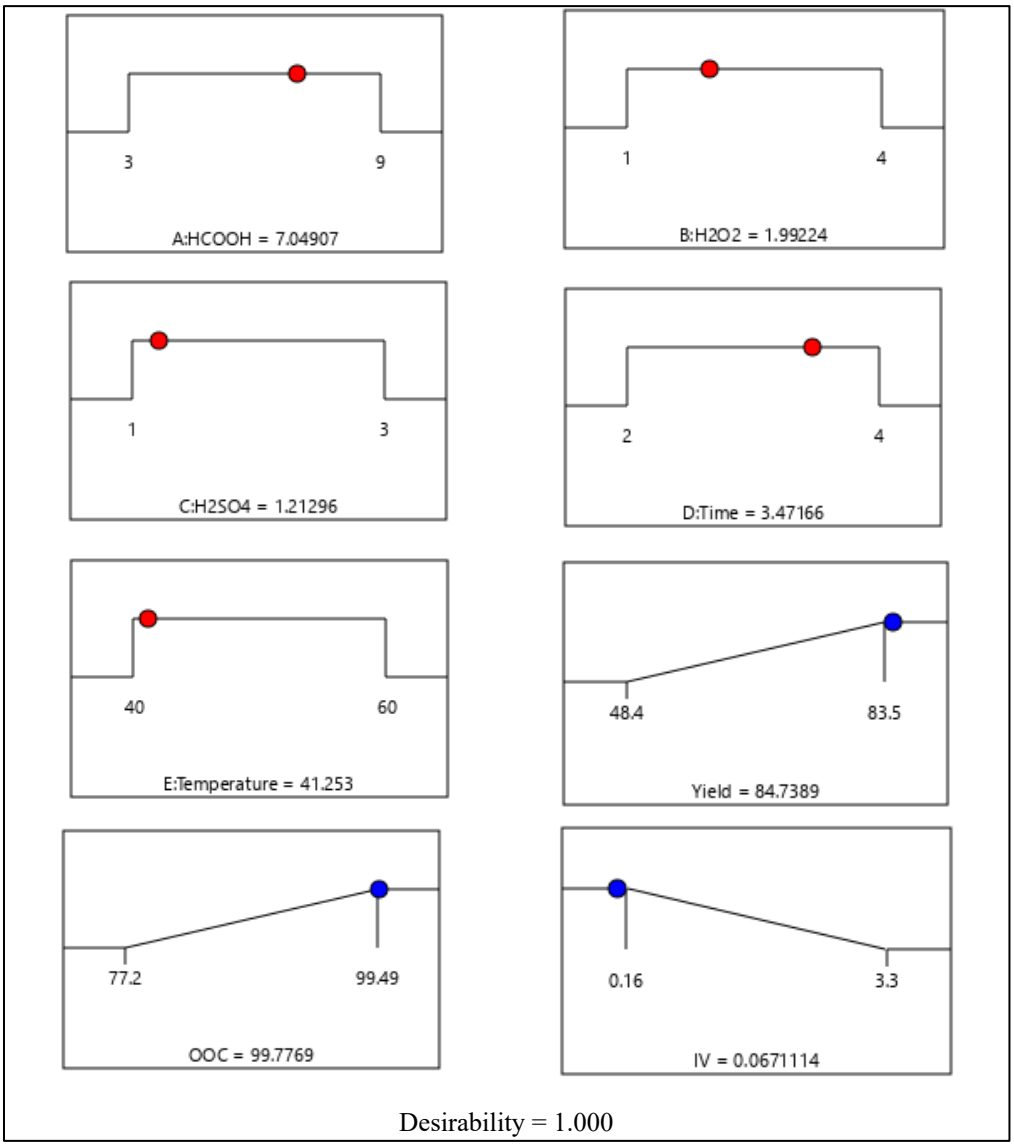


Figure 4.94 D-Optimal Predicted Model at Optimum Condition for Epoxidation of SFOUFATMPE

The accuracy of the model developed using the D-optimal design was validated by performing the reaction under three randomly selected sets of conditions. The predicted values were then compared with the experimental results by RSE for each run. Experiments with RSE values below 5% were considered acceptable. As shown in Table 4.86, Table 4.87 and Table 4.88, all RSE values were less than 5%, confirming that the model is reliable and suitable for predicting the response. However, the RSE for IV was not calculated because the IV values were close to zero, making the RSE calculation unreliable.

Table 4.86
Actual and Predicted Data for Verification Model for Percentage Yield of ESFOUFATMPE

Molar ratio HCOOH	Molar ratio H_2O_2	Catalyst (%)	Reaction time (h)	Reaction temp. (°C)	Yield (%)		
					Actual	Predicted	RSE
3	4	3	2.5	60	60.47	58.55	3.28
8	1	2	4	55	69.03	72.30	4.52
5	2.5	1	3	40	83.5	82.35	1.40

Table 4.87
Actual and Predicted Data for Verification Model for Percentage OOC of ESFOUFATMPE

Molar ratio HCOOH	Molar ratio H_2O_2	Catalyst (%)	Reaction time (h)	Reaction temp. (°C)	OOC (%)		
					Actual	Predicted	RSE
3	4	3	2.5	60	85.13	84.90	0.27
8	1	2	4	55	97.0	95.39	1.69
5	2.5	1	3	40	98.9	98.04	0.88

Table 4.88
Actual and Predicted Data for Verification Model for Iodine Value of ESFOUFATMPE

Molar ratio HCOOH	Molar ratio H_2O_2	Catalyst (%)	Reaction time (h)	Reaction temp. (°C)	IV		
					Actual	Predicted	RSE
3	4.0	3	2.5	60	2.5	2.44	2.5
8	1.0	2	4.0	55	0.47	0.635	-
5	2.5	1	3.0	40	0.29	0.33	-

4.8.3.6 Optimum Condition of Epoxidation Reaction

The D-optimal design successfully predicted the optimum conditions for the epoxidation reaction. The identified optimal parameters consisted of a molar ratio of HCOOH of 7, a molar ratio of H_2O_2 of 2, a percentage of catalyst of 1.2%, a reaction time of 3.5 h and a reaction temperature of 41°C. Under these optimized conditions, an epoxidized product yield of 85.7% was achieved, with high percentage OOC of 99.38% and a low IV of 0.097 g I_2/100 g, indicating effective conversion of double bonds to epoxide groups. The validity of the predicted optimum was confirmed by model validation, where the RSE values for the evaluated response parameters were below 5%, indicating good agreement between the experimental and predicted results and

confirming the adequacy of the D-optimal model. Table 4.89, Table 4.90 and Table 4.91 show the optimum condition of the epoxidation of SFOUFATMPE for each response. Figure 4.95 shows the epoxidation product which epoxidized sunflower oil unsaturated fatty acids trimethylolpropane ester (ESFOUFATMPE).

Table 4.89
Actual and Predicted Data for Optimum Condition for Percentage Yield of ESFOUFATMPE

Molar ratio HCOOH	Molar ratio H_2O_2	Catalyst (%)	Reaction time (h)	Reaction temp. (°C)	Yield (%)		
					Actual	Predicted	RSE
7	2	1.2	3.5	41	85.7	84.74	1.13

Table 4.90
Actual and Predicted Data for Optimum Condition for Percentage OOC of ESFOUFATMPE

Molar ratio HCOOH	Molar ratio H_2O_2	Catalyst (%)	Reaction time (h)	Reaction temp. (°C)	OOC (%)		
					Actual	Predicted	RSE
7	2	1.2	3.5	41	99.38	99.78	0.40

Table 4.91
Actual and Predicted Data for Optimum Condition for Iodine Value of ESFOUFATMPE

Molar ratio HCOOH	Molar ratio H_2O_2	Catalyst (%)	Reaction time (h)	Reaction temp. (°C)	IV		
					Actual	Predicted	RSE
7	2	1.2	3.5	41	0.097	0.067	-



Figure 4.95 Epoxidized Sunflower Oil Unsaturated Fatty Acids Trimethylolpropane Ester (ESFOUFATMPE)

4.8.4 Characterization of ESFOUFATMPE

4.8.4.1 Fourier Transform Infrared Spectroscopy

FTIR analysis was performed to identify the functional groups in SFOUFATMPE and ESFOUFATMPE, as shown in Figure 4.96. In the spectrum of SFOUFATMPE, the presence of C-H sp^2 was indicated by the C=C bending vibration at 3008.11 cm^{-1}, while the C–H stretching vibrations of aliphatic chains (C-H sp^3) appeared at 2926.97 and 2854.16 cm^{-1}. A strong absorption band at 1742.20 cm^{-1} corresponded to the C=O ester groups, supported by C-O stretching bands at 1236.12 and 1160.67 cm^{-1}. After the epoxidation reaction, the FTIR spectrum of ESFOUFATMPE showed the disappearance of the C=C band, indicating the conversion of double bonds. The ester carbonyl peak remained at 1742.32 cm^{-1}, along with C-O ester bands at 1239.03 and 1162.02 cm^{-1}. Additionally, a new absorption peak at 830.25 cm^{-1}, assigned to the C-O-C epoxide ring, confirmed the successful formation of ESFOUFATMPE. The functional groups identified in both samples were summarized in Table 4.92.

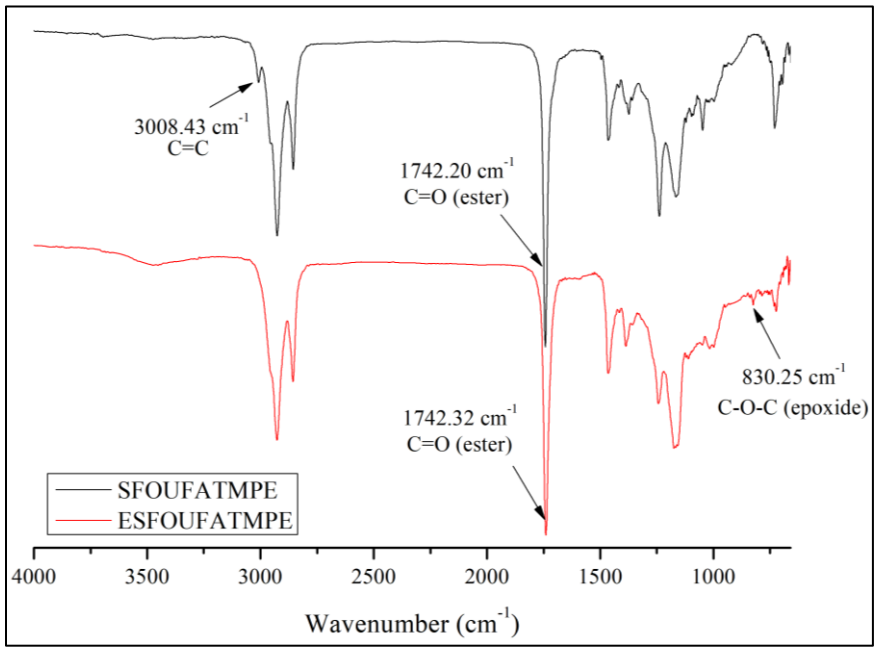


Figure 4.96 FTIR Spectra of SFOUFATMPE and ESFOUFATMPE

Table 4.92
Functional Group and Wavenumber for FTIR Spectra of SFOUFATMPE and ESFOUFATMPE

Functional group	Wavenumber (cm^{-1})	
	SFOUFATMPE	ESFOUFATMPE
C=C bending vibration (aliphatic)	3008.11	-
C-H stretching vibration (aliphatic)	2926.97 and 2854.16	2924.65 and 2850.58
C=O stretching vibration (ester)	1742.20	1742.32
-C-O stretching vibration (ester)	1236.12 and 1160.67	1239.03 and 1162.02
-C-O-C- epoxide	-	830.25

4.8.4.2 Nuclear Magnetic Resonance

Following epoxidation (Figure 4.97), significant changes were observed in the ^{1}H-NMR spectrum of ESFOUFATMPE. The disappearance of olefinic proton signals at 5.33 to 5.41 ppm, as well as allylic and bis-allylic proton signals at 2.03 to 2.10 ppm and 2.78 to 2.81 ppm, respectively, indicates the successful conversion of carbon–carbon double bonds. The appearance of a new signal in the range of 2.97 to 3.15 ppm, attributed to epoxide ring protons (-**H**C-O-CH-), provides clear evidence of epoxide formation. Table 4.93 shows the type of proton and chemical shift of SFOUFATMPE and ESFOUFATMPE.

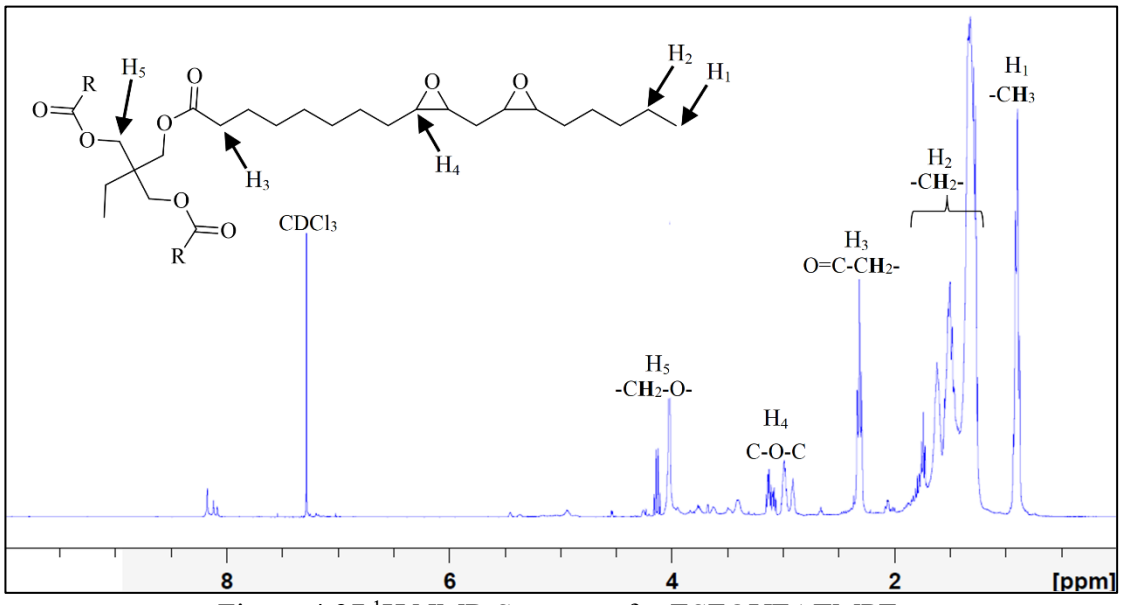


Figure 4.97 ^{1}H NMR Spectrum for ESFOUFATMPE

Table 4.93
Type of Proton and Chemical Shift for SFOUFATMPE and ESFOUFATMPE

	Type of proton	Chemical shift (ppm)		
		SFOUFATMPE	ESFOUFATMPE	Theoretical*
H_1	-C**H**$_3$	0.86-0.90	0.88-0.93	0.70-1.3
H_2	-C**H**$_2$-	1.23-1.36	1.26-1.39	1.2-1.4
-	-CH=CH-C**H**$_2$-	1.98-2.07	-	1.6-2.6
H_3	O=C-C**H**$_2$-	2.27-2.31	2.29-2.37	2.1-2.5
-	=CH-C**H**$_2$-CH=	2.75-2.78	-	2.5-3.0
H_4	-HC-O-C**H**- (epoxide)	-	2.97-3.15	2.5-3.5
H_5	-C**H**$_2$-O- (trimethylolpropane)	4.12-4.14	4.10-4.15	4.0-4.5
-	-CH=C**H**-	5.30-5.38	-	4.5-6.5

Source: *Pavia et al. (2015)

The success of the epoxidation reaction was further confirmed by ^{13}C-NMR analysis, as shown in Figure 4.98 and summarized in Table 4.94. After epoxidation, notable changes were observed in the ^{13}C-NMR spectrum of ESFOUFATMPE. The disappearance of olefinic carbon signals at 127.88 to 130.15 ppm indicates the successful consumption of carbon–carbon double bonds. New signals appeared in the range of 54.21 to 57.25 ppm, which were attributed to **C**-O-C carbons of the epoxide ring, providing direct evidence of epoxide formation.

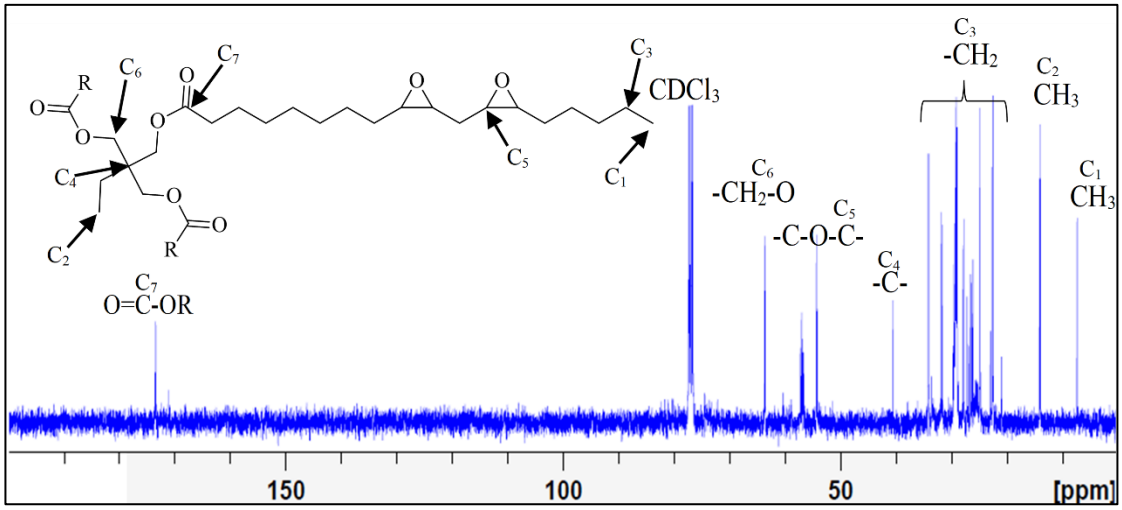


Figure 4.98 ^{13}C NMR Spectrum for ESFOUFATMPE

Table 4.94
Type of Carbon and Chemical Shift for SFOUFATMPE and ESFOUFATMPE

	Type of carbon	Chemical shift (ppm)		
		SFOUFATMPE	ESFOUFATMPE	Theoretical*
C_1	-**C**H_3 (trimethylolpropane)	8.12	8.15	8-30
C_2	-**C**H_3	14.02-14.15	13.99-14.19	8-30
C_3	-**C**H_2-	20.96-31.88	21.05-31.85	15-55
C_4	-**C**- (trimethylolpropane)	40.59	40.59	20-60
C_5	-**C**-O-C- (epoxide)	-	54.21-57.25	40-60
C_6	-CH_2-O- (trimethylolpropane)	63.67	60.41	40-80
-	-C=C-	127.88-130.15	-	100-150
C_7	O=C-OR (ester)	173.42	173.46	155-185

Source: *Pavia et al. (2015)

4.8.5 Physicochemical Properties of ESFOUFATMPE

The physicochemical properties of ESFOUFATMPE were evaluated based on pour point, flash point, kinematic viscosity, viscosity index, oxidative stability and rheology. The physicochemical properties of ESFOUFATMPE were compared with epoxidized TMPE derived from different plant oil, which were palm kernel oil (ETMPE A) and canola oil (ETMPE B), as shown in Table 4.95.

Table 4.95
Physicochemical Properties of ESFOUFATMPE and Others ETMPE

Physicochemical properties	ESFOUFATMPE	ETMPE A	ETMPE B
Pour point (°C)	-1	-19	-3
Flash point (°C)	296	335	298
Viscosity at 40 °C (cSt)	208.27	45.69	236.17
Viscosity at 100 °C (cSt)	66.84	10.54	27.02
Viscosity Index	140.67	187.00	157.00
Oxidative stability (min)	30	N/A	N/A
Rheology	Newtonian	Newtonian	N/A

Source: ETMPE A: Salimon and Salih (2023); ETMPE B: Kamyab et al. (2024)

This study shows that the pour point of ESFOUFATMPE was -1 °C, which was higher than ETMPE A (-19 °C) and slightly higher than ETMPE B (-3 °C). The higher pour point of ESFOUFATMPE due to the presence of epoxy groups formed during the epoxidation process. The conversion of double bonds into epoxide rings increases

molecular interactions and structural rigidity, which reduces molecular mobility and low-temperature fluidity, resulting in a higher pour point.

In terms of flash point, ESFOUFATMPE exhibited a flash point of 296 °C, which is slightly lower than ETMPE A (335 °C) but comparable to ETMPE B (298 °C), indicating good thermal stability. The kinematic viscosity of ESFOUFATMPE was 208.27 cSt at 40 °C and 66.84 cSt at 100 °C, which are significantly higher than ETMPE A but slightly lower than ETMPE B. The increase in viscosity of ESFOUFATMPE is due to the formation of epoxy rings, which increase molecular weight and intermolecular interactions, resulting in higher resistance to flow.

The viscosity index of ESFOUFATMPE (140.67) was lower than ETMPE A (187.00) and ETMPE B (157.00), indicating a slightly lower viscosity–temperature stability. However, ESFOUFATMPE exhibited an oxidative stability of 30 minutes, showing improvement compared to the non-epoxidized ester due to the conversion of double bonds into epoxy groups, which reduces susceptibility to oxidation. The rheological behaviour of ESFOUFATMPE was Newtonian, similar to ETMPE A. This behavior was confirmed by the linear relationship between shear stress and shear rate observed for ESFOUFATMPE, as shown in Figure 4.99, demonstrating that shear stress is directly proportional to shear rate. In addition, the viscosity–shear rate profile presented in Figure 4.100 shows that the viscosity of ESFOUFATMPE remains constant over the shear rate range of 20 to 100 s^{-1}, further confirming its Newtonian flow characteristics. Overall, ESFOUFATMPE demonstrates comparable physicochemical properties with ETMPE derived from other plan oils, with higher viscosity and improved oxidative stability resulting from the epoxidation modification.

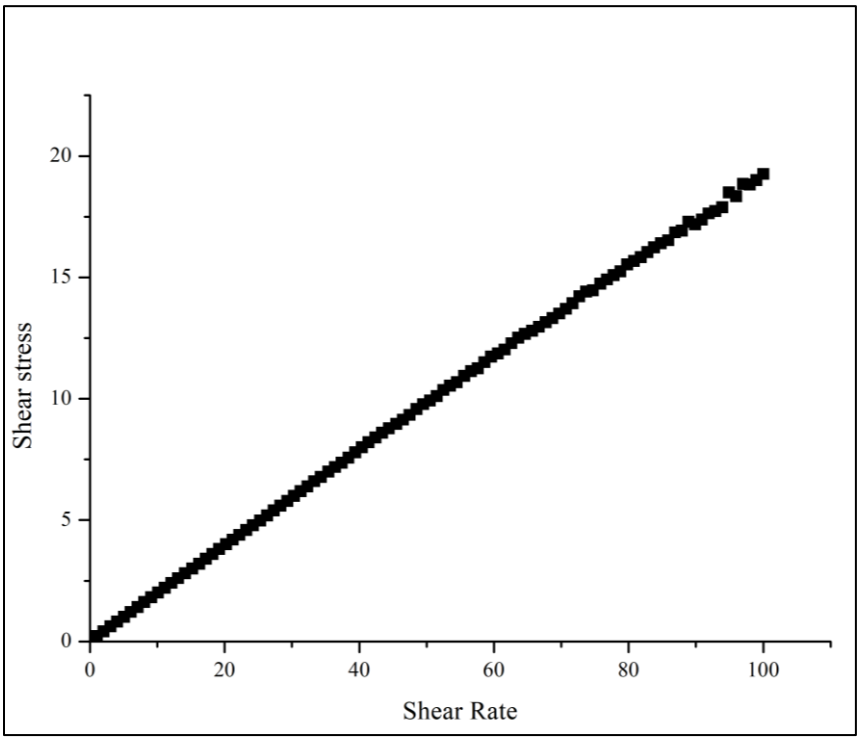


Figure 4.99 Shear Stress vesus Shear Rate of ESFOUFATMPE

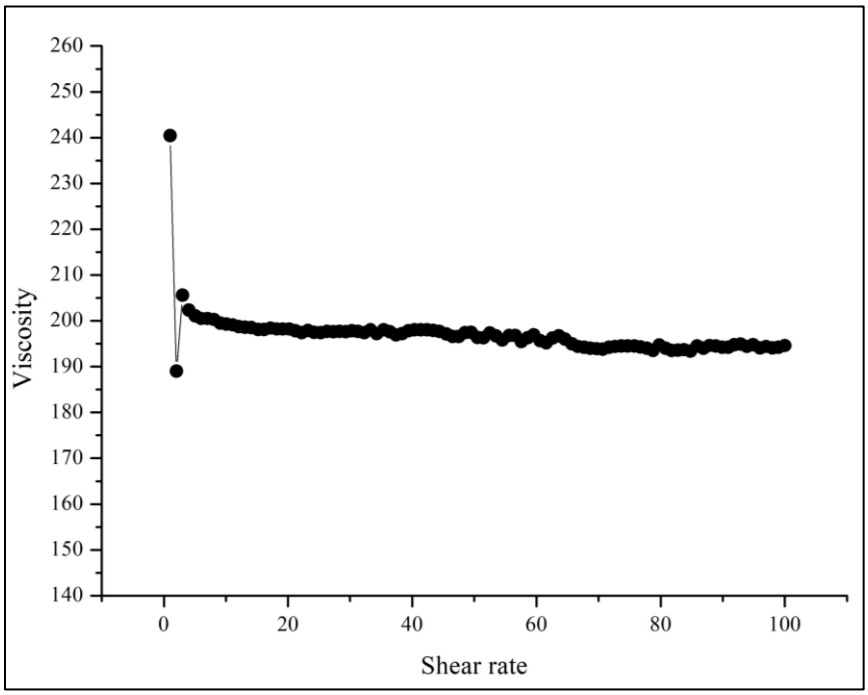


Figure 4.100 Viscosity versus Shear Rate of ESFOUFATMPE

4.9 Synthesis of Dioleate Sunflower Oil Unsaturated Fatty Acids Trimethylolpropane Ester

4.9.1 Ring Opening Reaction of ESFOUFATMPE with Oleic Acid

Ring-opening reactions of epoxidized polyol ester were widely employed as an effective chemical modification approach to enhance the physicochemical properties of biolubricant. The ring opening reaction of ESFOUFATMPE was carried out to produce dioleate sunflower oil unsaturated fatty acids trimethylolpropane ester (DOSFOUFATMPE). Figure 4.101 shows the ring opening reaction of ESFOUFATMPE.

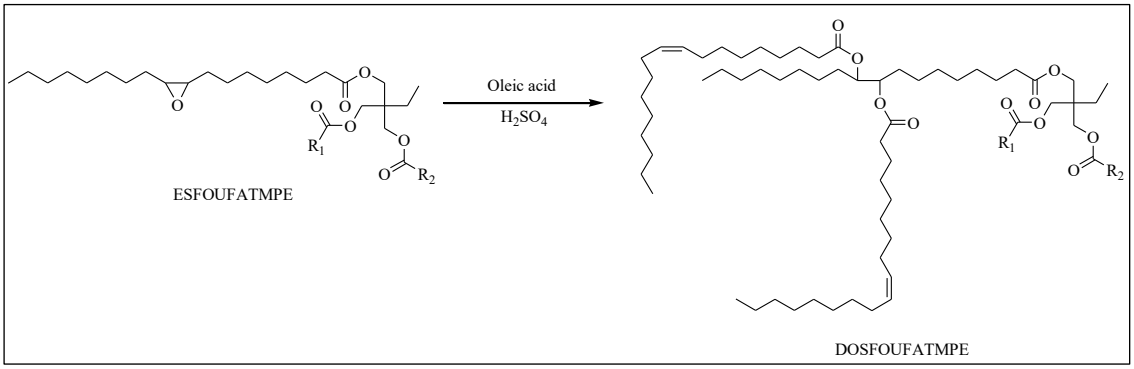


Figure 4.101 Ring Opening Reaction of ESFOUFATMPE

The reaction generally proceeds via an acid-catalyzed mechanism in which the epoxide oxygen is first protonated by H_2SO_4, leading to destabilization of the oxirane ring. This protonation step facilitates nucleophilic attack by fatty acids, resulting in cleavage of the epoxide ring and formation of β-hydroxy ester structures as a result, hydroxyl (-OH) groups were formed on the carbon backbone. These newly formed hydroxyl groups subsequently undergo esterification with oleic acid under the acidic reaction conditions, producing ester linkages and forming dioleate structures in the final product. Figure 4.102 shows the mechanism or ring opening reaction.

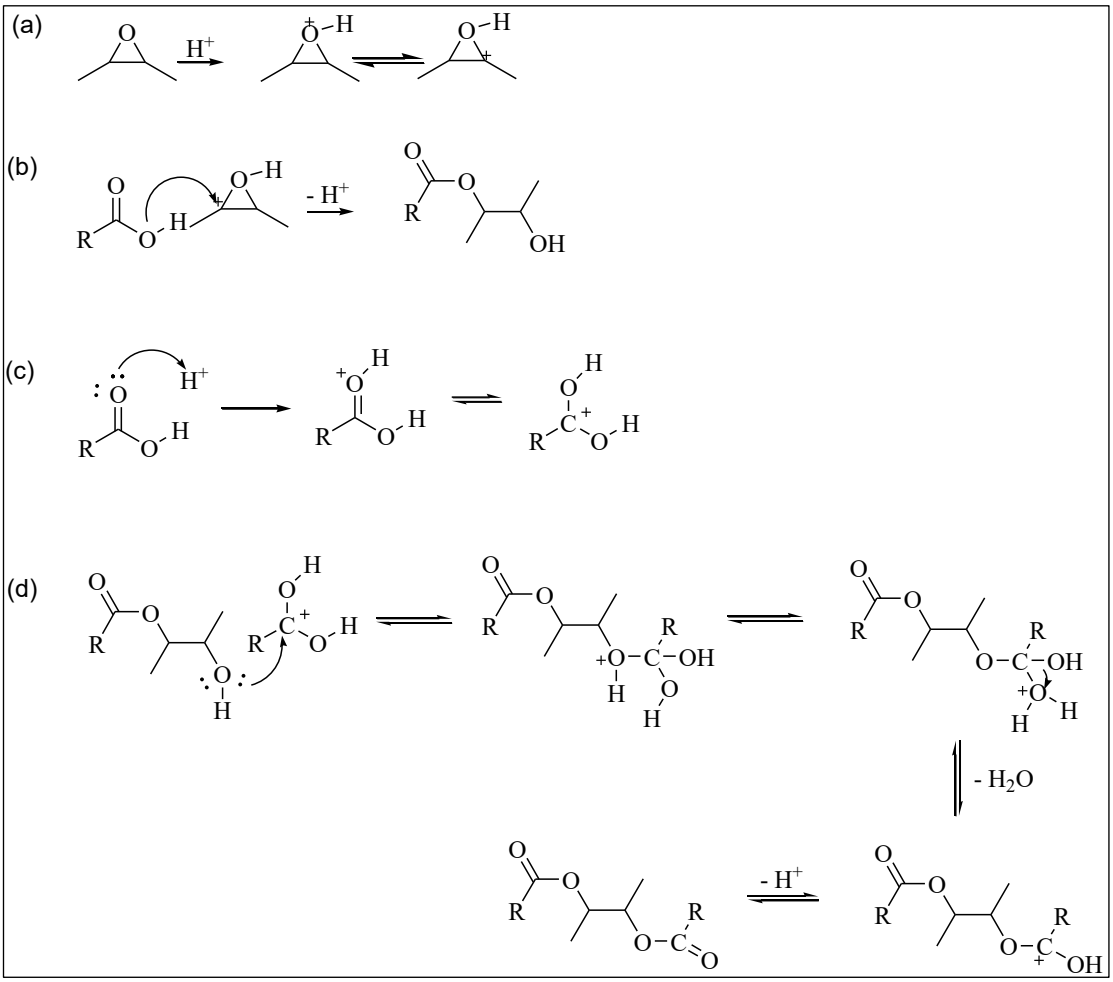


Figure 4.102 Reaction Mechanism of Ring Opening Reaction

The use of fatty acids, such as oleic acid, as nucleophiles in the acid catalyzed ring-opening reaction is particularly advantageous for lubricant applications (Adhvaryu et al. 2005). Fatty acids introduce long hydrocarbon chains and ester functionalities into the molecular structure, which enhance oil film strength, lubricity and biodegradability (Fox and Stachowiak 2007). Moreover, H_2SO_4 effectively catalyzes both the ring-opening and esterification steps, enabling high reaction efficiency at moderate temperatures without compromising the renewable nature of the product.

Oleic acid was used in the ring-opening reaction to balance oxidative stability and pour point, as its monounsaturated structure provides better oxidation while the incorporation of its long alkyl chain and branching lowers molecular packing efficiency, resulting in a reduced pour point. During the ring-opening reaction, the rigid epoxide structure was converted into a more branched molecular structure, which disrupts molecular packing and reduces crystallization at low temperatures. As a result, the pour point decreases, indicating better low-temperature flow behavior of the biolubricant.

4.9.2 Factor Screening Process

The factor screening results presented in Figure 4.103 indicate that all selected parameters have a significant influence on the percentage yield of ESFOUFAPEE. The parameters evaluated include the molar ratio of oleic acid (3 to 5 mol), percentage catalyst (1 to 3%), reaction temperature (120 to 140 °C) and reaction time (3 to 5 hours). Since each of these factors demonstrated a statistically significant effect on the ring opening reaction, all were retained for subsequent optimization. Accordingly, the specified ranges of these parameters were used in the optimization study employing a D-optimal design, as summarized in Table 4.96.

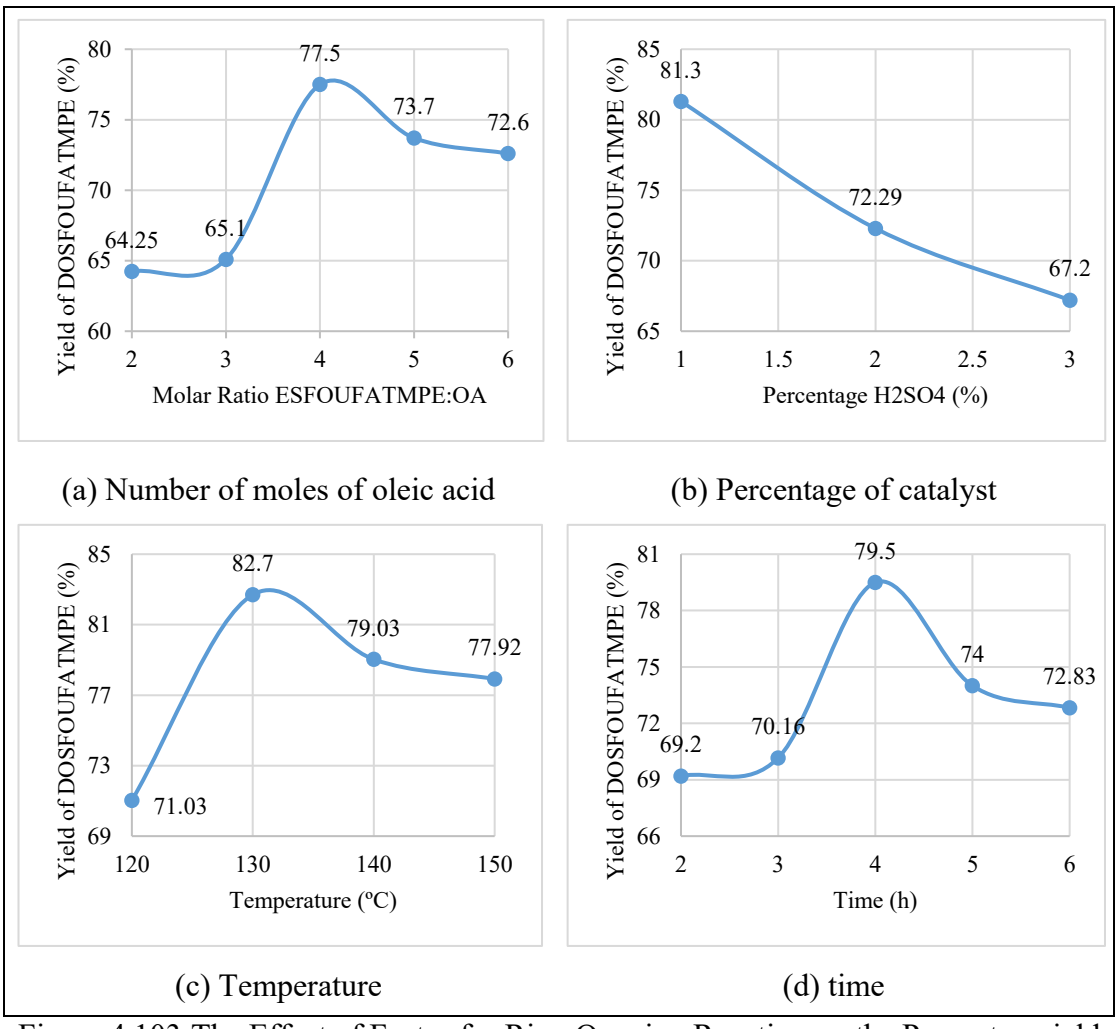


Figure 4.103 The Effect of Factor for Ring Opening Reaction on the Percentge yield of DOSFOUFATMPE

Table 4.96
Parameter and Level for D-Optimal Design of Ring Opening Reaction

Parameter	Unit	Variable level		
		-1	0	+1
Molar ratio of oleic acid	mole	3.0	4.0	5.0
Percentage of catalyst	%(w/w)	1.0	2.0	3.0
Time	h	3	4	5
Temperature	°C	120	130	140

4.9.3 Optimization of Ring Opening Reaction of ESFOUFATMPE

The optimization of dioleate SFOUFATMPE (DOSFOUFATMPE) synthesis was conducted through 25 experimental runs designed using D-optimal design. The study evaluated the effects of four key process variables: the molar ratio of ESFOUFATMPE to oleic acid, catalyst percentage, reaction time and reaction temperature. These factors were investigated to determine their effects on the selected response variables, namely percentage of yield of DOSFOUFATMPE, oxirane oxygen content (OOC), iodine value (IV) and hydroxyl value. The experiments generated both experimental and model-predicted values for each response, which were summarized in Table 4.97, Table 4.98, Table 4.99 and Table 4.100, respectively. A close agreement between the predicted and experimental results was observed, demonstrating the reliability and suitability of the developed model in predicting the yield, OOC, IV and hydroxyl value of DOSFOUFATMPE.

Table 4.97
Experimental Run, Factors and Response for Percentage Yield of DOSFOUFATMPE

Run	Factors				Response	
	Molar ratio OA	Catalyst (%)	Reaction time (h)	Reaction temp. (°C)	Yield (%)	
					Actual	Predicted
1	3	1	5	140	61.96	67.96
2	5	3	5	120	73.00	58.90
3	4	2	4	140	68.44	83.07
4	3	3	5	140	58.87	63.67
5	5	3	3	140	82.70	79.05
6	4	2	4	130	63.80	70.64
7	5	1	5	120	79.00	60.41
8	4	3	4	130	70.59	76.18
9	3	1	3	140	60.49	67.86
10	5	1	4	140	76.20	79.05
11	4	2	4	120	67.20	74.10
12	5	1	5	120	79.22	62.08
13	5	2	5	140	73.98	83.07
14	3	1	5	140	62.07	71.19
15	5	3	3	140	83.40	55.84
16	4	2	4	130	71.40	*80.32*
17	3	3	3	120	55.90	66.69
18	5	1	3	130	80.48	69.98
19	3	2	5	120	66.80	80.32
20	4	1	3	140	70.00	59.46
21	5	1	3	130	80.00	78.13
22	3	2	3	140	59.20	72.70
23	5	2	4	130	78.00	62.80
24	5	2	3	120	72.95	67.96
25	3	1	3	120	62.85	58.90

Table 4.98
Experimental Run, Factors and Response for Percentage OOC of DOSFOUFATMPE

Run	Factors				Response	
	Molar ratio OA	Catalyst (%)	Reaction time (h)	Reaction temp. (°C)	OOC (%)	
					Actual	Predicted
1	3	1	5	140	2.160	2.1300
2	5	3	5	120	0.840	0.8586
3	4	2	4	140	1.600	1.6100
4	3	3	5	140	2.840	2.8400
5	5	3	3	140	0.150	0.1282
6	4	2	4	130	2.050	2.0700
7	5	1	5	120	0.210	0.2031
8	4	3	4	130	1.160	1.1300
9	3	1	3	140	2.510	2.4900
10	5	1	4	140	0.590	0.6064
11	4	2	4	120	1.530	1.4900
12	5	1	5	120	0.192	0.2031
13	5	2	5	140	0.760	0.7438
14	3	1	5	140	2.100	2.1300
15	5	3	3	140	0.102	0.1282
16	4	2	4	130	1.080	1.1300
17	3	3	3	120	2.600	2.6000
18	5	1	3	130	0.390	0.4331
19	3	2	5	120	1.580	1.5800
20	4	1	3	140	1.350	1.3500
21	5	1	3	130	0.490	0.4331
22	3	2	3	140	2.750	2.7400
23	5	2	4	130	0.560	0.5325
24	5	2	3	120	1.360	1.3700
25	3	1	3	120	2.010	2.0200

Table 4.99
Experimental Run, Factors and Response for Iodine Value of DOSFOUFATMPE

Run	Factors				Response	
	Molar ratio OA	Catalyst (%)	Reaction time (h)	Reaction temp. (°C)	IV (%)	
					Actual	Predicted
1	3	1	5	140	95.40	95.76
2	5	3	5	120	103.69	104.00
3	4	2	4	140	99.28	99.97
4	3	3	5	140	91.30	91.05
5	5	3	3	140	117.40	118.11
6	4	2	4	130	96.40	96.03
7	5	1	5	120	109.60	110.59
8	4	3	4	130	101.70	101.79
9	3	1	3	140	94.90	94.09
10	5	1	4	140	108.00	107.76
11	4	2	4	120	98.60	98.84
12	5	1	5	120	111.79	110.59
13	5	2	5	140	106.24	106.00
14	3	1	5	140	95.69	95.76
15	5	3	3	140	119.00	118.11
16	4	2	4	130	102.26	101.37
17	3	3	3	120	90.15	90.19
18	5	1	3	130	109.00	108.39
19	3	2	5	120	99.63	99.59
20	4	1	3	140	101.00	100.87
21	5	1	3	130	107.10	108.39
22	3	2	3	140	93.08	93.80
23	5	2	4	130	107.89	108.37
24	5	2	3	120	102.90	102.31
25	3	1	3	120	95.90	96.16

Table 4.100
Experimental Run, Factors and Response for Hydroxyl Value of DOSFOUFATMPE

Run	Factors				Response	
	Molar ratio OA	Catalyst (%)	Reaction time (h)	Reaction temp. (°C)	IV (%)	
					Actual	Predicted
1	3	1	5	140	22.32	22.22
2	5	3	5	120	19.47	19.49
3	4	2	4	140	21.27	21.39
4	3	3	5	140	23.15	23.13
5	5	3	3	140	16.97	16.97
6	4	2	4	130	21.83	21.88
7	5	1	5	120	17.43	17.33
8	4	3	4	130	20.32	20.30
9	3	1	3	140	22.60	22.67
10	5	1	4	140	18.72	18.74
11	4	2	4	120	21.58	21.45
12	5	1	5	120	17.20	17.33
13	5	2	5	140	19.15	19.15
14	3	1	5	140	22.17	22.22
15	5	3	3	140	16.97	16.97
16	4	2	4	130	20.35	20.45
17	3	3	3	120	23.36	23.37
18	5	1	3	130	17.97	18.04
19	3	2	5	120	21.11	21.13
20	4	1	3	140	20.89	20.82
21	5	1	3	130	18.10	18.04
22	3	2	3	140	22.94	22.86
23	5	2	4	130	18.59	18.46
24	5	2	3	120	20.35	20.41
25	3	1	3	120	22.02	22.01

4.9.3.1 Determination of Selected Model

The selection of the appropriate analytical model was based on several statistical evaluations, including the sequential model sum of squares, lack-of-fit tests and model summary statistics The model was chosen according to the highest-order polynomial in which all additional terms were statistically significant and the model was non-aliased. Analysis of the sequential model sum of squares from Table 4.101, Table 4.102, Table 4.103 and Table 4.104 indicated that the quadratic model was the most suitable for

describing the relationship between the process variables and the responses in the synthesis of DOSFOUFATMPE, as supported by the corresponding *F*-values and *p*-values. For percentage yield, the quadratic model showed a highly significant result with an *F*-value of 63.28 and a *p*-value of < 0.0001. Similarly, the models for oxirane oxygen content (OOC) and hydroxyl value (HV) were highly significant, with *F*-values of 102.34 and 85.39 and *p*-values of < 0.0001, respectively. Although the iodine value (IV) exhibited a lower level of significance, the quadratic model remained statistically acceptable, with an *F*-value of 6.48 and a *p*-value of 0.0077. These results confirm that the quadratic model is appropriate and reliable for predicting the percentage yield, OOC, IV and HV of DOSFOUFATMPE.

Table 4.101
Sequential Model Sum of Squares of Percentage Yield of DOSFOUFATMPE

Source	Sum of Squares	dF	Mean Square	*F*-value	*p*-value model	
Mean vs Total	123700	1	123700			
Linear vs Mean	1404.17	4	351.04	32.61	< 0.0001	
2FI vs Linear	179.72	6	29.95	11.79	< 0.0001	
Quadratic vs 2FI	34.22	4	8.56	63.28	< 0.0001	Suggested
Cubic vs Quadratic	0.9617	6	0.1603	1.64	0.3286	Aliased
Residual	0.3905	4	0.0976			
Total	125300	25	5012.49			

Table 4.102
Sequential Model Sum of Squares of Percentage OOC of DOSFOUFATMPE

Source	Sum of Squares	dF	Mean Square	*F*-value	*p*-value model	
Mean vs Total	43.47	1	43.47			
Linear vs Mean	15.79	4	3.95	28.36	< 0.0001	
2FI vs Linear	2.09	6	0.3479	6.99	0.0014	
Quadratic vs 2FI	0.6803	4	0.1701	102.34	< 0.0001	Suggested
Cubic vs Quadratic	0.0085	6	0.0014	0.6988	0.6697	Aliased
Residual	0.0081	4	0.0020			
Total	62.04	25	2.48			

Table 4.103
Sequential Model Sum of Squares of Iodine Value of DOSFOUFATMPE

Source	Sum of Squares	dF	Mean Square	*F*-value	*p*-value model	
Mean vs Total	2.617E+05	1	2.617E+05			
Linear vs Mean	1087.52	4	271.88	17.01	< 0.0001	
2FI vs Linear	285.67	6	47.61	19.61	< 0.0001	
Quadratic vs 2FI	24.53	4	6.13	6.48	0.0077	Suggested
Cubic vs Quadratic	3.94	6	0.6564	0.4752	0.8017	Aliased
Residual	5.53	4	1.38			
Total	2.631E+05	25	10524.85			

Table 4.104
Sequential Model Sum of Squares of Hydroxyl Value of DOSFOUFATMPE

Source	Sum of Squares	dF	Mean Square	*F*-value	*p*-value model	
Mean vs Total	10275.07	1	10275.07			
Linear vs Mean	85.82	4	21.46	23.71	< 0.0001	
2FI vs Linear	13.54	6	2.26	6.94	0.0014	
Quadratic vs 2FI	4.42	4	1.11	85.39	< 0.0001	Suggested
Cubic vs Quadratic	0.0833	6	0.0139	1.20	0.4484	Aliased
Residual	0.0461	4	0.0115			
Total	560.42	25	22.42			

The lack-of-fit test results for DOSFOUFATMPE, as presented in Table 4.105, Table 4.106, Table 4.107 and Table 4.108, indicate that the developed models were statistically insignificant for all evaluated responses, confirming their adequacy. For percentage yield, the lack-of-fit *F*-value was 1.64 with a *p*-value of 0.3286, which is higher than 0.05, indicating no significant lack of fit. Similarly, the oxirane oxygen content (OOC) model exhibited an *F*-value of 0.6988 and a *p*-value of 0.6697, while the iodine value (IV) model showed an *F*-value of 0.4752 with a *p*-value of 0.8017. In addition, the hydroxyl value (HV) model presented an *F*-value of 1.20 and a *p*-value of 0.4484. The insignificance of the lack-of-fit for all responses demonstrates that the quadratic models adequately represent the experimental data and were suitable for predicting the percentage yield, OOC, IV and HV of DOSFOUFATMPE.

Table 4.105
Lack of Fit Test for Percentage Yield of DOSFOUFATMPE

Source	Sum of Squares	dF	Mean Square	*F*-value	*p*-value model	
Linear	214.90	16	13.43	137.60	0.0001	
2FI	35.18	10	3.52	36.04	0.0018	
Quadratic	0.9617	6	0.1603	1.64	0.3286	Suggested
Cubic	0.0000	0				Aliased
Pure error	0.3905	4	0.0976			

Table 4.106
Lack of Fit Test for Percentage OOC of DOSFOUFATMPE

Source	Sum of Squares	dF	Mean Square	*F*-value	*p*-value model	
Linear	2.78	16	0.1735	85.53	0.0003	
2FI	0.6888	10	0.0689	33.96	0.0020	
Quadratic	0.0085	6	0.0014	0.6988	0.6697	Suggested
Cubic	0.0000	0				Aliased
Pure error	0.0081	4	0.0020			

Table 4.107
Lack of Fit Test for Iodine Value of DOSFOUFATMPE

Source	Sum of Squares	dF	Mean Square	*F*-value	*p*-value model	
Linear	314.14	16	19.63	14.21	0.0099	
2FI	28.47	10	2.85	2.06	0.2533	
Quadratic	3.94	6	0.6564	0.4752	0.8017	Suggested
Cubic	0.0000	0				Aliased
Pure error	5.53	4	1.38			

Table 4.108
Lack of Fit Test for Hydroxyl Value of DOSFOUFATMPE

Source	Sum of Squares	dF	Mean Square	*F*-value	*p*-value model	
Linear	18.05	16	1.13	97.77	0.0002	
2FI	4.51	10	0.4506	39.05	0.0015	
Quadratic	0.0833	6	0.0139	1.20	0.4484	Suggested
Cubic	0.0000	0				Aliased
Pure error	0.0462	4	0.0115			

The model summary statistics for DOSFOUFATMPE (Table 4.109, Table 4.110, Table 4.111 and Table 4.112) indicate that the quadratic models provide an

excellent fit for all responses, as reflected by high R^2 and adjusted R^2 values close to unity and low standard deviation values. The percentage yield model showed strong reliability with an R^2 of 0.9992, an adjusted R^2 of 0.9980, a low standard deviation of 0.3677 and a PRESS value of 9.65. Similarly, the oxirane oxygen content (OOC) model exhibited an R^2 of 0.9991, an adjusted R^2 of 0.9979, a standard deviation of 0.1276 and a PRESS of 9.65. The iodine value (IV) model also demonstrated acceptable predictive performance with an R^2 of 0.9933, an adjusted R^2 of 0.9839, a standard deviation of 0.9728 and a PRESS value of 78.96. In addition, the hydroxyl value (HV) model showed excellent accuracy, with an R^2 of 0.9988, an adjusted R^2 of 0.9970, a standard deviation of 0.1138 and a PRESS value of 0.6840. Overall, these results confirm the suitability and reliability of the quadratic models for predicting the responses of DOSFOUFATMPE.

Table 4.109
Model Summary Statistic for Percentage Yield of DOSFOUFATMPE

Source	Standard Deviation	R^2	Adjusted R^2	Predicted R^2	PRESS	
Linear	3.28	0.8671	0.8405	0.7721	369.08	
2FI	1.59	0.9780	0.9623	0.9237	123.63	
Quadratic	0.3677	0.9992	0.9980	0.9940	9.65	Suggested
Cubic	0.3124	0.9998	0.9986			Aliased

Table 4.110
Model Summary Statistic for Percentage OOC of DOSFOUFATMPE

Source	Standard Deviation	R^2	Adjusted R^2	Predicted R^2	PRESS	
Linear	0.3731	0.8501	0.8201	0.7498	4.65	
2FI	0.2231	0.9625	0.9357	0.8479	2.83	
Quadratic	0.0408	0.9991	0.9979	0.9931	0.1276	Suggested
Cubic	0.0450	0.9996	0.9974			Aliased

Table 4.111
Model Summary Statistic for Iodine Value of DOSFOUFATMPE

Source	Standard Deviation	R^2	Adjusted R^2	Predicted R^2	PRESS	
Linear	4.00	0.7728	0.7274	0.6047	556.25	
2FI	1.56	0.9758	0.9586	0.9162	117.97	
Quadratic	0.9728	0.9933	0.9839	0.9439	78.96	Suggested
Cubic	1.18	0.9961	0.9764			Aliased

Table 4.112
Model Summary Statistic for Hydroxyl Value of DOSFOUFATMPE

Source	Standard Deviation	R^2	Adjusted R^2	Predicted R^2	PRESS	
Linear	0.9512	0.8259	0.7910	0.7112	30.01	
2FI	0.5702	0.9562	0.9249	0.8220	18.50	
Quadratic	0.1138	0.9988	0.9970	0.9934	0.6840	Suggested
Cubic	0.1074	0.9996	0.9973			Aliased

4.9.3.2 Identification of Model Accuracy

The adequacy and reliability of the developed RSM models for DOSFOUFATMPE were evaluated using several diagnostic plots, including normal plot of residuals (Figure 4.104), residuals versus predicted values (Figure 4.105), predicted versus actual values (Figure 4.106), residuals versus run number (Figure 4.107), Cook's distance plots (Figure 4.108) and Box-Cox plots (Figure 4.109).

The normal probability plots of residuals (Figure 4.104) show that the residuals were randomly scattered along the straight regression line, indicating that the residuals follow a normal distribution. This confirms that the assumption of normality is satisfied and supports the validity of the developed models.

The residuals versus predicted plots (Figure 4.105) demonstrate that all experimental data points fall within the acceptable limits of -4.29681 to +4.29681, indicating the absence of outliers and confirming the suitability of the selected models. In addition, the predicted versus actual plots (Figure 4.106) show close agreement between experimental and predicted values, highlighting the strong predictive capability of the models.

The residuals versus run number plots (Figure 4.107) exhibit random scatter without any discernible trend, indicating that the residuals were independent and that no systematic error occurred during the experimental runs. Furthermore, the Cook's

distance plots (Figure 4.108) show that all data points were below the critical value of 1, with most values below 0.2, confirming that no influential observations significantly affect the model performance.

The Box–Cox plots (Figure 4.109) yielded optimal lambda (λ) values of 1.3699 for percentage yield, 0.9986 for OOC, −0.9953 for IV and 0.9812 for HV. Since these values were close to unity, no data transformation was required for this optimization study. Overall, the diagnostic analyses confirm the reliability of the quadratic models developed for DOSFOUFATMPE.

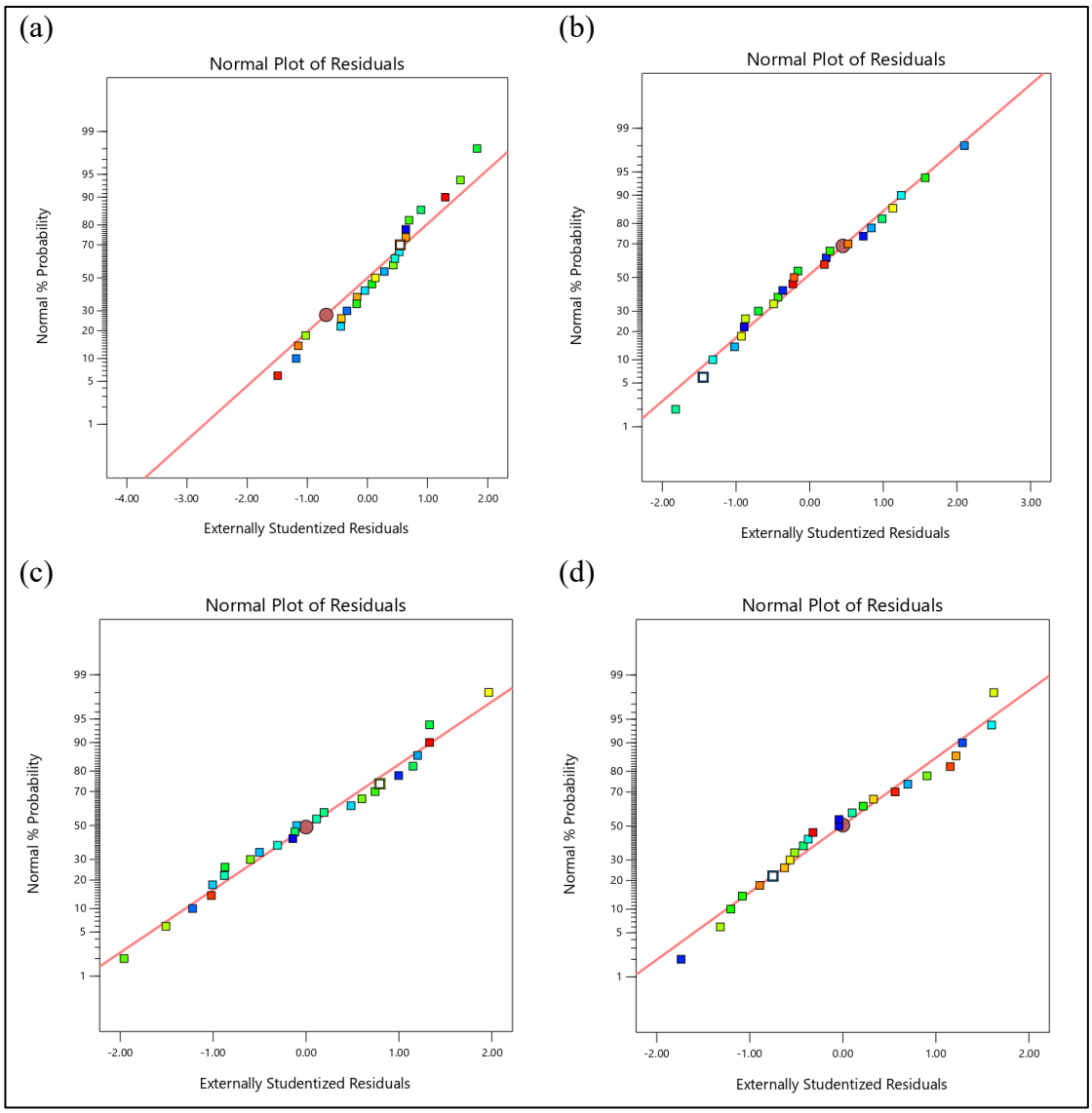


Figure 4.104 Normal Plot of Residual for (a) Percentage Yield, (b) Percentage OOC, (c) Iodine Value and (d) Hydroxyl Value of DOSFOUFATMPE

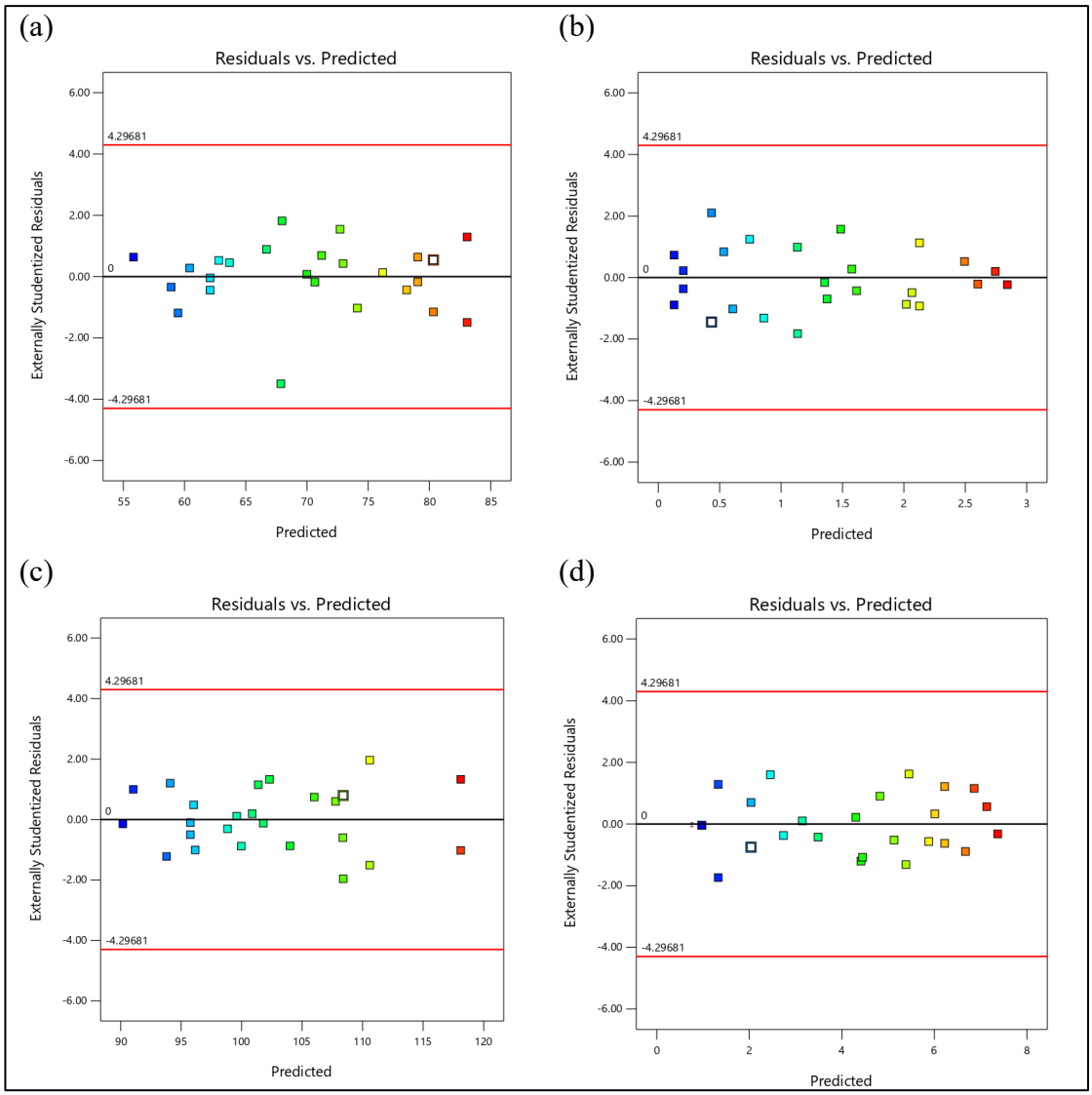


Figure 4.105 Residual versus Predicted Plot for (a) Percentage Yield, (b) Percentage OOC, (c) Iodine Value and (d) Hydroxyl Value of DOSFOUFATMPE

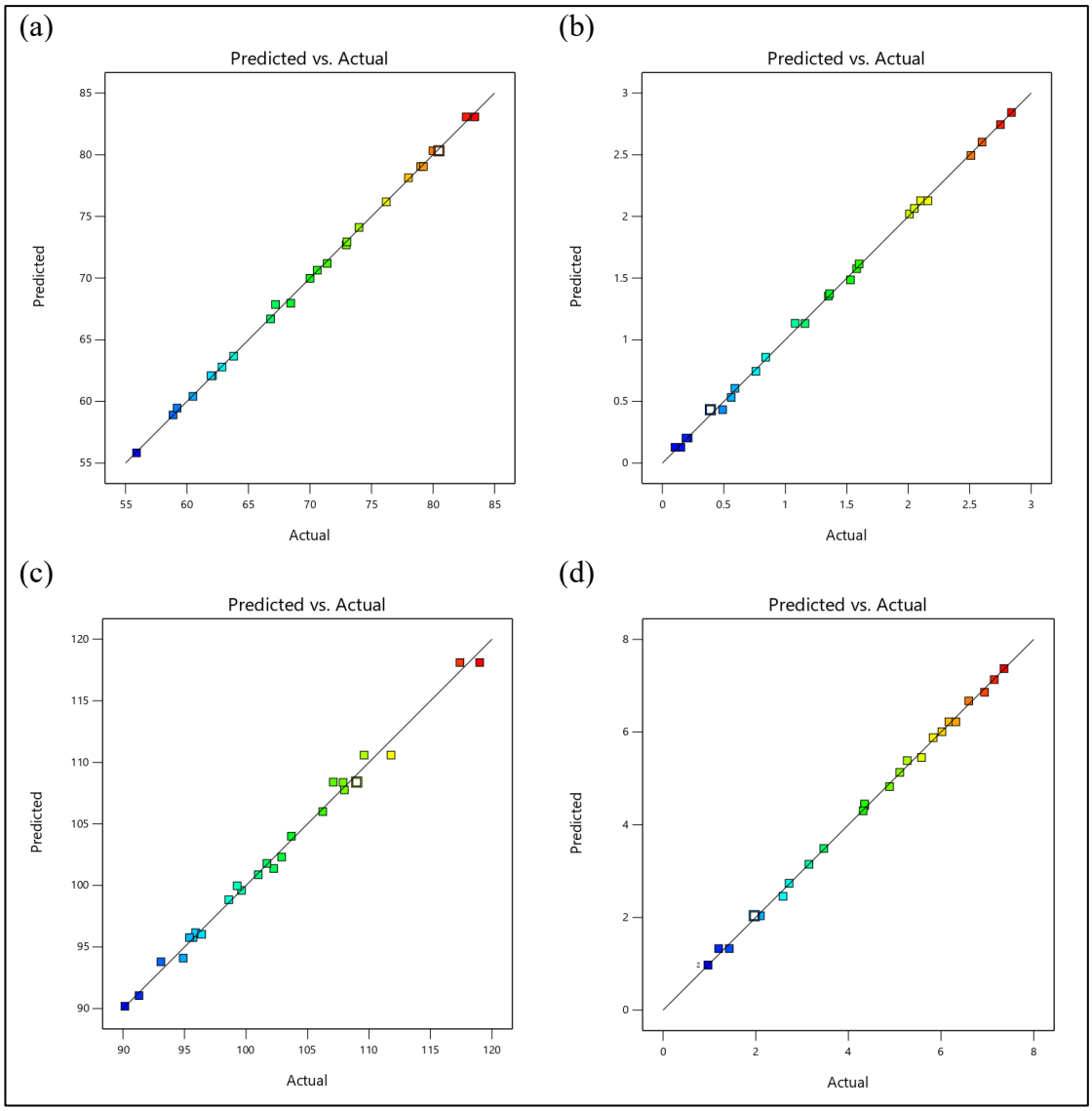


Figure 4.106 Predicted versus Actual for (a) Percentage Yield, (b) Percentage OOC, (c) Iodine Value and (d) Hydroxyl Value of DOSFOUFATMPE

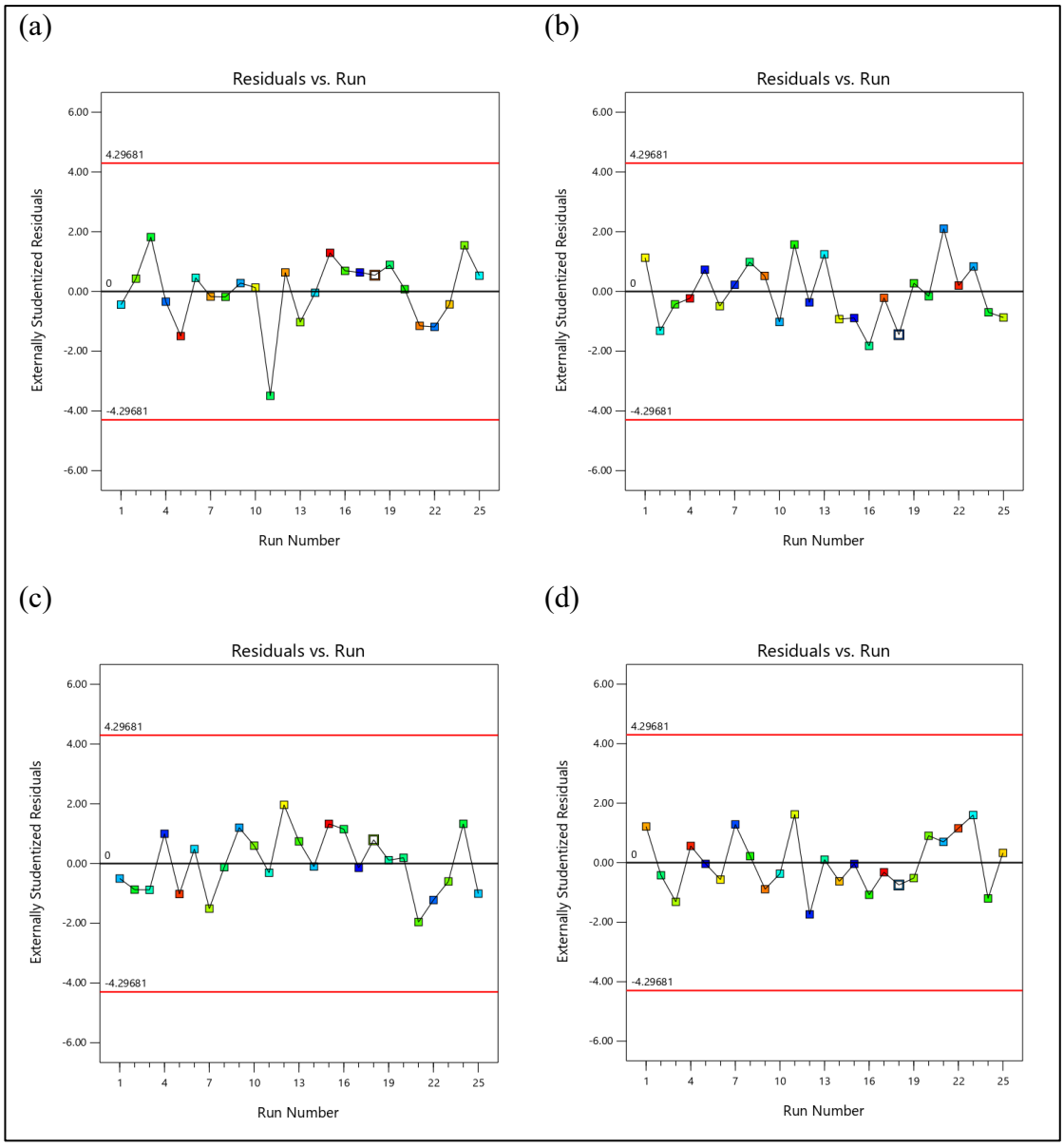


Figure 4.107 Residual versus Run Number for (a) Percentage Yield, (b) Percentage OOC, (c) Iodine Value and (d) Hydroxyl Value of DOSFOUFATMPE

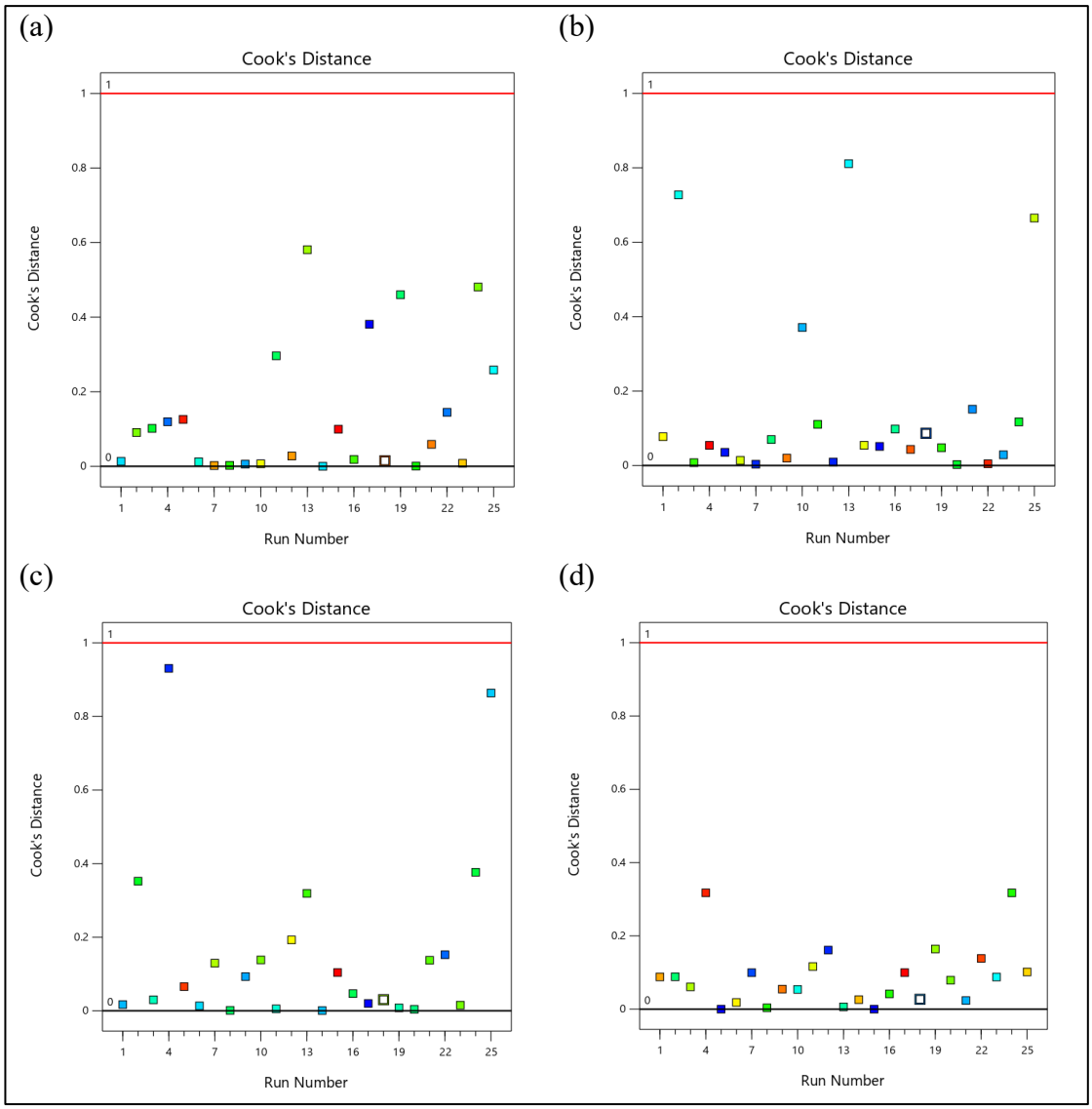


Figure 4.108 Cook's Distance for (a) Percentage Yield, (b) Percentage OOC, (c) Iodine Value and (d) Hydroxyl Value of DOSFOUFATMPE

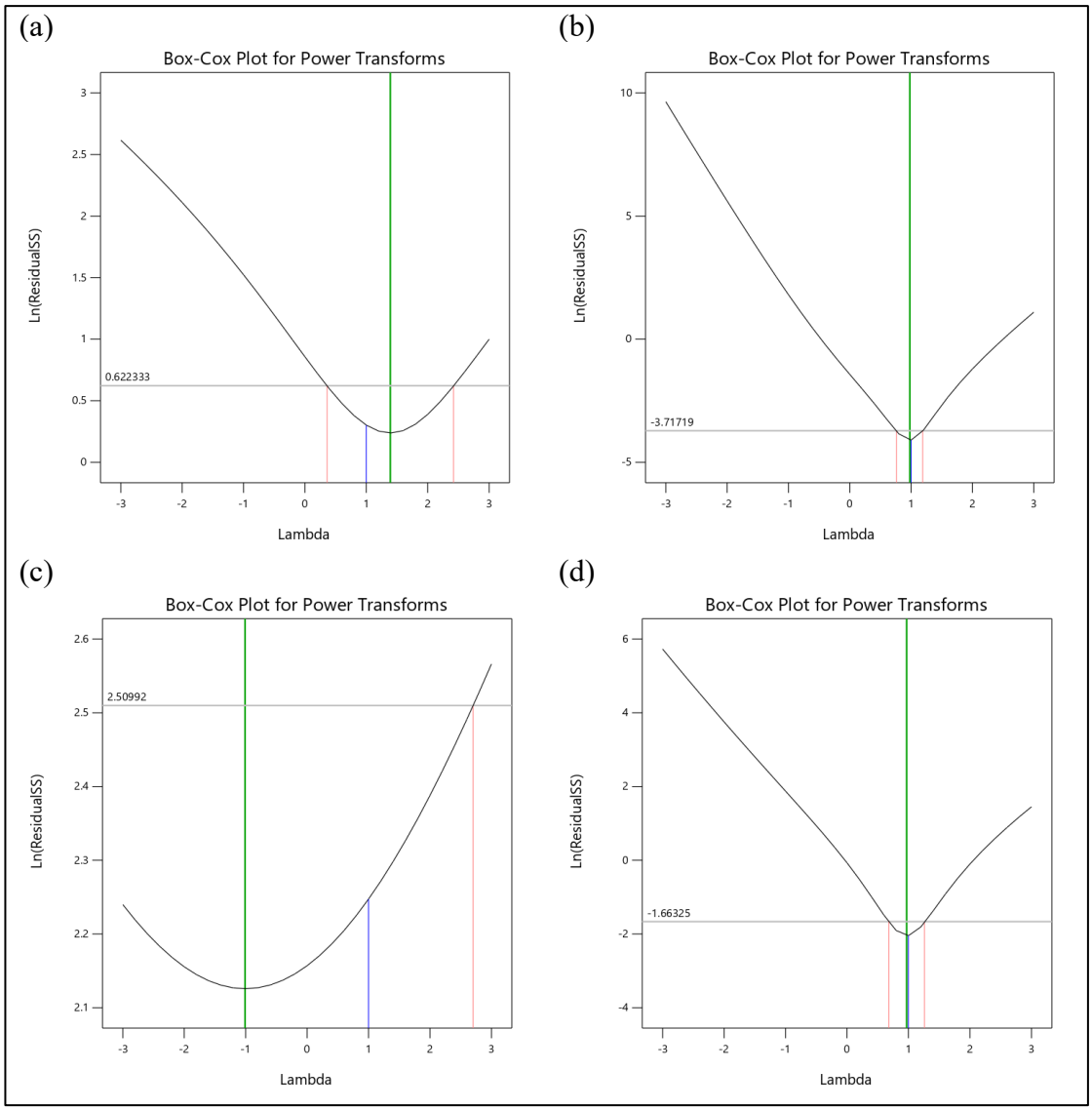


Figure 4.109 Box-Cox Plot for (a) Percentage Yield, (b) Percentage OOC, (c) Iodine Value and (d) Hydroxyl Value of DOSFOUFATMPE

4.9.3.3 Analysis of Variance

The ANOVA results for DOSFOUFATMPE were summarized in Table 4.113 and indicate that the developed quadratic models were statistically significant for all evaluated responses. The percentage yield model showed a *p*-value of < 0.0001 with a high *F*-value of 854.81, confirming strong model significance, while the lack-of-fit was not significant (*p*-value = 0.3286, *F*-value = 1.64), indicating good model adequacy. Similarly, the oxirane oxygen content (OOC) model exhibited a significant *p*-value of < 0.0001 with an *F*-value of 797.59 and a non-significant lack-of-fit (*p*-value = 0.6697, *F*-value = 0.6988). The iodine value (IV) model was also statistically significant, with

a *p*-value of < 0.0001 and an *F*-value of 105.50, while it lack-of-fit remained not significant (*p*-value = 0.8017, *F*-value = 0.4752). In addition, the hydroxyl value (HV) model demonstrated strong significance with a *p*-value of < 0.0001 and an *F*-value of 372.58, accompanied by a non-significant lack-of-fit (*p*-value = 0.4484, *F*-value = 1.20). The high R^2 values obtained for percentage yield (0.9992), OOC (0.9991), IV (0.9933) and HV (0.9988) further confirm the excellent agreement between experimental and predicted values.

Table 4.113
Summary of ANOVA Analysis for Percentage Yield, Percentage OOC Iodine Value and Hydroxyl Value of DOSFOUFATMPE

Source	Percentage yield	Percentage OOC	IV	HV
p-value model	< 0.0001	< 0.0001	< 0.0001	< 0.0001
F-value model	854.81	797.59	105.50	572.58
p-value Lack of Fit	0.3286	0.6697	0.8017	0.4484
F-value Lack of Fit	1.6400	0.6988	0.4752	1.2000
R^2	0.9992	0.9991	0.9933	0.9988
Adjusted R^2	0.9980	0.9979	0.9839	0.9970
Predicted R^2	0.9940	0.9931	0.9439	0.9934
Standard deviation	0.3677	0.0408	0.9728	0.1138
Coefficient of variation (C.V %)	0.5228	3.0900	0.9508	0.5613
Adequate precision	95.6183	85.9573	37.0521	72.5742

The ANOVA results show that the developed quadratic models were statistically significant for all responses of DOSFOUFATMPE, including percentage yield, oxirane oxygen content (OOC), iodine value (IV) and hydroxyl value (HV). For percentage yield (Table 4.114), the linear factors, most interaction terms and selected quadratic terms were significant, with *p*-values less than 0.05. Similarly, the ANOVA analysis for percentage OOC (Table 4.115) indicates that the model terms were statistically significant, with most *p*-values below 0.05, confirming a strong influence of the process variables on oxirane oxygen formation. The ANOVA results for iodine value (IV) (Table 4.116) show that the majority of linear and interaction terms were significant ($p < 0.05$), indicating that the reaction conditions significantly affect the degree of unsaturation. Likewise, for hydroxyl value (HV) (Table 4.117), most model terms

exhibited *p*-values below 0.05, demonstrating their significant effect on hydroxyl value. The regression equations for all the responses were shown below:

$$\text{Yield (\%)} = 84.50 + 6.07A + 0.5147B - 2.41C + 3.17D + 1.02AB - 1.50AC + 1.56AD - 0.8031BC + 1.75BD - 2.07CD - 0.2892A^2 + 0.9663B^2 + 0.6184C^2 - 3.28D^2$$

$$\text{OOC (\%)} = 0.2616 - 0.1057A - 0.0727B - 0.0391C - 0.4769D - 0.1324AB + 0.0699AC - 0.2708AD + 0.1506BC - 0.1174BD + 0.2157CD + 0.1652A^2 - 0.1652B^2 - 0.1054C2 + 0.4161D^2$$

$$\text{IV} = 117.02 + 9.48A + 2.17B - 1.78C + 4.48D + 1.16AB - 1.09AC + 1.96AD - 1.77BC + 2.08BD - 2.44CD + 0.8274A^2 + 1.47B^2 + 0.1931C^2 - 1.97D^2$$

$$\text{HV} = 15.90 - 2.83A - 0.0143B + 0.0104C - 0.9581D - 0.1940AB + 0.1486AC - 0.4626AD + 0.3936BC - 0.5063BD + 0.6044CD - 0.2801A^2 - 0.5199B^2 - 0.2510C^2 + 0.9704D^2$$

Table 4.114
ANOVA Analysis Factors for Percentage Yield of DOSFOUFATMPE

Source	Sum of Squares	dF	Mean Square	*F*-value	*p*-value model	Significance
A-mole OA	5.44	1	5.44	40.23	< 0.0001	Significant
B-catalyst	0.6880	1	0.6880	5.09	0.0477	Significant
C-time	14.71	1	14.71	108.79	< 0.0001	Significant
D-temperature	24.97	1	24.97	184.70	< 0.0001	Significant
AB	11.44	1	11.44	84.61	< 0.0001	Significant
AC	29.17	1	29.17	215.73	< 0.0001	Significant
AD	29.49	1	29.49	218.09	< 0.0001	Significant
BC	7.11	1	7.11	52.60	< 0.0001	Significant
BD	31.60	1	31.60	233.70	< 0.0001	Significant
CD	54.39	1	54.39	402.25	< 0.0001	Significant
A^2	0.1962	1	0.1962	1.45	0.2561	Not Significant
B^2	3.98	1	3.98	29.43	0.0003	Significant
C^2	0.6835	1	0.6835	5.06	0.0483	Significant
D^2	26.35	1	26.35	194.86	< 0.0001	Significant

Table 4.115
ANOVA Analysis Factors for Percentage OOC of DOSFOUFATMPE

Source	Sum of Squares	dF	Mean Square	*F*-value	*p*-value model	Significance
A-mole OA	0.0016	1	0.0016	0.9905	0.3431	Significant
B-catalyst	0.0137	1	0.0137	8.25	0.0166	Significant
C-time	0.0039	1	0.0039	2.33	0.1580	Not significant
D-temperature	0.5657	1	0.5657	340.42	< 0.0001	Significant
AB	0.1941	1	0.1941	116.79	< 0.0001	Significant
AC	0.0630	1	0.0630	37.91	0.0001	Significant
AD	0.8883	1	0.8883	534.50	< 0.0001	Significant
BC	0.2500	1	0.2500	150.43	< 0.0001	Significant
BD	0.1426	1	0.1426	85.78	< 0.0001	Significant
CD	0.5902	1	0.5902	355.15	< 0.0001	Significant
A^2	0.0640	1	0.0640	38.53	0.0001	Significant
B^2	0.1600	1	0.1600	96.30	< 0.0001	Significant
C^2	0.0199	1	0.0199	11.95	0.0062	Significant
D^2	0.4240	1	0.4240	255.15	< 0.0001	Significant

Table 4.116
ANOVA Analysis Factors for Iodine Value of DOSFOUFATMPE

Source	Sum of Squares	dF	Mean Square	*F*-value	*p*-value model	Significance
A-mole OA	13.24	1	13.24	13.99	0.0038	Significant
B-catalyst	12.19	1	12.19	12.88	0.0049	Significant
C-time	7.99	1	7.99	8.45	0.0157	Significant
D-temperature	50.02	1	50.02	52.86	< 0.0001	Significant
AB	28.80	1	28.80	30.44	0.0003	Significant
AC	15.45	1	15.45	16.32	0.0024	Significant
AD	46.45	1	46.45	49.08	< 0.0001	Significant
BC	34.40	1	34.40	36.35	0.0001	Significant
BD	44.77	1	44.77	47.31	< 0.0001	Significant
CD	75.40	1	75.40	79.68	< 0.0001	Significant
A^2	1.61	1	1.61	1.70	0.2218	Not significant
B^2	9.23	1	9.23	9.75	0.0108	Significant
C^2	0.0666	1	0.0666	0.0704	0.7961	Not significant
D^2	9.51	1	9.51	10.05	0.0100	Significant

Table 4.117
ANOVA Analysis Factors for Hydroxyl Value of DOSFOUFATMPE

Source	Sum of Squares	dF	Mean Square	*F*-value	*p*-value model	Significance
A-mole OA	13.24	1	13.24	13.99	< 0.0001	Significant
B-catalyst	12.19	1	12.19	12.88	0.0049	Significant
C-time	7.99	1	7.99	8.45	0.0157	Significant
D-temperature	50.02	1	50.02	52.86	< 0.0001	Significant
AB	28.80	1	28.80	30.44	0.0003	Significant
AC	15.45	1	15.45	16.32	0.0024	Significant
AD	46.45	1	46.45	49.08	< 0.0001	Significant
BC	34.40	1	34.40	36.35	0.0001	Significant
BD	44.77	1	44.77	47.31	< 0.0001	Significant
CD	75.40	1	75.40	79.68	< 0.0001	Significant
A^2	1.61	1	1.61	1.70	0.2218	Not significant
B^2	9.23	1	9.23	9.75	0.0108	Significant
C^2	0.0666	1	0.0666	0.0704	0.7961	Not significant
D^2	9.51	1	9.51	10.05	0.0100	Significant

4.9.3.4 Interaction Between Variables

The interactions between the process variables, namely the molar ratio of ESFOUFATMPE to oleic acid (A), catalyst percentage (B), reaction time (C) and reaction temperature (D), were illustrated using three-dimensional (3D) response surface plots. The 3D response surface plots present the combined effects of these variables on the selected responses, which include percentage yield (Figure 4.110), oxirane oxygen content (OOC) (Figure 4.111), iodine value (IV) (Figure 4.112) and hydroxyl value (HV) (Figure 4.113) of DOSFOUFATMPE. These plots provide a visual representation of how the interaction between two variables influences each response while the remaining variables were kept constant at their respective center levels.

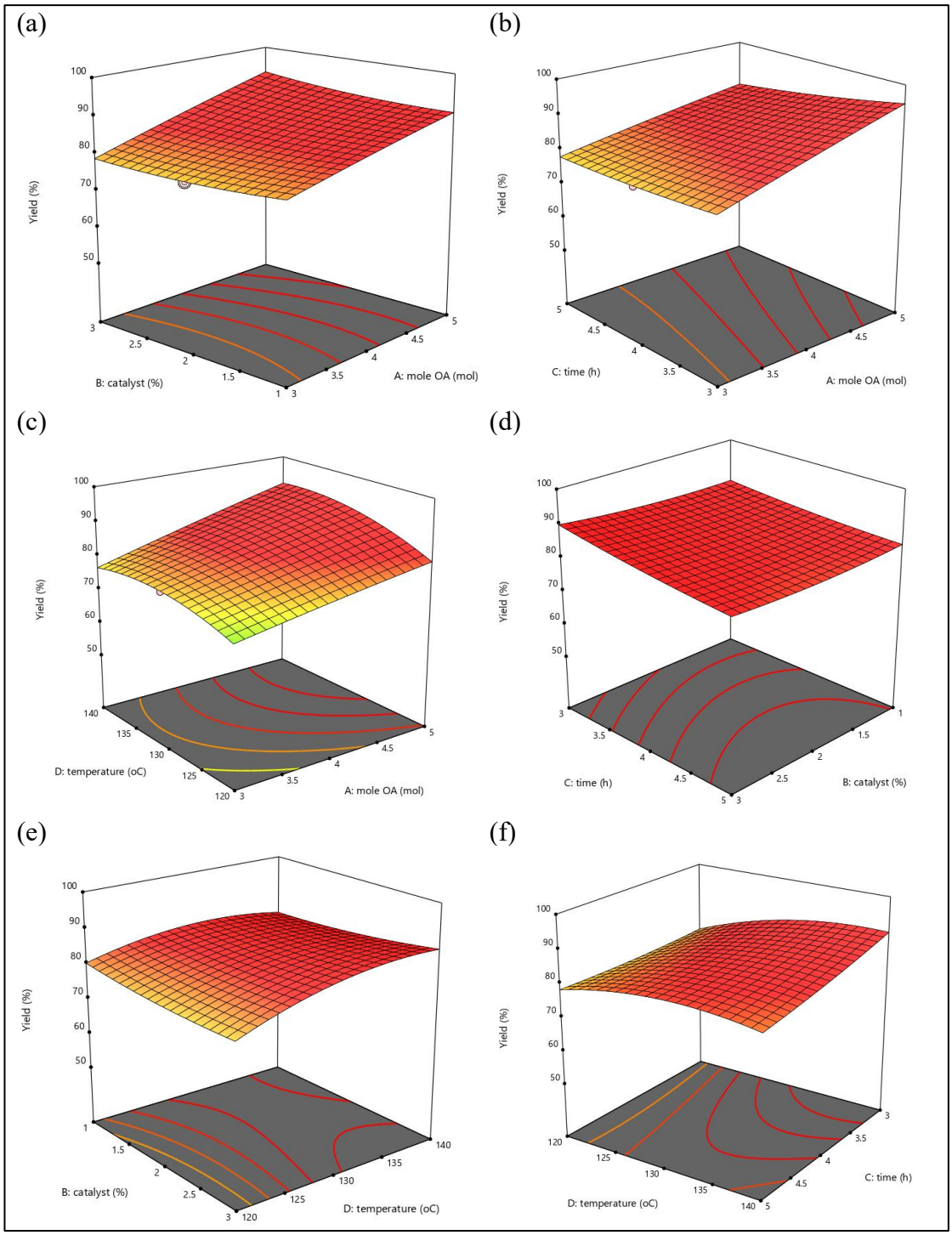


Figure 4.110 3D Surface Plot for a) AB, b) AC, c) AD, d) BC, e) BD and f) CD for Percentage Yield of DOSFOUFATMPE

The interaction effects between the process variables for the ring-opening reaction of ESFOUFATMPE to form DOSFOUFATMPE were illustrated using three-dimensional (3D) response surface plots. Overall, the plots showed that the percentage yield of DOSFOUFATMPE was strongly influenced by both individual factors and their interactions, indicating a non-linear relationship consistent with a quadratic model.

Figure 4.110 (a) shows the interaction between the molar ratio of ESFOUFATMPE to oleic acid (A) and catalyst percentage (B) demonstrated that increasing both variables led to a gradual increase in yield. At lower percentage catalyst, the yield increased moderately with increasing molar ratio, whereas at higher catalyst percentages, the yield improved more significantly, indicating a synergistic interaction between these two factors. This suggested that sufficient catalyst availability enhanced the efficiency of the ring-opening reaction when excess oleic acid was present. Figure 4.110 (b) shows the interaction between molar ratio (A) and reaction time (C), the response surface showed that the yield increased with increasing reaction time, particularly at higher molar ratios. At shorter reaction times, the conversion was limited, while prolonged reaction time allowed more complete ring opening of the epoxide groups, especially when an adequate amount of oleic acid was used.

Figure 4.110 (c) shows the interaction between molar ratio (A) and reaction temperature (D) revealed that higher temperatures significantly enhanced the yield, especially at higher molar ratios. The curved response surface indicated that temperature played a dominant role in promoting the ring-opening reaction, as elevated temperatures increased molecular mobility and reaction kinetics, resulting in higher conversion of epoxide groups to the dioleate structure. Figure 4.110 (d) shows the combined effects of catalyst percentage (B) and reaction time (C) showed that increasing both parameters resulted in a noticeable improvement in yield up to an optimum region. Excessively high catalyst loading or prolonged reaction time did not produce a proportional increase in yield, suggesting the existence of an optimum operating range for efficient ring opening.

Figure 4.110 (e) shows the interaction between catalyst percentage (B) and reaction temperature (D) indicated that higher temperatures amplified the catalytic effect, leading to higher yields. This confirmed that catalyst activity was temperature-dependent and that sufficient thermal energy was required to maximize the effectiveness of the ring-opening process. Figure 4.110 (f) shows the interaction between reaction time (C) and reaction temperature (D) showed a strong positive effect on the yield, with higher yields achieved at longer reaction times and elevated temperatures. The curvature of the response surface suggested that both parameters needed to be carefully optimized to achieve high conversion efficiency without unnecessary energy consumption.

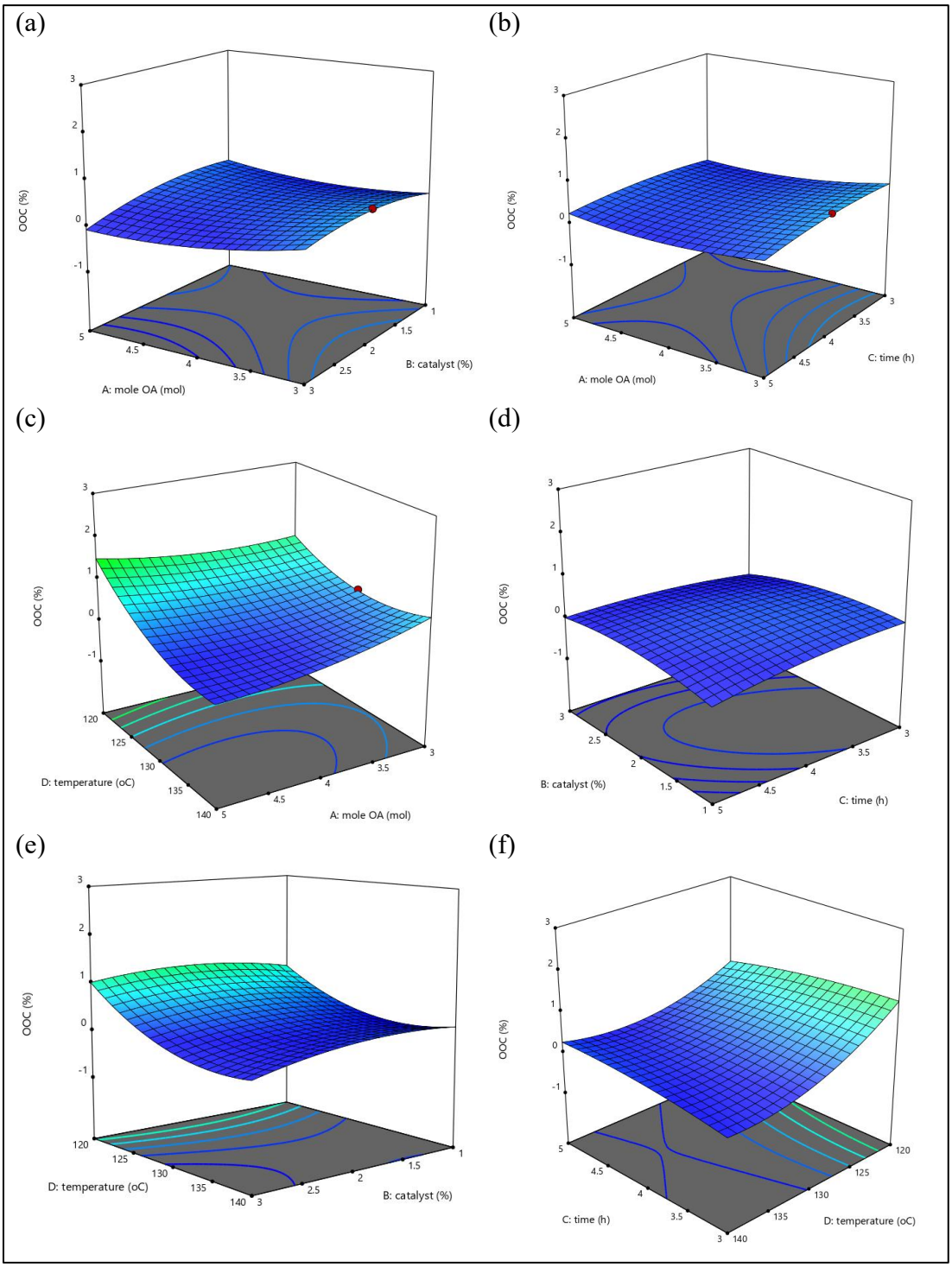


Figure 4.111 3D Surface Plot for a) AB, b) AC, c) AD, d) BC, e) BD and f) CD for Percentage OOC of DOSFOUFATMPE

The interaction effects between the process variables on the percentage OOC during the ring-opening reaction of ESFOUFATMPE to DOSFOUFATMPE were illustrated using 3D response surface plots. Overall, the plots showed that OOC was influenced by both individual factors and their combined interactions, indicating that the ring-opening process was governed by a non-linear relationship.

Figure 4.111 (a) demonstrated the interaction between the molar ratio of ESFOUFATMPE to oleic acid (A) and catalyst percentage (B) showed that OOC slightly decreased with increasing molar ratio, particularly at higher catalyst loadings. This trend suggested that a higher availability of oleic acid promoted ring opening, leading to a reduction in residual oxirane groups, especially when sufficient catalyst was present. Figure 4.111 (b) demonstrated the interaction between molar ratio (A) and reaction time (C), the response surface indicated that OOC decreased as reaction time increased, with a more pronounced effect observed at higher molar ratios. This behavior implied that longer reaction times allowed more complete ring opening of the epoxide groups, particularly when excess oleic acid was available to react with the epoxide rings.

Figure 4.111 (c) demonstrated the interaction between molar ratio (A) and reaction temperature (D) revealed a significant decrease in OOC at higher temperatures. At elevated temperatures, the reduction in OOC was more evident across all molar ratios, indicating that temperature played a dominant role in accelerating the ring-opening reaction and enhancing the consumption of oxirane groups. Figure 4.111 (d) demonstrated the combined effects of catalyst percentage (B) and reaction time (C) showed a gradual reduction in OOC with increasing time, especially at higher catalyst percentages. This suggested that higher catalyst loading enhanced the ring-opening efficiency over time, resulting in lower remaining oxirane content in the final product.

Figure 4.111 (e) demonstrated the interaction between catalyst percentage (B) and reaction temperature (D) demonstrated that increasing temperature led to a notable decrease in OOC, particularly at higher percentage of catalysts. This confirmed that catalyst activity was strongly temperature-dependent and that sufficient thermal energy was required to maximize oxirane ring opening. Figure 4.111 (f) demonstrated the interaction between reaction time (C) and reaction temperature (D) showed a strong combined effect on OOC reduction, where longer reaction times and higher temperatures resulted in the lowest OOC values. This trend indicated that prolonged exposure to elevated temperatures facilitated more complete conversion of epoxide groups during the ring-opening process.

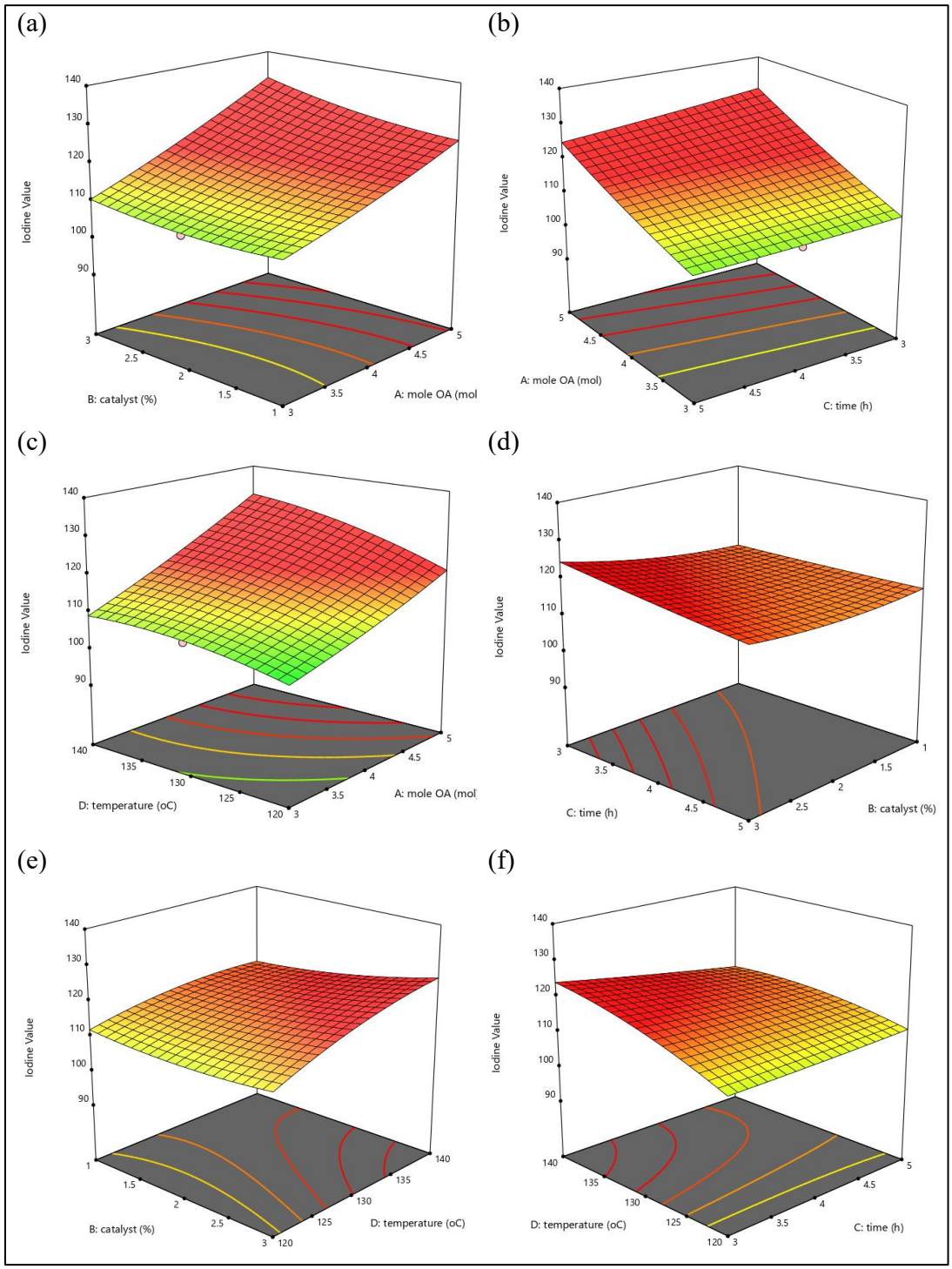


Figure 4.112 3D Surface Plot for a) AB, b) AC, c) AD, d) BC, e) BD and f) CD for Iodine Value of DOSFOUFATMPE

The interaction effects between the process variables on the iodine value (IV) during the ring-opening reaction of ESFOUFATMPE to DOSFOUFATMPE were illustrated using 3D response surface plots. Overall, the plots showed that the iodine value was strongly influenced by both individual factors and their interactions, reflecting changes in the degree of unsaturation as the ring-opening reaction progressed.

The interaction between the molar ratio of ESFOUFATMPE to oleic acid (A) and catalyst percentage (B) (Figure 4.112 (a)) showed that the iodine value increased with increasing molar ratio, particularly at higher catalyst loadings. This trend indicated that a higher amount of oleic acid contributed additional unsaturated bonds to the system, while the presence of catalyst facilitated the ring-opening reaction without significantly reducing the overall unsaturation level. For the interaction between molar ratio (A) and reaction time (C) (Figure 4.112 (b)), the response surface indicated a gradual increase in iodine value with increasing reaction time, especially at higher molar ratios. This behavior suggested that prolonged reaction time allowed more oleic acid to be incorporated into the product structure, leading to a higher iodine value.

The interaction between molar ratio (A) and reaction temperature (D) (Figure 4.112 (c)) revealed that increasing temperature resulted in a higher iodine value, particularly at higher molar ratios. This observation implied that elevated temperatures promoted efficient ring opening while preserving the unsaturated nature of the oleic acid moieties incorporated into DOSFOUFATMPE. The effects of catalyst percentage (B) and reaction time (C) (Figure 4.112 (d)) showed a moderate increase in iodine value with increasing reaction time, with catalyst percentage having a less pronounced effect. This indicated that reaction time played a more dominant role than catalyst loading in influencing the degree of unsaturation during the ring-opening process.

The interaction between catalyst percentage (B) and reaction temperature (D) (Figure 4.112 (e)) demonstrated that higher temperatures led to an increase in iodine value across the studied catalyst range. This suggested that temperature had a stronger influence than percentage of catalyst in determining the final iodine value. The interaction between reaction time (C) and reaction temperature (D) (Figure 4.112 (f)) showed that iodine value increased at longer reaction times and higher temperatures. The curvature of the response surface indicated that both parameters acted synergistically to enhance the incorporation of unsaturated fatty acid chains during ring opening.

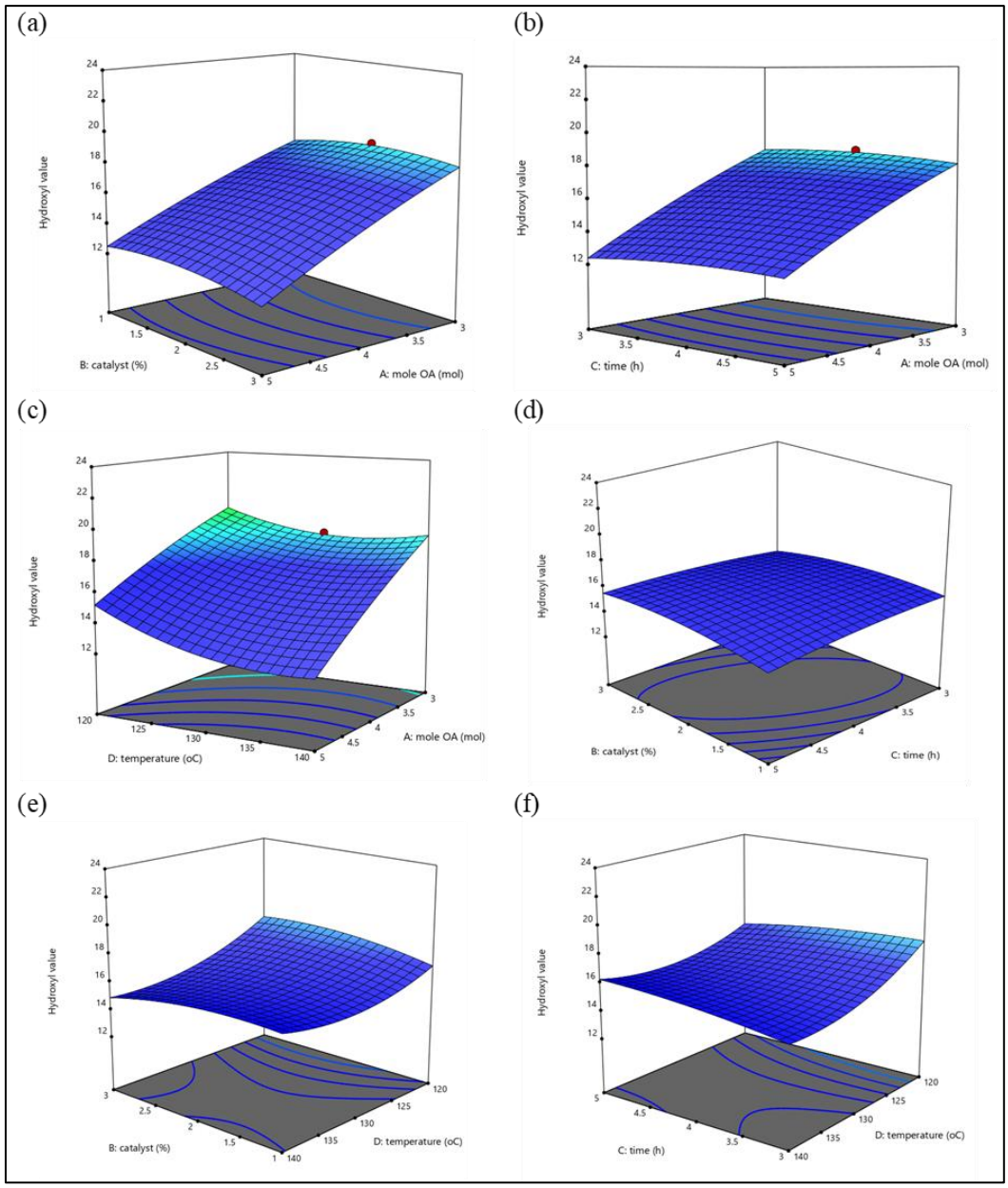


Figure 4.113 3D Surface Plot for a) AB, b) AC, c) AD, d) BC, e) BD and f) CD for Hydroxyl Value of DOSFOUFATMPE

The interaction effects between the process variables on the hydroxyl value (HV) during the ring-opening reaction of ESFOUFATMPE to DOSFOUFATMPE were illustrated using 3D response surface plots. Overall, the plots showed that the hydroxyl value was influenced by both individual factors and their interactions, reflecting the formation of hydroxyl groups as a result of epoxide ring opening.

The interaction between the molar ratio of ESFOUFATMPE to oleic acid (A) and catalyst percentage (B) (Figure 4.113 (a)) showed that the hydroxyl value increased with increasing molar ratio, particularly at higher catalyst percentages. This trend indicated that a higher availability of oleic acid, together with sufficient catalyst,

promoted more effective ring opening and lower the hydroxyl group formation. For the interaction between molar ratio (A) and reaction time (C) (Figure 4.113 (b)), the response surface demonstrated an increase in hydroxyl value with longer reaction time, especially at higher molar ratios. This suggested that extended reaction time allowed more complete conversion of epoxide groups into dioletae structures when adequate oleic acid was present.

The interaction between molar ratio (A) and reaction temperature (D) (Figure 4.113 (c)) revealed that higher temperatures led to an increase in hydroxyl value, particularly at higher molar ratios. This behavior indicated that elevated temperatures enhanced reaction kinetics, facilitating more efficient ring opening and dioleate formation. The combined effects of catalyst percentage (B) and reaction time (C) (Figure 4.113 (d)) showed that the hydroxyl value increased slightly with increasing reaction time, while the influence of catalyst percentage was less pronounced. This suggested that reaction time played a more dominant role than catalyst loading in determining hydroxyl group formation by lowering the hydroxyl value.

Similarly, the interaction between catalyst percentage (B) and reaction temperature (D) (Figure 4.113 (e)) demonstrated that increasing temperature resulted in higher hydroxyl values across the studied catalyst range. This confirmed that temperature strongly influenced the ring-opening process and the generation of hydroxyl functionalities. The interaction between reaction time (C) and reaction temperature (D) (Figure 4.113 (f)) showed a positive combined effect on hydroxyl value, with lower values obtained at longer reaction times and increasing temperatures. This trend indicated that prolonged exposure to higher temperatures promoted more complete epoxide ring opening to dioleate ester.

4.9.3.5 Verification Model

Numerical optimization was performed to determine the optimum conditions for the ring-opening reaction of ESFOUFATMPE to produce DOSFOUFATMPE. The process variables, namely molar ratio of oleic acid (A), catalyst percentage (B), reaction time (C) and reaction temperature (D), were set within specific ranges as shown in the optimization constraints as shown in Table 4.118. The responses were defined with different goals, where percentage yield and iodine value were maximized, while oxirane oxygen content (OOC) and hydroxyl value were minimized. All factors and responses

were assigned equal weight and importance during the optimization. The variables were varied simultaneously to obtain the desired response values and the numerical optimization resulted in a desirability value of 1.00, indicating that the predicted conditions represent the optimal and ideal solution as shown in Figure 4.114.

Table 4.118
Restraints for Optimization of Ring Opening of ESFOUFATMPE Parameter and Response for D-Optimal Design

Parameter and responses	Goal	Lower limit	Upper limit	Weight	Importance
A: mole OA	is in range	3	5	1	1
B: catalyst	is in range	1	3	1	1
C: time	is in range	3	5	1	1
D: temperature	is in range	120	140	1	1
Yield	maximize	55.9	83.4	1	1
OOC	minimize	0.102	2.840	1	1
Iodine Value	maximize	90.15	119.00	1	1
Hydroxyl value	minimize	16.97	23.36	1	1

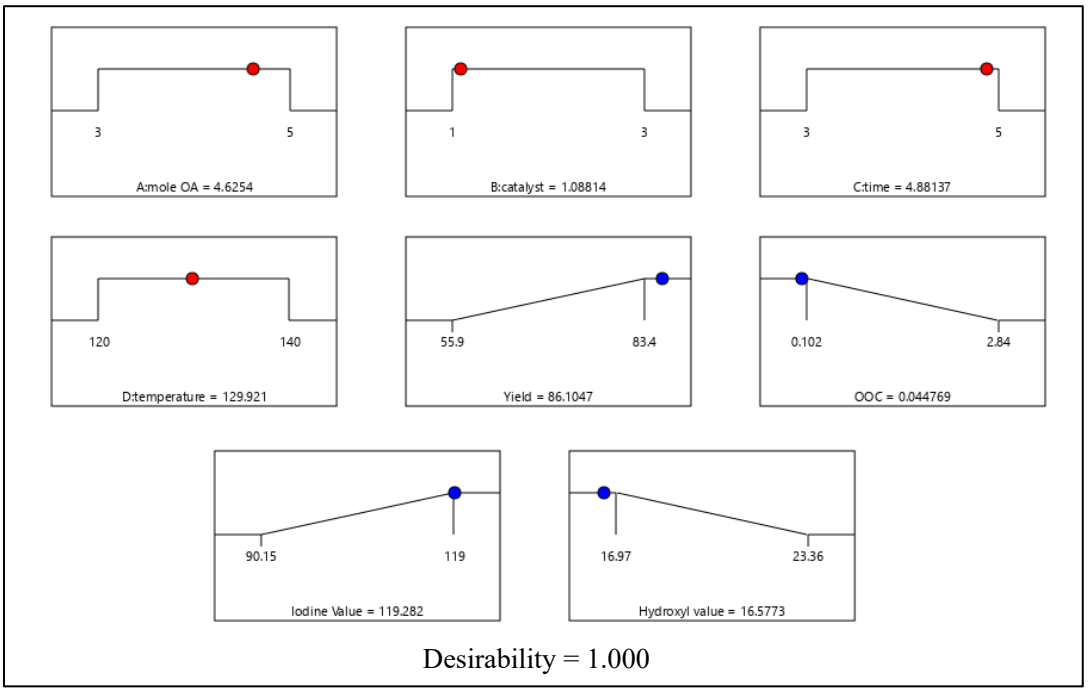


Figure 4.114 D-Optimal Predicted Model at Optimum Condition for Ring Opening of ESFOUFATMPE

The reliability of the model generated from the D-optimal design was assessed by conducting the reaction at three randomly selected experimental conditions. The experimental results obtained were compared with the corresponding model-predicted

values through the calculation of the RSE for each run. An RSE value of less than 5% was used as the acceptance criterion. The results presented in Table 4.119, Table 4.120, Table 4.121 and Table 4.122 show that all calculated RSE values were below this threshold, demonstrating good agreement between experimental and predicted data and confirming the suitability of the model for accurate response prediction.

Table 4.119
Actual and Predicted Data for Verification Model for Percentage Yield of DOSFOUFATMPE

Molar ratio	Catalyst (%)	Reaction time (h)	Reaction temperature (°C)	Yield (%)		
				Actual	Predicted	RSE
5	1	4	120	80.20	83.46	3.91
3	1	3	130	80.92	84.95	4.70
4	2	4	140	84.21	84.38	0.20

Table 4.120
Actual and Predicted Data for Verification Model for Percentage OOC of DOSFOUFATMPE

Molar ratio	Catalyst (%)	Reaction time (h)	Reaction temperature (°C)	OOC (%)		
				Actual	Predicted	RSE
5	1	4	120	1.62	1.37	-
3	1	3	130	0.21	0.14	-
4	2	4	140	0.31	0.20	-

Table 4.121
Actual and Predicted Data for Verification Model for Iodine Value of DOSFOUFATMPE

Molar ratio	Catalyst (%)	Reaction time (h)	Reaction temperature (°C)	IV (I_2/100g)		
				Actual	Predicted	RSE
5	1	4	120	116.2	118.68	2.09
3	1	3	130	118.42	116.30	1.82
4	2	4	140	115.32	119.28	3.32

Table 4.122
Actual and Predicted Data for Verification Model for Hydroxyl Value of DOSFOUFATMPE

Molar ratio	Catalyst (%)	Reaction time (h)	Reaction temperature (°C)	HV (mg KOH/g)		
				Actual	Predicted	RSE
5	1	4	120	14.97	14.36	4.25
3	1	3	130	18.39	18.04	1.94
4	2	4	140	15.43	15.92	3.08

4.9.3.6 Optimum Condition of Ring Opening Reaction

The D-optimal design successfully identified the optimum conditions for the ring-opening reaction of ESFOUFATMPE. The optimal parameters consisted of a molar ratio of oleic acid of 4.6, a percentage of catalyst of 1.09%, a reaction time of 4.9 h and a reaction temperature of 130 °C. Under these conditions, a percentage yield of 85.63% was achieved, with an oxirane oxygen content OOC of 0.054%, an iodine value of 121.7 I_2/100g and a hydroxyl value of 16.90 mg KOH/g. Model validation confirmed the reliability of the predicted optimum, as good agreement between experimental and predicted values was obtained, demonstrating the adequacy of the D-optimal model as shown in Table 4.123, Table 4.124, Table 4.125 and Table 4.126. Figure 4.115 shows the product from the ring opening reaction.

Table 4.123
Actual and Predicted Data for Optimum Condition for Percentage Yield of DOSFOUFATMPE

Molar ratio	Catalyst (%)	Reaction time (h)	Reaction temperature (°C)	Yield (%)		
				Actual	Predicted	RSE
4.6	1.09	4.9	130	85.63	86.11	0.56

Table 4.124
Actual and Predicted Data for Optimum Condition for Percentage OOC of DOSFOUFATMPE

Molar ratio	Catalyst (%)	Reaction time (h)	Reaction temperature (°C)	OOC (%)		
				Actual	Predicted	RSE
4.6	1.09	4.9	130	0.054	0.045	-

Table 4.125
Actual and Predicted Data for Optimum Condition for Iodine Value of DOSFOUFATMPE

Molar ratio	Catalyst (%)	Reaction time (h)	Reaction temperature (°C)	IV (I_2/100g)		
				Actual	Predicted	RSE
4.6	1.09	4.9	130	121.7	119.28	2.03

Table 4.126
Actual and Predicted Data for Optimum Condition for Hydroxyl Value of DOSFOUFATMPE

Molar ratio	Catalyst (%)	Reaction time (h)	Reaction temperature (°C)	HV (mg KOH/g)		
				Actual	Predicted	RSE
4.6	1.09	4.9	130	16.90	16.58	1.93



Figure 4.115 Dioleate Sunflower Oil Unsaturated Fatty Acids Trimethylolpropane Ester (DOSFOUFATMPE)

4.9.4 Characterization of DOSFOUFATMPE

4.9.4.1 Fourier Transform Infrared Spectroscopy

FTIR analysis was used to confirm the structural changes associated with the ring opening reaction of ESFOUFATMPE to DOSFOUFATMPE, as shown in Figure 4.116 and summarized in Table 4.127. After the ring-opening reaction, the epoxide peak at 830.25 cm^{-1} disappeared in the spectrum of DOSFOUFATMPE, confirming the successful opening of the epoxide ring. The ester carbonyl peak remained at 1742.32 cm^{-1}, demonstrating that the ester structure was preserved during the reaction. These key spectral changes verify the successful conversion of ESFOUFATMPE to DOSFOUFATMPE.

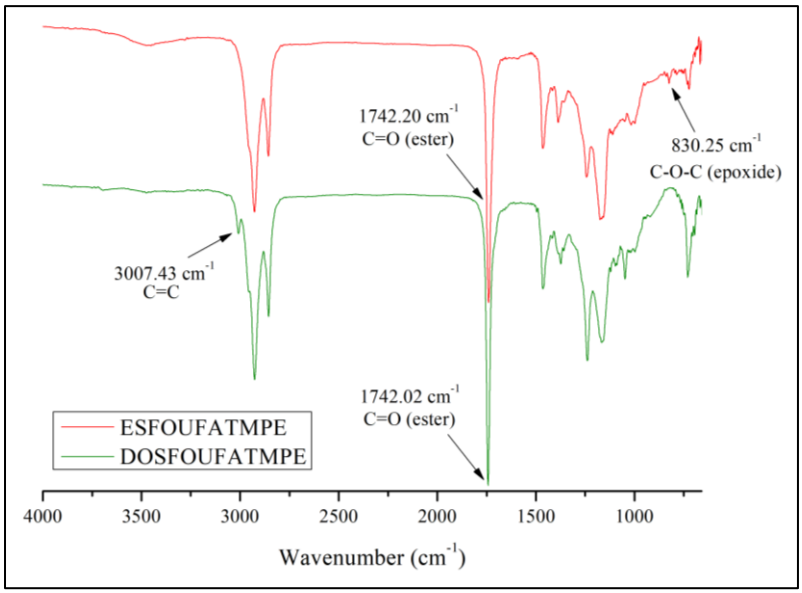


Figure 4.116 FTIR Spectra of ESFOUFATMPE and DOSFOUFATMPE

Table 4.127
Functional Group And Wavenumber for FTIR Spectra of ESFOUFATMPE and DOSFOUFATMPE

Functional group	Wavenumber (cm^{-1})	
	ESFOUFATMPE	DOSFOUFATMPE
C=C bending vibration (aliphatic)	-	3007.43
C-H stretching vibration (aliphatic)	2927.04 and 2854.11	2924.65 and 2850.58
C=O stretching vibration (ester)	1742.20	1742.32
-C-O stretching vibration (ester)	1236.12 and 1160.67	1239.03 and 1162.02
-C-O-C- epoxide	830.25	-

4.9.4.2 Nuclear Magnetic Resonance

The ring-opening reaction was determined using ^{1}H-NMR analysis, as summarized in Table 4.128. After the ring-opening reaction, significant changes were observed in the ^{1}H-NMR spectrum of SFOUFATMPE. The epoxide proton signal at 2.97 to 3.15 ppm disappeared, indicating successful opening of the epoxide ring. Concurrently, the reappearance of signals at 2.03 to 2.10 ppm, assigned to allylic protons (-CH=CH-C**H**$_2$-) and 5.33 to 5.41 ppm, corresponding to olefinic protons (-C**H**=CH-), suggests structural modification resulting from the ring-opening process with oleic acid.

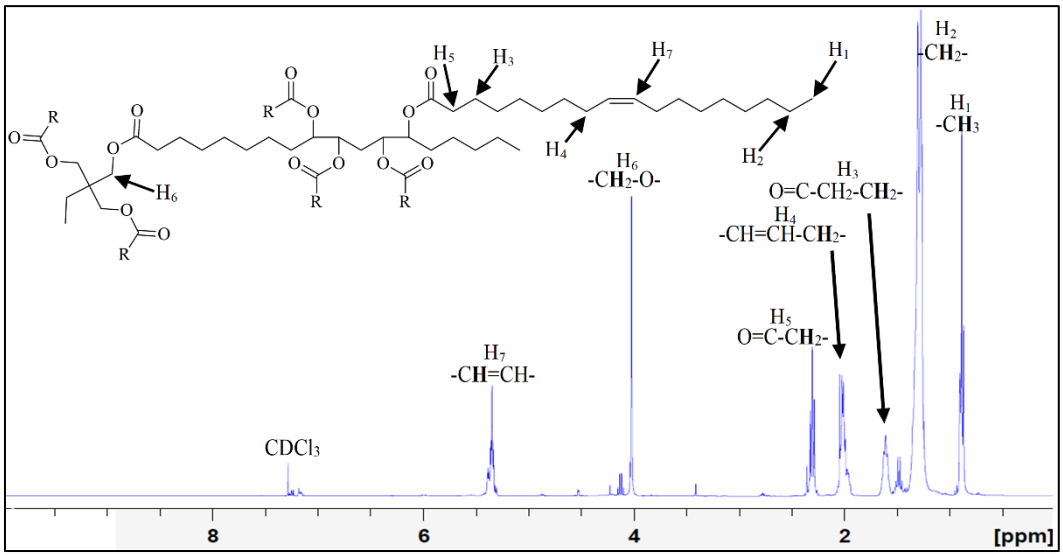


Figure 4.117 ^{1}H NMR Spectrum for DOSFOUFATMPE

Table 4.128
Type of Proton and Chemical Shift for ESFOUFATMPE and DOSFOUFATMPE

	Type of proton	Chemical shift (ppm)		
		ESFOUFATMPE	SFOUFATMPE	Theoretical*
H_1	-C**H**$_3$	0.88-0.93	0.89-0.93	0.70-1.3
H_2	-C**H**$_2$-	1.26-1.39	1.28-1.39	1.2-1.4
H_3	O=C-CH$_2$-C**H**$_2$-	-	1.58-1.61	1.5-2.0
H_4	-CH=CH-C**H**$_2$-	-	2.03-2.10	1.6-2.6
H_5	O=C-C**H**$_2$-	2.29-2.37	2.34-2.38	2.1-2.5
-	-HC-O-CH- (epoxide)	2.97-3.15	-	2.5-3.5
H_6	-C**H**$_2$-O- (trimethylolpropane)	4.10-4.15	4.12-4.14	4.0-4.5
H_7	-C**H**=CH-	-	5.33-5.41	4.5-6.5

Source: *Pavia et al. (2015)

The structural changes associated with the ring-opening reaction were further examined using ^{13}C-NMR analysis (Figure 4.118), as summarized in Table 4.129. Following the ring-opening reaction, notable changes were observed in the ^{13}C-NMR spectrum of DOSFOUFATMPE. The epoxide-related carbon signals at 54.21 to 57.25 ppm completely disappeared, indicating successful opening of the epoxide ring. Concurrently, the appearance of olefinic carbon signals at 127.88 to 130.15 ppm, assigned to **C**=C carbons, reflects the structural modification after ring opening. The -**C**H$_2$-O- carbons of trimethylolpropane shifted to 63.67 ppm, while the quaternary carbon of trimethylolpropane remained unchanged at 40.59 ppm, demonstrating that the core ester structure was preserved. In addition, the ester carbonyl carbon (O=**C**-OR)

was consistently observed at 173.42 to 173.46 ppm in both spectra, confirming the stability of the ester linkage during the ring-opening process.

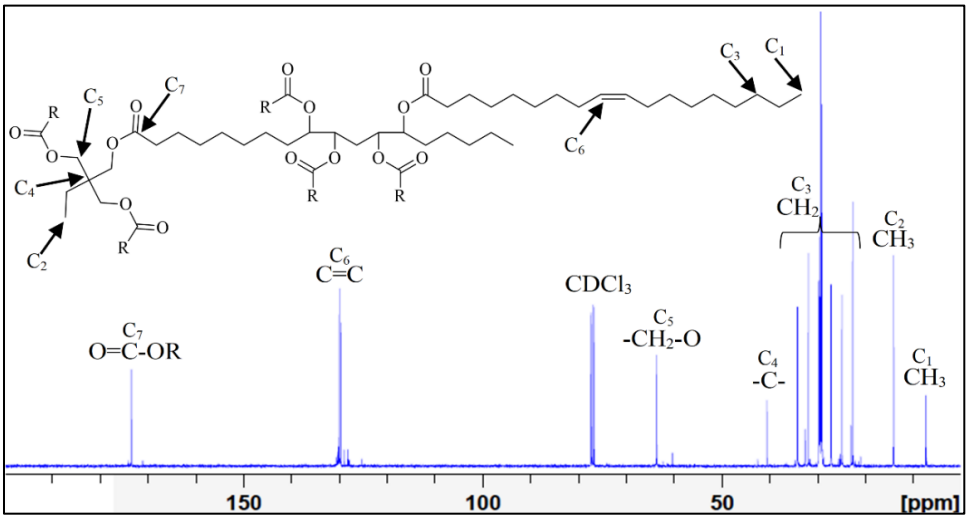


Figure 4.118 ^{13}CNMR Spectrum for DOSFOUFATMPE

Table 4.129
Type of Carbon and Chemical Shift for ESFOUFATMPE and DOSFOUFATMPE

	Type of carbon	Chemical shift (ppm)		
		ESFOUFATMPE	SFOUFATMPE	Theoretical*
C_1	-**C**H$_3$ (trimethylolpropane)	8.15	8.12	8-30
C_2	-**C**H$_3$	13.99-14.19	14.02-14.15	8-30
C_3	-**C**H$_2$-	21.05-31.85	20.96-31.88	15-55
C_4	-**C**- (trimethylolpropane)	40.59	40.59	20-60
-	-**C**-O-C- (epoxide)	54.21-57.25	-	40-60
C_5	-**C**H$_2$-O- (trimethylolpropane)	60.41	63.67	40-80
C_6	-**C**=C-	-	127.88-130.15	100-150
C_7	O=**C**-OR (ester)	173.46	173.42	155-185

Source: *Pavia et al. (2015)

4.9.5 Physicochemical Properties of DOSFOUFATMPE

The physicochemical properties of DOSFOUFATMPE were evaluated based on pour point, flash point, kinematic viscosity, viscosity index, oxidative stability and rheology. The physicochemical properties of DOSFOUFATMPE were compared with dioleate polyol ester (DOPE) derived from different plant oil, which were jatropha *curcas* oil (DOPE A) and palm oil (DOPE B), as shown in Table 4.130.

Table 4.130
Physicochemical Properties of DOSFOUFATMPE and Others DOPE

Physicochemical properties	DOSFOUFATMPE	DOPE A	DOPE B
Pour point (°C)	-24	-29	-10
Flash point (°C)	310	250	315
Viscosity at 40 °C (cSt)	60.02	220.00	83.45
Viscosity at 100 °C (cSt)	12.03	22.29	15.3.3
Viscosity Index	151.1	135.0	146.0
Oxidative stability (min)	33	N/A	N/A
Rheology	Newtonian	N/A	N/A

Source: DOPE A: Nor et al. (2021); DOPE B: Nor et al. (2022)

From the study, the pour point of DOSFOUFATMPE was -24 °C, which was slightly higher than DOPE A (-29 °C) but significantly lower than DOPE B (-10 °C), indicating good low-temperature flow properties. The relatively low pour point of DOSFOUFATMPE can be attributed to the presence of unsaturated fatty acid chains from oleic acids that come from ring opening reaction, which reduce crystallization at lower temperatures.

In terms of flash point, DOSFOUFATMPE exhibited a flash point of 310 °C, which was higher than DOPE A (250 °C) and comparable to DOPE B (315 °C), indicating good thermal stability and low volatility. The higher flash point of DOSFOUFATMPE can also be attributed to the additional of oleic acid during synthesis, which increases the molecular weight of the ester. An increase in molecular weight generally reduces volatility and enhances resistance to thermal degradation, resulting in an increased flash point.

The kinematic viscosity of DOSFOUFATMPE was 60.02 cSt at 40 °C and 12.03 cSt at 100 °C, which are significantly lower than DOPE A but slightly lower than DOPE B. This difference may be due to variations in fatty acid composition and molecular structure of the esters derived from different feedstocks. The viscosity index of DOSFOUFATMPE (151.1) was higher than DOPE A (135.0) and slightly higher than DOPE B (146.0), indicating good viscosity to temperature behaviour.

DOSFOUFATMPE showed an oxidative stability of 33 minutes, suggesting improved stability compared to non-modified esters due to structural modification through epoxidation and ring-opening reactions that reduce the reactivity of double bonds. The rheological behaviour of DOSFOUFATMPE was Newtonian. Rheological

analysis confirms that DOSFOUFATMPE exhibits Newtonian flow behavior, as evidenced by the linear dependence of shear stress on shear rate and the shear-rate-independent viscosity observed over the range of 40 to 100 s^{-1} as shown in Figure 4.119 and Figure 4.120. Overall, DOSFOUFATMPE demonstrates comparable physicochemical properties with DOPE derived from other plant oils, with good low-temperature properties, thermal stability and viscosity to temperature performance.

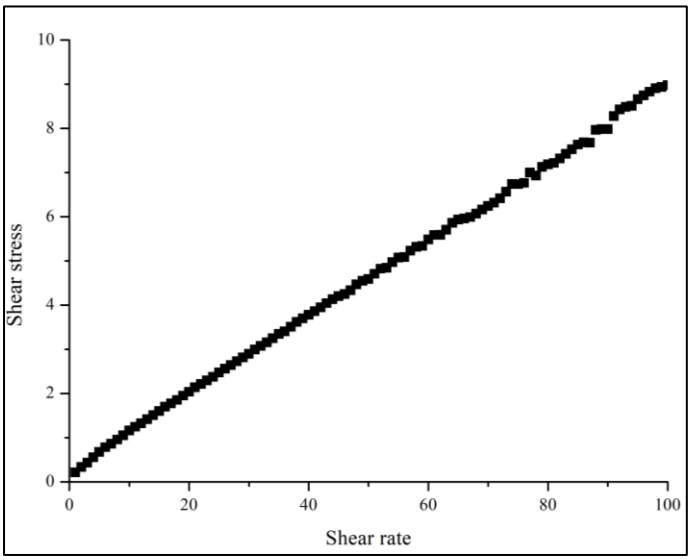


Figure 4.119 Shear Stress versus Shear Rate of DOSFOUFATMPE

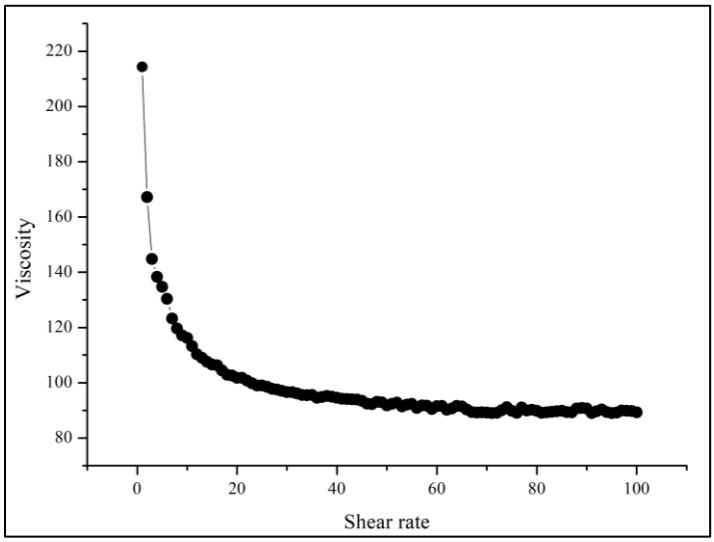


Figure 4.120 Viscosity versus Shear Rate of DOSFOUFATMPE

4.10 Comparison on Physicochemical Properties of Synthesized Polyol Ester as Biolubricant Base Stock

The physicochemical properties of synthesized polyol ester (SFOUFANPGE, SFOUFATMPE, SFOUFAPEE, ESFOUFATMPE and DOSFOUFATMPE) were compared with the SFO based on the pour point, flash point, kinematic viscosity, viscosity index, oxidative stability and rheology. Table 4.131 shows the physicochemical properties of SFO, SFOUFANPGE, SFOUFATMPE, SFOUFAPEE, ESFOUFATMPE and DOSFOUFATMPE.

Table 4.131
The Physicochemical Properties of SFO, SFOUFANPGE, SFOUFATMPE, SFOUFAPEE, ESFOUFATMPE and DOSFOUFATMPE.

Physiochemical Properties	SFO	NPGE	TMPE	PEE	ETMPE	DOTMPE
Pour point (°C)	-13	-15	-18	-21	-1	-24
Flash point (°C)	280	268	290	302	296	310
Kinematic viscosity at 40 °C (cSt)	30.54	21.24	32.47	80.49	208.27	60.02
Kinematic viscosity at 100 °C (cSt)	7.22	5.35	7.21	14.66	66.84	12.03
Viscosity index	163.56	174.50	157.48	145.93	140.67	151.10
Oxidative stability (min)	22.0	22.4	24.0	19.0	30.0	33.0
Rheological	Newtonian	Newtonian	Newtonian	Newtonian	Newtonian	Newtonian
ISO VG Lubricant	32	22	32	68	220	68
Potential application	Mobile hydraulics	Textile machinery	Mobile hydraulics	Hydraulic presses	Marine gear systems	Hydraulic presses

NPGE: SFOUFANPGE; TMPE: SFOUFATMPE; PEE: SFOUFAPEE; ETMPE: ESFOUFATMPE and DOTMPE: DOSFOUFATMPE

Based on the pour point of SFO (-13 °C) the decrease to -15 °C for SFOUFANPGE, -18 °C for SFOUFATMPE and -21 °C for SFOUFAPEE indicate that the improvement for low temperature properties after the esterification. This reduction in pour point was attributed to the formation of branched polyol ester structures, which

disrupt the molecular packing and reduce the crystallization at low temperatures (Fortunato et al., 2025; Suemanotham et al. 2026). The number of ester linkages in polyol ester also influence the pour point (Soodoo et al., 2023). SFOUFANPGE contains two ester chain, SFOUFATMPE contains three ester chains and SFOUFAPEE contain four ester chain s that attach to the polyol backbone. The used of SFOUFA as starting material for the esterification further contributes to the lower pour point due to the presence of double bond that prevent thigh molecular packing (Jumaah et al., 2022). A higher number of ester chain result in greater number of double bonds within the molecular structure, which increase the molecular brunching and structural irregularity. As a result, SFOUFAPEE exhibited the lowest pour point compared to SFOUFANPGE and SFOUFATMPE.

In term of flash point, SFO showed a flash point of 280 °C, while SFOUFANPGE, SFOUFATMPE and SFOUFAPEE recorded value of 268 °C, 290 °C and 302 °C, respectively. The flash point generally increased with the esterification, particularly for SFOUFATMPE and SFOUFAPEE due to the formation of higher molecular weight of ester that exhibit lower volatility and greater thermal stability (Raof et al., 2022; Ribeiro et al., 2025). The increasing in molecular weight was associated with the increasing number of ester chains in polyol structure (Ijeoma et al., 2026). The slightly lower flash point of SFOUFANPGE compared to SFO may attributed to it lower molecular weight, as it contains fewer ester chains compared to SFOUFATMPE and SFOUFAPEE.

Kinematic viscosity of SFO at 40 °C (30.54 cSt) decreased to 21.24 cSt for SFOUFANPGE but increased to 32.27 cSt and 80.49 cSt for SFOUFATMPE and SFOUFAPEE, respectively. Similar trends were observed at 100 °C. The decrease in viscosity for SFOUFANPGE due to its fewer ester chain, while the increase for SFOUFATMPE and SFOUFAPEE were associated with high molecular wight and number of ester chains, resulting in stronger intermolecular interaction and greater resistance to flow Jumaah et al. (2024). The viscosity index of SFO (163.56) improved to 174.50 for SFOUFANPGE, but slightly decrease for SFOUFATMPE (157.48) and SFOUFAPEE (145.93).

Oxidative stability shows varying trends among the polyol ester. SFO exhibited an oxidative stability of 22.0 minutes while SFOUFANPGE and SFOUFATMPE shows comparable value of 22.4 and 24.0 minutes, respectively. However, SFOUFAPEE showed a lower oxidative stability of 19.0 minutes. The reduced in oxidative stability

of SFOUFA due to the higher unsaturated fatty acids content and increased exposure of bis allylic proton in double bond in the ester structure, making it more susceptible to oxidation (Nor et al., 2017). All samples exhibited Newtonian for the rheological behaviour, indicating consistent viscosity independent of shear rate. Overall, esterification improved the low temperature properties and thermal stability while influencing the viscosity and oxidative stability depending on the type of polyol used.

Further structural modification of SFOUFATMPE through epoxidation and ring opening reaction resulted in ESFOUFATMPE and DOSFOUFATMPE, respectively. The pour point increased from -18 °C for SFOUFATMPE to -1 °C for ESFOUFATMPE but decreased to -24 °C for DOSFOUFATMPE. The increasing in pour point after the epoxidation was attributed to the conversion of double bond in the fatty acids chains to epoxide ring which increase the molecular rigidity and intermolecular interaction, which reduce the low temperature fluidity (Salimon and Salih, 2023). In contract, the ring opening reaction and incorporation of oleic acid in DOSFOUFATPE increasing the branching which lowering the pour point.

The flash point of SFOUFATMPE increase from 290 °C to 296 °C for ESFOUFATMPE and further to 310 °C for DOSFOUFATMPE. The flash point was associated with higher molecular weight and reduced volatility following the structural modification, particularly with the additional of oleic acid in DOSFOUFATMPE, which increase the molecular weight and thermal stability (Raof et al., 2022).

A significant increase in viscosity was observed after the epoxidation, where ESFOUFATMPE exhibited very high viscosity at 208.27 cSt at 40 °C and 66.84 cSt at 100 °C compared to SFOUFATMPE (32.47 and 7.21 cSt). This increase was due to the formation of epoxide ring that enhance the intermolecular interaction (Salimon and Salih, 2023). After the ring opening, the viscosity decreases to 60.02 cSt at 40 °C and 12.03 cSt at 100 °C for DOSFOUFATMPE but remained higher than the original SFOUFATMPE, indicating modification of molecular structure and improved flow properties compared to the epoxidized form.

The viscosity index decreases from 157.48 for SFOUFATMPE to 140.67 ESFOUFATMPE and increased to 151.10 for DOSFOUFATMPE, reflecting the changes in temperature to viscosity behaviour due to the structural modification. The oxidative stability improves significantly from 24.0 minutes for SFOUFATMPE to 30.0 minutes for ESFOUFATMPE and further to 33.0 minutes for DOSFOUFATMPE. The improvement in oxidative stability was attributed to the reduction of bis allylic proton

in double bond through epoxidation and ring opening reaction which decrease the susceptibility to oxidation (Salimon and Salih, 2023). ESFOUFATMPE and DOSFOUFATMPE exhibited Newtonian rheological behaviour.

The physicochemical properties of DOSFOUFATMPE were compared with commercial lubricant (CL) (Petronas Arbor Hydraulic 68 HV) to evaluate its performance as a potential biolubricant base stock. The pour point of DOSFOUFATMPE (-24 °C) was higher than the CL (-42 °C), suggesting slightly lower low-temperature fluidity. For the flash point DOSFOUFATMPE shows a higher value (310 °C) compared to CL (234 °C) that shows good thermal stability and low volatility. DOSFOUFATMPE exhibited kinematic viscosity of 60.02 cSt at 40 °C which was slightly lower than CL which was 69.7 cSt but still within the ISO VG 68 range. The viscosity index of DOSFOUFATMPE (151.10) was higher than CL (145.0), indicating better viscosity stability with changes in temperature. The result shows that DOSFOUFATMPE had comparable properties to the CL which highlighting its potential as a biolubricant base stock.

The final product, DOSFOUFATMPE, demonstrated significant improvement in physicochemical properties compared to SFO, particularly in oxidative stability, which increased from 22.0 to 33.0 minutes. This indicates that the chemical modification successfully addresses the main limitation of plant oil especially in SFO which has low oxidative stability. The improvement can be attributed to the removal of the beta hydrogen and bis allylic proton associated with the double bond through the structural modification. Overall, chemical modification through epoxidation and ring opening successfully enhance the pour point, flash point and oxidative stability while influencing the low temperature properties.

CHAPTER 5
CONCLUSION AND RECOMMENDATION

5.1 Conclusion

This research successfully demonstrated the modification of SFO into potential biolubricant base stocks through a series of chemical modification steps. The physicochemical properties of SFO were evaluated to determine the suitability as starting material. The IV value of SFO was recorded at 118.01 g I_2/100 g, confirming the high degree of unsaturation due to the presence of linoleic and oleic acid. The acid value and free fatty acid content were 0.14 mg KOH/g and 0.0721%, respectively, indicating good oil quality. The pour point, flash point, viscosity, viscosity index and oxidative stability of SFO were -13 °C, 280 °C, 30.54 cSt (40 °C), 7.22 cSt (100 °C), 163.56 and 22.0 minutes, respectively, demonstrating that SFO possesses good baseline properties for further chemical modification.

Optimization of reaction parameters for hydrolysis, esterification, epoxidation and ring-opening reactions was successfully carried out using RSM via D-optimal design. The optimum hydrolysis conditions were achieved at 2.4 M ethanolic KOH, 51 °C and 1.4 h, producing 96.41% of SFOFA. The esterification of sunflower oil unsaturated fatty acids with NPG, TMP and PE achieved high ester yields under optimized conditions of 3.2 mol ratio, 1.37 w/w% catalyst, 149 °C and 4 h for NPG, 4.0 mol ratio, 1.13 w/w% catalyst, 154 °C and 6 h for TMP and 5.0 mol ratio, 1.08 w/w% catalyst, 177 °C and 6.9 h. Subsequent epoxidation and ring opening reactions were optimized at 7 mol HCOOH, 2 mol H_2O_2, 1.2 w/w% catalyst, 41 °C and 3.5 h, producing 85.70% of ESFOUFATMPE and 4.6 mol ratio, 1.09 w/w% catalyst, 130 °C and 4.9 h producing 85.63% DOSFOUFATMPE. These optimized conditions confirmed the effectiveness of RSM in enhancing reaction efficiency and product yield.

The chemical composition and structural characteristics of the synthesized products were successfully confirmed through analytical techniques. GC-MS analysis verified the fatty acid composition of SFO, SFOFA, SFOSFA and SFOUFA, showing unsaturated fatty acid content of approximately 84.77%. GC-FID analysis confirmed the formation of polyol esters with 100% diester for SFOUFANPGE, 100% triester for

SFOUFATMPE and 94.6% tetraester for SFOUFAPEE. FTIR and NMR analyses further confirmed successful hydrolysis, separation, esterification, epoxidation and ring-opening reactions.

The physicochemical evaluation of the synthesized esters showed significant improvement compared to SFO. Where the SFOUFATMPE shows the best oxidative stability when compared with SFOUFANPGE and SFOUFAPEE. Epoxidation of SFOUFATMPE increased viscosity and oxidative stability by converting double bonds into epoxy rings, while ring opening and incorporation of oleic acid improved both oxidative stability and low-temperature performance. Among all synthesized esters, DOSFOUFATMPE exhibited the most balanced performance, with a pour point of -24 °C, flash point of 310 °C, viscosity index of 151.10 and oxidative stability of 33.0 minutes, making it the most promising biolubricant base stock for hydraulic and industrial lubrication applications.

Overall, the results showed that DOSFOUFATMPE exhibits significantly improved physicochemical properties compared to the SFO, in term of oxidative stability, flash point and pour point. The oxidative stability increased from 22.0 minutes to 33.0 minutes for DOSFOUFATMPE indicating enhance the resistance to oxidation after the chemical modification. The improvement in flash point reflects the better thermal stability, while the improved of pour point suggests enhance the low temperature properties. These results confirm that the structural modification successfully addressed the limitation in plant oil (SFO) which was the low oxidative stability, thereby enhancing its suitability to become a biolubricant based stock.

5.2 Recommendation

Based on the findings and limitations of this study, several recommendations are proposed to further enhance the development and application of sunflower oil-based biolubricants. Future research may explore the use of alternative polyhydric alcohols, such as di-pentaerythritol (di-PE) and di-trimethylolpropane (di-TMP), during the esterification process to produce higher molecular weight polyol esters. The incorporation of these polyhydric alcohols is expected to increase molecular branching and structural complexity, which may improve the viscosity index, thermal stability, load-carrying capacity and overall lubrication performance. Such modifications could

expand the applicability of the synthesized biolubricants to more demanding industrial operating conditions.

Further chemical modification through epoxidation of the synthesized polyol esters, particularly SFOUFAPEE and SFOUFANPGE, is also recommended. The introduction of oxirane functional groups may provide additional reactive sites for subsequent ring-opening reactions, enabling the production of tailored biolubricants with enhanced polarity, oxidative stability, anti-wear properties and tribological performance. This approach could further improve the thermal and chemical robustness of the lubricants while maintaining their renewable and environmentally friendly characteristics.

The esterification of saturated fatty acids should also be investigated as an alternative to SFOUFA. Saturated fatty acid-based polyol esters are expected to exhibit superior oxidative stability and resistance to thermal degradation owing to the absence of carbon–carbon double bonds. A comparative investigation between saturated and unsaturated fatty acid-derived polyol esters would provide valuable insights into the relationship between molecular structure and lubricant performance, facilitating the development of formulations for specific industrial applications.

Comprehensive tribological evaluation of the synthesized biolubricants should be conducted under boundary lubrication conditions. Although the present study successfully characterized the physicochemical, rheological, thermal and oxidative properties of the synthesized polyol esters, their anti-wear and extreme-pressure performances were not investigated. Therefore, future work should evaluate the tribological characteristics of the optimum product, DOSFOUFATMPE, using a Four-Ball Wear Tester in accordance with ASTM D4172. Parameters such as the coefficient of friction, wear scar diameter and load-carrying capacity should be determined to establish its suitability for practical lubricant applications under high mechanical loads.

The compatibility of the synthesized biolubricants with commercial lubricant additives should also be evaluated. Investigating the solubility and response of additives, including antioxidants, anti-wear agents, corrosion inhibitors, viscosity modifiers and pour point depressants, would provide valuable information regarding formulation stability and performance enhancement. Such studies are essential for assessing the feasibility of incorporating the synthesized biolubricants into commercial lubricant formulations while maintaining desirable physicochemical and tribological properties.

Consideration should also be given to the industrial scale-up of the optimized synthesis process. Although the present work demonstrated the feasibility of producing sunflower oil-based biolubricants at laboratory scale, further studies are required to evaluate pilot-scale production, process economics, catalyst recovery, energy consumption and process sustainability. In addition, long-term storage stability, production consistency and life-cycle assessment should be investigated to facilitate the commercialization and industrial implementation of the developed biolubricants.

REFERENCES

Abdullah, B. M., & Salimon, J. (2010). Epoxidation of vegetable oils and fatty acids: catalysts, methods and advantages. *Journal of Applied Sciences*, *10*(15), 1545–1553.

Abdullah, A., Abd Gani, S. S., Yun Hin, T. Y., Haiyee, Z. A., Zaidan, U. H., Kassim, M. A., & Effendi Halmi, M. I. (2019). Lipase-catalyzed synthesis of red pitaya (*Hylocereus polyrhizus*) seed oil esters for cosmeceutical applications: Process optimization using response surface methodology. *RSC Advances, 9*(10), 5599–5609.

Aboki, M. A., Mohammed, M., Musa, S. H., Zuru, H. M., Aliyu, G. M., Alibe, I. M., & Inuwa, B. (2012). Physicochemical and anti-microbial properties of sunflower (*Helianthus Annuus L.*) seed oil. *International Journal of Science and Technology*, *2*(4), 151–194.

Adeleke, B. S., & Babalola, O. O. (2020). Oilseed crop sunflower (*Helianthus annuus*) as a source of food: Nutritional and health benefits. *Food Science and Nutrition*, *8*(9), 4666–4684.

Adhvaryu, A., Liu, Z., & Erhan, S. Z. (2005). Synthesis of novel alkoxylated triacylglycerols and their lubricant base oil properties. *Industrial Crops and Products*, *21*(1), 113–119.

Aerts, H. A. J., & Jacobs, P. A. (2004). Epoxide yield determination of oils and fatty acid methyl esters using ^{1}H NMR. *Journal of the American Oil Chemists' Society*, *81*(9), 841–846.

Aguieiras, E. C. G., Cavalcanti, E. D. C., da Silva, P. R., Soares, V. F., Fernandez-Lafuente, R., Assuncao, C. L. B., d Silva, J. A. C., & Freire, D. M. G. (2020). Enzymatic synthesis of neopentyl glycol-based biolubricant using biodiesel from soybean oil and castor bean as raw materials. *Renewable Energy, 148* (2020), 689-696.

Akkaya, M. R. (2018). Prediction of fatty acid composition of sunflower seeds by near-infrared reflectance spectroscopy. *Journal of Food Science and Technology, 5*, 2318-2325.

Almasi, S., Ghobadian, B., Najafi, G., & Soufi, M. D. (2021). A review on bio-lubricant production from non-edible oil-bearing biomass resources in Iran: Recent progress and perspectives. *Journal of Cleaner Production*, *290*. 125830.

Almeida, M., Erthal, R., Padua, E., Silveira, L., & Am, L. (2008). Talanta response surface methodology (RSM) as a tool for optimization in analytical chemistry. *Talanta*, *76*(5), 965–977.

Annisa, A. N., & Widayat, W. (2018). A review of bio-lubricant production from vegetable oils using esterification transesterification process. *MATEC Web of Conferences*, *156*, 06007.

Arianto, A., & Cindy, C. (2019). Preparation and evaluation of sunflower oil nanoemulsion as a sunscreen. *Macedonian Journal of Medical Sciences*, *7*(22), 3757–3761.

Ashrafi J., Semnani A., Langeroodi H., & Shirani M. (2017). Direct acetylation of sunflower oil in the presence of boron trioxide catalyst and the adduct usage as the base stock and lubricant additive. *Bulletin of the Chemical Society of Ethiopia, 31*(1), 39-49.

Aziz, N. A. M., Yunus, R., Rashid, U., & Syam, A. M. (2014). Application of response surface methodology (RSM) for optimizing the palm-based pentaerythritol ester synthesis. *Industrial Crops and Products*, *62*, 305–312.

Bach, R. D., Canepa, C., Winter, J. E., & Blanchette, P. E. (1997). Mechanism of acid-catalyzed epoxidation of alkenes with peroxy acids. *Journal of Organic Chemistry*, *62*(15), 5191–5197.

Bahadi, M., Salimon, J., & Derawi, D. (2022). Synthesis of ISO grade 46 and 68 biolubricant from palm kernel fatty acids. *Sains Malaysiana*, *51*(8), 2507–2529.

Bahadi, M., Yusoff, M. F., Salimon, J., & Derawi, D. (2020). Optimization of response surface methodology by D-optimal design for alkaline hydrolysis of crude palm kernel oil. *Sains Malaysiana*, *49*(1), 29–41.

Baş, D., & Boyacı, İ. H. (2007). Modeling and optimization I : Usability of response surface methodology. *Journal of Food Engineering, 78*(3), 836-845.

Bellini, M., Bianchi, S., Zaccheria, F., & Ravasio, N. (2021). Tribology international vegetable oils as triple bottom line compliant lubricants. *Tribology International*, *161*, 107103.

Borugadda, V. B., & Goud, V. V. (2015). Response surface methodology for optimization of bio-lubricant basestock synthesis from high free fatty acids castor oil. *Energy Science and Engineering*, *3*(4), 371–383.

Cecilia, J. A., Plata, D. B., Saboya, R. M. A., de Luna, F. M. T., Cavalcante, C. L., & Rodríguez-Castellón, E. (2020). An overview of the biolubricant production process: Challenges and future perspectives. *Processes*, *8*(3), 1–24.

Cermak, S. C., Evangelista, R. L. & Kenar, J. A. (2012) Distillation of natural fatty acids and their chemical derivatives. *Distillation-advances from Modeling to Applications* (pp. 109-140).

Charoo, M. S., & Wani, M. F. (2016). Friction and wear properties of nano - Si_3N_4/ nano - SiC composite under nanolubricated conditions. *Journal of Advanced Ceramics*, *5*(2), 145–152.

Chiplunkar, P. P., & Pratap, A. P. (2016). Utilization of sunflower acid oil for synthesis of alkyd resin. *Progress in Organic Coatings*, *93*, 61–67.

Choe, E., & Min, D. B. (2006). Mechanisms and factors for edible oil oxidation. *Comprehensive Reviews in Food Science and Food Safety*, *5*(4), 169–186.

Dabai, M. U., Owuna, F. J., Sokoto, M. A., & Abubakar, A. L. (2018). Assessment of quality parameters of ecofriendly biolubricant from waste cooking palm oil. *Asian Journal of Applied Chemistry Research*, *1*(4), 1–11.

Derawi, D., & Salimon, J. (2010). Optimization on epoxidation of palm olein by using performic acid. *E-Journal of Chemistry*, *7*(4), 1440–1448.

Derawi, D., & Salimon, J. (2013). Palm olein based biolubricant basestocks: synthesis, characterisation, tribological and rheological analysis. *Malaysian Journal of Analytical Sciences*, *17*(1), 153–163.

Dian, N. L. H. M., Lin, S. W., Let, C. C., & Sundram, K. (2018). Characteristics of simple and chemically interesterified blends containing palm stearin, sunflower oil and palm kernel olein and potential application of the blends in fats spread. *Oil Palm Bulletin*, *43*, 38–49.

Di Pietro, M. E., Mannu, A. & Mele, A. (2020). NMR determination of free fatty acids in vegetable oils. *Processes, 8*(4), 410.

Dwivedi, A., & Sharma, G. (2014). A review on heliotropism plant: *Helianthus annuus L*. *The Journal of Phytopharmacology*, *3*(2), 149–155.

Erhan, S. Z., Sharma, B. K., & Perez, J. M. (2006). Oxidation and low temperature stability of vegetable oil-based lubricants. *Industrial Crops and Products*, *24*, 292–299.

Esipovich, A. L., Kanakov, E. A., Smirnov, M. A., Mityukova, Y. A., & Belousov, A. S. (2025). Processing *Chlorella vulgaris* into trimethylolpropane-based bio-lubricant. *Journal of Enviromental Chemical Engineering, 13* (6), 120202.

Fadzel, F. M., Salimon, J., & Derawi, D. (2021). Low-energy separation technique on purification of unsaturated fatty acids of palm stearin using methanol crystallization method. *Sains Malaysiana*, *50*(1), 151–160.

Fernández-Luqueño, F., López-Valdez, F., Miranda-Arámbula, M., Rosas-Morales, M., Pariona, N., & Espinoza-Zapata, R. (2014). An introduction to the sunflower crop. *Sunflowers: Growth and Development, Environmental Influences and Pests/Diseases*, *June*, 1–18.

Findley, T. W., Swern, D., & Scanlan, J. T. (1945). Epoxidation of unsaturated fatty materials with peracetic acid in glacial acetic acid solution. *Journal of the American Chemical Society*, *67*(3), 412–414.

Foreman, H. D., & Brown, J. B. (1944). Solubilities of the fatty acids in organic solvents at low temperatures. *Oil and Soap*, *21*, 183–187.

Fortunato, M. E., Vitiello, R., Taddeo, F., Faro, L., Mallardo, S., Turco, R., Tesser, R., Russo, V., & Di Serio, M. (2025). Engineering diesters from saturated fatty acids and C2–C4 diols: how branching influence rheological, flow, and crystallization properties. *European Journal of Lipid Science and Technology, 127*(7), e202400211.

Fox, N. J., & Stachowiak, G. W. (2007). Vegetable oil-based lubricants - A review of oxidation. *Tribology International*, *40*, 1035–1046.

Geiger, E. O. (2014). Statistical methods for fermentation optimization. In *Fermentation and Biochemical Engineering Handbook* (Third Ed.) (pp. 415-422). Elsevier Inc.

Goud, V. V., Patwardhan, A. V., & Pradhan, N. C. (2006). Studies on the epoxidation of mahua oil (*Madhumica indica*) by hydrogen peroxide. *Bioresource Technology*, *97*(12), 1365–1371.

Greenspan, F. P., & Gall, R. J. (1956). Epoxy fatty acid ester plasticizers. Preparation and properties. *Journal of the American Oil Chemists Society*, *33*(9), 391–394.

Hambali, M. H. A. M., & Raof, N. A. (2026). Optimization of green enzymatic synthesis of palm-based NPG diester biolubricant for electric vehicle applications. *Process Biochemistry 164*, 31-39.

Hamdan, S. H., Chong, W. W. F., Ng, J., Chong, C. T., & Zhang, H. (2018). Nano-tribological characterisation of palm oil-based trimethylolpropane ester for application as boundary lubricant. *Tribology International 127*, 1–9.

He, D., & Liu, L. (2019). Analytical Aspects of rice bran oil. In *Rice Bran and Rice Bran Oil* (pp. 169–181). Elsevier Inc.

Hincapie, B., Llano, S. M., Garces, H. F., Espinal, D., Suib, S. L., & Garces, L. J. (2018). Epoxidation of cyclopentene by a low cost and environmentally friendly bicarbonate/peroxide/manganese system. *Adsorption Science and Technology, 36* (1-2), 9-12.

Hong, L. K., Yusop, R. M., Salih, N., & Salimon, J. (2015). Optimization of the in situ epoxidation of linoleic acid of Jatropha curcas oil with performic acid. *Malaysian Journal of Analytical Sciences*, *19*(1), 144–154.

Igwe, I. O. (2004). The effects of temperature on the viscosity of vegetable oils in solution. *Industrial Crops and Products*, *19*, 185–190.

Ijeoma, M. W., Hunt, Z., Chen, H., & CarbajalesDale M. (2026). From fossil to biobased: a life cycle assessment of commercial-scale polyol ester lubricant base oils. *RSC Sustainability 4*(5), 2337–2354.

Ivanova, M., Hanganu, A., Dumitriu, R., Tociu, M., Ivanov, G., Stavarache, C., Popescu, L., Ghendov-Mosanu, A., Sturza, R., Deleanu, C., & Chira, N. A. (2022). Saponification value of fats and oils as determined from ^{1}H-NMR data: The case of dairy fats. *Foods*, *11*(10), 1–13.

Jain, A., & Suhane, A. (2012). Research Approach and Prospects of Non edible vegetable oil as a potential resource for biolubricant-A review. *Advanced Engineering and Applied Sciences:An International Journal*, *1*(1), 23–32.

Jamaluddin, F. I., Khairuddin, M. M., Abdullah, A., & Nor. N. M. (2024). Synthesis of TMP ester via esterification of corn oil fatty acids and trimethylolpropane as a potential biolubricant base stock. *Malaysia Journal of Chemistry, 26*(3), 312-319.

Japir, A. A. W., Salimon, J., Derawi, D., Bahadi, M., Al-Shuja'A, S., & Yusop, M. R. (2017). Physicochemical characteristics of high free fatty acid crude palm oil. *OCL - Oilseeds and Fats, Crops and Lipids*, *24*(5).

Japir, A. A. W., Salimon, J., Derawi, D., Yahaya, B. H., Bahadi, M., Al-Shuja'A, S., & Yusop, M. R. (2018). A highly efficient separation and physicochemical characteristics of saturated fatty acids from crude palm oil fatty acids mixture

using methanol crystallisation method. *Oilseeds and Fats, Crops and Lipids*, *25*(2), A203.

Jumaah, M. A., Yusoff, M. F. M., Salimon, J., & Bahadi, M. (2019). Separation of saturated and unsaturated fatty acids of palm fatty acid distilled via low-temperature methanol crystallization. *Malaysian Journal of Chemistry*, *21*(2), 8–16.

Jumaah, M. A., Salih, N., & Salimon, J. (2021). Optimization for esterification of saturated palm fatty acid distillate by D-optimal design response surface methodology for biolubricant production. *Turkish Journal of Chemistry*, *45*(5), 1391–1407.

Jumaah, M. A., Salih, N., & Salimon, J. (2022). D-optimal design optimization of unsaturated palm fatty acid distillate and trimethylolpropane esterification for biolubricant production. *Comptes Rendus Chimie, 25*(S2), 93-112.

Jumaah, M. A., Khaleel, F. L., Salih, N., & Salimon, J. (2024). Synthesis of tri, tetra, and hexa-palmitate polyol esters from Malaysian saturated palm fatty acid distillate for biolubricant production. *Biomass Conversion and Biorefinery, 14*, 1919–1937.

Jurid, L. S., Zubairi, S. I., Kasim, Z. M., & Kadir, I. A. A. (2020). The effect of repetitive frying on physicochemical properties of refined, bleached and deodorized Malaysian tenera palm olein during deep-fat frying. *Arabian Journal of Chemistry*, *13*(7), 6149–6160.

Kamyab, B., Wang, H., Razipour, T. Chambers, D. W., Bassi, A. S., & Xu, C. (2024). Production of high-end bio-lubricant products via epoxidation of canola oil trimethylolpropane (COTMP) esters. *Industrial Crops & Products, 222* (2024), 119791.

Kania, D., Yunus, R., Omar, R., Abdul Rashid, S., & Mohamad Jan, B. (2015). A review of biolubricants in drilling fluids: Recent research, performance, and applications. *Journal of Petroleum Science and Engineering*, *135*, 177–184.

Karmakar G., Ghosh P., & Sharma B. (2017). Chemically modified vegetanle oils to prepare green lubricants. *Lubricant, 5*(4), 1-17.

Klein, D. (2021). *Organic Chemistry* (Fourth Ed.). Wiley.

Lai, W. T., Khong, N. M. H., Lim, S. S., Hee, Y. Y., Sim, B. I., Lau, K. Y., & Lai, O. M. (2017). A review: Modified agricultural by-products for the development

and fortification of food products and nutraceuticals. *Trends in Food Science and Technology*, *59*, 148–160.

Latourette, H. K., Castrantas, H. M., Gall, R. J., & Dierdorff, L. H. (1960). A novel continuous countercurrent epoxidation process. *Journal of the American Oil Chemists Society*, *37*(11), 559–563.

Lee, K., Hailan, C., Yinhua, J., Kim, Y., & Chung, K. (2008). Modification of soybean oil for intermediates by epoxidation, alcoholysis and amidation. *Korean J. Chem Eng*, *25*(3), 474–482.

Madadi, S., Charbonneau, L., Bergeron, J., & Kaliaguine, S. (2020). Aerobic epoxidation of limonene using cobalt substituted mesoporous SBA- 16 Part 1: Optimization via Response Surface Methodology (RSM). *Applied Catalysis B: Environmental*, *260*, 118049.

Mäkelä, M. (2018). Experimental design and response surface methodology in energy applications : A tutorial review. *Energy Conversion and Management*, *151*, 630–640.

Moser, B. R., & Erhan, S. Z. (2007). Preparation and evaluation of a series of Æ - hydroxy ethers from 9 , 10-epoxystearates. *European Journal of Lipid Science and Technology*, *109*(3), 206–213.

Nakayama, Y. (2018). *Introduction to Fluid Mechanics* (A. Valutkevich (ed.); second ed.). Mathew Deans.

Nor, N. M., Derawi, D., & Salimon, J. (2017). Chemical modification of epoxidized palm oil for biolubricant application. *Malaysian Journal of Analytical Sciences, 21*(6), 1423–1431

Nor, N. M. (2019). *Kajian Pengubahsuaian Minyak Sawit Mentah Untuk Penghasilan Stok Asas Biopelincir* (Doctoral dissertation). Universiti Kebangsaan Malaysia.

Nor, N. M., Derawi, D., & Salimon, J. (2018a). Synthesis of palm oil fatty acid and trimethylolpropane based ester for biolubricant base stocks. *AIP Conference Proceedings*, *1940*, 1–7.

Nor, N. M., Derawi, D., & Salimon, J. (2018b). The optimization of RBD palm oil epoxidation process using D-optimal design. *Sains Malaysiana*, *47*(7), 1359–1367.

Nor, N. M., Derawi, D., & Salimon, J. (2019). Esterification and evaluation of palm oil as biolubricant base stock. *Malaysian Journal of Chemistry*, *21*(2), 28–35.

Nor, N. M., & Salimon, J. (2019a). Preparation of Epoxidized Palm Oil by using Performic Acid. *Malaysian Journal of Chemistry, 21*(3), 11-19.

Nor, N. M., Salih, N., & Salimon, J. (2021a). Chemically modified Jatropha curcas oil for biolubricant applications. *Hemijska Industrija*, *75*(2), 117–128.

Nor, N. M., Salih, N., & Salimon, J. (2021b). Optimization of the ring opening of epoxidized palm oil using D-optimal design. *Asian Journal of Chemistry,* 33(1), 67-75.

Nor, N. M., Salih, N., & Salimon, J. (2022a). Optimization and lubrication properties of Malaysian crude palm oil fatty acids based neopentyl glycol diester green biolubricant. *Renewable Energy*, *200*, 942–956.

Nor, N. M., Salih, N., & Salimon J. (2022b). Syntehsis of green-renewable biolubricant base stock from Malaysian palm oil. *Malaysian Journal of Analytical Sciences, 26*(3), 492-506.

Nor, N. M. & Salimon, J. (2023). Syntehsis and characterization of palm oil pentaerythritol ester-based biolubricant from Malaysia palm oil. *Malaysian Journal of Analytical Sciences, 27*(4), 716-727.

Odoom, W., & Edusei, V. O. (2015). Evaluation of saponification value, iodine value and insoluble impurities in coconut oils from Jomoro district in the western region of Ghana. *Asian Journal of Agriculture and Food Sciences*, *03*(5), 2321–1571.

Ohifuemen, A., Fagbemi, E. A., & Fasina, K. A. (2020). Bio-lubricants: A renewable alternative to mineral oils. *International Journal of Agriculture, Environment and Bioresearch*, *05*(2), 22–32.

Owuna, F. J. (2020). Stability of vegetable based oils used in the formulation of ecofriendly lubricants – a review. *Egyptian Journal of Petroleum*, *29*(3), 251–256.

Owuna, F. J., Dabai, M. U., Sokoto, M. A., Dangoggo, S. M., Bagudo, B. U., Birnin-Yauri, U. A., Hassan, L. G., Sada, I., Abubakar, A. L., & Jibrin, M. S. (2020). Chemical modification of vegetable oils for the production of biolubricants using trimethylolpropane: A review. *Egyptian Journal of Petroleum*, *29*(1), 75–82.

Oyedepo, S. O. (2012). Energy and sustainable development in Nigeria: the way forward *Energy, Sustainability and Society*, *2*(15), 1–17.

Padmaja, K. V., Rao, B. V. S. K., Reddy, R. K., Bhaskar, P. S., & Rao, T. M. (2012). 10- Undecenoic acid-based polyol esters as potential lubricant base stocks. *Industrial Crops and Products, 35*(1), 237-240.

Palagi, S., Walker, D., Qiu, T., & Fischer, P. (2017). Chapter 8 - Micro- and nanorobots in Newtonian and biological viscoelastic fluids. In *Microbiorobotics* (2nd ed.) (pp. 133-162). Elsevier Inc.

Panchal, T. M., Patel, A., Chauhan, D. D., Thomas, M., & Patel, J. V. (2017). A methodological review on bio-lubricants from vegetable oil based resources. *Renewable and Sustainable Energy Reviews*, *70*, 65–70.

Pattanaik, A., & Rayasam, V. (2018). Analysis of reverse cationic iron ore fines flotation using RSM-D-optimal design – An approach towards sustainability. *Advanced Powder Technology*, *29*(12), 3404–3414

Pavia, D. L., Lampman, G. M., Kriz, G. S., & Vyvyan, J. R. (2015). *Introduction To Spectroscopy* (fifth ed.). Cengage Learning.

Pawar, R. V., Hulwan, D. B., & Mandale, M. B. (2022). Recent advancements in synthesis, rheological characterization, and tribological performance of vegetable oil-based lubricants enhanced with nanoparticles for sustainable lubrication. *Journal of Cleaner Production*, *378*, 134454.

Pilorgé, E. (2020). Sunflower in the global vegetable oil system: situation, specificities and perspectives. *Oilseeds and Fats Crops and Lipids*, *27*, 1–11.

Prathiba, S., Vaishnavi, A., Saranya, R., Chandrasatheesh, C., & Jayapriya, J. (2022). Synthesis of hydroxyl ether based biolubricant from poultry waste and to evaluate the friction performance with titania nanoparticles. *Chemical Engineering Research and Design*, *185*, 291–300.

Pulassery, S., Abraham, B., Ajikumar, N., Munnilath, A., & Yoosaf, K. (2022). Rapid iodine value estimation using a handheld Raman Spectrometer for on-site, reagent-free authentication of edible oils. *ACS Omega*, *7*(11), 9164–9171.

Quinchia, L. A., Delgado, M. A., Reddyhoff, T., Gallegos, C., & Spikes, H. A. (2014). Tribological studies of potential vegetable oil-based lubricants containing environmentally friendly viscosity modifiers. *Tribology International*, *69*, 110–117.

Rahman, S. M. A., Sharma, P., & Said, Z. (2022). Application of response surface methodology based d-optimal design for modeling and optimisation of osmotic dehydration of zucchini. *Digital Chemical Engineering*, *4*, 100039.

Raof, N. A., Hamid, H. A., Aziz, N. A. M., & Yunus, R. (2022). Prospects of plant-based trimethylolpropane esters in the biolubricant formulation for various applications: A review. *Frontiers in Mechanical Engineering, 8*(2022), 833438.

Ribeiro, D. C. M., Ramalho, A., Serra, A. C., & Coelho, J. (2025). Biolubricants based on epoxidized vegetable oils: A review on chemical modifications, tribological properties, and sustainability. *Lubricants, 13*(12), 510.

Rudnick, L. R. (2020). *Synthetics, mineral oils, and bio-based lubricants*. In L. R. Rudnick (Ed.), *Chemistry and technology of lubricants* (3rd ed., pp. 21–33). CRC Press, Taylor & Francis Group.

Ruggieroa, A., D'Amatob, R., Merolaa, M., Valašekc, P., & Miroslav Müller. (2017). Tribological characterization of vegetal lubricants : Comparative experimental investigation on *Jatropha curcas L*. oil, Rapeseed Methyl Ester oil, Hydrotreated Rapeseed oil. *Tribology International*, *109*, 529–540.

Salih, N., & Salimon, J. (2021). A review on eco-friendly green biolubricants from renewable and sustainable plant oil sources. *Biointerface Research in Applied Chemistry*, *11*(5), 13303–13327.

Salih, N., Salimon, J., & Yousif, E. (2013). The effect of chemical structure on pour point, oxidative stability and tribological properties of oleic acid triester derivatives. *Malaysian Journal of Analytical Sciences*, *17*(1), 119–128.

Salimon, J., Said, M., Ramli, S,. & Lazim, M. A. S. M. (2006). *Oils and Fats Analysis*. Universiti Kebangsaan Malaysia.

Salimon, J., & Nadia, S. (2010). Modification of epoxidized ricinoleic acid for biolubricant base oil with improved flash and pour points. *Asian Journal of Chemistry, 22*(7), 5468–5476.

Salimon, J., Abdullah, B. M., & Salih, N. (2011). Hydrolysis optimization and characterization study of preparing fatty acids from Jatropha curcas seed oil. *Chemistry Central Journal*, *5*(67), 1–9.

Salimon, J. & Salih, N. (2011). Epoxidized Malaysian *Elaeis guineensis* palm kernel oil trimethylolpropane polyol ester as green renewable biolubricants. *Biomass and Bioenergy,* 175(2023), 106883.

Salimon, J., Abdullah, B. M., Yusop, R. M., & Salih, N. (2014). Synthesis, reactivity and application studies for different biolubricants. *Chemistry Central Journal*, *8*(1), 1–11.

Salimon, J., Salih, N., & Yousif, E. (2010). Biolubricants: Raw materials, chemical modifications and environmental benefits. *European Journal of Lipid Science and Technology*, *112*(5), 519–530.

Salimon, J., Salih, N., & Yousif, E. (2011). Chemically modified biolubricant basestocks from epoxidized oleic acid: Improved low temperature properties and oxidative stability. *Journal of Saudi Chemical Society*, *15*(3), 195–201.

Salimon, J., Abdullah, B. M. & Salih, N. (2012). Selectively increasing of polyunsaturated (18:2) and monounsaturated (18:1) fatty acids in Jatropha curcas seed oil by crystallization using D-optimal design. Chemistry Central Journal, 6(1), 65.

Salimon, J., Salih, N., & Yousif, E. (2012b). Triester derivatives of oleic acid: The effect of chemical structure on low temperature, thermo-oxidation and tribological properties. *Industrial Crops and Products*, *38*(1), 107–114.

Salimon, J., & Salih, N. (2023). Epoxidation Malaysian *Elaeis guineensis* palm kernel oil trimethylolpropane polyol ester as green renewable biolubricants. *Biomass and Bioenergy, 175*(2023), 106883.

Sarma, R. N., & Vinu, R. (2022). Current Status and Future Prospects of Biolubricants : Properties and Applications. *Lubricants*, *10*(4), 1–21.

Saurabh, T., Patnaik, M., Bhagt, S. L., & Renge, V. C. (2011). Epoxidation of vegetable oils: a review. *Int. J. Adv. Eng. Technol*, *2*(4), 491–501.

Sazzad, M. R. I., Rahman, M. M., Hassan, T., Al Rifat, A., Al Mamun, A., Adib, A. R., Meraz, R. M., & Ahmed, M. (2024). Advancing sustainable lubricating oil management: Re-refining techniques, market insights, innovative enhancements, and conversion to fuel. *Heliyon*, *10*(20), e39248.

Senaras, A. E. (2019). Parameter optimization using the surface response technique in automated guided vehicles. *Sustainable Engineering Products and Manufacturing Technologies*, 187–197.

Seneviratne, K., & Jayathilaka, N. (2016). Coconut Oil: Chemistry and Nutrition. In *Lakva Publisher* (Issue August).

Singh, C. P., & Chhibber, V. K. (2013). Research Article Chemical Modification In Karanja Oil For Biolubricant Industrial. *Journal of Drug Delivery and Therapeutics*, *3*(3), 117–122.

Singh, Y., Farooq, A., Raza, A., Mahmood, M. A., & Jain, S. (2017). Sustainability of a non-edible vegetable oil based bio-lubricant for automotive applications: A review. *Process Safety and Environmental Protection*, *111*, 701–713.

Soodoo, N., Bouzidi, L., & Narine, S. S. (2023). Fundamental structure–function relationships in vegetable oil-based lubricants: A critical review. *Lubricants, 11*(7), 284.

Srivastava, A., & Sahai, P. (2013). Vegetable oils as lube basestocks: A review. *African Journal of Biotechnology*, *12*(9), 880–891.

Srivyas, P. D., & Charoo, M. S. (2018). A review on tribological characterization of lubricants with nano additives for automotive applications. *Tribology in Industry*, *40*(4), 594–623.

Stachowiak, G. W., & Batchelor, A. W. (2014). Physical Properties of Lubricants. In *Engineering Tribology* (pp. 12–49).

Suemanotham A., Lao-ubol, S., Sisuthog, W., Khamdaeng, P., Thanmongkhon, Y., & Attanatho, L. (2026). Valorization of palm fatty acid distillate into polyol-based biolubricants via solid acid catalysis. *Biomass and Bioenergy, 211* (2016), 109188.

Sun, X., Zhao, X., Du, W., & Liu, D. (2011). Kinetics of formic acid-autocatalyzed preparation of performic acid in aqueous phase. *Chinese Journal of Chemical Engineering*, *19*(6), 964–971.

Syed, A. (2016). Oxidative stability and shelf life of vegetable oils. In *Oxidative Stability and Shelf Life of Foods Containing Oils and Fats* (pp. 187–207). Elsevier Inc.

Thanh, L. T., Okitsu, K., Boi, L. Van, & Maeda, Y. (2012). Catalytic technologies for biodiesel fuel production and utilization of glycerol: A review. *Catalysts*, *2*(1), 191–222.

Trzepieciński, T. (2020). Tribological performance of environmentally friendly bio-degradable lubricants based on a combination of boric acid and bio-based oils. *Materials*, *13*(17), 1–19.

Vilvert, E., Lana, M., Zander, P., & Sieber, S. (2018). Multi-model approach for assessing the sunflower food value chain in Tanzania. *Agricultural Systems*, *159*, 103–110.

Wagner, H., Luther, R., & Mang, T. (2001). Lubricant base fluids based on renewable raw materials: Their catalytic manufacture and modification. *Applied Catalysis A: General*, *221*(1–2), 429–442.

Wahyudi, Wardana, I. N. ., Widodo, A., & Wijayanti, W. (2018). Improving vegetable oil properties by transforming fatty acid chain length in jatropha oil and coconut oil blends. *Energies*, *11*(2), 394.

Wai, P. T., & Jiang, P. (2019). Catalytic developments in the epoxidation of vegetable oils and the analysis methods of epoxidized products. *RSC Advances*, *9*(65), 38119–38136.

Wanasundara, P. K. J. P. D., Wanasundara, U. N., & Shahidi, F. (1999). Changes in flax (*Linum usitatissimum L.*) seed lipids during germination. *Journal of the American Oil Chemists' Society*, *76*(1), 41–48.

Widyatmoko, I. (2016). Sustainability of bituminous materials. In *Sustainability of Construction Materials* (Second Ed.). Elsevier Ltd.

Yara-Varón, E., Li, Y., Balcells, M., Canela-Garayoa, R., Fabiano-Tixier, A. S., & Chemat, F. (2017). Vegetable oils as alternative solvents for green oleo-extraction, purification and formulation of food and natural products. *Molecules*, *22*(9), 1–24.

Zahid, R., Hj. Hassan, M., Alabdulkarem, A., Varman, M., Kalam, M. A., Mufti, R. A., Mohd Zulkifli, N. W., Gulzar, M., Bhutta, M. U., Ali, M. A., Abdullah, U., & Yunus, R. H. (2018). Tribological characteristics comparison of formulated palm trimethylolpropane ester and polyalphaolefin for cam/tappet interface of direct acting valve train system. *Industrial Lubrication and Tribology*, *70*(5), 888–901.

Zainal, N. A., Zulki, N. W. M., Gulzar, M., & Masjuki, H. H. (2018). A review on the chemistry , production , and technological potential of bio- based lubricants. *Renewable and Sustainable Energy Reviews*, *82*(September 2017), 80–102.

Zhang, X., Li, C., Zhou, Z., Liu, B., Zhang, Y., Yang, M., Gao, T., Liu, M., Zhang, N., Said, Z., Sharma, S., & Ali, H. M. (2023). Vegetable oil-based nanolubricants in machining: from physicochemical properties to application. *Chinese Journal of Mechanical Engineering, 36*(76), 2023.

APPENDICES

APPENDIX 1

Preparation of Chemical Solution

5% sodium hydrogen carbonate ($NaHCO_3$) solution

The solution was prepared by dissolving 25 g of sodium hydrogen carbonate powder in 50 mL of distilled water.

5% sodium chloride (NaCl) solution

The solution was prepared by dissolving 50 g of potassium iodide in distilled water and making up the volume to 500 mL in a volumetric flask.

10% potassium iodide (KI) solution

The solution was prepared by dissolving 50 g of potassium iodide in distilled water and making up the volume to 500 mL in a volumetric flask.

0.1 N sodium thiosulfate ($Na_2S_2O_3$) solution

The solution was prepared by dissolving 24.8 g of sodium thiosulfate in distilled water and diluting to a final volume of 1000 mL in a volumetric flask.

0.1 N sodium hydroxide (NaOH) solution

The solution was prepared by calculating the required mass using the equation:

Required mass = normality × molecular weight × desired volume.

= 0.1N x 40 g/mol x 1L

= 4 g

Accordingly, 4 g of sodium hydroxide pellets were dissolved in distilled water and diluted to a final volume of 1 L.

0.5 N potassium hydroxide (KOH) solution

The solution was prepared by dissolving 14.025 g of potassium hydroxide powder in 500 mL of distilled water.

0.1 N hydrobromic acid (HBr) solution

The solution was prepared by diluting 7.1218 mL of hydrobromic acid with glacial acetic acid and making up the volume to 500 mL in a volumetric flask. The prepared solution was stored in a dark environment and protected from light by wrapping the flask with aluminium foil.

1 M sodium methoxide ($NaOCH_3$) solution

The solution was prepared by dissolving 1.15 g of sodium methoxide in 50 mL of methanol to obtain 50 mL of a 1 M solution.

1% phenolphthalein indicator solution

The solution was prepared by dissolving 1 g of phenolphthalein powder in 100 mL of 95% ethanol.

1% crystal violet solution

The solution was prepared by dissolving 1 g of crystal violet powder in 100 mL of glacial acetic acid. The solution was stored in a dark glass bottle.

1% starch solution

The solution was prepared by dissolving 0.1 g of starch in 10 mL of boiling water, heating for 3 minutes and allowing the solution to cool to room temperature.

APPENDIX 2

Standardization of Chemical Solution

0.1 N sodium hydroxide (NaOH) Solution

Potassium hydrogen phthalate (KHP) was dried in an oven at 120 °C for 2 hours and stored in a desiccator prior to use. For the standardization procedure, approximately 0.4 g of KHP was weighed directly into a conical flask. Then, 50 mL of distilled water and a few drops of phenolphthalein indicator were added. The mixture was gently heated on a hot plate while being continuously swirled until complete dissolution occurred. The solution was titrated with the prepared NaOH solution until a stable pale pink color persisted, indicating the endpoint. The volume of NaOH used was recorded and the normality of the NaOH solution was calculated using the following equation:

$$\text{Normality of NaOH} = \frac{W \times 1000}{T \times 204.2}$$

Where,

W = mass of KHP used (g)

T = volume (mL) of NaOH solution used

0.1 N sodium Thiosulfate ($Na_2S_2O_3$) Solution

The 0.1 N sodium thiosulfate solution was standardized according to the AOCS Cd 1d-92 method. Approximately 0.16 to 0.22 g of dried potassium dichromate ($K_2Cr_2O_7$) was dissolved in distilled water and diluted to a final volume of 25 mL in a volumetric flask. Subsequently, 5 mL of concentrated hydrochloric acid (HCl) and 20 mL of 10% potassium iodide (KI) solution were added and the mixture was shaken until homogeneous. The solution was allowed to stand for 5 minutes, after which 100 mL of distilled water was added. The resulting solution was titrated with the prepared sodium thiosulfate solution while continuously swirling until the yellow color began to fade. Then, 1–2 mL of starch solution was added as an indicator and the titration was continued until the blue color disappeared completely, yielding a light green endpoint. The actual normality of the sodium thiosulfate solution was calculated using the following equation:

$$\text{Normality of } Na_2S_2O_3 = \frac{20.394 \times W}{V}$$

Where,

W = mass of $K_2Cr_2O_7$ used (g)

T = volume (mL) of sodium thiosulfate solution used

Hydrogen Bromide (HBr) Solution

Approximately 0.4 g of potassium hydrogen phthalate was weighed into a 50 mL conical flask, followed by the addition of 10 mL of glacial acetic acid. Gentle heating was applied to facilitate dissolution of the potassium hydrogen phthalate. A few drops of crystal violet solution were added as an indicator. The solution was then titrated with the hydrogen bromide solution until the color changed from deep blue to bluish-green and remained stable for at least 30 seconds, indicating the endpoint. The normality of the hydrogen bromide solution was calculated using the following equation:

$$\text{Normality of HBr} = \frac{\text{Mass of potassium hydrogen phthalate}}{0.2042 \times \text{Volume of HBr titrant}}$$

APPENDIX 3

Calculation of Esterification of SFOUFA with Neopentyl Glycol

Calculation of mole number and mass of NPG and SFOUFA for the esterification process:

	NPG	SFOUFA
Ratio	1.0	3.2
Mole	0.0192	0.061
Mass (g)	2.00	17.27

Where:

$$\text{Mole of NPG} = \frac{\text{Mass of NPG (g)}}{\text{RMM of NPG (g/mol)}} = \frac{2.0\ \text{g}}{104.14\ \text{g/mol}}$$

$$= 0.0192 \text{ mole}$$

$$\text{Mole of SFOUFA} = \text{Mole of NPG x ratio SFOUFA}$$

$$= 0.0192 \times 3.2$$

$$= 0.061 \text{ mole}$$

Relative molecular mass of SFOUFA:

Fatty Acids	Molar Mass (g/mole)	Percentage (%)	Relative Molecular Mass (RMM)
Palmitic acid	256.43	1.11	284.64
Oleic acid	282.46	38.35	10832.34
Linoleic acid	280.45	59.91	16801.76
Linolenic acid	278.43	0.34	94.67
Paullinic acid	310.52	0.29	90.05
Total			28103.46/100
RMM of SFOUFA			281.03

$$\text{Mass of SFOUFA} = \text{Mole of SFOUFA x RMM of SFOUFA}$$

$$= 0.061 \times 281.03$$

$$= 17.27 \text{ g}$$

APPENDIX 4

Calculation for Esterification of SFOUFA with Trimethylolpropane

Calculation of mole number and mass of TMP and SFOUFA for the esterification process:

	TMP	SFOUFA
Ratio	1.0	4.0
Mole	0.0149	0.0596
Mass (g)	2.00	16.75

Where:

$$\text{Mole of NPG} = \frac{\text{Mass of TMP (g)}}{\text{RMM of TMP (g/mol)}} = \frac{2.0\ \text{g}}{134.17\ \text{g/mol}}$$

$$= 0.0149 \text{ mole}$$

Mole of SFOUFA = Mole of NPG x ratio SFOUFA

= 0.0149 x 4.0

= 0.0596 mole

Relative molecular mass of SFOUFA:

Fatty Acids	Molar Mass (g/mole)	Percentage (%)	Relative Molecular Mass (RMM)
Palmitic acid	256.43	1.11	284.64
Oleic acid	282.46	38.35	10832.34
Linoleic acid	280.45	59.91	16801.76
Linolenic acid	278.43	0.34	94.67
Paullinic acid	310.52	0.29	90.05
Total			28103.46/100
RMM of SFOUFA			281.03

Mass of SFOUFA = Mole of SFOUFA x RMM of SFOUFA

= 0.0596 x 281.03

= 16.75 g

APPENDIX 5

Calculation for Esterification of SFOUFA with Pentaerythritol

Calculation of mole number and mass of PE and SFOUFA for the esterification process:

	PE	SFOUFA
Ratio	1.0	5.0
Mole	0.0147	0.0734
Mass (g)	2.00	20.64

Where:

$$\text{Mole of NPG} = \frac{\text{Mass of PE (g)}}{\text{RMM of PE (g/mol)}} = \frac{2.0\ \text{g}}{136.15\ \text{g/mol}}$$

$$= 0.0147 \text{ mole}$$

Mole of SFOUFA = Mole of NPG x ratio SFOUFA

= 0.0147 x 5.0

= 0.0734 mole

Relative molecular mass of SFOUFA:

Fatty Acids	Molar Mass (g/mole)	Percentage (%)	Relative Molecular Mass (RMM)
Palmitic acid	256.43	1.11	284.64
Oleic acid	282.46	38.35	10832.34
Linoleic acid	280.45	59.91	16801.76
Linolenic acid	278.43	0.34	94.67
Paullinic acid	310.52	0.29	90.05
Total			28103.46/100
RMM of SFOUFA			281.03

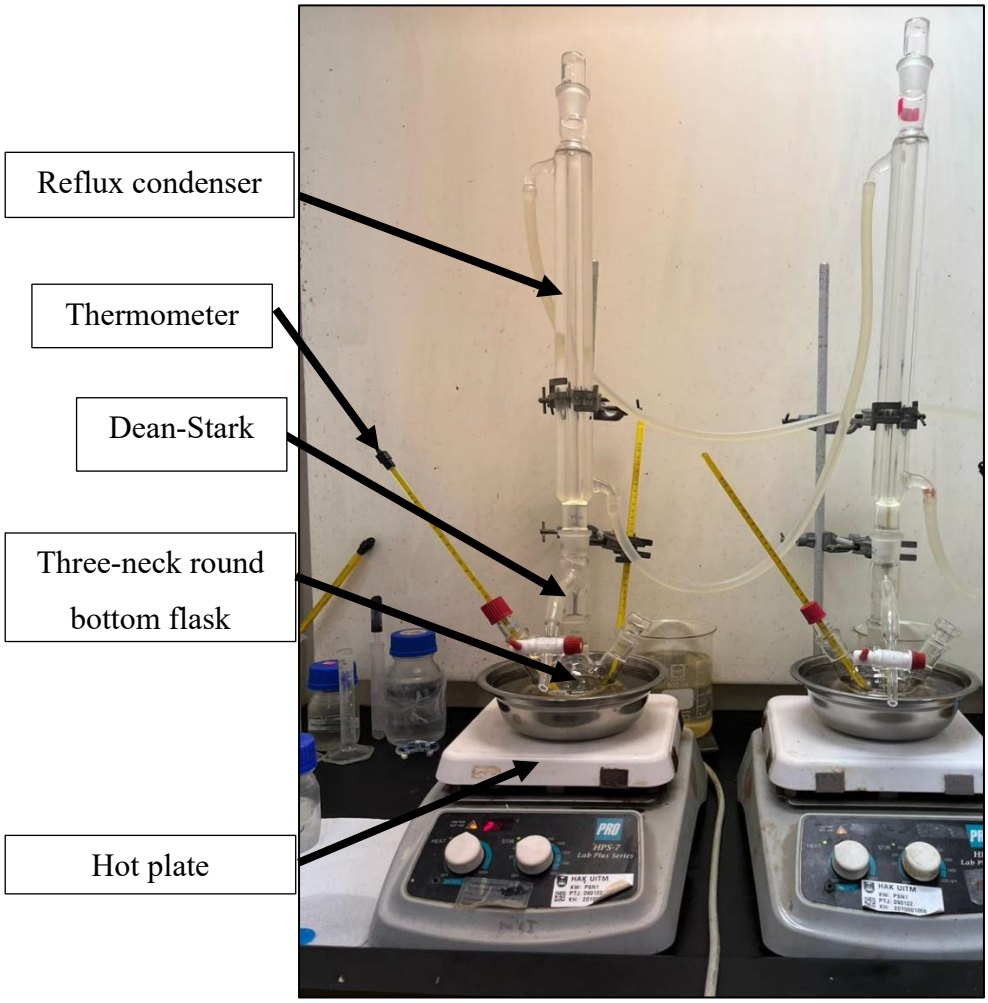
Mass of SFOUFA = Mole of SFOUFA x RMM of SFOUFA

= 0.0734 x 281.03

= 20.64 g

APPENDIX 6

Apparatus Setup for Esterification



APPENDIX 7

Calculation of Epoxidation of SFOUFATMPE

Calculation of mole number and mass of SFOUFATMPE, HCOOH and H_2O_2 for the epoxidation process:

	ESFOUFATMPE	HCOOH (98%)	H_2O_2 (30%)
Ratio	1	7	2
Mole	0.2277	3.3873	0.9484
Mass (g)	100.00	155.89	107.52

Where:

$$\text{Mole of SFOUFATMPE} = \frac{\text{IV}_{\text{SFOUFATMPE}}}{\text{RMM of } I_2 \text{ (g/mol)}} = \frac{122.73 \text{ g}}{258.8 \text{ g/mol}} = 0.4742 \text{ mole}$$

For 100 g of SFOUFATMPE = 0.4742 mole

Mole of formic acid (HCOOH) = 0.4742 mole x 7 = 3.3196 mole

Concentration HCOOH used was 98%, so $= \frac{3.3196 \text{ x } 100}{98} = 3.3873$ mole

Mass of HCOOH used = Mole of HCOOH x RMM of HCOOH

= 3.3873 x 46.02 g/mole

= 155.89 g

Mole of hydrogen peroxide (H_2O_2) = 0.4742 mole x 2 = 0.9484 mole

Concentration H_2O_2 used was 30%, so $= \frac{0.9484 \text{ x } 100}{30} = 3.1613$ mole

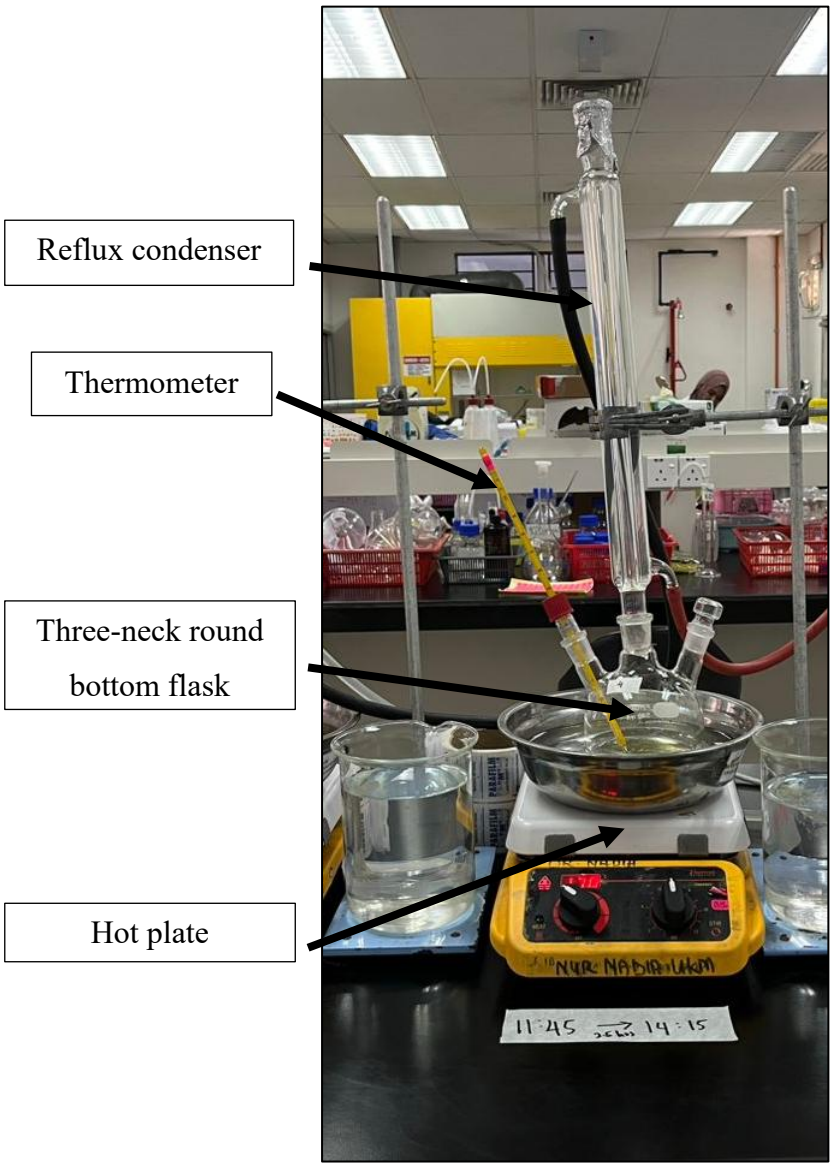
Mass of HCOOH used = Mole of H_2O_2 x RMM of H_2O_2

= 3.1613 x 34.01 g/mole

= 107.52 g

APPENDIX 8

Apparatus Setup for Epoxidation



APPENDIX 9

Calculation of Ring Opening of ESFOUFATMPE

Calculation of mole number and mass of ESFOUFATMPE and oleic acid for the ring opening process:

	ESFOUFATMPE	Oleic acid
Ratio	1.0	4.6
Mole	0.4346	2.221
Mass (g)	100.00	627.38

Where:

$$\text{Mole of ESFOUFATMPE} = \frac{\text{OOC value}}{\text{RMM of O (g/mol)}} = \frac{6.953\ \text{g}}{16\ \text{g/mol}} = 0.4346\ \text{mole}$$

$$\text{For 100 g of ESFOUFATMPE} = 0.4346\ \text{mole}$$

$$\text{Mole of oleic acid} = 0.4742\ \text{mole} \times 4.6 = 1.999\ \text{mole}$$

$$\text{Concentration oleic acid used was 90\%, so} = \frac{1.999 \times 100}{90} = 2.221\ \text{mole}$$

$$\text{Mass of HCOOH used} = \text{Mole of HCOOH} \times \text{RMM of HCOOH}$$

$$= 2.221 \times 282.46\ \text{g/mole}$$

$$= 627.38\ \text{g}$$

APPENDIX 10

Formula for Calculating Percentage Yield of Each Products

Hydrolysis of SFO

$$\text{Percentage yield of SFOFA} = \frac{\text{SFOFA}}{\text{SFO}} \times 100$$

Separation of SFOFA to SFOUFA and SFOSFA

$$\text{Percentage yield of SFOUFA} = \frac{\text{SFOUFA}}{\text{SFOFA}} \times 100$$

$$\text{Percentage yield of SFOSFA} = \frac{\text{SFOSFA}}{\text{SFOFA}} \times 100$$

Esterification of SFOUFA with polyhydric alcohol

$$\text{Percentage yield of SFOUFANPGE} = \frac{\text{SFOUFANPGE}}{\text{SFOUFA} + \text{NPG}} \times 100$$

$$\text{Percentage yield of SFOUFATMPE} = \frac{\text{SFOUFATMPE}}{\text{SFOUFA} + \text{TMP}} \times 100$$

$$\text{Percentage yield of SFOUFAPEE} = \frac{\text{SFOUFAPEE}}{\text{SFOUFA} + \text{PE}} \times 100$$

Epoxidation of SFOUFATMPE

$$\text{Percentage yield of SFOUFATMPE} = \frac{\text{ESFOUFATMPE}}{\text{SFOUFATMPE}} \times 100$$

Ring Opening of ESFOUFATMPE

$$\text{Percentage yield of DOSFOUFATMPE} = \frac{\text{DOSFOSUFATMPE}}{\text{ESFOUFATMPE} + \text{Oleic acid}} \times 100$$

APPENDIX 11

Experimental Run and Factors from RSM for Hydrolysis of SFO

Run	Factors		
	Molarity ethanolic KOH (M)	Reaction temp. (°C)	Reaction time (h)
1	1.7	50	1.60
2	1.0	57	2.50
3	2.4	60	0.59
4	1.7	61	1.91
5	1.7	61	0.53
6	2.5	70	0.50
7	1.0	50	0.50
8	1.7	61	0.53
9	2.5	50	2.50
10	1.7	50	1.60
11	1.0	57	1.39
12	2.0	70	2.50
13	2.5	61	1.60
14	1.0	70	2.50
15	2.0	70	2.50
16	1.0	70	1.25
17	2.5	61	1.60
18	1.8	70	1.20
19	1.7	61	1.91
20	2.5	50	0.50

APPENDIX 12

Experimental Run and Factors from RSM for Esterification of SFOUFA with NPG

Run	Factors			
	Molar ratio SFOUFA	Percentage catalyst (%)	Reaction time (h)	Reaction temp. (°C)
1	2.5	2.9	4	130
2	2.4	0.5	2	148
3	2.6	2.3	2	144
4	2.2	0.5	2	130
5	2.5	3.0	5	145
6	3.5	0.5	5	148
7	3.5	2.9	5	130
8	2.0	1.7	4	138
9	2.9	1.5	4	150
10	2.0	3.0	6	130
11	2.9	1.7	6	138
12	2.5	3.0	5	145
13	2.9	1.5	4	150
14	2.0	0.5	6	150
15	2.4	0.5	5	130
16	3.5	3.0	2	130
17	2.5	3.0	5	145
18	2.0	1.7	4	138
19	3.5	1.1	2	131
20	3.5	1.8	5	140
21	2.0	2.2	6	150
22	2.0	3.0	4	150
23	3.5	2.9	2	148
24	2.9	1.7	6	138
25	3.5	3.0	6	150

APPENDIX 13

Experimental Run and Factors from RSM for Esterification of SFOUFA with TMP

Run	Factors			
	Molar ratio SFOUFA	Percentage catalyst (%)	Reaction time (h)	Reaction temp. (°C)
1	3.0	1.3	3	130
2	3.5	1.8	5	153
3	3.5	3.0	3	130
4	4.5	2.5	3	130
5	3.5	0.5	5	130
6	3.9	0.5	7	170
7	3.5	2.5	3	130
8	3.0	0.7	3	170
9	3.5	3.0	3	130
10	3.0	0.7	7	130
11	3.9	2.5	7	170
12	3.0	3.0	7	130
13	3.9	1.8	3	153
14	3.9	2.5	7	170
15	3.9	2.5	3	170
16	3.5	1.3	5	154
17	3.0	0.5	7	170
18	3.5	2.5	5	153
19	3.0	0.7	3	170
20	3.5	2.5	7	153
21	3.9	0.5	7	170
22	3.5	0.5	7	130
23	3.5	3.0	3	170
24	3.5	0.7	3	153
25	4.5	1.8	5	153

APPENDIX 14

Experimental Run and Factors from RSM for Esterification of SFOUFA with PE

Run	Factors			
	Molar ratio SFOUFA	Percentage catalyst (%)	Reaction time (h)	Reaction temp. (°C)
1	5.5	1.1	4	140
2	4.0	0.5	10	180
3	4.9	1.7	6	180
4	4.9	1.7	10	156
5	4.5	2.9	4	140
6	4.0	3.0	10	140
7	4.6	2.3	4	164
8	5.5	3.0	4	140
9	4.0	1.7	6	156
10	5.5	2.9	8	140
11	4.9	1.7	10	156
12	5.5	0.5	8	170
13	4.5	3.0	8	166
14	4.4	0.5	8	140
15	5.5	1.8	7	158
16	4.0	3.0	4	180
17	4.9	1.7	6	180
18	4.0	2.2	10	180
19	4.5	3.0	8	166
20	5.5	2.9	4	168
21	4.2	0.5	4	140
22	4.0	1.7	6	156
23	5.5	3.0	10	180
24	4.5	3.0	8	166
25	4.4	0.5	4	170

APPENDIX 15

Experimental Run and Factors from RSM for Epoxidation of SFOUFATMPE

Run	Factors				
	Molar ratio HCOOH	Molar ratio H_2O_2	Percentage catalyst (%)	Reaction time (h)	Reaction temp. (°C)
1	9	4	2	3	50
2	5	4	3	2	59
3	6	1	2	3	40
4	9	1	2	3	53
5	3	4	1	4	60
6	7	3	3	3	41
7	3	2	1	3	54
8	7	2	3	4	60
9	3	4	3	4	44
10	9	1	1	4	56
11	9	4	3	2	40
12	3	1	2	4	50
13	3	1	1	2	40
14	9	1	3	2	60
15	6	3	2	2	50
16	6	3	1	4	40
17	5	3	2	4	51
18	3	2	2	3	40
19	4	4	1	2	60
20	9	2	1	2	41
21	3	4	1	2	40
22	3	2	2	3	40
23	3	2	1	3	54
24	6	3	2	2	50
25	3	1	3	2	60
26	9	4	2	3	50
27	6	1	3	3	47
28	9	1	3	4	40
29	9	4	1	2	60
30	6	1	2	3	60
31	6	1	3	3	47

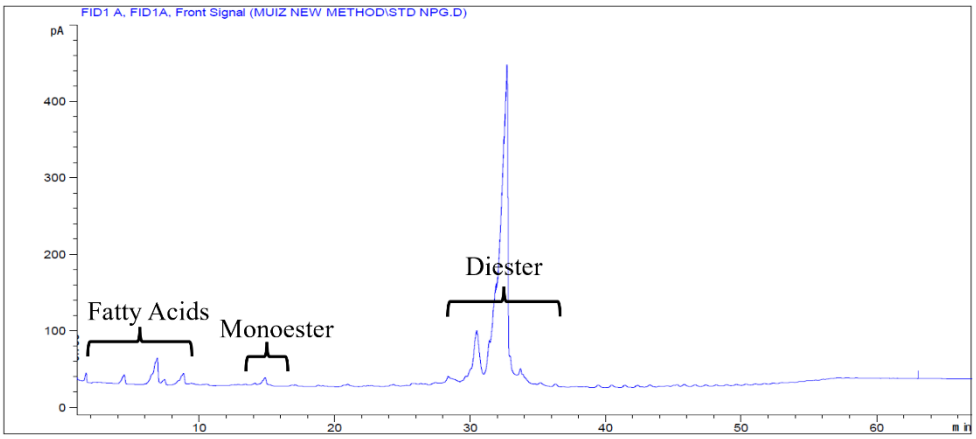
APPENDIX 16

Experimental Run and Factors from RSM for Ring Opening of ESFOUFATMPE

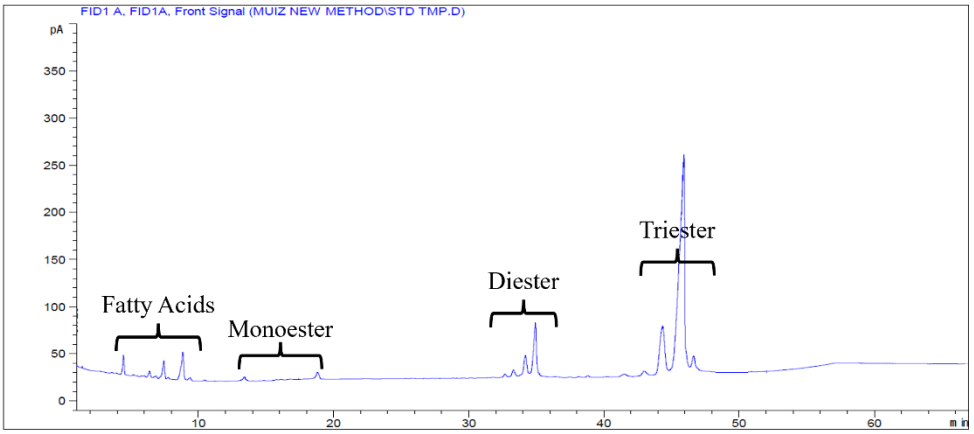
Run	Factors			
	Molar ratio SFOUFA	Percentage catalyst (%)	Reaction time (h)	Reaction temp. (°C)
1	3	1	5	140
2	5	3	5	120
3	4	2	4	140
4	3	3	5	140
5	5	3	3	140
6	4	2	4	130
7	5	1	5	120
8	4	3	4	130
9	3	1	3	140
10	5	1	4	140
11	4	2	4	120
12	5	1	5	120
13	5	2	5	140
14	3	1	5	140
15	5	3	3	140
16	4	2	4	130
17	3	3	3	120
18	5	1	3	130
19	3	2	5	120
20	4	1	3	140
21	5	1	3	130
22	3	2	3	140
23	5	2	4	130
24	5	2	3	120
25	3	1	3	120

APPENDIX 17

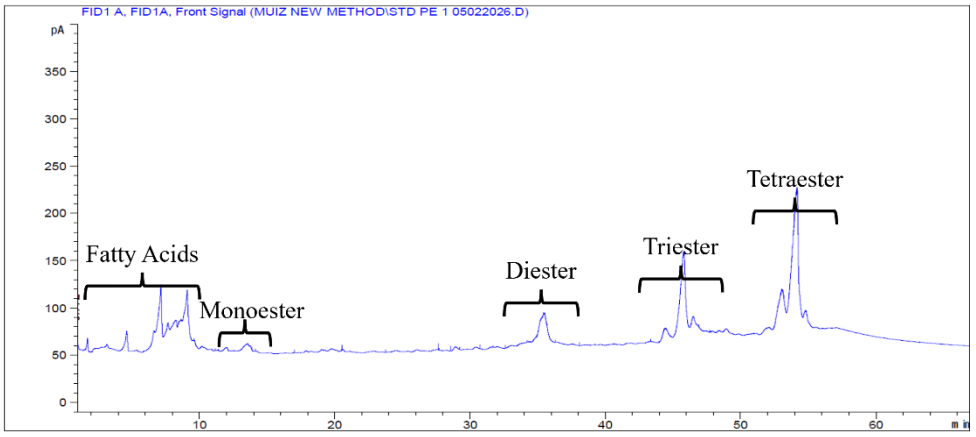
GC-FID Standard Chromatograms of Diester, Triester and Tetraester



Neopentyl Glycol Dioleate Ester (Diester)



Trimethylolpropane Trioleate Ester (Triester)



Pentaerythritol Tetraoleate Ester (Tetraester)

APPENDIX 18

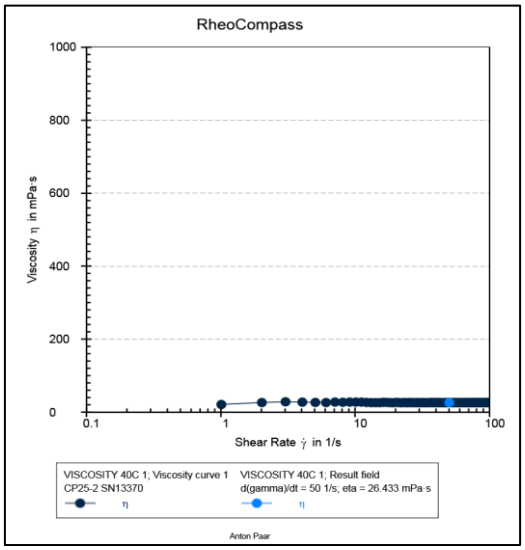
Kinematic Viscosity at 40 °C and 100 °C and Viscosity Index

TABLE 1 Basic Values for *L* and *H* for Kinematic Viscosity in 40 °C to 100 °C System

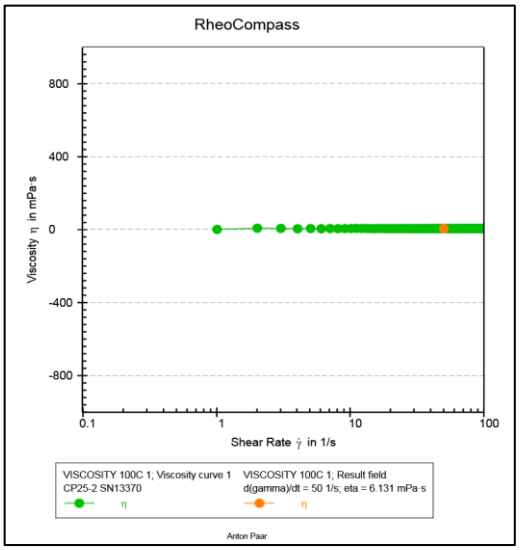
Kinematic Viscosity at 100 °C, mm²/s	*L*	*H*	Kinematic Viscosity at 100 °C, mm²/s	*L*	*H*	Kinematic Viscosity at 100 °C, mm²/s	*L*	*H*	Kinematic Viscosity at 100 °C, mm²/s	*L*	*H*	Kinematic Viscosity at 100 °C, mm²/s	*L*	*H*	Kinematic Viscosity at 100 °C, mm²/s	*L*	*H*
2.00	7.994	6.394	7.00	78.00	48.57	12.0	201.9	108.0	17.0	369.4	180.2	24.0	683.9	301.8	42.5	1935	714.9
2.10	8.640	6.894	7.10	80.25	49.61	12.1	204.8	109.4	17.1	373.3	181.7	24.2	694.5	305.6	43.0	1978	728.2
2.20	9.309	7.410	7.20	82.39	50.69	12.2	207.8	110.7	17.2	377.1	183.3	24.4	704.2	309.4	43.5	2021	741.3
2.30	10.00	7.944	7.30	84.53	51.78	12.3	210.7	112.0	17.3	381.0	184.9	24.6	714.9	313.0	44.0	2064	754.4
2.40	10.71	8.496	7.40	86.66	52.88	12.4	213.6	113.3	17.4	384.9	186.5	24.8	725.7	317.0	44.5	2108	767.6
2.50	11.45	9.063	7.50	88.85	53.98	12.5	216.6	114.7	17.5	388.9	188.1	25.0	736.5	320.9	45.0	2152	780.9
2.60	12.21	9.647	7.60	91.04	55.09	12.6	219.6	116.0	17.6	392.7	189.7	25.2	747.2	324.9	45.5	2197	794.5
2.70	13.00	10.25	7.70	93.20	56.20	12.7	222.6	117.4	17.7	396.7	191.3	25.4	758.2	328.8	46.0	2243	808.2
2.80	13.80	10.87	7.80	95.43	57.31	12.8	225.7	118.7	17.8	400.7	192.9	25.6	769.3	332.7	46.5	2288	821.9
2.90	14.63	11.50	7.90	97.72	58.45	12.9	228.8	120.1	17.9	404.6	194.6	25.8	779.7	336.7	47.0	2333	835.5
3.00	15.49	12.15	8.00	100.0	59.60	13.0	231.9	121.5	18.0	408.6	196.2	26.0	790.4	340.5	47.5	2380	849.2
3.10	16.36	12.82	8.10	102.3	60.74	13.1	235.0	122.9	18.1	412.6	197.8	26.2	801.6	344.4	48.0	2426	863.0
3.20	17.26	13.51	8.20	104.6	61.89	13.2	238.1	124.2	18.2	416.7	199.4	26.4	812.8	348.4	48.5	2473	876.9
3.30	18.18	14.21	8.30	106.9	63.05	13.3	241.2	125.6	18.3	420.7	201.0	26.6	824.1	352.3	49.0	2521	890.9
3.40	19.12	14.93	8.40	109.2	64.18	13.4	244.3	127.0	18.4	424.9	202.6	26.8	835.5	356.4	49.5	2570	905.3
3.50	20.09	15.66	8.50	111.5	65.32	13.5	247.4	128.4	18.5	429.0	204.3	27.0	847.0	360.5	50.0	2618	919.6
3.60	21.08	16.42	8.60	113.9	66.48	13.6	250.6	129.8	18.6	433.2	205.9	27.2	857.5	364.6	50.5	2667	933.6
3.70	22.09	17.19	8.70	116.2	67.64	13.7	253.8	131.2	18.7	437.3	207.6	27.4	869.0	368.3	51.0	2717	948.2
3.80	23.13	17.97	8.80	118.5	68.79	13.8	257.0	132.6	18.8	441.5	209.3	27.6	880.6	372.3	51.5	2767	962.9
3.90	24.19	18.77	8.90	120.9	69.94	13.9	260.1	134.0	18.9	445.7	211.0	27.8	892.3	376.4	52.0	2817	977.5
4.00	25.32	19.56	9.00	123.3	71.10	14.0	263.3	135.4	19.0	449.9	212.7	28.0	904.1	380.6	52.5	2867	992.1
4.10	26.50	20.37	9.10	125.7	72.27	14.1	266.6	136.8	19.1	454.2	214.4	28.2	915.8	384.6	53.0	2918	1007
4.20	27.75	21.21	9.20	128.0	73.42	14.2	269.8	138.2	19.2	458.4	216.1	28.4	927.6	388.8	53.5	2969	1021
4.30	29.07	22.05	9.30	130.4	74.57	14.3	273.0	139.6	19.3	462.7	217.7	28.6	938.6	393.0	54.0	3020	1036
4.40	30.48	22.92	9.40	132.8	75.73	14.4	276.3	141.0	19.4	467.0	219.4	28.8	951.2	396.6	54.5	3073	1051
4.50	31.96	23.81	9.50	135.3	76.91	14.5	279.6	142.4	19.5	471.3	221.1	29.0	963.4	401.1	55.0	3126	1066
4.60	33.52	24.71	9.60	137.7	78.08	14.6	283.0	143.9	19.6	475.7	222.8	29.2	975.4	405.3	55.5	3180	1082
4.70	35.13	25.63	9.70	140.1	79.27	14.7	286.4	145.3	19.7	479.7	224.5	29.4	987.1	409.5	56.0	3233	1097
4.80	36.79	26.57	9.80	142.7	80.46	14.8	289.7	146.8	19.8	483.9	226.2	29.6	998.9	413.5	56.5	3286	1112
4.90	38.50	27.53	9.90	145.2	81.67	14.9	293.0	148.2	19.9	488.6	227.7	29.8	1011	417.6	57.0	3340	1127
5.00	40.23	28.49	10.0	147.7	82.87	15.0	296.5	149.7	20.0	493.2	229.5	30.0	1023	421.7	57.5	3396	1143
5.10	41.99	29.46	10.1	150.3	84.08	15.1	300.0	151.2	20.2	501.5	233.0	30.5	1055	432.4	58.0	3452	1159
5.20	43.76	30.43	10.2	152.9	85.30	15.2	303.4	152.6	20.4	510.8	236.4	31.0	1086	443.2	58.5	3507	1175
5.30	45.53	31.40	10.3	155.4	86.51	15.3	306.9	154.1	20.6	519.9	240.1	31.5	1119	454.0	59.0	3563	1190
5.40	47.31	32.37	10.4	158.0	87.72	15.4	310.3	155.6	20.8	528.8	243.5	32.0	1151	464.9	59.5	3619	1206
5.50	49.09	33.34	10.5	160.6	88.95	15.5	313.9	157.0	21.0	538.4	247.1	32.5	1184	475.9	60.0	3676	1222
5.60	50.87	34.32	10.6	163.2	90.19	15.6	317.5	158.6	21.2	547.5	250.7	33.0	1217	487.0	60.5	3734	1238
5.70	52.64	35.29	10.7	165.8	91.40	15.7	321.1	160.1	21.4	556.7	254.2	33.5	1251	498.1	61.0	3792	1254
5.80	54.42	36.26	10.8	168.5	92.65	15.8	324.6	161.6	21.6	566.4	257.8	34.0	1286	509.6	61.5	3850	1270
5.90	56.20	37.23	10.9	171.2	93.92	15.9	328.3	163.1	21.8	575.6	261.5	34.5	1321	521.1	62.0	3908	1286
6.00	57.97	38.19	11.0	173.9	95.19	16.0	331.9	164.6	22.0	585.2	264.9	35.0	1356	532.5	62.5	3966	1303
6.10	59.74	39.17	11.1	176.6	96.45	16.1	335.5	166.1	22.2	595.0	268.6	35.5	1391	544.0	63.0	4026	1319
6.20	61.52	40.15	11.2	179.4	97.71	16.2	339.2	167.7	22.4	604.3	272.3	36.0	1427	555.6	63.5	4087	1336
6.30	63.32	41.13	11.3	182.1	98.97	16.3	342.9	169.2	22.6	614.2	275.8	36.5	1464	567.1	64.0	4147	1352
6.40	65.18	42.14	11.4	184.9	100.2	16.4	346.6	170.7	22.8	624.1	279.6	37.0	1501	579.3	64.5	4207	1369
6.50	67.12	43.18	11.5	187.6	101.5	16.5	350.3	172.3	23.0	633.6	283.3	37.5	1538	591.3	65.0	4268	1386
6.60	69.16	44.24	11.6	190.4	102.8	16.6	354.1	173.8	23.2	643.4	286.8	38.0	1575	603.1	65.5	4329	1402
6.70	71.29	45.33	11.7	193.3	104.1	16.7	358.0	175.4	23.4	653.8	290.5	38.5	1613	615.0	66.0	4392	1419
6.80	73.48	46.44	11.8	196.2	105.4	16.8	361.7	177.0	23.6	663.3	294.4	39.0	1651	627.1	66.5	4455	1436
6.90	75.72	47.51	11.9	199.0	106.7	16.9	365.6	178.6	23.8	673.7	297.9	39.5	1691	639.2	67.0	4517	1454
												40.0	1730	651.8	67.5	4580	1471
												40.5	1770	664.2	68.0	4645	1488
												41.0	1810	676.6	68.5	4709	1506
												41.5	1851	689.1	69.0	4773	1523
												42.0	1892	701.9	69.5	4839	1541
															70.0	4905	1558

Kinematic Viscosity at 40 °C and 100 °C and Viscosity Index of SFO

40 °C



100 °C

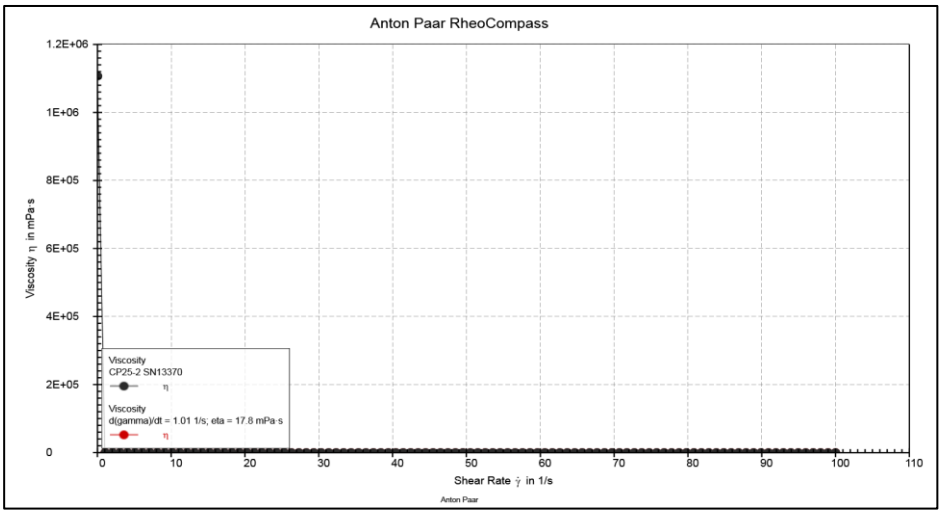


SFO	**40** °C	**100** °C
Density	0.8654	0.8654
mPa.s	26.4330	6.2483
cSt	30.54	7.22

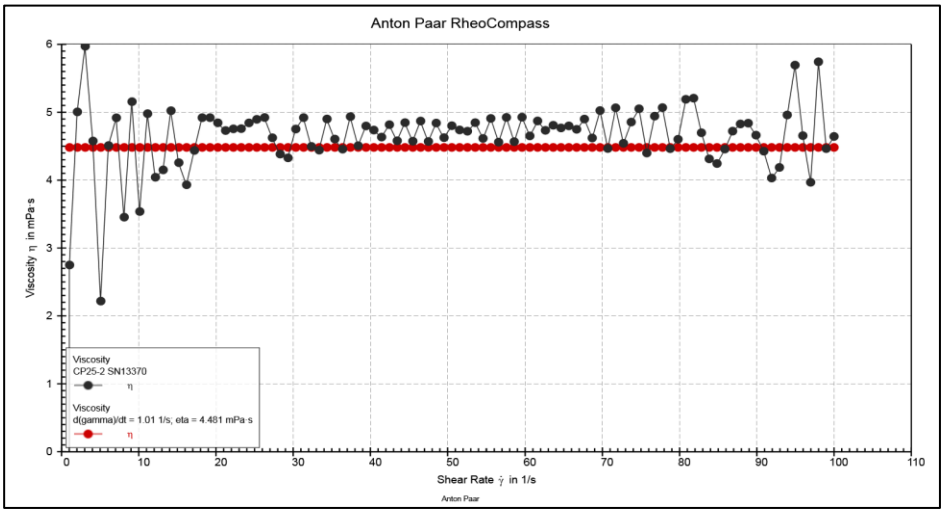
Formula Viscosity Index	:	$\frac{L - cSt \text{ at } 40^{O}C}{L - H} \times 100$
Value from Viscosity table at 100°C	:	L= 82.39 H= 50.69
Viscosity Index	:	163.56

Kinematic Viscosity at 40 °C and 100 °C and Viscosity Index of SFOUFANPGE

40 ºC



100 ºC

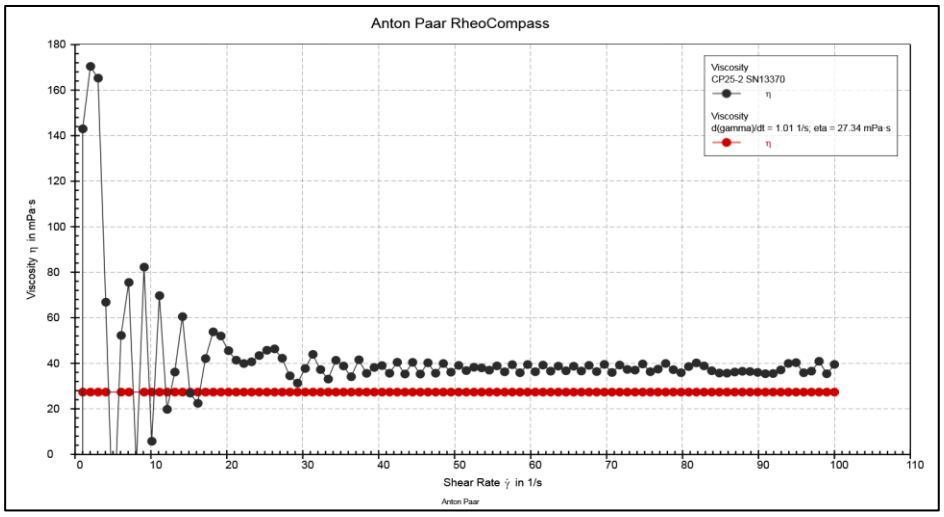


SFOUFANPGE	**40** ºC	**100** ºC
Density	0.838	0.838
mPa.s	17.800	4.481
cSt	21.24	5.35

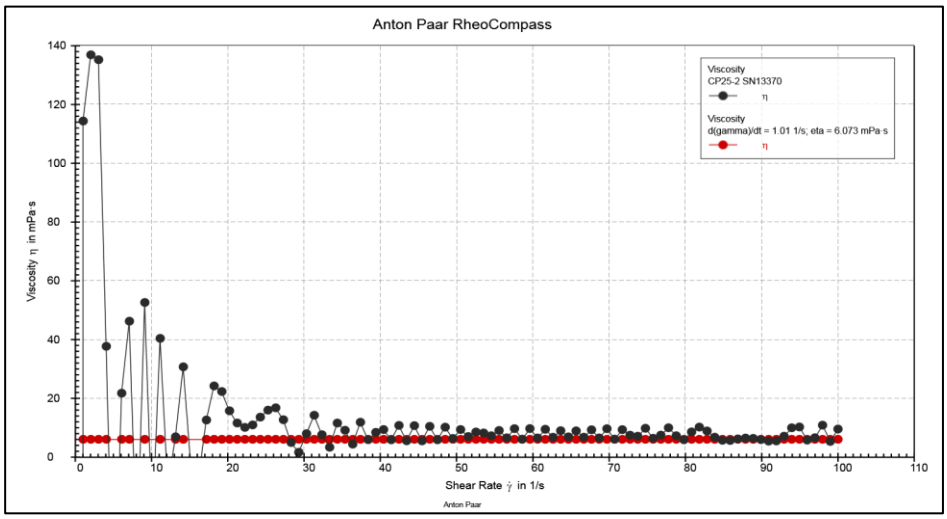
Formula Viscosity Index	:	$\frac{L - cSt\ at\ 40^{O}C}{L - H} x\ 100$	
Value from Viscosity table at 100ºC	:	L= 47.31	H= 32.37
Viscosity Index	:	174.5	

Kinematic Viscosity at 40 °C and 100 °C and Viscosity Index of SFOUFATMPE

40 ºC



100 ºC

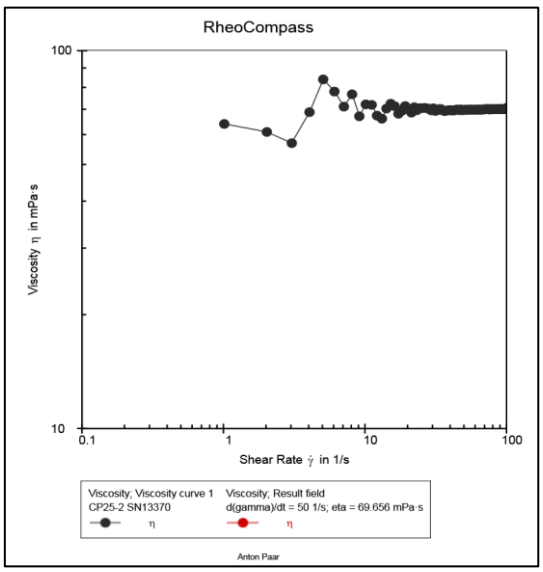


SFOUFATMPE	**40** ºC	**100** ºC
Density	0.842	0.842
mPa.s	27.340	6.073
cSt	32.47	7.21

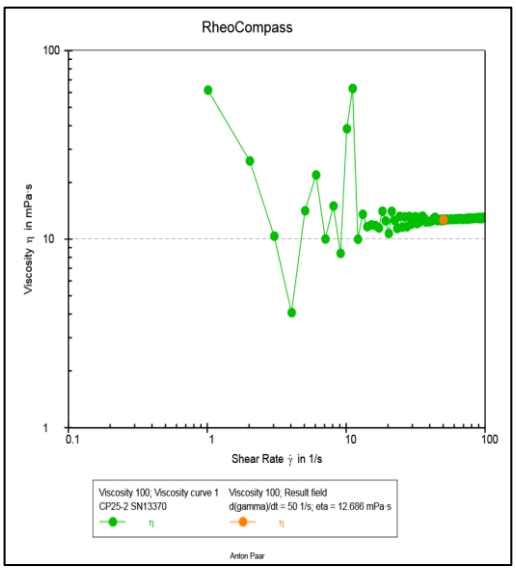
Formula Viscosity Index	:	$\frac{L - cSt \text{ at } 40^{O}C}{L - H} x\ 100$	
Value from Viscosity table at 100ºC	:	L= 82.39	H= 50,69
Viscosity Index	:	157.48	

Kinematic Viscosity at 40 °C and 100 °C and Viscosity Index of SFOUFAPEE

40 ºC



100 ºC

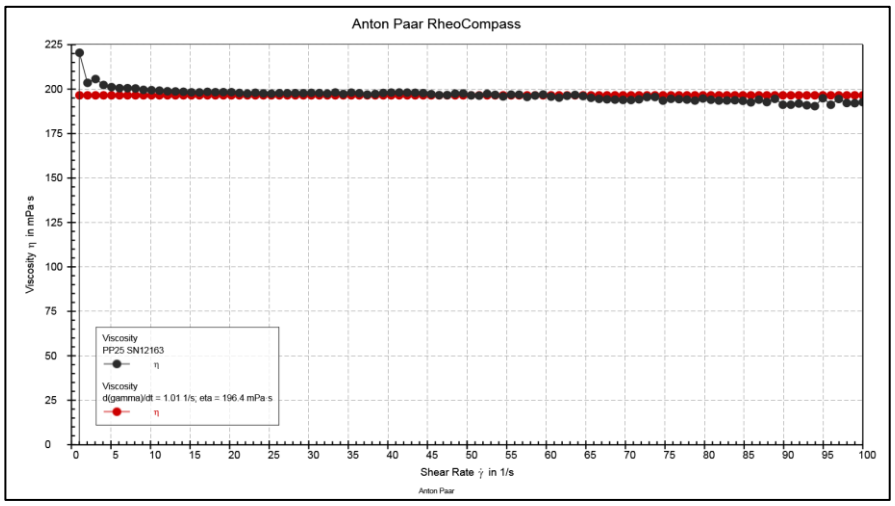


SFOUFAPEE	**40** ºC	**100** ºC
Density	0.8654	0.8654
mPa.s	69.656	12.686
cSt	80.49	14.66

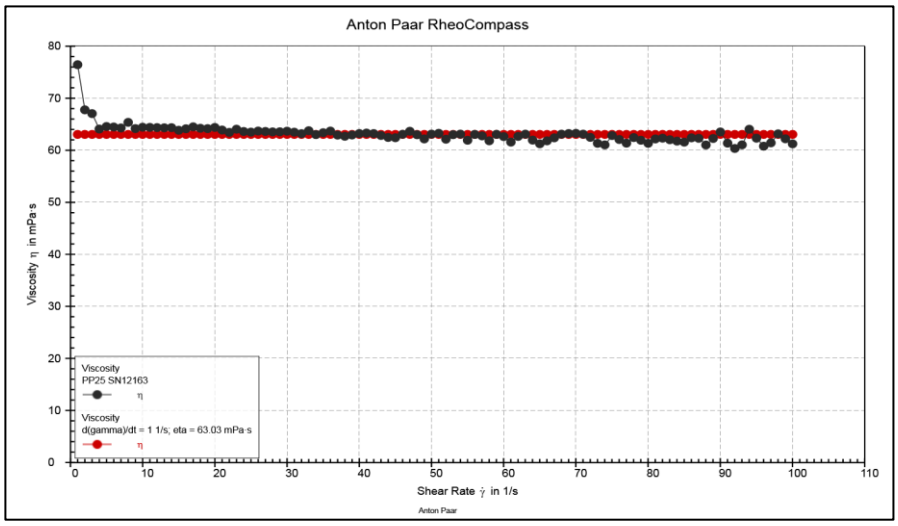
Formula Viscosity Index	:	$\frac{L - \text{cSt at } 40^{O}C}{L - H} \text{x } 100$	
Value from Viscosity table at 100ºC	:	L= 286.4	H= 145.3
Viscosity Index	:	145.93	

Kinematic Viscosity at 40 °C and 100 °C and Viscosity Index of ESFOUFATMPE

40 ºC



100 ºC

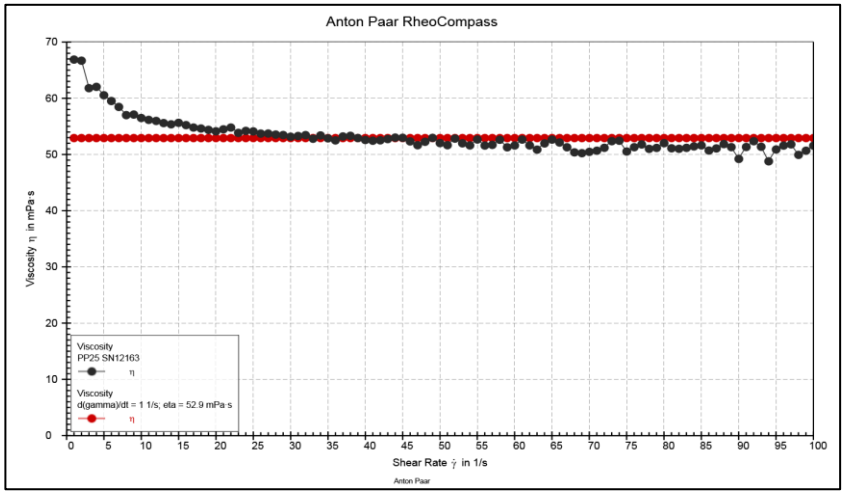


ESFOUFATMPE	**40** ºC	**100** ºC
Density	0.943	0.943
mPa.s	196.40	63.03
cSt	208.27	66.84

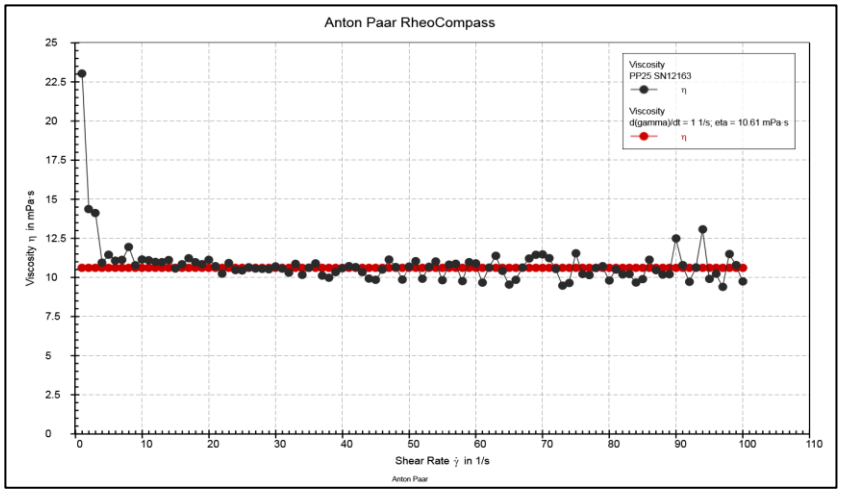
Formula Viscosity Index	:	$\frac{L - cSt \text{ at } 40^{O}C}{L - H} x\ 100$
Value from Viscosity table at 100ºC	:	L= 4517 H= 1454
Viscosity Index	:	140.67

Kinematic Viscosity at 40 °C and 100 °C and Viscosity Index of DOSFOUFATMPE

40 ºC



100 ºC



DOSFOUFATMPE	**40** ºC	**100** ºC
Density	0.8813	0.8813
mPa.s	52.90	10.61
cSt	60.02	12.03

Formula Viscosity Index	:	$\frac{\text{L} - \text{cSt at } 40^{\text{O}}\text{C}}{\text{L} - \text{H}} \text{x } 100$	
Value from Viscosity table at 100ºC	:	L= 201.9	H= 108.0
Viscosity Index	:	151.1	

AUTHOR'S PROFILE



Muhammad Muizzuddin Khairuddin obtained his Bachelor of Science in Chemistry (Hons.) with Management in 2022 from Universiti Teknologi MARA (UiTM), Negeri Sembilan Branch, Kuala Pilah Campus. He subsequently pursued a Master of Science (Chemistry) for one year before being upgraded to the Doctor of Philosophy Sciences program. His PhD research focuses on the development of biolubricants derived from sunflower oil, with particular emphasis on investigating the physicochemical properties of biolubricants produced from various types of backbone for biolubricant. In addition to his academic research, Muizzuddin is actively involved in chemistry-related innovation and has participated in numerous Corporate Social Responsibility (CSR) programs, both locally and internationally, including in Indonesia. His innovative works have received several gold awards at innovation competitions, reflecting the significance and impact of his research and product development efforts.

LIST OF PUBLICATIONS:

Muhammad Muizzuddin Khairuddin, Asiah Abdullah, Nur Nadia Dzulkifli and Nurazira Mohd Nor (2023). Optimization of Sunflower Oil Hydrolysis Using The D-optimal Design. *Malayian Journal of Analytical Sciences, 27*(5), 1062-1078.

Muhammad Muizzuddin Khairuddin, Asiah Abdullah and Nurazira Mohd Nor (2024). Synthesis and Characterization of Sunflower Oil Unsaturated Fatty Acid

Pentaerythritol Ester as Green Biolubricant Base Stock. *Malaysian Journal of Chemistry, 26*(3), 373-382.

Muhammad Muizzuddin Khairuddin, Asiah Abdullah and Nurazira Mohd Nor (2024). Physicochemical Properties, Fatty Acids Composition and Characterization of *Helianthus Annuus*. *Malayian Journal of Analytical Sciences, 28* (6), 1258 - 1269.

Muhammad Muizzuddin Khairuddin, Asiah Andullah, Nurul Fatin Nazira Norshahimy, Muhammad Affifuddin Mat Sa'ad and Nurazira Mohd Nor (2025). Separation of Sunflower Oil Fatty Acds Mixture to Saturated and Unsaturated Fatty Acids Via Methanol Crystallization Method. *Malaysian Journal of Chemistry, 27*(3), 224-236.

Muhammad Muizzuddin Khairuddin, Asiah Abdullah, Sheikh Ahmad Izaddin Sheikh Mohd Ghazali, Is Fatimah, Nur Sulihatimarsyila Abd Wafti and Nurazira Mohd Nor. Stepwise Production of Potential Biolubricant Base Stock from Sunflower Oil: Hydrolysis, Fatty Acid Separation and Esterification. *Trends in Sciences, 23*(9), 13023.

LIST OF CONFERENCES:

1. Third Virtual International Symposium on Sciences 2023 (3rd VISoS 2023). **(Presenter)** Date: 5-6 September 2023.
2. Second International Science and Technology Colloquium (2nd i-COSTEH 2024). **(Presenter)** Date: 9-10 October 2024.

LIST OF INNOVATIONS:

1. Helianthus 68 Lubricant: Potential Biolubricant Base Stock from Sunflower Oil. Negeri Sembilan International Exposition 2024 (NSIEx 2024). (**GOLD**) Date: 10 October 2024.
2. Sunflower Oil-Based Biolubricant: A Sustainable Alternative to Petroleum-Based Lubricants. Graduate Digital Invention, Innovation and Design 2025 (GDIID 2025). (**GOLD**) Date: 1 July 2025.
3. Biolube-S: Nature-Powered Sustainable Lubricant. Invention, Innovation and Design Exposition 2025 (iidex2025)**. (Bronze)** Date: 28-30 October 2025.

LIST OF COPYRIGHT:

1. Biolube-S: Nature-Powered Sustainable Lubricant. (Notification number: CRLY2025W10687)